**Multicompartmental biomaterials via electrohydrodynamic co-jetting**

**by**

**Srijanani Bhaskar**

A dissertation submitted in partial fulfillment
of the requirements for the degree of
Doctor of Philosophy
(Macromolecular Science and Engineering)
in the University of Michigan
2011

**Doctoral Committee**

Associate Professor Joerg Lahann, Chair
Professor Ronald G. Larson
Professor David C. Martin
Professor Michael J. Solomon
Assistant Professor Omolola Eniola-Adefeso

To my parents
To thatha (my deceased grandfather)

## ACKNOWLEDGEMENTS

It is a pleasure to have been a part of the wonderful family that is the University of Michigan for the last four and a half years and pursue graduate education in this esteemed institution. The memories that I have made here with my friends and colleagues will be forever etched in my heart.

First and foremost, I would like to thank my advisor, Professor Joerg Lahann. I do not have enough words to express my gratitude for his guidance and mentorship. He has always encouraged me to find solutions by asking the right questions, and above all, persevere in the face of failure. Under his guidance, I daresay that I have grown tremendously not only as a researcher but also as a human being. I hope I can be like him someday. I would also like to thank the other members of my thesis committee, Prof. Michael J. Solomon, Prof. David C. Martin, Prof. Omolola Eniola-Adefeso and Prof. Ronald Larson for their constant support and encouragement.

I would like to express my sincere gratitude to all my collaborators outside of UM, Prof. Samir Mitragotri and Nishit Doshi from the University of California, Santa Barbara, and Prof. Nicholas A. Voelcker and Dr. Christopher A. Gibson

from Flinders University, Australia. These collaborations were extremely fruitful, they resulted in great research as well as great friendships!

I have had the immense good fortune of learning from a multitude of senior grad students as well as post doctoral scholars. I would like to thank Dr. Kyung-Ho Roh who was the first student to perform electrohydrodynamic co-jetting experiments in our lab and familiarized me with the concept and technique. I would like to thank Dr. Mutsumi Yoshida, who is a treasure trove of knowledge, and trained me in general lab practices and very patiently explained all concepts from scratch. I am really indebted to her for her wonderful guidance. I would like to thank Dr. Himabindu Nandivada, who has been a wonderful friend. I wish to express my sincere gratitude to all the wonderful post doctoral scholars who have not only been amazing collaborators, but also valuable mentors, namely, Dr. Suparna Mandal, Dr. Sangyeul Hwang, Dr. Sampa Saha, Dr. Hsien-Yeh Chen, Dr. Tae-Hong Park, Dr. Kyung-Jin lee, Dr. Dongwoo Lim, Dr. Aiwu Sun and Dr. Abbass Kazemi.

I would like to extend a warm thank you to the undergraduate students whom I had the pleasure of mentoring, and who played a major role in the execution of experiments, Kelly Marie Pollock, Laura Chang, Jonathan Hitt and Nicholas Clay. I would also like to thank the all past and present members of the Lahann lab who added to the fun of this journey: Aftin Ross, Xiaopei Deng, Jaewon Yoon, Asish Misra, Thomas Eyster, Dr. David Peng, Sahar Rahmani, Asish Misra, Dr. Yaseen Elkasabi, Allison Bourke, Allan Ahmadi, and Sridhar Valluri. In addition, I would like to express my gratitude for all the generous intellectual and material

help from members of the Kotov, Solomon, Glotzer and Tuteja groups. I would like to acknowledge Chris Edwards, Shelly Almburg, Sasha Meshinchi, Bruce Donohoe and Dotty Sorenson from the microscopy and image analysis laboratory (MIL), and John Mansfield, Kai Sun and Haiping Sun at EMAL for teaching me the intricacies of optical and electron microscopy. They made my work simpler.

I would also like to express my gratitude to all my friends in the Macro Program, especially its ray of light, Nonna Hamilton.

Last, but not the least, I would like to thank my family, Mr. Salem Ramaswamy Bhaskar, Ms. Neela Bhaskar, Dr. Ajit Bhaskar, Vignesh Sankaran and Nandini Vishwanath who made this dream possible with their unending encouragement, faith and support. I could not have done this without them.

## TABLE OF CONTENTS

## LIST OF FIGURES

# CHAPTER 1

# INTRODUCTION

## 1.1 Motivation and background

### 1.1.1 Design parameters for biomaterials

Biomaterials, defined as 'materials intended to interact with biological systems,[1] have revolutionized modern medicine: they form the basis of heart valve prostheses, artificial hip joints, dental implants, intraocular lenses, ventricular assist devices, hybrid artificial organs and scaffolds for regenerative medicine.[1] Spanning over length scales of a few nanometers to a few centimeters, and equipped with precisely definable properties, they have not only emerged as therapeutic agents but also as an important tool to improve our fundamental understanding of interactions between cells and their surrounding media, examples include stem cell proliferation,[2] phagocytosis[3] and endosomal trafficking.[4] In spite of tremendous growth in this field over a relatively short span of ~30 years, there are several challenges that need to be addressed: for instance, in cancer therapeutics, novel synthetic strategies are needed to assemble particles that exhibit long circulation times and localized tumor targeting,[5] in tissue engineering, there is a need for scaffolds that not only match on a macroscopic level the properties of organs they would replace but also

mimic the complex micro/nanoscale internal environment present in the ECM.[6] There is always room for faster, cheaper, yet highly orthogonal diagnostic assays.[1, 7] In order to tackle these challenges, a lot of attention is being devoted to custom-tailored nano- and microstructured materials with a tunable gradient of properties and structures that generate a predictable set of responses to improve materials design.[8] Researchers have often resorted to chemistry based approaches to address this issue, examples include combinatorial screening of polymers for gene delivery,[9] synthetic antigen capture molecules via click chemistry,[10] liposomes, aptamers and siRNA therapeutics.[11] However, it is increasingly being recognized that crucial properties of materials are driven by their physical attributes in addition to chemical structure. Physical attributes include size, shape,[12] elastic modulus, surface microstructure, porosity, roughness, and anisotropy.[8] For instance, particle shape has been found to affect phagocytosis by macrophages,[3] cellular internalization[13] and circulation time.[14] Nature frequently utilizes physical attributes to induce function. The best example are perhaps red blood cells (RBCs), that escape clearance in the sinusoidal slits of the spleen owing to their discoid shape and circulate for long times in the body.[8] Indeed, shape-mimicry of RBCs was recently used to synthesize particles with improved function.[15, 16] Control over particle shape has been demonstrated previously via photolithographic techniques,[17] fabrication in non-wetting templates,[18], modification of spherical particles via stretching in solvents[19] and electrospraying.[20] Particle size is also an important property. Several key factors that influence the performance of particle based formulations

for drug delivery depend on size: circulation, immune response, opsonization, internalization, localization and transport.[21-23] Examples of methods that offer particle size control include microfluidic flow focusing,[24] emulsion polymerization[25] and self-assembly.[26] Stiffness, another physical property, is known to translate into biochemical signals that can influence formation of stem cell differentiation markers.[2, 27-29] Overall, it is abundantly clear that if the above-mentioned physical properties of biomaterials can be tailored in conjunction with their chemical properties, precise control of the corresponding biological response can be achieved. This dissertation focuses on control of a physical attribute that has only recently come to attention: anisotropy or distribution of matter. This is described in the next section.

### 1.1.2 Importance of Anisotropy

Since DeGennes' Nobel lecture in 1991,[30] where he first employed the term 'Janus', after the two-faced Roman God, to describe amphiphilic colloids that could potentially act as 'breathable skins' or media for chemical exchange at an air-water interface, there has been a tremendous interest in the synthesis of particles with anisotropic surface or bulk structure for applications in a variety of fields such as bionanotechnology,[31] medicine[32] and electronics.[33] The concept of control of anisotropy or distribution of matter in a micro/nanostructure is inspired by nature itself.[8] Perhaps the best example of an anisotropic microstructure is the basic building block of life, a biological cell, comprised of several organelles, which perform distinct functions controlled in space and over time.[8] This anisotropy extends to tissues, organs and organ systems and finally

the entire body to improve efficiency and provide overall sustenance. In order to mimic the analogy between synthesis of complex molecular structures in the body and complex assemblies of micro/nanoparticles, it is critical to endow particles with anisotropy and directionality.[34] An example of an anisotropic tissue is the cardiac muscle tissue, where cardiac muscle fibers are surrounded by and enclosed within a honeycomb shaped network of collagen fibers, which create a directionally dependent anisotropy w.r.t electrical and mechanical properties.[35] This feature was recently mimicked in cardiac tissue engineering scaffolds to culture cardiomyocytes closely resembling natural myocardium.[35] Cellular metabolism is driven by transport to and from interfacial anisotropy that exists between the cell and its surrounding media, with the membranes themselves being formed by self-assembly of amphiphilic proteins.

The simplest arrangement of two compartments can be visualized in the form of core/shell architectures, where a shell compartment surrounds a central unit.[36] A large number of multifunctional core shell particles have been synthesized,[32, 37-40] some of which have already demonstrated biomedical utility by releasing two different drugs.[32] Oriented assemblies of cells and biphasic Janus particles have been employed to create biohybrid materials wherein the orientation (and change thereof) can signal changes in the cells and their surrounding environment.[41] Anisotropy opens up a wide variety of applications, as individual compartments may have distinct chemical compositions or can be selectively surface-modified. For example, one could envision sequential release of anti-angiogenic and chemotherapeutic drugs from multicompartmental

particles made of biodegradable polymers with independent release kinetics. Coupled with incorporation of imaging agents in a slowly degrading compartment, multicompartmental particles offer possibilities of real time monitoring of circulation and degradation behavior, combining therapeutics with diagnostics. Anisotropic particles may enable complex hierarchical assemblies needed for a diverse array of applications such as photonic band gap materials,[42, 43] multiplexed bioassays,[7] biological sensors, biohybrid materials[41, 44] and miniaturized energy storage and conversion devices.[45] By combining properties such as shape, size, surface microstructure, and chemical structure along with compartmentalization, the design space can be amplified over orders of magnitude, forging a way for the next generation of smart materials.[46] The next section provides a brief overview of the recent advances in the fabrication of anisotropic micro/nanostructures.

### 1.1.3 Current techniques for fabrication of anisotropic materials

Anisotropic particles can exist in several forms: selectively surface modified isotropic particles,[47] particles with anisotropy extending into the bulk[48] or particles made by the fusion of two or more particles.[49] Techniques for anisotropic particle fabrication and their assemblies have been the subject of numerous excellent reviews.[34, 50-54] One of the early methods for synthesis of Janus particles was via a spinning disk to yield 100 μm diameter bichromal balls used in a Gyricon display.[55] Perhaps the simplest and most commonly employed synthetic strategy for Janus particles is the spatio-selective surface modification of isotropic particles. This can be achieved via masking of one

hemisphere followed by the surface modification of the other, for instance deposition of particles onto a flat substrate followed by surface modification of the top exposed half via metal[56, 57] or vapor deposition,[58] layer by layer adsorption,[59] UV-induced polymerization[60] or plasma polymerization.[61] Variations of this process include the Pickering emulsion technique developed by Granick et al,[58, 62] selective particle modification via microcontact printing to produce half raspberry[63] and snowman[64] shaped particles, and use of directional reactive fluxes for particle modification that eliminate the need of partial masking.[65] Though simple and relatively easier to perform, selective masking approaches produce very low yields.

A flow focusing technique developed by Kumacheva et al[66] utilized the shear influenced breakup of a bi- or tri-component monomer droplet in a microfluidic device followed by photopolymerization to produce monodisperse bi- and tri-compartmental particles. A combination of microfluidic flow focusing and photolithography was developed by Doyle et al[17, 67-69] to produce particles with highly complex shapes as well as internal architectures, which were employed for multiplexed biomolecule analysis.[7] Other examples of Janus particles via microfluidic and lithographic techniques include thermally induced spatial polymer aggregation in a microfluidic droplet[70] and particle replication in low surface energy templates.[13, 18] While microfluidic techniques are potentially scalable and provide high efficiency and monodispersity, these techniques are suitable for production of particle sizes of the order of tens of microns. Another design approach is template assisted self-assembly of isotropic colloidal particles

wherein assembly occurs due to minimize local or global energy, resulting in particles with good mechanical stability.[71, 72] Complex geometries can be attained by controlling the size and shape of the pattern in the template and of the particles undergoing assembly. Other techniques for fabricating organic and inorganic anisotropic particles include selective crosslinking of polybutadiene segments of block terpolymers,[73] lithographic patterning of microspheres,[47] electrochemical[74] and photochemical[75] reduction, templating of porous membranes[76, 77] and nanotubes,[78] surfactant aided growth,[79] seeded polymerization[80, 81] and processes based on controlled surface nucleation.[82]

Desirable attributes for any process for production of anisotropic particles, particularly for biomedical applications include simplicity, high efficiency, scalability and above all versatility via control over particle/fiber attributes such as size, shape, number of independent compartments among others. While several of the above mentioned processes offer one or more of these attributes, from the standpoint of versatility and scalability, the electrohydrodynamic co-jetting process pioneered by Lahann *et al* [83] is particularly attractive due to its ability to produce a vast repertoire of particles through control of select process variables. This process, which forms the framework of this dissertation, is described in the next section.

### 1.1.4 Electrohydrodynamic co-jetting

When a liquid droplet is subjected to an electric field, it experiences two major forces: coulombic forces due to the external field, and repulsive forces between the surface charges on the droplet. At a certain critical field strength, the

coulombic forces exceed the surface tension. This results in the distortion of the droplet into a conical shape and an electrified jet containing millions of secondary droplets ensues from the tip of this cone.[84, 85] This jet is initially linear due to stabilizing longitudinal stresses,[86] which relax along the jet. Then the jet takes a spiral path due to repulsive forces between surface charges in the droplets.[36, 87] This process, called electrohydrodynamic atomization (EHDA), is capable of generating fine sprays (with droplet diameters ranging from few nanometers to several microns) and is applied widely in generation of aerosols[88], and also in mass spectroscopy.[89]

The phenomenon of formation of charged jets on subjecting a liquid to electric fields was first observed by Rayleigh, who described the radius of the charged jet, $r_j$ as:

$$r_j = \left(\frac{9\varepsilon_0\gamma}{2\pi^2}\right)^{1/3}\left(\frac{F}{I}\right)^{2/3} \quad \ldots(1)$$

Where $\varepsilon_0$ , $\gamma$ , $F$ and $I$ are the liquid dielectric constant, liquid surface tension, flow rate and injection current respectively.[20, 90, 91] Zeleny then studied the formation of electrified sprays of varying viscosities using ethanol and glycerine.[92] Experimental evidence as well theoretical explanation for existence of the conical shape of the protrusion from which the spray is ejected was provided by Taylor in 1964,[93] and for this reason the conical apex of the droplet is often referred to as the Taylor cone. When EHDA is carried out from a polymer solution, the high surface: volume ratio of droplets results in rapid solvent

evaporation and particle formation. Higher solution viscosities lead to more continuous jets, and in this case solvent evaporation leads to fiber formation, otherwise known as electrospinning.[36] Beginning with the initial observations of Raleigh and Zeleny, the field of EHDA has simply exploded in the last 20 years, with a variety of aligned and nonwoven electrospun fibers being synthesized from polymers,[36] inorganic materials,[94] metal-organic frameworks,[95] extracellular matrix components,[96] and even live cells.[97] Electrospun fibers are being applied in areas ranging from fuel cells,[98] water purification and detoxification[99] to gas sensors,[100] clean energy,[101] photocatalysis[102] and regenerative medicine.[103] Fibrous networks have been extensively investigated for biomedical applications such as drug delivery,[104] stem cell engineering,[105] as well as regeneration of tissues such as bone, nerves, and urinary bladder.[106-108]

As indicated in Eq 1, several parameters influence jet breakup and particle characteristics during EHDA. These can be classified into a) Process parameters such as flow rate, electric field strength and collection distance, b) solution parameters, including viscosity, conductivity, surface tension, volatility and dielectric constant of the solution as well the medium into which the jet is being ejected, c) Material parameters such as polymer molecular weight, molecular weight distribution, radius of gyration and persistence length, and finally d) environmental parameters such as temperature, dielectric constant and relative humidity of the atmosphere into which the jet is sprayed. Thus, a complex interplay of all these forces can be employed to create particles for a host of applications, which have been the subject of numerous review articles.[36, 109-112]

The electrohydrodynamic co-jetting and co-spinning process reported in this dissertation is derived from EHDA. During co-jetting, added complexity is introduced via incorporation of two or more capillaries arranged in a side by side configuration.[48, 83] The droplet that is generated at the tip of the capillary comprises of two or more solutions, the interface between which is maintained under laminar flow. Application of an electric field results in Taylor cone formation, jet ejection and particle or fiber formation via solvent evaporation. The resulting particles are 'bicompartmental', i.e. the two components are kinetically trapped into a side-by-side configuration. This process was pioneered by Roh, Martin and Lahann[83] for aqueous solutions of polyacrylic acid-co-acrylamide polymers, and is schematically shown in Figure 1.1.

Electrohydrodynamic co-jetting offers several advantages: the experimental setup is extremely easy to assemble and cost effective, furthermore, drugs and other functional biomolecules can directly be incorporated into particles by dissolving them along with the polymers in the jetting solution. This gives 100% encapsulation efficiency, unlike double emulsion particle preparation methods. It is noteworthy that while EHDA is capable of producing sprays even in the absence of a Taylor cone, whereas in case of electrohydrodynamic co-jetting, the presence of a Taylor cone is crucial to maintain the interface between the different solutions inside the compound droplet. Failure to achieve this mode can result in multiple sprays, compromising particle anisotropy. Hence, only Taylor cone mode EHDA is described in this dissertation.

Figure 1.2 represents the experimental setup used for fabrication of anisotropic particles. It contains three major components: a stainless steel capillary outlet comprising of two or more needles held together in the desired configuration (the simplest being two capillaries held together in a side by side fashion, resulting in bicompartmental particles), a voltage source for supplying the desired DC potential to the needles, and a syringe pump for controlling solution flow rate. The capillary needle assembly is attached to the syringe pump and the assembly is placed atop a Plexiglas box, at the bottom of which is a grounded aluminum foil that acts as the collecting substrate for particles. The distance between the needles and the substrate can be controlled through a lab-jack.

Due to the very large parameter space involved, the dynamics of jet breakup and particle formation are rather complicated. For every solution, there is a threshold flow rate below which the Taylor cone mode cannot be sustained.[84] Three jet breakup modes have been identified: (a) at low flow rates and currents, the jet breakup happens due to axisymmetric or varicose instabilities. This mode of jet breakup is commonly observed in organic solutions with low dielectric constants. (b) As flow rate increases, the current through the droplet increases, due to which the surface charge on the jet also increases. Above a certain surface charge, jet break-up occurs due to lateral instabilities in the jet, also called kink instabilities, which produce a whipping motion in the jet. (c) At even higher charges, the jet is no longer circular; this is known as the ramified breakup mode.[84] Jet thinning during electrospinning is believed to be

governed by electrically driven bending instabilities.[113] In electrohydrodynamic co-jetting, the process becomes even more complex due to the involvement of multiple solutions.

## 1.2 Objectives of this work

The major objectives of this dissertation are

1. To fabricate multicompartmental particles and fibers from commercially available, biodegradable poly(lactide-co-glycolide) (PLGA) based copolymers for biomedical applications. This will involve the electrohydrodynamic co-jetting process, hitherto demonstrated only for aqueous hydrogel solutions[83] to be carried out of organic solutions of hydrophobic PLGA polymers. A change in the solvent system results in a shift in solution and process properties and influences the mechanism of jet breakup. Further complexity is introduced by simultaneous flow of two or more solutions in a side by side manner.
2. To synthesize, via precise control of the exhaustive parameter space in electrohydrodynamic co-jetting, a library of micro/nanostructures with an extensive range of properties and narrow size distributions, including but not limited to size, shape, internal architecture, surface chemistry, surface and bulk microstructure, and number of independent compartments, from a wide range of biodegradable and biocompatible materials. The above mentioned properties would not only be tailored for the particle as a whole

but also in between different compartments of the same particle. This would exponentially increase the complexity and variety in the materials' scientist's toolbox.

3. To demonstrate the applicability of multicompartmental particles and fibers synthesized above in areas such as displays (this may be accomplished in two ways, anisotropic encapsulation of magnetite nanocrystals, or by impacting visibility of individual compartments by controlling their size. This in turn can be achieved by incorporating polymers with different swelling characteristics in each compartment), anisotropic scaffolds for tissue engineering, anisotropic particles as building blocks for assembling higher order structures, and particles for biosesing and theranostics.

### 1.3 Overview of the dissertation

With an understanding behind the need for degradable anisotropic micro/nano-materials in areas such as drug and gene delivery, tissue engineering, sensing, and controlled assembly based on the design parameters of biomaterials outlined in the introduction, an overview of this dissertation is now presented.

**Chapter 2** describes the proof of concept of fabrication of bicompartmental particles and particles from electrohydrodynamic co-jetting of PLGA, using chloroform and DMF as solvents. Design principles such as differences between electrohydrodynamic co-jetting in aqueous and organic

solutions, selection of chloroform as the primary solvent, DMF as co-solvent, effect of solution and process properties on jet-breakup, jet-stability and final structure obtained (i.e. particle or fiber) are described in detail. In addition, characterization tools for anisotropic particles and fibers such as Scanning Electron Microscopy (SEM) and Confocal Laser Scanning Microscopy (CLSM), which are the two major techniques employed frequently in this dissertation, would also be introduced. The bicompartmental nature of particles and fibers is conclusively established via their spatioselective surface modification using Huisgen 1, 3-dipolar cycloaddition reaction.[114]

In the first part of **chapter 3**, the jetting parameter space is explored in greater detail. A solution parameter, concentration, and a process parameter, flow rate are chosen and their systematic control over a specified range is shown to control two key particle attributes: size and shape, whereby discoid, rod-like and spherical bicompartmental particles of varying diameters and aspect ratios are fabricated. Furthermore, control over the number of compartments is shown: tri- and tetracompartmental PLGA particles are synthesized by simply increasing the number of capillaries carrying PLGA solutions. Quantitative analysis of compartmentalization is carried out via flow cytometry.[115] As an example of physical attributes of particles providing key function, the fabrication of red-blood cell mimicking biomaterials using PLGA particle templates in turn produced via electrohydrodynamic jetting is shown in the second part of chapter 3.[15]

In **Chapter 4**, electrohydrodynamic co-spinning is employed to produce aligned multicompartmental microfiber scaffolds with precisely engineered,

micrometer-scale patterns. Because the local structure of the cellular microenvironment plays a pivotal role for many biological functions, a wide range of methods have been developed to design precisely engineered substrates for fundamental biological studies and biotechnological applications. To date, most of this work has been limited to flat substrates, where a vast variety of microstructures has been generated using micro- and nanopatterning methods. At the same time, fiber-based scaffolds have been widely used as cell culture substrates because of their superior recognisability by cells and their ability to provide a three-dimensional growth environment. However, these three-dimensional scaffolds are typically not amendable to the type of sophisticated microstructuring known for two-dimensional scaffolds. Therefore, microstructured fiber scaffolds have long been sought after as the missing link between precisely engineered two-dimensional substrates and porous three-dimensional structures. In this chapter, fibers with two, three, four and even seven independent compartments are synthesized via a highly stable electrohydrodynamic co-jetting process that does not exhibit the bending instabilities seen previously in electrospinning,[113] where individual compartments have distinct chemical compositions or are selectively surface-modified. Furthermore, control over orientation, size, and arrangement of the fiber compartments in a highly predictable fashion is shown.[116] When multicompartmental fiber scaffolds are modified via spatially controlled peptide immobilization, a unique type of scaffold is obtained, which exhibits highly selective cell guidance at spatial resolutions that have thus far been exclusively reserved for flat substrates.

Encouraged by the remarkable degree of control over fiber internal architecture that can be exerted via electrohydrodynamic co-spinning, in **Chapter 5**, the spinning is combined with a microsectioning step, thereby creating a simple, reliable, and scalable process for the fabrication of cylindrical, multifunctional colloids with controlled sizes, aspect ratios, shapes, chemistries and compartmentalization. In doing so, we have established a versatile, low-cost, and potentially high throughput method that can yield near monodisperse microcylinders with tunable properties, thereby maximizing their efficacy, utility, and performance as multifunctional colloids in biomedical applications.[117]

A major goal of this dissertation is to show incorporation of different functional materials in different compartments. This compositional anisotropy is described in two parts. In **Chapter 6**, PLGA particles and cylinders with anisotropic encapsulation of magnetite nanoparticles (MNPs) and optical pigments, titanium dioxide ($TiO_2$) and carbon black (CB) of different sizes are fabricated and preliminary data for a two-color display are shown. In **Chapter 7**, compositional anisotropy is achieved by compartmentalization of different polymers in a each hemisphere of a bicompartmental particle, namely poly(ethyleneimine) (PEI) and PLGA in one compartment and PLGA only in the other. The pH sensitive properties of PEI are used to induce anisotropic particle swelling or dissolution. Thus, control over relative size of compartments is shown. This concept is also extended towards a two-color display, for which preliminary data are presented.

In **Chapter 8**, anisotropic chemical functionality is discussed in greater detail. Visualization of anisotropic distribution of acetylene functional groups in particles achieved via Confocal Raman Spectromicroscopy (CRS). Selective surface functionalization of bi- and tetracompartmental particles with biotin and streptavidin is demonstrated. The biotin-streptavidin interaction is employed to induce self-assembly of these particles in solution and suspension. The effect of particle internal architecture on the nature of the assemblies is discussed. Finally, conclusions and future directions are presented in **Chapter 9**.

## 1.4 Figures and Tables

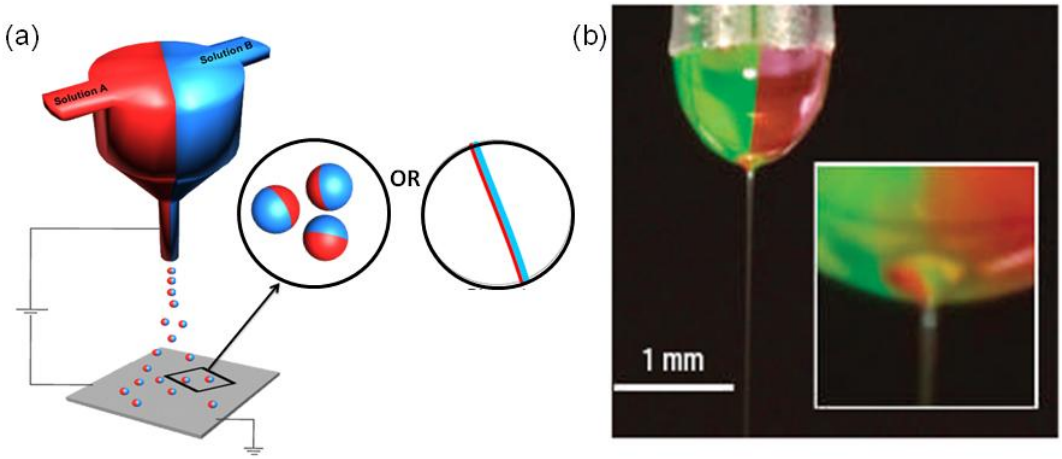


**Figure 1.1** (a) schematic and (b) digital micrograph of the electrified jetting process (reproduced from Ref.83). A liquid droplet comprising of two polymer solutions is generated by pumping them through a side-by-side capillary system. Application of electric potential to the droplet distorts it into a cone (Taylor cone), and a liquid jet ensues from the vortex at the tip of the cone (as shown in inset). Evaporation of solvent produces bicompartmental particles (or fibers in case of solutions with greater viscosity) which migrate downwards under the influence of electric field.

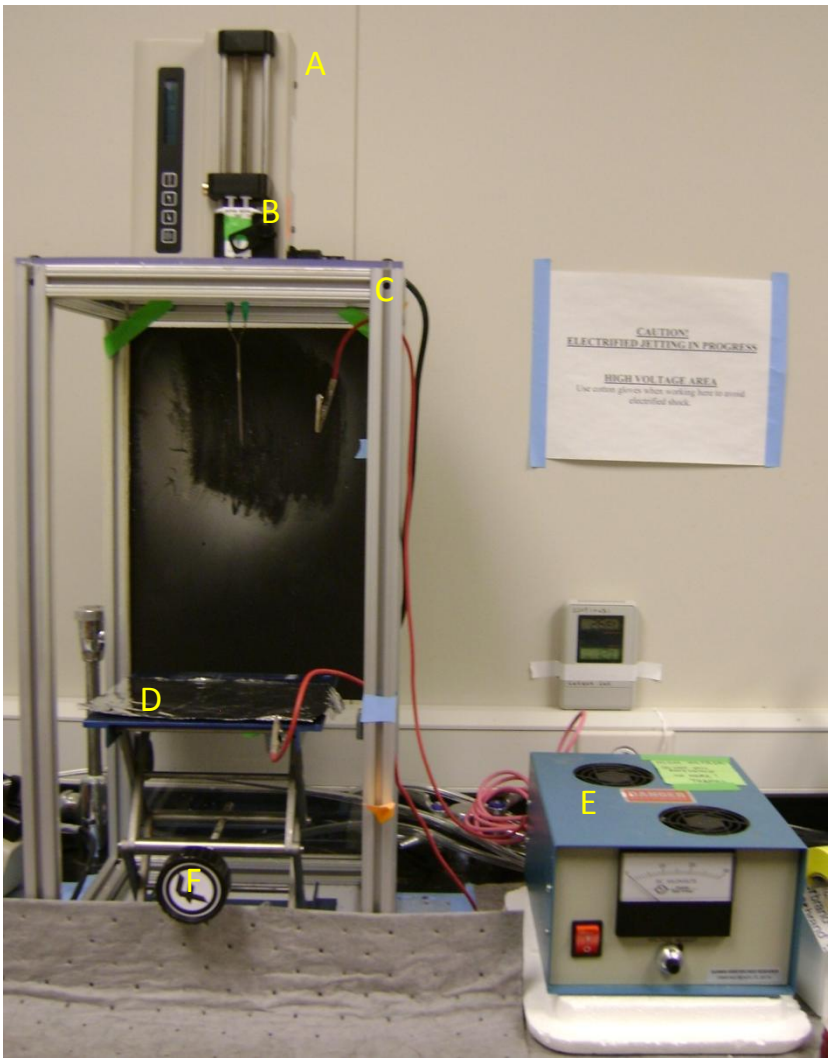


**Figure 1.2** Experimental setup for electrohydrodynamic co-jetting. (a) Syringe pump for controlling flow rate (b) Dual capillary needle setup for bicompartmental particles or fibers (c) Steel frame with Plexiglas walls for holding the syringe pump and needle assembly (d) Grounded aluminum foil which acts as collecting substrate (e) DC voltage source (f) Lab jack for controlling distance between capillaries and the collecting substrate.

## 1.5 References


[1] B. D. Ratner, "*Biomaterials: An introduction ot materials in medicine*", Academic Press, 2004.
[2] A. J. Engler, S. Sen, S. H. L., D. E. Discher, *Cell* **2006**, *126*, 677.
[3] J. A. Champion, S. Mitragotri, *Proc. Natl. Acad. Sci. USA* **2006**, *103*, 4930.
[4] J. Rejman, V. Oberle, I. S. Zuhorn, D. Hoekstra, *Biochem J* **2004**, *377*, 159.
[5] M. E. Davis, J. E. Zuckerman, C. H. J. Choi, D. Seligson, A. Tolcher, C. A. Alabi, Y. Yen, J. D. Heidel, A. Ribas, *Nature* **2010**, *464*, 1067.
[6] T. Dvir, B. P. Timko, D. S. Kohane, R. Langer, *Nat Nanotech* **2011**, *6*, 13.
[7] D. C. Pregibon, M. Toner, P. S. Doyle, *Science* **2007**, *315*, 1393.
[8] S. Mitragotri, J. Lahann, *Nat. Mater.* **2009**, *8*, 15.
[9] A. Akinc, E. al., *Nat Biotechnol* **2008**, *26*, 561.
[10] H. Agnew, R. D. Rohde, S. W. Millward, A. Nag, W. S. Yeo, J. E. Hein, S. M. Pitram, A. A. Tariq, V. M. Burns, R. J. Krom, V. V. Fokin, K. B. Sharpless, J. R. Heath, *Angew Chem Int Ed* **2009**, *48*, 1.
[11] K. A. Whitehead, R. Langer, D. G. Anderson, **2009**, *8*.
[12] J. A. Champion, Y. K. Katare, *J. Cont. Rel.* **2007**, *121*, 3.
[13] S. E. A. Gratton, P. A. Ropp, P. D. Pohlhaus, J. C. Luft, V. J. Madden, M. E. Napier, J. M. DeSimone, *Proc. Natl. Acad. Sci. USA* **2008**, *105*, 11613.
[14] Y. Geng, P. Dalhaimer, S. S. Cai, R. Tsai, M. Tewari, T. Minko, D. E. Discher, *Nat. Nanotechnol.* **2007**, *2*, 249.
[15] N. Doshi, A. Zahr, S. Bhaskar, J. Lahann, S. Mitragotri, *Proc. Natl. Acad. Sci. U S A* **2009**, *106*, 21495.
[16] T. J. Merkel, S. W. Jones, K. P. Herlihy, F. R. Kersey, A. R. Shields, M. Napiera, J. C. Luft, H. Wug, W. C. Zambonic, A. Z. Wang, J. E. Bear, J. M. DeSimone, *Proc. Natl. Acad. Sci. U S A* **2011**, 10.1073/pnas.1010013108
[17] D. Dendukuri, D. C. Pregibon, J. Collins, T. A. Hatton, P. S. Doyle, *Nat. Mater.* **2006**, *5*, 365.
[18] J. P. Rolland, B. W. Maynor, L. E. Euliss, A. E. Exner, G. M. Denison, J. M. DeSimone, *J. Am. Chem. Soc.* **2005**, *127*, 10096.
[19] J. A. Champion, Y. K. Katare, S. Mitragotri, *Proc. Natl. Acad. Sci. USA* **2007**, *104*, 1901.
[20] C. Berkland, D. W. Pack, K. Kim, *Biomaterials* **2004**, *25*, 5649.
[21] D. S. Kohane, *Biotechnol. Bioeng.* **2007**, *96*, 203.
[22] M. Singh, A. Chakrapani, D. O'Hagan, *Expert Rev. Vaccines* **2007**, *6*, 797.
[23] H. Gao, W. Shi, L. B. Freund, *Proc. Natl. Acad. Sci. U S A* **2005**, *102*, 9469.
[24] S. Xu, Z. Nie, M. Seo, P. Lewis, E. Kumacheva, H. A. Stone, P. Garstecki, D. B. Weibel, I. Gitlin, G. M. Whitesides, *Angew. Chem. Int. Ed.* **2005** *44*, 724
[25] K. P. Lok, C. K. Ober, *Can. J. Chem.* **1985**, *63*, 209.
[26] S. M. Moghimi, A. C. Hunter, J. C. Murray, *FASEB J* **2005**, *19*, 311.
[27] D. E. Discher, P. Janmey, Y. Wang, *Science* **2005**, *310*, 1139.
[28] F. Rehfeldt, A. J. Engler, A. Eckhardt, F. Ahmed, D. E. Discher, *Adv Drug Deliv Rev* **2007**, *59*, 1329.
[29] A. Engler, L. Bacakova, C. Newman, A. Hategan, M. Griffin, D. Discher, *Biophys J* **2004**, *86*, 617.

[30] P. G. de Gennes, *Rev Mod Phys* **1992**, *64*, 645.
[31] R. C. Nagarwal, S. Kant, P. N. Singh, P. Maiti, J. K. Pandit, *J. Cont. Rel.* **2009**, *136*, 2.
[32] S. Sengupta, D. Eavarone, I. Capila, G. Zhao, N. Watson, T. Kiziltepe, R. Sasisekharan, *Nature* **2005**, *436*, 568.
[33] V. Wood, M. J. Panzer, J. M. Caruge, J. E. Halpert, M. G. Bawendi, V. Bulović, *Nano Lett* **2010**, *24*, 9.
[34] F. Li, D. P. Josephson, A. Stein, *Angew Chem Int Ed* **2010**, *50*, 360.
[35] G. C. Engelmayr, M. Cheng, C. J. Bettinger, J. T. Borenstein, R. Langer, L. E. Freed, *Nat Mater* **2008**, *7*, 1003.
[36] D. Li, Y. N. Xia, *Advanced Materials* **2004**, *16*, 1151.
[37] C. Berkland, E. Pollauf, N. Varde, D. W. Pack, K. Kim, *Pharm. Res.* **2007**, *25*, 1007.
[38] F. Caruso, R. A. Caruso, H. Mohwald, *Science* **1998**, *282*, 1111.
[39] D. G. Shchukin, G. B. Sukhorukov, H. Mohwald, *Angew. Chem. Int. Ed.* **2003**, *42*, 4472.
[40] A. Kazemi, J. Lahann, *Small* **2008**, *4*, 1756.
[41] M. Yoshida, K.-H. Roh, S. Mandal, S. Bhaskar, D. Lim, H. Nandivada, X. Deng, J. Lahann, *Adv Mater* **2009**, *21*, 4920.
[42] A. M. Smith, S. Nie, *Acc. Chem. Res.* **2009**, *43*, 190.
[43] S. M. Yang, S. H. Kim, J. M. Lima, G. R. Yi, *J Mater Chem* **2008**, *18*, 2161.
[44] A. J. Swiston, J. B. Gilbert, D. J. Irvine, R. E. Cohen, M. F. Rubner, *Biomacromolecules* **2010**, *11*, 1826.
[45] G. J. Snyder, E. S. Toberer, *Nat Mater* **2008**, *7*, 105.
[46] M. Yoshida, J. Lahann, *ACS Nano* **2008**, *2*, 1101.
[47] H. Y. Chen, J. M. Rouillard, E. Gulari, J. Lahann, *Proc. Natl. Acad. Sci. USA* **2007**, *104*, 11173.
[48] K. H. Roh, D. C. Martin, J. Lahann, *J. Am. Chem. Soc.* **2006**, *128*, 6796.
[49] Y. D. Yin, Y. Lu, B. Gates, Y. N. Xia, *Journal of the American Chemical Society* **2001**, *123*, 8718.
[50] A. Perro, S. Reculusa, S. Ravaine, E. B. Bourgeat-Lami, E. Duguet, *Journal of Materials Chemistry* **2005**, *15*, 3745.
[51] A. Walther, A. H. E. Muller, *Soft Matter* **2008**, *4*, 663.
[52] A. B. Pawar, I. Kretzschmar, *Macromol Rapid Comm* **2010**, *31*, 150.
[53] S. C. Glotzer, M. J. Solomon, *Nat. Mater.* **2007**, *6*, 557.
[54] K. J. Lee, J. Yoon, J. Lahann, *Curr Opin Coll Int Sci* **2011**, *in press*.
[55] N. K. Sheridon, E. A. Richley, J. C. Mikkelsen, D. Tsuda, J. M. Crowley, K. A. Oraha, M. E. Howard, M. A. Rodkin, R. S. R. Swidler, *Proceeding of the IDRC, SID/IEEE* **1997**.
[56] A. B. Pawar, I. Kretzschmar, *Langmuir* **2007**, *24*, 355.
[57] D. Suzuki, H. Kawaguchi, *Colloid & Polymer Science* **2006**, *284*, 1471.
[58] S. Jiang, M. J. Schultz, Q. Chen, J. S. Moore, S. Granick, *Langmuir* **2008**, *24*, 10073.
[59] Z. F. Li, D. Y. Lee, M. F. Rubner, R. E. Cohen, *Macromolecules* **2005**, *38*, 7876.
[60] L. Liu, M. Ren, W. Yang, *Langmuir* **2009**, *25*, 11048.

[61] K. D. Anderson, M. Luo, R. Jakubiak, R. R. Naik, T. J. Bunning, V. V. Tsuktruk, *Chem Mater* **2010**, *22*, 3259.
[62] S. Jiang, Q. Chen, M. Tripathy, E. Luijten, K. S. Schweizer, S. Granick, *Advanced Materials* **2010**, *22*, 1060.
[63] K. Fujimoto, K. Nakahama, M. Shidara, H. Kawaguchi, *Langmuir* **1999**, *15*, 4630.
[64] H. Y. Koo, D. K. Yi, S. J. Yoo, D.-Y. Kim, *Adv Mater* **2004**, *16*, 274.
[65] H. Takei, N. Shimizu, *Langmuir* **1997**, *13*, 1865.
[66] Z. Nie, W. Li, M. Seo, S. Xu, E. Kumacheva, *J Am Chem Soc* **2006**, *128*, 9408.
[67] D. Dendukuri, T. A. Hatton, P. S. Doyle, *Langmuir* **2007**, *23*, 4669.
[68] K. P. Yuet, D. K. Hwang, R. Haghgooie, P. S. Doyle, *Langmuir* **2010**, *26*, 4281.
[69] K. W. Bong, K. T. Bong, D. C. Pregibon, P. S. Doyle, *Angew Chem Int Ed* **2010**, *49*, 87.
[70] R. K. Shah, K. J. W., D. A. Weitz, *Adv Mater* **2009**, *21*, 1949.
[71] Y. Yin, Y. Lu, Y. Xia, *J Am Chem Soc* **2001**, *123*, 771.
[72] Y. Yin, Y. Lu, B. Gates, Y. Xia, *J Am Chem Soc* **2001**, *123*, 8717.
[73] A. Walther, X. André, M. Drechsler, V. Abetz, A. H. Müller, *J. Am. Chem. Soc.* **2007**, *129*, 6187.
[74] Y. Y. Yu, S. S. Chang, C. L. Lee, C. R. C. Wang, *J. Phys. Chem. B* **1997**, *101*, 6661.
[75] K. Esumi, K. Matsuhisa, K. Torigoe, *Langmuir* **1995**, *11*, 3285.
[76] V. M. Cepak, C. R. Martin, *J. Phys. Chem. B* **1998**, *102*, 9985.
[77] B. R. Martin, D. J. Dermody, B. D. reiss, M. M. Fang, L. A. Lyon, M. J. Nathan, T. E. Mallouk, *Adv Mater* **1999**, *11*, 1021.
[78] S. Fullam, D. Cottel, H. Rensmo, D. Fitzmauritce, *Adv Mater* **2000**, *12*, 1430.
[79] N. R. Jana, L. Gearheart, C. J. Murphy, *Adv Mater* **2000**, *13*, 1389.
[80] J. W. Kim, R. J. Larsen, D. A. Weitz, *J Am Chem Soc* **2006**, *128*, 14374.
[81] J. W. Kim, R. J. Larsen, D. A. Weitz, *Adv. Mater.* **2007**, *19*, 2005.
[82] H. Yu, M. Chen, P. M. Rice, S. X. Wang, R. L. White, S. Sun, *Nano Lett* **2005**, *5*, 379.
[83] K. H. Roh, D. C. Martin, J. Lahann, *Nat. Mater.* **2005**, *4*, 759.
[84] R. P. A. Hartman, D. J. Brunner, D. M. A. Camelot, J. C. M. Marijnissen, B. Scarlett, *J. Aerosol Sci.* **2000**, *31*, 65.
[85] M. Cloupeau, B. Prunet-Foch, *J. Electrostat.* **1989**, *22*, 135.
[86] T. Han, A. L. Yarin, D. H. Reneker, *Polymer* **2008**, *49*, 1651.
[87] J. Zeleny, *Proc Camb Phil Soc* **1915**, *18*, 71.
[88] D. R. Chen, D. Y. H. Pui, S. L. Kaufman, *J. Aerosol Sci.* **1995**, *26*, 963.
[89] W. B. Cai, X. Y. Che, *Small* **2007**, *3*, 1840.
[90] L. Rayleigh, *Philos Mag S G* **1882**, *14*, 184.
[91] J. Woosley, R. Turnbull, K. Kim, *J Appl Physiol* **1988**, *64*, 4278.
[92] J. Zeleny, *Phys. Rev.* **1917**, *10*, 1.
[93] G. Taylor, *Proc R Soc Lond* **1964**, *A280*, 383.
[94] D. Li, Y. L. Wang, Y. N. Xia, *Nano Letters* **2003**, *3*, 1167.

[95] R. Ostermann, J. Cravillon, C. Weidmann, M. Wiebcke, B. M. Smarsly, *Chem. Commun.* **2011**, *47*, 442.
[96] J. A. Matthews, G. E. Wnek, D. G. Simpson, G. L. Bowlin, *Biomacromolecules* **2002**, *3*, 232.
[97] P. K. Odenwalder, S. Irvine, J. R. McEwan, S. N. Jayasinghe, *Biotechol. J.* **2007**, *2*, 622.
[98] I. Shabania, M. M. Hasani-Sadrabadia, V. Haddadi-Asla, *J. Membrane Sci.* **2011**, *368*, 233.
[99] D. Navarathnea, Y. Nera, M. Jainb, J. G. Grotec, G. A. Sotzing, *Mater Lett* **2011**, *65*, 219.
[100] D. J. Yang, I. Kamienchick, D. Y. Youn, A. Rothschild, I. Kim, *Adv Funct Mater* **2010**, *20*, 4258.
[101] S. Ramakrishna, R. Jose, P. S. Archana, A. S. Nair, R. Balamurugan, J. Venugopal, W. E. Teo, *J. Mater. Sci.* **2010**, *45*, 6283.
[102] C. Pan, L. Dong, Z. Z. Gu, *Int. J. App. Ceramic Tech.* **2010**, *7*, 895.
[103] X. Zhang, M. R. Reagan, D. L. Kaplan, *Adv Drug Deliv Rev* **2009**, *61*, 988.
[104] B. Wang, Y. Wang, T. Yin, Q. Yu, *Chem. Engg. Commun.* **2010**, *197*, 1315.
[105] S. H. Lim, H. Q. Mao, *Adv. Drug. Del. Rev.* **2009**, *61*, 1084.
[106] J. H. Jang, O. Castano, H. W. Kim, *Adv Drug Deliv Rev* **2009**, *61*, 1065.
[107] K. J. Aitken, D. J. Bägli, *Nature Rev. Urol.* **2009**, *6*, 612.
[108] B. S. Jha, R. J. Colello, J. R. Bowman, S. A. Sell, K. D. Lee, J. W. Bigbee, G. L. Bowlin, W. N. Chow, B. E. Mathern, D. G. Simpson, *Acta Biomaterialia* **2011**, *7*, 203.
[109] J. Xie, X. Li, Y. Xia, *Macromol Rapid Comm* **2008**, *29*, 1775.
[110] T. J. Silla, H. A. von Recum, *Biomaterials* **2008**, *29*, 1989.
[111] S. Agarwal, J. H. Wendorff, A. Greiner, *Adv Mater* **2009**, 32.
[112] F. L. Zhou, R. H. Gong, *Polymer International* **2008**, *57*, 837.
[113] D. H. Reneker, A. L. Yarin, H. Fong, S. Koombhongse, *J. App. Phys.* **2000**, *87*, 4531.
[114] S. Bhaskar, K. H. Roh, X. Jiang, G. L. Baker, J. Lahann, *Macromol. Rapid Commun.* **2008**, *29*, 1655.
[115] S. Bhaskar, K. M. Pollock, M. Yoshida, J. Lahann, *Small* **2010**, *6*, 404.
[116] S. Bhaskar, J. Lahann, *J. Am. Chem. Soc.* **2009**, *131*, 6650.
[117] S. Bhaskar, J. Hitt, S. L. Chang, J. Lahann, *Angew. Chem. Int. Ed.* **2009**, *48*, 4589.

# CHAPTER 2

# BICOMPARTMENTAL BIODEGRADABLE PARTICLES AND FIBERS VIA ELECTROHYDRODYNAMIC CO-JETTING

This chapter has been adapted with minor modifications from the following published article:

Bhaskar, S., Roh, K. H., Jiang, X. Baker, G. L., Lahann, J., 'Spatioselective modification of bicompartmental polymer particles and fibers via Huisgen 1,3-dipolar cycloaddition', Macromolecular Rapid Communications 2008, 29, 20, 1655-1660.

## 2.1 Introduction

Nano- and microstructured biomaterials with controlled chemical, physical, and biological properties have been widely used for a range of different biomedical applications including tissue engineering, drug delivery, medical imaging, and diagnostics. Size, for instance, is a well-studied parameter in the context of biomaterials development, as cellular morbidity, inflammation potential, and cellular uptake are strongly dependent on particle size.[1-5] In addition, particle shape has been discussed as an influential materials parameter, as

phagocytosis of particles by macrophages has been shown to strongly vary with the local shape of the particle at the point where the cell is attached.[6] Recently, however, there is growing recognition that crucial physico-chemical properties of materials may go well beyond size and shape and may include anisotropic distribution of matter, localized surface modification, or controlled compartmentalization.[7] The increasing emphasis of anisotropy has been partially driven by the introduction of novel synthetic concepts. Synthesis of anisotropic particles include the use of a spinning disk,[8, 9]self-assembly,[10, 11] fusion of pre-existing particles,[12] surface modification with partial masking,[13-17], selective deposition,[18, 19] surface modification through partial contact with reactive media,[20-22] microcontact printing[23, 24] and template-assisted self-assembly,[25, 26] flow-focusing lithography[27-29] or microfluidic techniques. [30-33]

An alternative strategy towards anisotropic micro- and nanoparticles uses electrohydrodynamic co-jetting.[34-36] In this method, the interface between the two jetting solutions is sustained during jet fragmentation and size reduction. In principle, such novel particle geometries enable independent control of key parameters, such as chemical composition, surface functionalization, biological loading, shape, and size for each compartment, thereby effectively mimicking many of nature's complex architectures. This approach towards designer nanoparticles leads to unique capabilities that enable design of particles with multiple and distinct surface patterns or nano-compartments. Because of its intrinsic simplicity and generality, the electrohydrodynamic co-jetting process can be applied to a wide range of specialty and non-specialty materials including

many of the currently FDA approved materials. The fact that each compartment can be designed independently from the other compartment(s) enables combination of multiple, essential materials functions. Biphasic particles that are made of semiconducting polymers, hydrogels, biodegradable or bioinert polymers as well as magnetic nanocomposites constitute examples that demonstrate the potential versatility of electrohydrodynamic co-jetting. Especially, cases where incompatible materials ought to be engineered in close proximity to each other; electrohydrodynamic co-jetting can be successfully employed.[35, 36] In particular, electrohydrodynamic co-jetting can be employed successfully in cases where the functions of incompatible materials must be engineered in close proximity to one another. The ability to selectively modify individual areas on the surface of a particle or a fiber is another important physico-chemical property, which requires anisotropic distribution of interfacial binding sides paired with orthogonal immobilization chemistries.

In this chapter, we use a combination of electrohydrodynamic co-jetting and highly specific surface modification via Huisgen heterocycloaddition to prepare particles and fibers with highly specific regional surface modification. First, we demonstrate the preparation of biphasic particles and fibers from commercially available PLGA polymers via electrohydrodynamic co-jetting of two organic polymer solutions loaded with different macromolecules including polythiophenes as well as acetylene-functionalized PLGA derivatives [poly (lactide-co-propargyl glycolide) or PLPG]. Next, selective loading in one compartment only is achieved by spatially controlled reaction of PLPG with

azide-PEG-amine, followed by reaction of newly introduced amino groups with FITC, which in turn results in selective surface modification of one compartment only.

## 2.2 Methods

### 2.2.1Materials

PLGA copolymers with lactide: glycolide ratios 85:15 (Mw= 40-75,000) and 50:50 (Mw= 50-75,000), Chloroform, N, N–dimethylformamide (DMF), ethanol, O-(2-Aminoethyl)- O'-(2-Azidoethyl)heptaethylene glycol (Azide-PEG-amine), Copper Sulfate Pentahydrate (CuSO4.5H2O), Sodium ascorbate, FITC, BSA, PBS and Tween-20 were purchased from Sigma-Aldrich, USA and used as received. Polythiophene polymers, sold under commercial names ADS 306PT (Mw= 20-70,000) ADS 406PT (Mw= 30-80,000) were purchased from American Dye Source, Canada. Ethyl glyoxylate (Alfa Aesar, 50 wt % in toluene) was distilled before use.

### 2.2.2 Synthesis of PLPG

PLPG was synthesized via a previously described route.[37] Briefly, propargyl bromide was reacted with ethyl glyoxylate in the presence of activated zinc to produce ethyl 2-hydroxy-3-butynoate. Hydrolysis of the ester in refluxing water resulted in 2-hydroxy-3-butynoic acid, which was refluxed with catalytic p-toluenesulfonic acid in toluene. This cyclization reaction produced the monomer,

meso/rac-3, 6-Di-2-propynyl-1, 4-dioxane-2, 5-dione or propargyl glycolide (PGL). Co-polymerization of PGL with rac-lactide, catalyzed by Sn (2-ethylhexanoate)$_2$ using tert-butyl benzyl alcohol as the initiator, yielded PLPG.

### 2.2.3 Electrohydrodynamic Co-jetting

A schematic depicting the electrohydrodynamic co-jetting process and a photograph of the basic experimental setup are shown in Figures 1.1a and 1.2 respectively. Each of the two jetting solutions was drawn in a syringe (capacity: 1 ml, Becton-Dickinson, USA). The two syringes were held together using a syringe holder and connected to a dual cannula applicator tip (Micromedics Inc, USA) consisting of two capillaries (diameter: 26 gauge, length: 3.25 in) held together in a side by fashion via a transparent plastic tube. The needles were connected to the cathode of a DC voltage source (range: 0-30 kV, Gamma High Voltage Research, USA). The flow rate was controlled by a syringe pump (Kd Scientific, USA). The syringe pump holding the dual syringe assembly was placed atop a rectangular box-like frame with aluminum supports and Plexiglas top to facilitate control of distance between the capillary tip and substrate. This distance was maintained in the range of 11-13 in for particles and 2-3 in for fibers. A square piece of aluminum foil was used as collecting substrate. All experiments were performed at room temperature (23$^{o}$C) and pressure with the system placed inside a fume hood with average face velocity of 20 ft/min.

### 2.2.4 Chemical modification of biphasic particles and fibers

Particles were harvested from the substrate with a razor blade. To 7.5 mg of particles, Azide-PEG-amine (10 times molar excess of acetylene groups) was

added, followed by $CuSO_4.5H_2O$ solution (2 times molar excess of azide) and freshly prepared Sodium Ascorbate solution (100 times molar excess of $Cu^{++}$ ions) was added. The reaction was carried out in DI water containing 0.001% v/v Tween-20, for 15h at room temperature and pressure. The particles were washed by centrifuging with DI water, followed by washing repeatedly with aqueous phosphate buffer (PBS containing 0.02% (v/v) Tween20 and 0.1% (w/v) BSA). This was followed by addition of equimolar (w.r.t acetylene groups) amount of FITC dissolved in ethanol. The reaction was carried out at room temperature for 5h, after which the particles were washed repeatedly with PBS containing 2 vol% Tween-20. In case of fibers, the mesh deposited on the foil was reacted in 6 well plates, and washed similarly. The particles and fibers were then examined by CLSM.

### 2.2.5 SEM

The particles and fibers jetted on top of an aluminum substrate were sputter coated with gold and their surface morphology was examined by a Scanning Electron Microscope (Philips XL30 ESEM, high vacuum mode).

### 2.2.6 CLSM

Samples for CLSM were prepared by jetting on top of glass cover slips (24x50 mm, Fisher Scientific, USA) which in turn were placed on top of the aluminum substrate. The cover slips were mounted on glass slides using DI water and examined with a Confocal Laser Scanning Microscope (CLSM) (Olympus FluoView 500, USA). For selectively modified particles, ~20 µl of the aqueous

particle suspension was mounted on a cover-slip. The selectively modified fibers were detached from the foil, and mounted on coverslips. ADS406PT, FITC and ADS306PT were excited by a 405 nm UV laser, a 488 nm Argon laser and a 533 nm He-Ne Green laser respectively. 430-460 nm, 505-525nm and 560-600 nm emission filters were used to visualize the fluorescence of ADS 406PT, FITC and ADS306PT respectively.

## 2.3 Results and Discussion

Figures 2.1a and 2.1b show representative SEM and CLSM micrographs of biphasic microfibers and microparticles, with red and blue depicting PLGA 85:15 and PLGA 50:50 phases respectively. The jet (and hence, particle) diameter and stability, are found to have a complex dependence on several solution and process parameters. The chief solution parameters are surface tension and conductivity, both of which depend on the solvent, which constitutes the majority of the jetting solution. PLGA microspheres have previously been made from a variety of solvents, such as chloroform, methylene chloride, ethyl acetate, acetone, and acetonitrile.[38] We chose a mixture of 97:3 (v/v) Chloroform: DMF. The use of two different solvents combines the advantages offered by a highly volatile solvent with some performance features of a less volatile solvent. Rapid evaporation of the more volatile chloroform, which constitutes a majority of the solution, increases the charge to volume ratio of the droplet, which facilitates rapid jet formation (and breakup).[39] Quick solvent evaporation is highly

desirable; in fact, this is the main factor driving the jet formation because the low conductivity (~0.01-0.05 µS/cm) of the jetting solution limits its ability to induce charge and undergo jet formation. On the other hand, addition of a small portion of the co-solvent DMF increases the dielectric constant of the solution, thereby reducing jet (and particle) diameter and enhances the long-term stability of the droplet (and hence, the Taylor cone). A 4.5:100 w/w solution of PLGA 85:15 in one phase and PLGA 50:50 in the other, with trace amounts (~0.01% by wt. of PLGA) of the polythiophene fluorophores, produced biphasic particles at a flow rate of 0.2 ml/h (Figure 2.1b). As reported previously,[38] a gradual increase in the applied voltage lead to the dripping mode, followed by the "cone jet mode", i.e., the point of formation of a Taylor cone and the appearance of a jet at its tip. Due to the lower conductivity, the base of the Taylor cone was observed to extend well into the droplet, and not confined to the droplet tip (as in the case of solutions with higher conductivity, for e.g. aqueous solutions)[39]. An increase in the voltage caused a lateral shift in the droplet, but the interface of the two solutions was not disrupted, and biphasic particles could still be produced. A further increase in voltage disrupted the interface by formation of twin cones, followed by a multi-jet spray. Cone stability was enhanced by increasing the flow rate, which would ensure that it is supplied with the jetting solution in a more sustained manner. However, this also resulted in an increase in jet diameter, and hence particle size. SEM micrographs of biphasic particles revealed spherical particles ranging from 2-5 µm in diameter, with a small percentage (< 8%) of the population comprising of flattened, donut shaped biphasic structures of about

8µm. These could be attributed to particles formed from an intermittent, partly "solidified" Taylor cone with a higher viscosity.

In contrast, a higher polymer concentration (18:100 w/w PLGA in 95:5 v/v Chloroform: DMF in each phase), coupled with lower flow rates (0.02 ml/h) resulted in biphasic fibers (Figure 2.1 a), with a single fiber being ejected from the cone tip. Higher concentration also resulted in greater cone stability when compared to particles, and the Taylor cone could be maintained for very long periods of time (~3 h) relative to particles (~10-15 min). In fact, the bending instability and whipping motion typically associated with electrospinning[40, 41] were not observed at all. Confocal micrographs revealed a near to perfect "half-half" phase distribution, which again, arises from the fact that the interface between the two solutions in the droplet was maintained in a stable manner for sufficiently long periods of time. Since no swirling was observed, this reinforces the argument that the sandwich shaped particles might be arising out of rapid solvent evaporation. The entire population of fibers and particles examined via CLSM was observed to be comprised of two phases.

Once the synthesis of biphasic particles and fibers based on organic solvents was established, we conducted a series of surface modification experiments. For this purpose, we employed Huisgen 1, 3-dipolar cycloaddition between azides and terminal alkynes, a widely used "click" reaction. This reaction was chosen because of its multitude of biological applications such as targeted drug delivery and self assembly, and also its simplicity.[42-44] We first prepared monophasic particles by mixing a small amount (25:100 w/w of PLGA

85:15 polymer) of PLPG with PLGA 85:15 in the jetting solution. The particles were reacted with Azide-PEG-amine in presence of $Cu^{+}$ ions (produced by reduction of $Cu^{++}$ by sodium ascorbate). The free amine groups were then conjugated with FITC. Green peripheral fluorescence due to FITC seen in confocal micrographs showed that the particles were uniformly surface modified (Figure 2.2a). On the other hand, particles made without acetylene groups did not exhibit any green fluorescence when treated similarly (Figure 2.2b). This proved that the surface modification was the result of triazole formation and not non-specific surface adsorption. We then repeated the same reaction with biphasic particles containing acetylene groups in one phase (amount of acetylene PLGA added in one phase was 25% w/w of PLGA 85:15) , and only PLGA 85:15 in the other. The addition of the acetylene-modified PLGA to one phase did not affect the jetting of particles or fibers. Green fluorescence was seen only in the acetylene containing phase, indicating successful selective phase modification (Figure 2.3). This reaction was repeated on biphasic fibers and the same results were observed (Figure. 2.4). Even though PLPG is incorporated into the bulk of the particle (or fiber), uniform fluorescence of FITC, a small molecule, suggests that a sufficient number of acetylene groups are available for click reaction.

## 2.4 Conclusions

With the extension of electrohydrodynamic co-jetting for preparation of bicompartmental objects from organic solvents (in addition to previous work on aqueous biomaterials systems)[45] and the first-time realization of bicompartmental PLGA microfibers, a new materials architecture has been realized on the basis of the well-established electrospinning technology. In the past, electrospinning has been used to prepare isotropic as well as coaxial[46] micro- and nanofibers with potential use for various biomedical applications, such as tissue engineering.[47, 48] However, all of these scaffold materials fall short in providing spatially differentiated control of cell functions, which is a critical feature of biological scaffolds. Using electrohydrodynamic co-jetting, we have now addressed this challenge by synthesizing fibers with anisotropically distributed surface chemistries. In this work, a fluorescent ligand was selected for imaging purposes, but future bioligands may include cell adhesion peptides, antibodies, growth factors, or lectins. The herein demonstrated selective presentation of bioligands is a useful first step towards biomimetic scaffold materials, but much work still lies ahead. Beyond fiber meshes with randomly oriented fibers, well ordered scaffolds with controlled orientation of fiber compartments relative to each other are within the reach of this technology. The anisotropic surface modification concepts demonstrated herein on the basis of model reactions will soon be extended towards the synthesis of selectively surface modified scaffolds that can locally support promotion or inhibition of cell adhesion. Moreover, simple inclusion of materials, such as poly (N-isopropylacrylamide) or elastin-based

polypeptides should result in bicompartmental fibers with unique, environmentally responsive material properties.

## 2.5 Figures and Tables

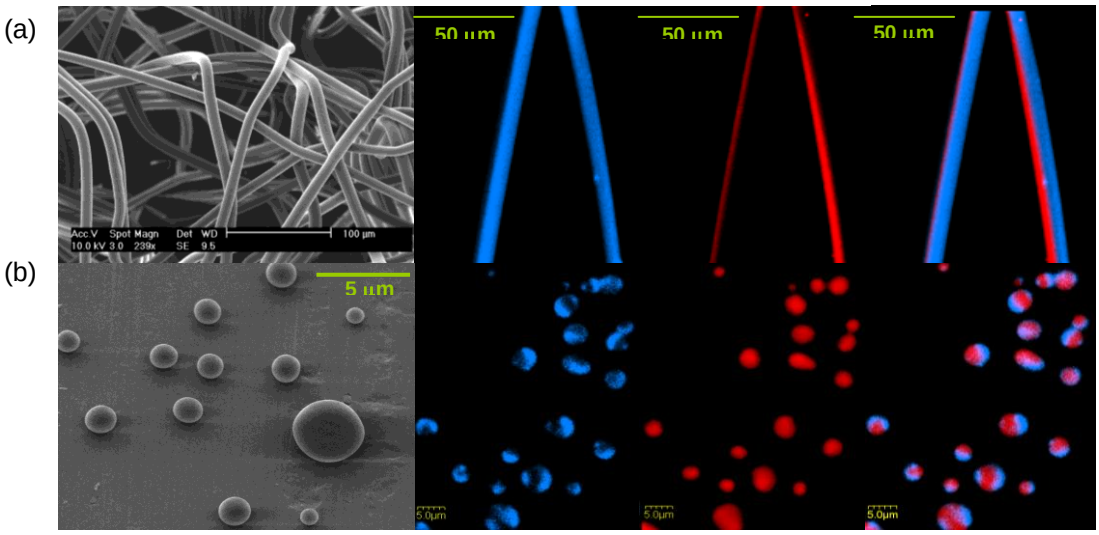


**Figure 2.1** SEM and CLSM images of (a) biphasic microfibers, and (b) biphasic microparticles made from PLGA 85:15 (red) and PLGA 50:50 (blue). Blue fluorescence represents ADS406PT and red fluorescence represents ADS306PT.

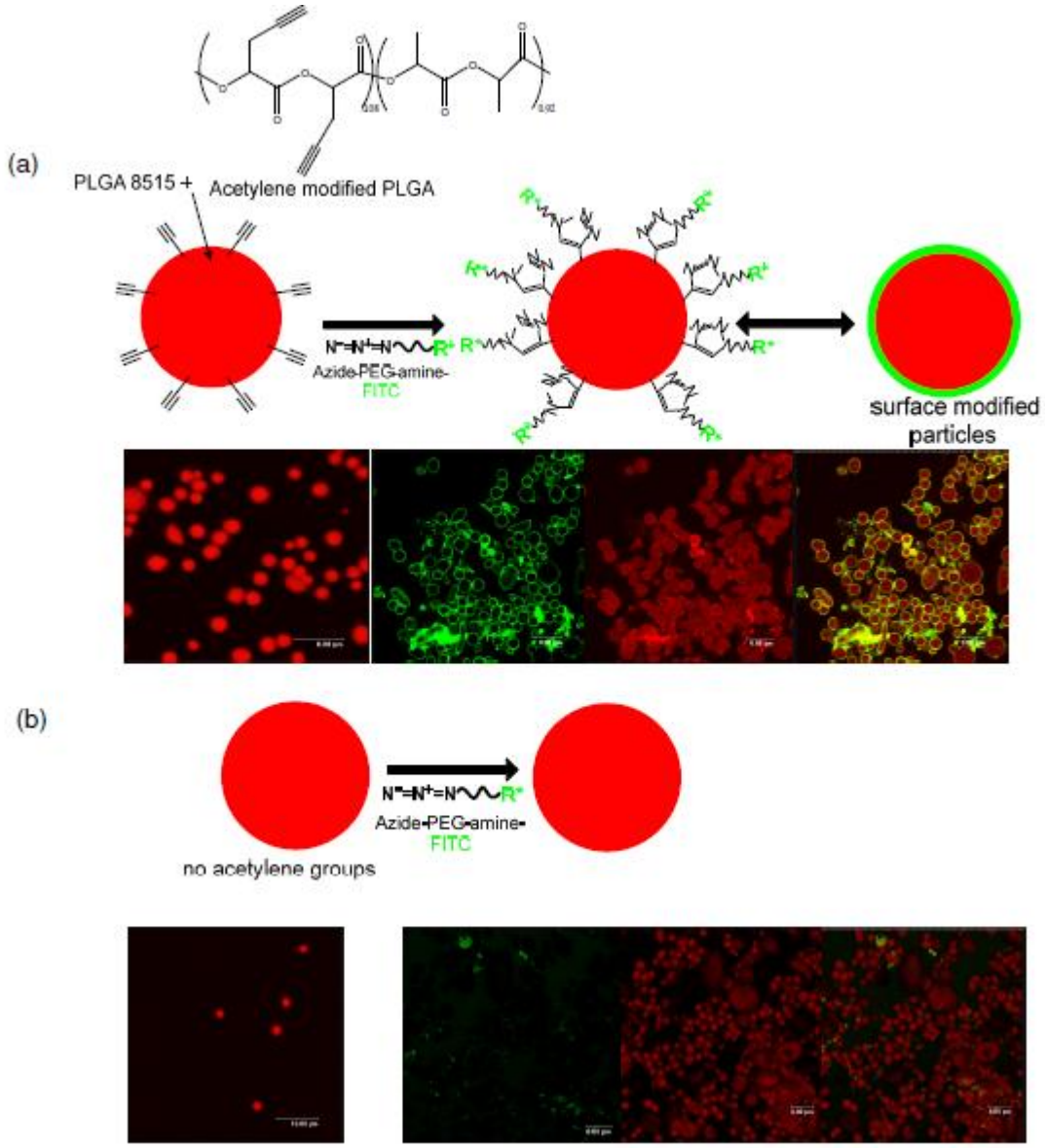


**Figure 2.2** Proof of concept of selective chemical modification on monophasic PLGA microparticles. (a) Monophasic particles containing free acetylene groups (via incorporation of PLPG in the jetting solution) were reacted with azide-PEG-amine (in presence of $Cu^{+}$ ions), and the free amine groups were reacted with FITC. Uniform green peripheral fluorescence due to FITC established surface modification. (b) microparticles without acetylene groups, when treated according to the same protocol, did not exhibit green fluorescence.

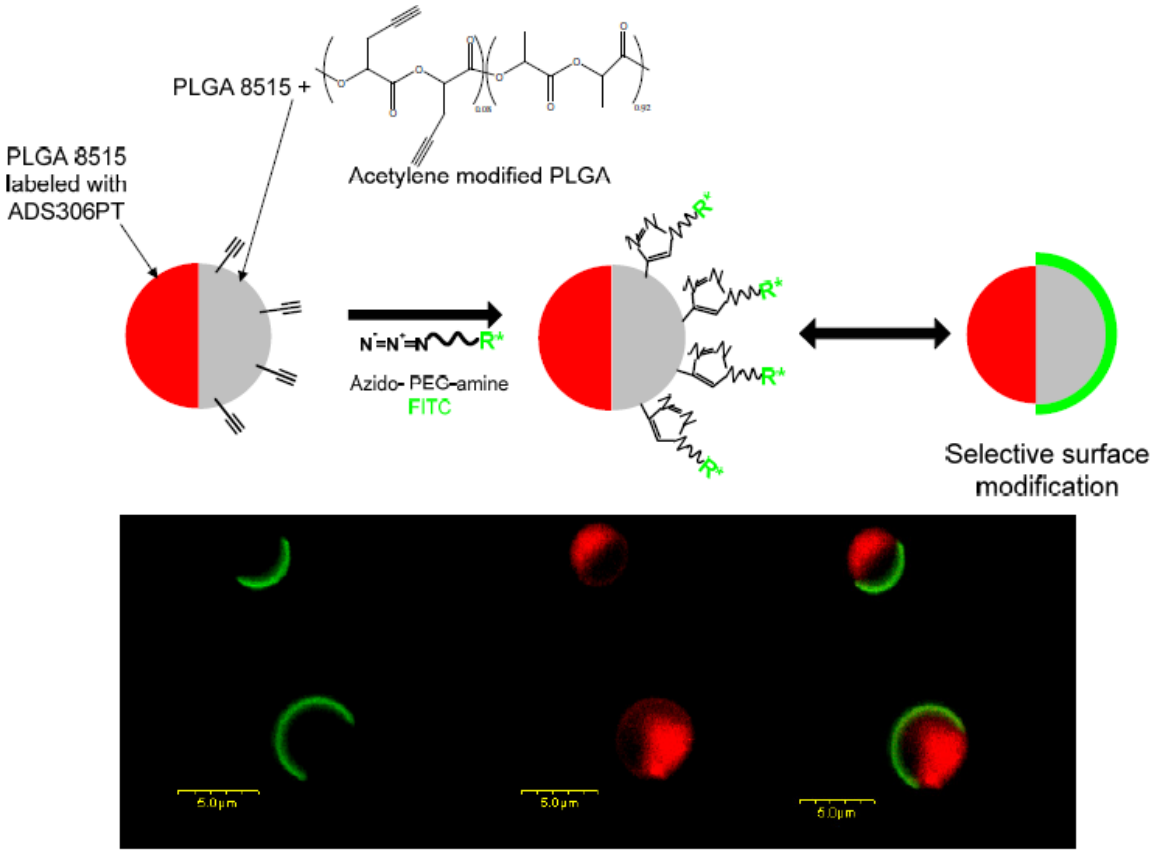


**Figure 2.3** Biphasic microparticles labeled with ADS306PT in one compartment, and containing free acetylene groups in the other were prepared by adding PLPG to one of the jetting solutions. The acetylene groups were reacted with azide-PEG-amine, and the free amine groups were then reacted with FITC (PEG-amine-FITC shown as R*). Green peripheral fluorescence on one side of the particles due to FITC indicates uniform surface modification of the acetylene containing phase.

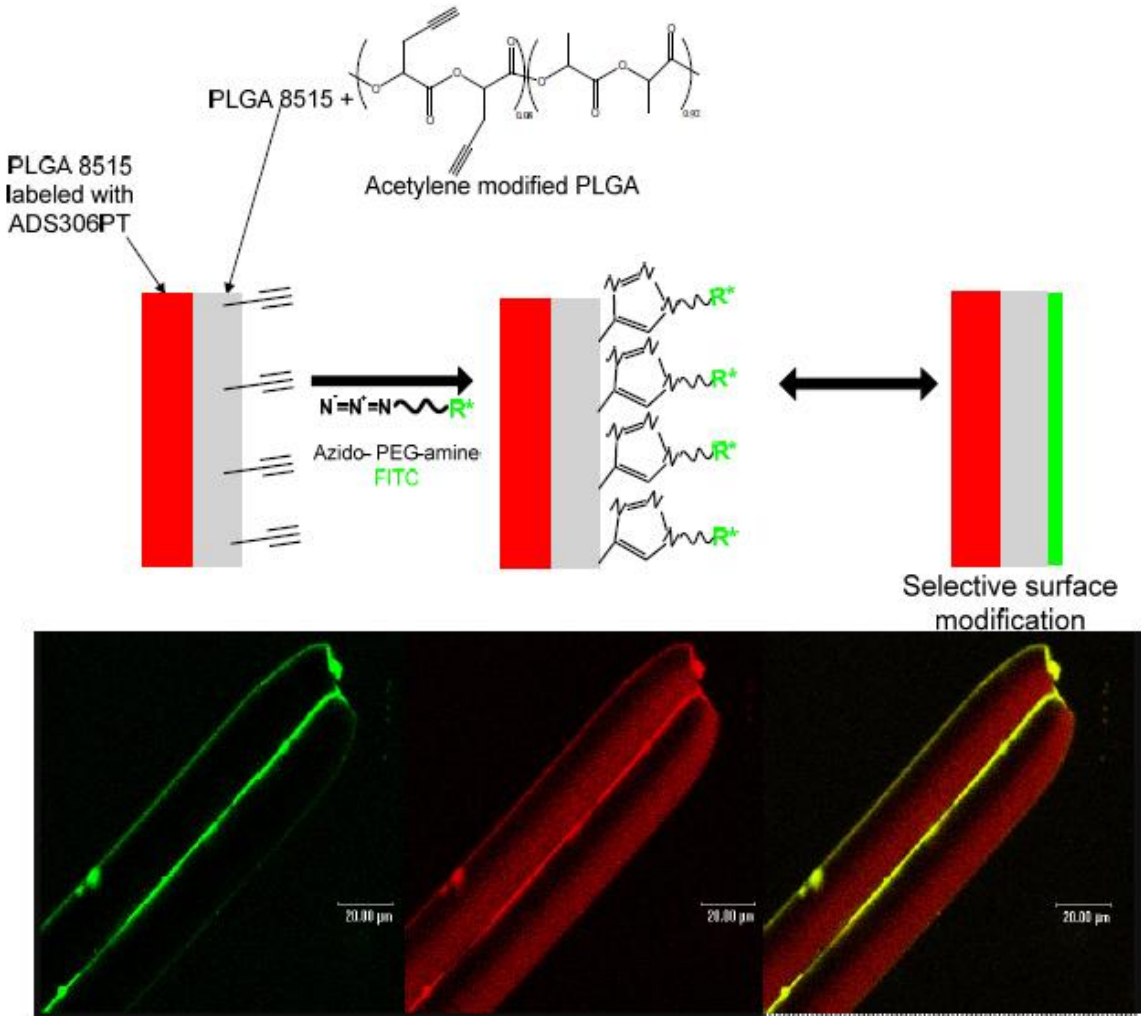


**Figure 2.4** Selective phase modification of biphasic microfibers containing acetylene groups in one compartment and ADS 306PT in the other. The acetylene containing compartment was "clicked" with azide-PEG-amine followed by FITC (PEG-amine-FITC shown as R*). Green peripheral FITC fluorescence on one half of the fibers indicates spatioselective modification.

## 2.6 References


[1] O. Gonzalez, R. L. Smith, S. B. Goodman, *J. Biomed. Mat. Res.* **1996**, *30*, 463.
[2] I. Catelas, O. L. Huk, A. Petit, D. J. Zukor, R. Marchand, L. Yahia, *J. Biomed. Mater. Res.* **1998**, *41*, 600.
[3] V. J. Tomazic-Jezic, K. Merritt, T. H. Umbreit, *J. Biomed. Mater. Res.* **2001**, *55*, 523.
[4] A. Grandjean-Laquerriere, P. Laquerriere, M. Guenounou, D. Laurent-Maquin, T. M. Phillips, *Biomaterials* **2004**, *26*, 2361.
[5] K. Donaldson, D. Brown, A. Clouter, R. Duffin, W. MacNee, L. Renwick, L. Tran, V. Stone, *J. Aerosol. Med.* **2002**, *15*, 213.
[6] J. A. Champion, S. Mitragotri, *Proc Natl Acad Sci U S A* **2006**, *103*, 4930.
[7] S. Mitragotri, J. Lahann, *Nat. Mater.* **2009**, *8*, 15.
[8] http://www2.parc.com/hsl/projects/gyricon/, accessed Feb. 2008.
[9] N. K. Sheridon, E. A. Richley, J. C. Mikkelsen, D. Tsuda, J. M. Crowley, K. A. Oraha, M. E. Howard, M. A. Rodkin, R. S. R. Swidler, *Proceeding of the IDRC, SID/IEEE* **1997**.
[10] S. Kubowicz, J. F. Baussard, J. F. Lutz, A. F. Thunemann, H. von Berlepsch, A. Laschewsky, *Angew Chem Int Ed Engl* **2005**, *44*, 5262.
[11] Z. Li, E. Kesselman, Y. Talmon, M. A. Hillmyer, T. P. Lodge, *Science* **2004**, *306*, 98.
[12] S.-H. Kim, G.-R. Yi, K. H. Kim, S.-M. Yang, *Langmuir* **2008**.
[13] Z. Bao, L. Chen, M. Weldon, C. E, O. Cherniavskaya, Y. Dai, J. B. H. Tok, *Chem Mater* **2002**, *14*, 24.
[14] Z. N. Bao, L. Chen, M. Weldon, E. Chandross, O. Cherniavskaya, Y. Dai, J. B. H. Tok, *Chemistry of Materials* **2002**, *14*, 24.
[15] V. N. Paunov, *Langmuir* **2003**, *19*, 7970.
[16] V. N. Paunov, O. J. Cayre, *Advanced Materials* **2004**, *16*, 788.
[17] C. Casagrande, P. Fabre, E. Raphael, M. Veyssie, *Europhys. Lett.* **1989**, *9*, 251.
[18] E. Hugonnot, A. Carles, M. H. Delville, P. Panizza, J. P. Delville, *Langmuir* **2003**, *19*, 226.
[19] H. Takei, N. Shimizu, *Langmuir* **1997**, *13*, 1865.
[20] K. Nakahama, H. Kawaguchi, K. Fujimoto, *Langmuir* **2000**, *16*, 7882.
[21] L. Petit, E. Sellier, E. Duguet, S. Ravaine, C. Mingotaud, *J. Mater. Chem.* **2000**, *10*, 253.
[22] L. Petit, J. P. Manaud, C. Mingotaud, S. Ravaine, E. Duguet, *Mater. Lett.* **2001**, *51*, 478.
[23] O. Cayre, V. N. Paunov, O. D. Velev, *Chemical Communications* **2003**, 2296.
[24] H. Y. Koo, D. K. Yi, S. J. Yoo, D. Y. Kim, *Adv. Mater.* **2004**, *16*, 274.
[25] L. Nagle, D. Fitzmaurice, *Advanced Materials* **2003**, *15*, 933.
[26] Y. D. Yin, Y. Lu, Y. N. Xia, *Journal of the American Chemical Society* **2001**, *123*, 771.

[27] A. S. Utada, E. Lorenceau, D. R. Link, P. D. Kaplan, H. A. Stone, D. A. Weitz, *Science* **2005**, *308*, 537.
[28] S. Q. Xu, Z. H. Nie, M. Seo, P. Lewis, E. Kumacheva, H. A. Stone, P. Garstecki, D. B. Weibel, I. Gitlin, G. M. Whitesides, *Angew Chem Int Ed* **2005**, *44*, 724.
[29] L. Martin-Banderas, M. Flores-Mosquera, P. Riesco-Chueca, A. Rodriguez-Gil, A. Cebolla, S. Chavez, A. M. Ganan-Calvo, *Small* **2005**, *1*, 688.
[30] T. Nisisako, T. Torii, T. Higuchi, *Chem Eng J* **2004**, *101*, 23.
[31] T. Nisisako, T. Torii, T. Takahashi, Y. Takizawa, *Advanced Materials* **2006**, *18*, 1152.
[32] Z. H. Nie, W. Li, M. Seo, S. Q. Xu, E. Kumacheva, *Journal of the American Chemical Society* **2006**, *128*, 9408.
[33] R. F. Shepherd, J. C. Conrad, S. K. Rhodes, D. R. Link, M. Marquez, D. A. Weitz, J. A. Lewis, *Langmuir* **2006**, *22*, 8618.
[34] K. H. Roh, D. C. Martin, J. Lahann, *Nat. Mater.* **2005**, *4*, 759.
[35] K. H. Roh, D. C. Martin, J. Lahann, *J. Am. Chem. Soc.* **2006**, *128*, 6796.
[36] K. H. Roh, M. Yoshida, J. Lahann, *Langmuir* **2007**, *23*, 5683.
[37] X. Jiang, E. B. Vogel, M. R. Smith III, G. L. Baker, *Macromolecules* **2008**, *41*, 1937.
[38] C. Berkland, D. W. Pack, K. Kim, *Biomaterials* **2004**, *25*, 5649.
[39] M. Cloupeau, B. Prunet-Foch, *J. Electrostat.* **1989**, *22*, 135.
[40] D. H. Reneker, A. L. Yarin, H. Fong, S. Koombhongse, *J. App. Phys.* **2000**, *87*, 4531.
[41] T. Han, D. H. Reneker, A. L. Yarin, *Polymer* **2007**, *48*, 6064.
[42] J.-F. Lutz, *Angewandte Chemie, International Edition* **2007**, *46*, 1018.
[43] J. E. Moses, A. D. Moorehouse, *Chemical Society Reviews* **2007**, *36*, 1249.
[44] H. Nandivada, X. Jiang, J. Lahann, *Adv Mater* **2007**, *19*, 2197.
[45] M. Yoshida, K. H. Roh, J. Lahann, *Biomaterials* **2007**, *28*, 2446.
[46] D. H. Reneker, I. Chun, *Nanotechnology* **1996**, *7*, 216.
[47] L. Huang, R. A. McMillan, R. P. Apkarian, B. Pourdeyhimi, V. P. Conticello, E. L. Chaikof, *Macromolecules* **2000**, *33*, 2989.
[48] E. H. Sanders, R. Kloefkorn, G. L. Bowlin, D. G. Simpson, G. E. Wnek, *Macromolecules* **2003**, *36*, 3803.

# CHAPTER 3

# TOWARDS 'DESIGNER' MICRO/NANOPARTICLES: CONTROL OVER SIZE, SHAPE AND COMPARTMENTALIZATION

This chapter has been adapted from the following published articles (with minor modifications):

1. Bhaskar, S., Pollock, K. M., Yoshida, M., Lahann, J. 'Towards designer microparticles: control over anisotropy, shape, and size', Small **2010**, 6, 3, 404-411.

2. Bhaskar, S., Gibson, C. T., Yoshida, M., Nandivada, H., Deng, X., Voelcker, N. H, Lahann, J., 'Engineering, characterization and directional self-assembly of anisotropically modified nanocolloids', Small **2011**, in press.

3. Doshi, N., Zahr, A., Bhaskar, S., Lahann, J., Mitragotri, S., 'Synthetic red blood cells: bridging the gap between synthetic and biological materials', Proc. Nat. Acad. Sci. USA **2009**, 106, 51, 21495–21499.

## 3.1 Introduction

Custom-tailored nano- and microparticles with potential use for biomedical applications, such as targeted drug delivery or medical imaging, require narrowly controlled chemical compositions as well as precisely engineered physical properties.[1] Hence, materials scientists have increasingly sought to delineate materials effects by considering physical particle attributes, such as size, surface microstructure, roughness, or anisotropy of particles without altering the particle chemistry.[1] Although colloidal structures showing individual control over shape,[2-4] size,[5, 6] anisotropy[7] and surface chemistry have been previously fabricated, traditional fabrication processes are best suited to control one of these parameters at a time. The establishment of versatile particle fabrication processes that enable simultaneous control of several physical attributes remains a key challenge in the biomedical arena.[8]

We previously demonstrated control over particle anisotropy at nanometer scales by fabricating bi- and tri-compartmental micro- and nanostructures via electrohydrodynamic co-jetting of two (or three) aqueous polymeric solutions.[7, 9-12] In Chapter 2, we extended this process to biodegradable particles and fibers with two independent compartments, which were prepared by electrohydrodynamic co-jetting of organic polymer solutions.[13] Owing to the low propensity of organic solvents to accumulate surface charges, a fine interplay of forces, such as attractive electrical forces and surface tension, combined with fast solvent evaporation is necessary to enable particle formation through this process. While electrohydrodynamic co-jetting typically results in fibers or spherical particles, precise orchestration of process parameters may offer the

distinct possibility to obtain a wider range of particle shapes. This is schematically depicted in Figure 3.1. Several examples of control over particle shape and surface morphology via manipulation of different jetting solution and process parameters exist, notably the production of tapered, porous, and blood cell shaped particles made from PLGA,[14] controlled fabrication of biodegradable collapsed and spherical microstructures,[15, 16] cup shaped polystyrene and poly(methyl methacrylate) particles,[17] and also drug loaded particles of controllable shapes.[18] In this chapter, the fabrication of multifunctional particles based on electrohydrodynamic co-jetting, whereby appropriate selection of process parameters allows for variation of the three basic physical attributes: anisotropy, shape, and size is reported.

## 3.2 Methods

### 3.2.1 Electrohydrodynamic co-jetting

The materials and procedure employed for electrohydrodynamic co-jetting are described in Chapter 2. In addition, poly[tris(2,5-bis(hexyloxy)-1,4-phenylenevinylene)-alt-(1,3-phenylenevinylene) (PTDPV), a green fluorophore was purchased from Sigma Aldrich, USA. Briefly, the jetting solutions were pumped through a modified dual capillary system (capillary diameter: 26 gauge, length: 8.2 cm) held together in a side by fashion. The capillaries were connected to the cathode of a DC voltage source (Gamma High Voltage Research, USA) and the flow rate was controlled via a syringe pump (Kd Scientific, USA). It

should be noted that the flow rates reported correspond to the setting on the pump, and due to flow from two capillaries, the actual flow rate equals the product of value assigned to the pump and the number of capillaries employed. A flat piece of aluminum foil was used as a counter electrode, which also acted as a substrate for harvesting particles. The distance between the capillary tip and the substrate was maintained in the range of 28-33 cm. In case of tri- and tetracompartmental particles, the number of capillaries was changed to three and four, which were arranged in a triangular and square configuration respectively. All experiments were performed inside a fume hood at room temperature (23$^{o}$C). For filtration, particles were suspended in DI water containing 2% v/v Tween-20 to a final concentration of 1 mg/ml. Filtration was performed using 40 µm, 10 µm and 5 µm nylon mesh filters (Spectrum Labs, USA) in succession.

### 3.2.2 Particle characterization and size distribution analysis

Particles jetted on to the substrate were sputtered with gold and observed under a Philips XL30FEG ESEM (high vacuum mode). In case of filtered particles, ~ 20µL of a concentrated aqueous suspension was cast on an SEM stub, and the water was allowed for evaporate at room temperature. Size distribution analysis was performed on the SEM images using 'Image J' software.[19] For CLSM, glass coverslips were placed on top of the aluminum substrate during electrohydrodynamic co-jetting. The particles deposited on the coverslips were then examined at 100X magnification. ADS406PT, PTDPV and ADS306PT were excited by 405nm UV, 488 nm Argon, and 533 nm Helium-Neon green lasers, respectively. Optical filters of emission wavelength 430-460 nm, 505-525 nm,

and 560-600 nm were used to visualize the fluorescence of ADS406PT, PTDPV, and ADS306PT, respectively.

### 3.2.3 Flow Cytometry

For bicompartmental particles, a ~1 mg/ml particle suspension (loaded with the desired permutations of ADS306PT and ADS406PT dyes) was suspended in PBS and analyzed using a FACS DiVa Cell Sorter (BD Biosciences, 3-laser: 457/488/514 nm, 350 nm, and 633 nm). Signals from ADS406PT and ADS 306PT were resolved in two channels, (i) excitation: 351 nm laser, emission: 424 ± 44 nm bandpass filter, and (ii) excitation: 488 nm laser, emission: 585±42 nm bandpass filter. For each sample, 10,000 events were collected. Data acquisition and analysis were performed using CellQuest Pro (BD Biosciences). For tricompartmental particles, a filtered, ~2.5 mg/ml suspension of particles (loaded with the desired permutations of ADS306PT, ADS406PT and PTDPV) was suspended in PBS and analyzed using a FACS Vantage cell sorter (BD Biosciences, 3-laser: 488nm, 351nm and 633 nm). ADS406PT was excited using the 351 nm laser whereas PTDPV and ADS 306PT were excited using the 488 nm laser. Dichroic filters of emission wavelengths 424 ± 44 nm, 530 ± 30 nm and 585±47 nm were used to collect the fluorescence emission from ADS406PT, PTDPV and ADS306PT. Data acquisition and analysis were performed using CellQuest Pro (BD Biosciences).

## 3.3 Results and Discussion

Here, we systematically investigate the effect of process parameters on particle shape and morphology during electrohydrodynamic co-jetting of biodegradable PLGA polymers from organic solvents. Initially, we focused on the concentration of the PLGA-containing jetting solutions. Starting at the lower concentration boundary, defined by the ability to support a stable jetting cone, electrohydrodynamic co-jetting of a 1.3:100 w/w solution (in 95:5 v/v chloroform: DMF) of each polymer (PLGA 85:15 and PLGA 50:50), at a flow rate of 0.15 ml/h, yielded discoid biphasic particles (Figure 3.2a). CLSM micrographs revealed that the bicompartmental nature of the particles was extremely well-preserved, as indicated by the near perfect “half-half” anisotropy of the disks shown in Figure 3.2a. The pronounced compartmentalization is reflective of an inherent stability of the Taylor cone, in spite of more complex evaporation processes encountered during co-jetting from chloroform and DMF mixtures. Interestingly, PLGA discs with a range of different surface morphologies were observed including very smooth and slightly rough discs. The latter displayed increased surface roughness predominantly at the surface ridges as determined by SEM. Both the discoid shape and the uneven surface morphology of the bicompartmental colloids may be attributed to the rapid collapse of particles during solidification. Because the jetting solutions used for electrohydrodynamic jetting are dilute polymer solutions, particles will have to undergo substantial shrinkage during the transition from liquid droplets to solid particles. If particle shrinkage prior to solidification is gradual and homogenous throughout the particle, close-to-perfect spheres will be formed. If, however, rapid solvent

evaporation occurs during jetting, the polymer concentration at the surface of the solidifying droplet will be higher than in the core. This difference in the evaporation rates arises from the difference in solution concentrations, with solutions of lower concentration (1.3:100 w/w) showing a greater propensity to rapidly form a 'skin' of polymer at the outer surface, compared to solutions with a higher concentration (4.5:100 w/w), wherein the skin formation is also accompanied by a slow, gradual deposition of polymer in the core. Thus, for the jetting solutions with lower concentrations, higher polymer concentrations may be quickly established in the outside region of the droplet resulting in localized polymer precipitation. This preferential solidification in the shell region further inhibits solvent evaporation in the core and gives rise to an anisotropic particle formation mechanism. Ultimately, solvent will also evaporate from the core of the capsules creating a void in the particle center that causes the initially spherical particles to collapse.[15, 20] Consequentially, discoid particles, shown in Figure 3.2a, are formed. This hypothesis is supported by the fact that the peripheral portions of the discs are of relatively greater thickness and density in comparison with the inner areas, as visualized in SEM images (Figure 3.2a). Similar to the bicompartmental particles, monophasic jetting experiments performed with the same PLGA-based jetting solutions at comparable flow rates yielded discs as well. In order to rule out the possibility that these structures might have resulted from collapse of the droplet on the surface of the substrate owing to insufficient time for evaporation, a series of control experiments were carried out, where the distances between the capillary and the substrate was systematically varied.

Independent of the distance between needle and counter-electrode, all jetting experiments yielded discoid shapes suggesting that the shape setting occurred during solvent evaporation in the jet and not during contacting the counter electrode (Figure 3.3). Moreover, subtle variations of the solvent and flow rate yielded disc-shaped particles of different sizes and surface morphologies (Figure 3.4). In contrast, further increase of the PLGA concentration in both jetting solutions to 3.6:100, while maintaining flow rates of about 0.45 ml/h, yielded predominantly rod-shaped biphasic particles (Figure 3.2b). Confocal micrographs revealed a mixture of different compartment architectures. A typical particle population included bicompartmental rods with compartments along their radial axis as well as colloids with compartments oriented along the longitudinal axis (Figure 3.2b, Figure 3.5). In addition, rod-shaped microparticles with one compartment sandwiched in between the other were also observed (Figure 3.5). In contrast to spheres and discs, micro-rods originate from droplets that are solidified before the droplets can assume their spherical form, *i.e.,* the solidification is so rapid, that the filamentous region that connects successive droplets[21] is partly retained during the jet breakup, giving rise to a rod shaped configuration. This is also reflected in the SEM images of the rods (Figure 3.2b), some of which are tapered towards the end, and others that are spindle shaped, indicative of solidification via rapid solvent evaporation at various time points during jet defragmentation. In this respect, rod-like particles constitute a link between microspheres and microfibers.

In general, micro-rods were typically more heterogeneous than particles and disks and were typically accompanied by a minor fraction of spherical particles, possibly arising from secondary droplets due to higher flow rates.[21] Addition of a small amount of triethylamine (3.63 vol. % of solvent) as co-solvent yielded the most reliable formation of biphasic microrods in our hands. In addition to the use of triethylamine as co-solvent, the appropriate choice of flow rates was another essential factor for the formation of rods. If the same PLGA solutions were jetted at flow rates below 0.45 ml/h, bicompartmental discs were predominantly obtained. Furthermore, lowering the PLGA concentrations from 3.6:100 (w/w) to 1.3:100 (w/w), while maintaining the same flow rates of 0.45 ml/h yielded biphasic discs, not rods (albeit of a larger diameter). Taken together, these data suggest the existence of an optimum concentration/flow rate/volatility combination, which favors formation of biphasic rod-shaped particles. To the best of our knowledge, PLGA-based micro-rods have not yet been reported in literature. As a matter of fact, the co-jetting experiments with two jetting solutions in a side-by-side configuration were repeated with a single jetting solution processed through a single nozzle under otherwise identical jetting conditions. This monophasic jetting did not result in formation of majority of rods, implying that the formation of rods might be a unique aspect of electrohydrodynamic co-jetting using the unique side-by-side jetting configuration described herein.

Upon further increase of the PLGA concentrations to 4.5:100 (w/w), close-to-perfectly spherical bicompartmental microparticles were obtained (Figure 3.2c). The larger polymer concentration favors isotropic solvent evaporation and

gives raise to almost-perfect spherical shapes. In general, increased PLGA concentrations lead to a higher solution viscosity, resulting in a decreased propensity of jet-breakup and increased droplet sizes. In this scenario, reduction of the surface-to-volume-ratio causes more isotropic solvent evaporation, which drives the homogenous solidification that yields bicompartmental particles. In contrast, rapid evaporation rates typically associated with the higher surface-to-volume-ratios of smaller droplets may result in anisotropic evaporation and, hence, can yield non-equilibrium shapes, such as discs. Furthermore, increased viscosities might result in increased chain entanglement effects in the droplet, inhibiting polymer migration to the surface, thereby imparting higher structural stability to the core, further contributing to the formation of spherical shapes.[18] Specific jetting conditions that lead to different shapes are summarized in Table 3.1. With respect to compartmentalization within individual microspheres, it is noteworthy that 'sandwich' type anisotropies were observed in addition to the previously observed 'half-half' phase distribution.[13]

Encouraged by our ability to form bicompartmental particles, we employed three solutions, each containing 4.5: 100 w/w PLGA in 97:3 volume ratio of chloroform and N,N-dimethyl formamide (DMF). To assist the visualization of the multicompartmental character of the particles, the jetting solutions further contained fluorophores with distinct emission characteristics, specifically, PTDPV (green), as well as the polythiophene-based polymers ADS406PT (blue) and ADS306PT (red). These solutions were pumped through three capillary needles arranged in a triangular configuration. The flow rate was maintained at 0.15 ml/h.

Figure 3.6a shows CLSM images of the resulting tricompartmental microparticles, which were collected at the counter-electrode. Blue, green, and red channels are shown individually, followed by their overlay, which confirms the presence of distinct compartments with well-defined interfaces. We then extended this process to include four capillary needles arranged in a square configuration. In this case, we reduced the flow rate to 0.1 ml/h to maintain similar droplet volumes, which were processed with similar voltages. Because of the limited availability of suitable dyes with distinct fluorescence emission spectra, three solutions contained the ADS306PT dye and the fourth one contained PTDPV. Jetting in the cone jet mode described above resulted in the formation of tetracompartmental particles, shown in Figure 3.6b, with a well defined 'quarter' compartment which is green and a larger red compartment which is a composite of three remaining compartments.

In addition to shape, particle size is a critical base property for many biomedical applications. To better understand differences in the size and size distributions of particles made by electrohydrodynamic co-jetting, we conducted a detailed statistical analysis of spheres, disks, and rods, on the basis of SEM. Size distribution data for diameters of different types of bicompartmental particles are shown in Figure 3.7. The histograms were obtained by analysis of SEM images of a larger population of particles directly after jetting.[19] The discs varied from circular to slightly elongated, and exhibited an average diameter of 3.41±0.72 µm (Figure 3.7a). The latter corresponds to an average particle volume of 2.05±0.01 $\mu m^3$. The volume was calculated based on a disk thickness

of 0.225±0.03 µm, which was estimated based on SEM images. Prepared from jetting solutions with a higher polymer concentration, but with similar flow rates, microspheres showed an average diameter of 3.05±1.21 µm (Figure 3.7d) and an average particle volume of 14.85±0.92 $\mu m^3$. The relatively broad size distributions may in this case be attributed to lack of a long-term stability of the Taylor cone. In case of rods, the average lengths of 18.37±6.17 µm (Figure 3.7b) and average aspect ratios of 9.00±3.69 µm (Figure 3.7c) indicate preferential fabrication of larger particles. These rod dimensions translated into larger average particle volumes of 60.15±13.55 $\mu m^3$. The larger particle volumes may be attributed to the higher flow rates employed during electrohydrodynamic co-jetting of rods. Polydispersity of rod-like particles with respect to rod lengths and diameters are indications of an increasingly randomized jet break-up mechanism.

In order to quantify the anisotropic character of the bicompartmental microparticles, flow cytometry was performed for a representative population. [10] Prior to analysis of bicompartmental particles, a number of different reference groups were obtained including (i) particles without dye, (ii) particles with ADS406PT in one compartment only, and (iii) particles with ADS306PT dye in one compartment only. During these experiments, the dye concentrations of all jetting solutions were maintained equal. After these reference samples were obtained and analyzed by flow cytometry, a fourth sample of particles, containing ADS306PT in one compartment and ADS406PT in the other compartment was investigated. Figures 3.8 a-d show the four dot plots of the corresponding particles. Being negative for both the dyes, sample (i) fell in the lower left

quadrant (Figure 3.8a). Microparticles loaded with one dye only, *i.e.*, sample groups (ii) and (iii), were characterized by fluorescence signals that were clearly confined to their respective quadrants (Figures 3.8b and 3.8c). Sample group (iv), thatcomprised of bicompartmental particles loaded with ADS306PT in one compartment and ADS406PT in the other, was indicated by fluorescence signals located almost exclusively in the upper right quadrant (Figure 3.8d), confirming the presence of both dyes. Furthermore, sample (iv) showed excellent correlation between fluorescent intensities of ADS306PT and ADS406PT, which exhibit almost a linear relationship, indicating that the relative sizes of the compartments were retained irrespective of particle size. Based on combined qualitative and quantitative data from the CLSM micrographs and flow cytometry analysis respectively, close to a 100% of the particle population appears to be bicompartmental.

For tricompartmental particles, first, a negative control group of particles without any fluorescent dyes was analyzed. The blue, green and red fluorescence emission observed from this population was designated as background signal, which is depicted by a vertical line in each of the three plots shown in Figure 3.9a. Next, we fabricated particles that were tricompartmental, but loaded with only one fluorescent dye per group. Each of these populations exhibited an increase in fluorescence intensity corresponding to the representative channel (Figures 3.9b, 3.9c and 3.9d). For instance, tricompartmental particles loaded with ADS406PT dye exhibited an increase in fluorescence intensity in the blue channel (Fig. 3.9b). Moreover, the fluorescence

intensities of the other channels (here: green and red) were still below the background threshold level, indicating negligible bleed-through of spectral emissions. This was further confirmed using particles that were loaded with different dyes in two out of three compartments. The fluorescence histograms of these particles also presented a similar trend, i.e., an increase in fluorescence intensity in the channels corresponding to the two respective dyes (Figures 3.9e, 3.9f and 3.9g). Finally, tricompartmental particles containing blue, green and red dyes were analyzed. A significant increase in fluorescence intensity in all the three channels was observed in this case, confirming the tricompartmental nature of the particles (Figure 3.9h). For a population of 10,000 particles, at least 80% of the particles were positive for blue, green and red fluorescence (Figure 3.10).

After the quantitative analysis of compartmentalization, we turned our intention to optimization of particle shape and size. We therefore investigated the formation of optimized spherical particles with two compartments in further detail. For biological applications, such as drug delivery, control over particle size has been shown to impact their performance *in vivo*, by affecting several properties such as circulation times, clearance, penetration across biological barriers, and cellular uptake.[1] In addition, particle aggregation and interaction with blood and tissues is also size-dependent.[1] With a goal of delivering therapeutics to antigen-presenting cells (APCs), which can undergo particle uptake via phagocytosis,[22] we chose to optimize bicompartmental microparticles to conform to a diameter range of 3-5 μm, a size range that previously been shown to be effective in the delivery of genetic vaccines[23] and immunosuppressants[24] to

APCs, such as macrophages and dendritic cells. In order to achieve optimum uptake results, narrower size distributions are important, which could be obtained through effective filtering methods. With these goals in mind, we fine-tuned the co-jetting parameters and developed a suitable filtration protocol.

During electrohydrodynamic jetting, organic solutions are known to exhibit varicose instabilities to a lesser extent than their aqueous counterparts owing to their lower conductivities and dielectric constants, thereby producing lesser number of satellite droplets. This may potentially result in narrower and uniform size distributions.[25] On the other hand, the higher volatility of chloroform used in this study as solvent for electrohydrodynamic co-jetting gives rise to intermittently solidified jetting cones, which may result in larger particles that can be deposited on to the substrate before complete evaporation and appear as donut-like shapes. After establishing appropriate jetting solution conditions, which are of primary importance in determining shape and bicompartmental architecture, we evaluated process conditions, namely flow rate and voltage, for further optimization of size and shape. It is known that larger flow rates induce a greater number of satellite particles in the jet stream, [21] resulting in reduced monodispersity. On the other hand, very low flow rates result in a droplet of higher viscosity due to a mismatch between rates of solvent evaporation and supply of fresh jetting solution, giving rise not only to beaded fibers, fibers, and polydisperse particles in the population, but also creating problems in maintaining the interface between two solutions. For the desired diameter range, we found that a flow rate of 0.17±0.01 ml/h balanced the aforementioned issues. This was

combined with a slightly higher operating voltage of 6±0.1 kV, which reduced the formation of donut like shapes and ensured that the jet could be sustained for longer periods of time (~3h). Donut like shapes, nonetheless, could not be removed completely, and filtration was subsequently employed for their removal. This approach resulted in milligram-scale particle quantities of close-to-perfect spheres, with excellent bicompartmental architecture, as seen in the CLSM image in Figure 3.11. In particle populations obtained directly after jetting, 'donut' like shapes constituted approximately 8.2% of the entire population. These were completely eliminated via microfiltration, as seen in the SEM images shown in Figures 3.12a and b. After filtration, 84% of the particle population was found to exhibit diameters in the range of 3-5 μm (Figure 3.12c), compared to 58% immediately after jetting, reflective of a uniformly sized particle population. The yield after filtration was found to be 60%.

In electrohydrodynamic processing of polymer solutions, the physical attributes of particles, as well as the parameters that can be controlled to produce them, constitute a truly multidimensional design space, as outlined in Chapter 1. The controllable parameters can be based on the jetting solution, which includes surface tension, dielectric constant, electrical conductivity, density, and vapor pressure of the solvent, and the viscosity of the solution, which in turn depends on density and concentration of the polymer used. In addition, process parameters involve flow rate, current, separation distance between the electrodes and diameter of the capillary. Furthermore, there are environmental variables that affect solvent evaporation, such as ambient

temperature, pressure and humidity. Simultaneous control over these variables may widen the access to particles with a multitude of sizes, shapes, surface morphologies and porosities. In electrohydrodynamic co-jetting of two or more solutions, the parameter space is complicated further due to the presence of a compound Taylor cone.[7] Aiming to clearly delineate transitions with respect to shape and size, we further investigated the effect of polymer concentration and flow rate on particle characteristics. This is depicted in Figure 3.13. At a given polymer concentration, an increase in polymer flow rate results in increased particle size, due to an increase in radius of the jet,[14] and hence increased droplet size in the jet stream.[21] Thus, at a concentration of 1.3:100, increasing the flow rate from 0.15 to 0.7 ml/h resulted in an increase in disc diameter. Similarly, at a concentration of 4.5:100 w/w, flow rates of 0.17, 0.35, and 0.5 ml/h, respectively, yielded bicompartmental microspheres that were correspondingly larger in diameter. On the other hand, polymer concentration directly influenced particle shape by affecting solution viscosity, which in turn influences jet break-up and evaporation rate. Since solutions of higher viscosities resist jet breakup, these conditions resulted in fibers. However, this effect was only observed at low flow rates, when evaporation rates were much higher than solution flow rates. At these concentrations, however, as the flow rate is increased, a successive transition from fibers to beaded fibers, and then to distinct microspheres was observed. These observations may be attributed to an increase in volume of the primary droplet, which can enhance breakup even at higher viscosities. Thus, the same 8:100 w/w PLGA solution resulted in fibers at

a flow rate of 0.02 ml/h, and beaded fibers at 0.04 ml/h. However, a higher PLGA concentration of 12:100 resulted in distinct particles at flow rates as high as 0.7 ml/h. As the concentration was further increased, the minimum flow rate required to produce distinct spheres also increased. Concentration was also found to influence the shape of discs, because, the discs seemed more 'collapsed', when jetted from lower concentrations. This is most likely due to the presence of polymer at the core of the droplet at higher concentrations, which impedes microparticle collapse. Thus, for a given solvent system, individual or simultaneous control of flow rates and concentrations can be a straightforward, yet extremely precise and effective means for obtaining particles of different sizes and shapes. The complexity that arises from co-jetting of two distinct solutions could also possibly give rise to interesting effects, such as the rods observed herein. Choice of solvent is another aspect to controlling size and shape, as more volatile solvents can result in particles of larger diameter (Figure 3.4).

### 3.4 Fabrication of complex shapes: red blood cell mimicking biomaterials

Recent advances in biomaterials have been marked by a sharp progression from tuning the chemical makeup of materials alone, to a combinational approach wherein physical properties such as size, shape, surface characteristics and distribution of materials are tailored in conjunction with chemical architecture to create the next generation of materials which would

possess a more holistic ‘toolbox’ to tackle several aspects of disease simultaneously.[1] RBCs constitute a significant proportion of the human body, with an extremely crucial function: transfer of oxygen and exchange of nutrients between different parts of the body. Remarkably, the properties that are key for normal RBC function are a consequence of its physical constitution: shape, deformability and aggregability.[26] RBC’s possess a biconcave discoid shape and are equipped with a highly deformable membrane. Together, these characteristics impart a high surface-to-volume ratio which facilitates large reversible elastic deformations of the RBC as it repeatedly passes through capillaries, sometimes smaller than its own size during circulation. This flexibility is essential for circulation, which helps transport oxygen and carbon dioxide. Indeed, pathological conditions affecting RBC functions are known to manifest as significant alterations to their shape, for example, hereditary elliptocytosis.[27] Changes to the RBC shape, and hence surface area can compromise cell deformability and disrupt circulation.

Despite the obvious advantages offered by the biconcave discoid shape, it is non-trivial to realize it *ex vivo* and there is tremendous interest mimic their physico-chemical architecture. Such flexible, long-circulating synthetic microstructures would not only resist clearance in the spleen and participate in oxygen and nutrient exchange, but could also potentially serve as drug delivery vehicles and imaging agents, thereby providing increased functionality. As demonstrated in the previous section, a major advantage of the electrohydrodynamic co-jetting process is the ability to synthesize a vast

repertoire of shapes and sizes by controlling two parameters, namely solution concentration and process flow rate. We first focused on preparing monocompartmental RBC-shaped template PLGA particles (Figure 3.14c). For this purpose, a solution concentration of 4.5:100 w/w of PLGA in 97:3 v/v chloroform: DMF was employed. At lower flow rates of 0.4 ml/h, electrohydrodynamic jetting from a single capillary resulted in spherical particles (Figure 3.14a), as already elucidated in Figure 3.13 However, at higher flow rates of 1.4 ml/h, the particles obtained possessed a discoidal shape, as shown in Figure 3.14c. This transition in shape could be the result of the increasing concentration gradients inside the particle during solvent evaporation that result from higher droplet volumes (which in turn arise from higher flow rates), which result in particle collapse and formation of disc shapes. The effect of flow rate is clearly seen in Figure 3.14b where, at flow rates of 1 ml/h, small indentations are clearly seen in the particle. The flatness of the discs increases as the flow rate is increased to 2 ml/h (Figure 3.14d), as does particle diameter. Thus, we can not only control the size of PLGA particles via flow rate, but also the shape (in another synthetic route, PLGA templates were synthesized via the incubation of spherical particles in isopropanol. This is discussed in detail in the Appendix).

PLGA is biodegradable and biocompatible, making it an ideal material choice as template RBCs. These templates were used to yield soft, protein based biocompatible particles using a modified layer-by-layer (LBL) technique (Figure 3.15a). Nine alternate layers of either Hb/BSA or PAH/BSA were assembled on the templates, the layers were cross-linked, and the underlying PLGA core

(Figure 3.15b) was removed using 1:2 2-propanol:THF to form synthetic RBCs ( or sRBCs, Figure 3.15c) The choice of solvent was important, and deviation from this solvent mixture led either to incomplete dissolution (excess 2-propanol) or complete collapse (excess THF). sRBCs synthesized by this method demonstrated close resemblance to natural RBCs (Figure 3.15d).

sRBCs were found to be flexible owing to the dissolution of the template PLGA core, which leaves behind a soft protein shell. The elastic modulus of sRBCs was measured using atomic force microscopy (AFM). The elastic modulus of sRBCs was obtained from force-indentation curves obtained by inducing deformations comparable to the capsule wall thickness, where the elastic response is expected. The typical loading-unloading cycle used for this study and the corresponding force curves obtained for sRBCs can be found elsewhere.[27] The elastic modulus of sRBCs (92.8 ± 42 kPa) was found to be four orders of magnitude lower than that of PLGA template particles (1.6 ± 0.6 GPa) and of the same order of magnitude as that of natural RBCs, as shown in Figure 3.16a. The elastic modulus of mouse RBCs was found to be 15.2 ± 3.5 kPa, which is consistent with the values reported in literature.[28] Further studies are required to facilitate a detailed comparison of various mechanical properties of sRBCs and natural RBCs; however, the data in Figure 3.16a clearly indicate that sRBCs are far closer to natural RBCs than to routine polymer particles with respect to mechanical properties.

The flexibility of sRBCs (7 ± 2 μm) was confirmed by flowing them through narrow glass capillaries (5 μm inner diameter) and visualizing the stretching

(Figure 3.16b, two sRBCs, one inside the capillary and one outside the capillary). While the particle outside the capillary is symmetric and circular, the particle inside the capillary is stretched due to flow. The average aspect ratio of stretching was found to be 170 ± 20% (n = 20). Thus, similar to their natural counterparts, sRBCs maintain the ability to flow through channels smaller than their resting diameter and stretch in response to flow. Further detailed studies of the kinetics of shape transition while passing through the capillaries are necessary to gain further insight into the mechanical flexibility of sRBCs.

sRBCs reported in this study have numerous biomedical applications. Because the primary function of natural RBCs is to deliver oxygen to the various tissues of the body, we assessed the ability of sRBCs to bind oxygen (Figure 3.16c). Cross-linking and exposure to solvent during particle preparation leads to deactivation of Hb, thereby limiting its oxygen carrying capacity (Figure 3.16c, sRBC without Hb). To enhance oxygen carrying capacity of sRBCs, particles were further fortified with additional, uncrosslinked Hb. This procedure resulted in high oxygen binding levels. (Figure 3.16c, sRBC with Hb, t=0) compared to the positive control, which was mouse blood. Approximately 90% of this oxygen carrying capacity was retained even after 1 week (Figure 3.16c, sRBC with Hb, t = 1 week). Also included is a negative control, BSA-coated particles, which showed no ability to bind oxygen (Figure 3.16c, control).

sRBCs are also excellent candidates for delivery of drugs, especially in the vascular compartment. These particles can be loaded with drugs by incubation in solutions containing the drug. Heparin is widely used as an

anti-coagulant for the treatment of thrombosis.[29] The sRBCs showed high amounts of heparin loading (70 µg heparin/ mg particles) and continuous release over a period of several days in vitro (Figure 3.16d).

sRBCs also have potential applications in medical imaging. For example, iron oxide nanocrystals with an average diameter of 30 nm were encapsulated inside the PLGA particles prepared via electrohydrodynamic jetting. Incorporation of iron oxide nanoparticles makes particles suitable as contrast agents for MRI.[30] An important requirement for this use is homogenous dispersion of the iron oxide nanocrystals. As shown in Figure 3.16e, TEM images show well-distributed iron oxide particles in the PLGA matrix. Magnetic particles are currently being developed for a wide spectrum of applications such as MRI contrast agents for diseases, such as atherosclerotic plaque, targeted therapeutic delivery, and hyperthermia treatment for cancerous tumors.[31] The interior of the particles described here can be further engineered by the formation of separate compartments using electrohydrodynamic co-jetting. At the same time, the surface can be engineered by adsorption of additional proteins such as CD47, a ubiquitous self-marker expressed on the surface of RBCs[32] or modification of the particle surface with hydrophilic polymers, such as PEG, depending on the application.

## 3.5 Conclusions

In summary, we have demonstrated the fabrication of discoid, rod-like and spherical bicompartmental biodegradable microparticles of different sizes via

electrohydrodynamic co-jetting. Furthermore, we have extended this process to synthesize tri- and tetracompartmental PLGA particles with remarkably precise internal architectures. In addition, the effect of flow rate and concentration on shape and size was systematically studied. In case of bicompartmental particles, solutions with lower concentrations (up to 3.5:100) yielded disc-shaped particles at flow rates from 0.02-0.7 ml/h, whereas an increase in concentration (4.5:100-12:100) resulted in spherical particles. However, at higher concentrations, lower flow rates produced fibers, and, as flow rate were further increased, beaded fibers and spheres. Rods were obtained at a concentration of 3.6:100 and at higher flow rates (0.45 ml/h) upon addition of triethylamine. Flow rate was found to be a key variable affecting particle size, whereas concentration predominantly influenced particle shape, and also size (Figures 3.13 and 3.14). Spherical particles were further optimized with respect to size and shape via tuning of co-jetting parameters, followed by microfiltration to obtain monodisperse, spherical microparticles in the size range of 3-5 μm. Multifunctional microparticles with simultaneously controlled size, shape and compartmentalization may have applications in drug delivery, cell targeting and biomedical imaging. In addition, we have demonstrated the fabrication of discoid PLGA templates via electrohydrodynamic jetting followed by the synthetic mimicry of many key attributes of RBCs including the size, shape, elastic modulus, ability to deform under flow, and oxygen-carrying capacity. We also report incorporation of additional functionalities such as therapeutic and diagnostic agents in these carriers, which enable further capabilities. These particles, which mimic the

structural and functional properties of RBCs, have the potential to address some of the key challenges faced by current drug delivery carriers. Upon further confirmation of RBC mimicry through in vivo experiments focused on circulation and biocompatibility, the particles reported here may open opportunities in drug delivery, medical imaging, and the establishment of improved disease models.

## 3.6 Figures and Tables

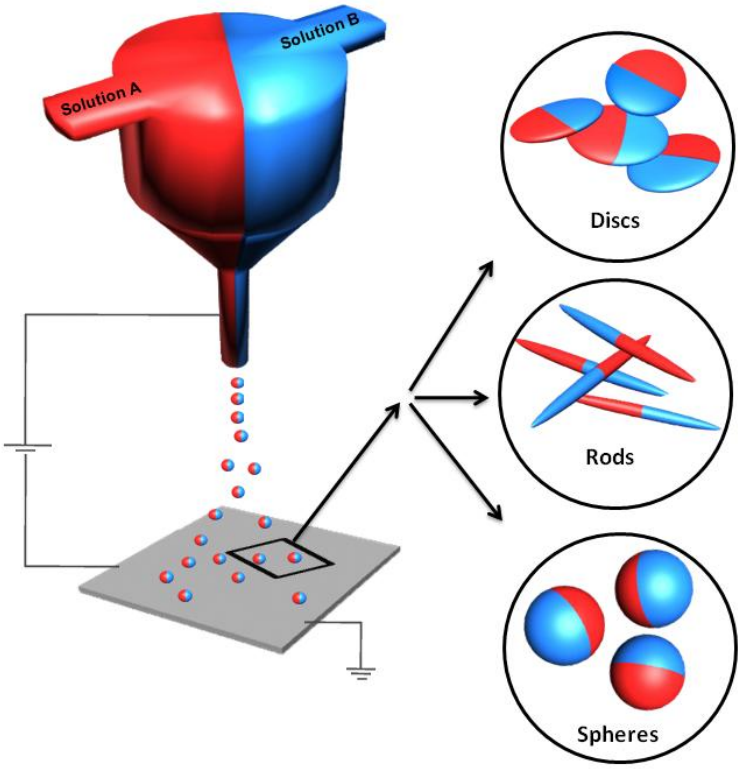


**Figure 3.1** Schematic of the electrohydrodynamic co-jetting process yielding bicompartmental discoid, rod shaped and spherical microparticles.

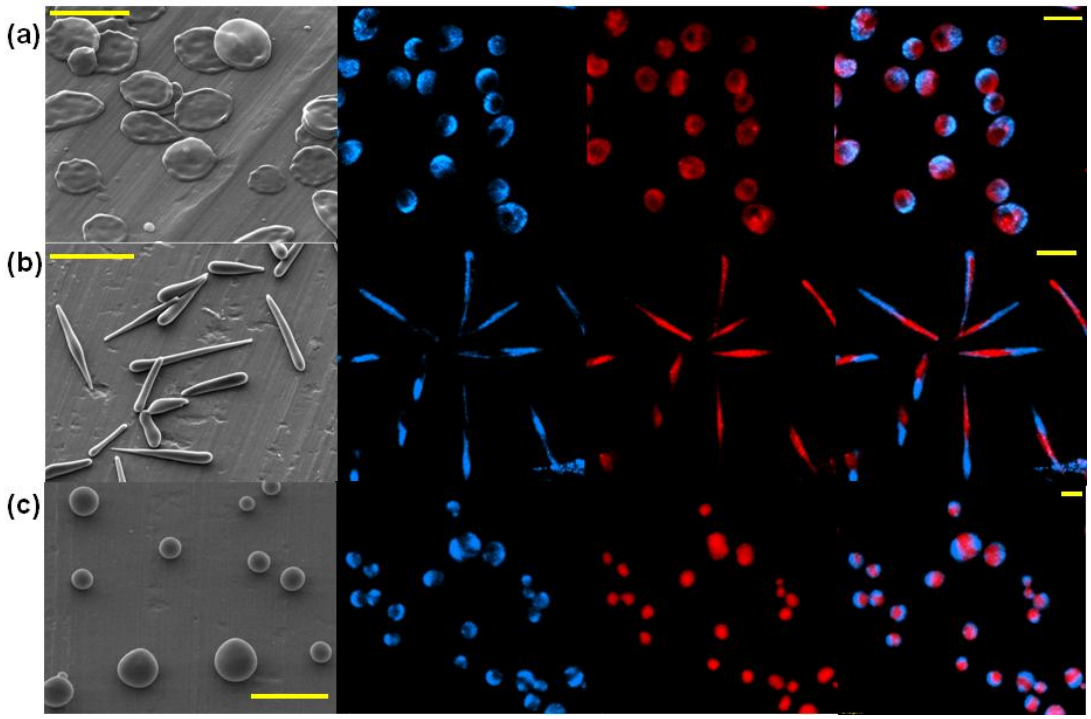


**Figure 3.2** SEM and CLSM images of bicompartmental particles of different shapes, (a) discs, (b) rods and (c) spheres made from PLGA polymers via electrohydrodynamic co-jetting. Blue fluorescence represents ADS406PT and red fluorescence represents ADS306PT. Individual blue and red CLSM images are shown, followed by their overlay. Scale bars represent (a) 5 µm, (b) 20 µm and (c) 10 µm for SEM and 5 µm for CLSM.

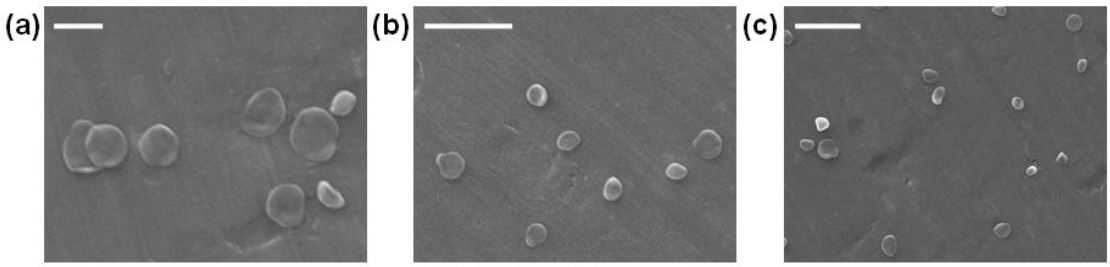


**Figure 3.3** Monophasic disc shaped particles prepared at different distances between counter-electrodes during electrohydrodynamic jetting. (a) 33cm (b) 40 cm (c) 51 cm. A 1.3:100 solution of PLGA 85:15 in 95:5 (by vol.) Chloroform: DMF was used as the jetting solution. Flow rate and voltage were 0.2 ml/h and 8 kV respectively. The needle-to-collection substrate distance was not found to significantly affect the voltage required to achieve the cone-jet mode. Disc shaped morphology observed at different distances confirms that the shape arises from anisotropic evaporation in the jet stream, and not from incomplete evaporation and consequent collapse onto the substrate. Scale bars denote 2 μm for (a) and 5 μm for (b) and (c).

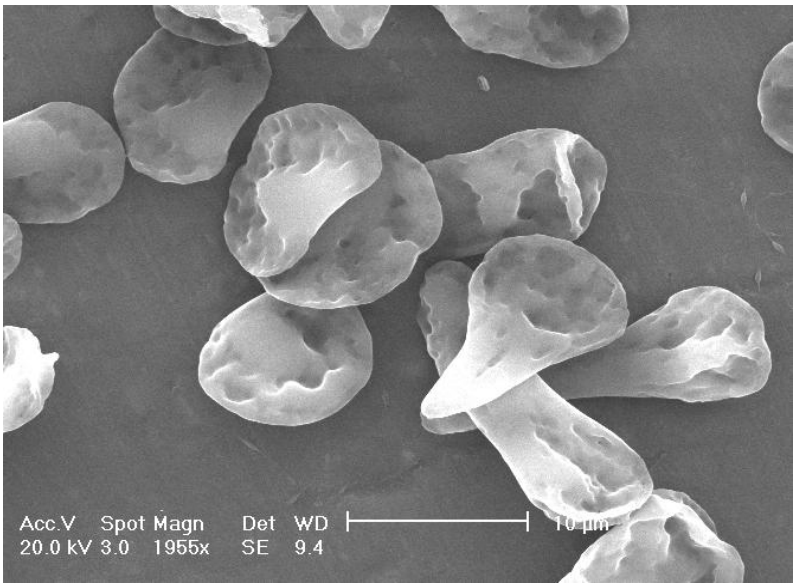


**Figure 3.4** Size control of disc shaped monophasic particles by simultaneously varying solvent ratio and flow rate. A 1.3:100 w/w solution of PLGA was prepared in 98:2 Chloroform : DMF, and jetted at a flow rate of 0.2 ml/h. Increasing the amount of chloroform in the jetting solution resulted in even more rapid evaporation, due to which particles possess surface roughness.

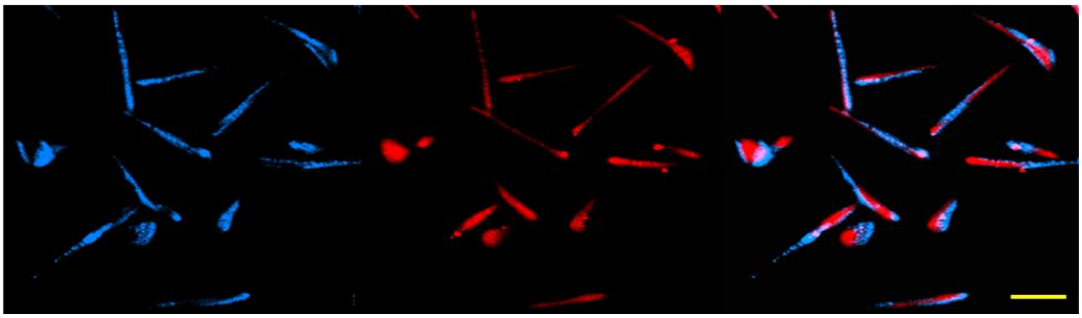

**Figure 3.5** CLSM images of bicompartmental rod shaped particles exhibiting anisotropy along their longitudinal axis. Blue and red fluorescence represent ADS406PT and ADS306PT respectively. Individual fluorescence channels are shown, followed by their overlay. Scale bar represents 10 μm.

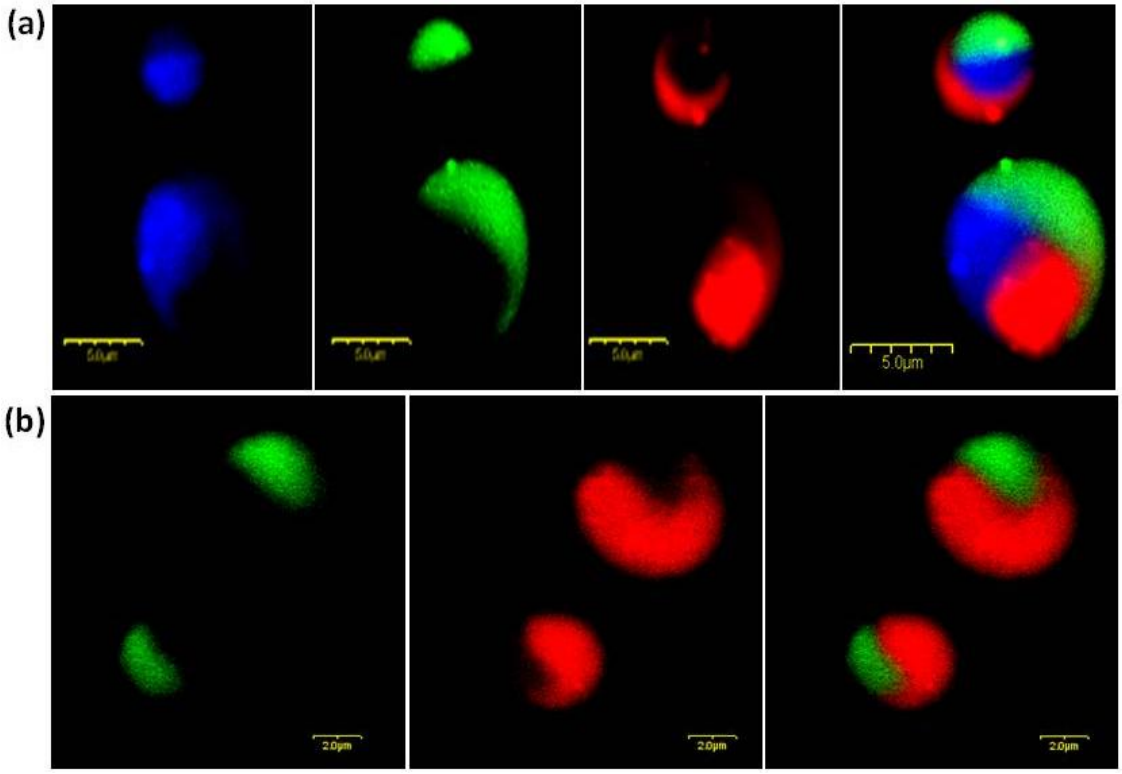


**Figure 3.6** (a) CLSM image of tricompartmental PLGA microparticles synthesized via electrohydrodynamic co-jetting from three capillaries held together in a triangular configuration. Individual fluorescence channels resulting from blue (ADS406PT), green (PTDPV), and red (ADS306PT) dyes are shown, followed by the overlay. (b) CLSM image of tetracompartmental microparticles made via co-jetting from four capillary needles arranged in a square configuration. Three solutions were labeled with ADS306PT (red) and the fourth solution was labeled with PTDPV (green). Scale bars represent 5µm and 2 µm for (a) and (b), respectively.

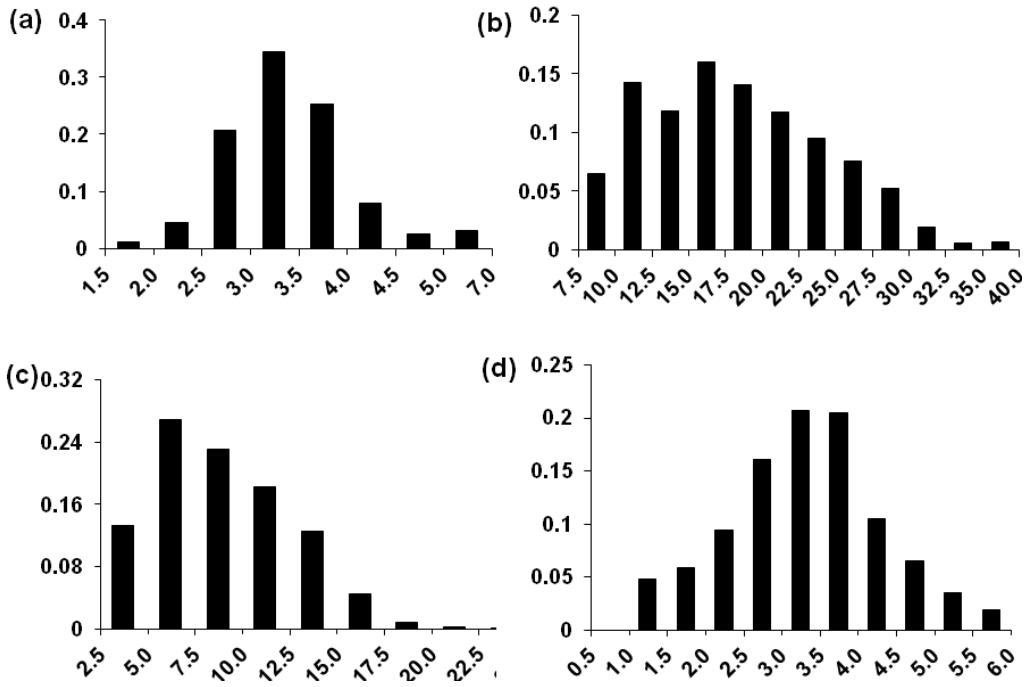


**Figure 3.7** Size distribution analyses for discoid, rod-like and spherical microparticles. X axis depicts particle diameter (µm) for a and d, length (µm) for b, and aspect ratio (µm) for c; y axis represents number fraction of population. Number of particles measured was ~800 for each population. (a) Discs: diameters indicate arithmetic mean of values along perpendicular axes through the center. (b), (c) Rods: the arithmetic mean of diameter values measured at the top, middle and bottom of each particle was used to determine the aspect ratio. 72% of the particles analyzed were rods, and only these were considered in the size distribution. (d) Spheres: 8.2% of the particles measured were > 6 µm in diameter and, being non-spherical, these were not considered in the size distribution.

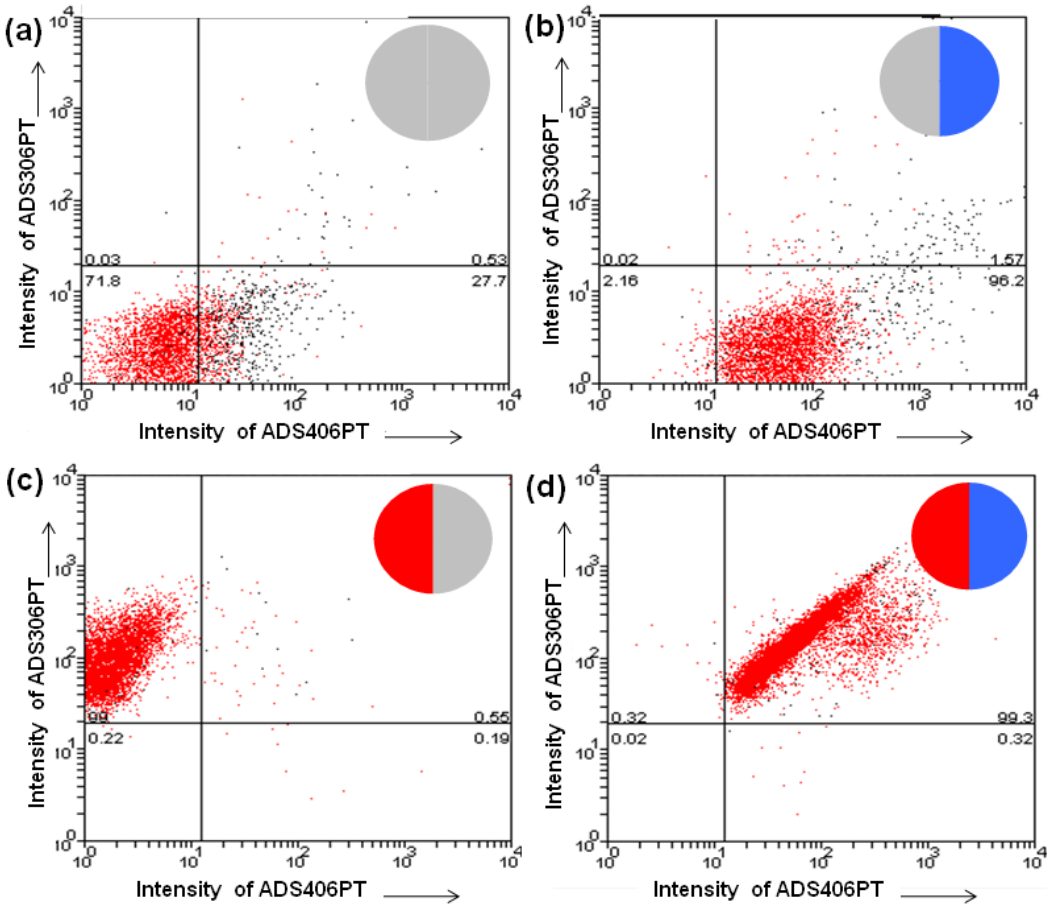


**Figure 3.8** Flow cytometry analysis of spherical bicompartmental microparticles. Inset indicates the nature of dye loading in the particle. (a) Bicompartmental particles fabricated without any dyes. These exhibit low ADS306PT and ADS406PT fluorescence intensities and fall in the lower left quadrant (b) Bicompartmental particles loaded with ADS406PT in one compartment and no dye in the other, these fall in the lower right quadrant (c) Particles loaded with ADS306PT in one compartment and no dye in the other which exhibit high ADS306PT intensities and lie in the top left quadrant. (d) Microparticles with ADS306PT in one compartment and ADS406PT in the other. Owing to high ADS306PT and ADS406PT intensities, these lie in the upper right quadrant.

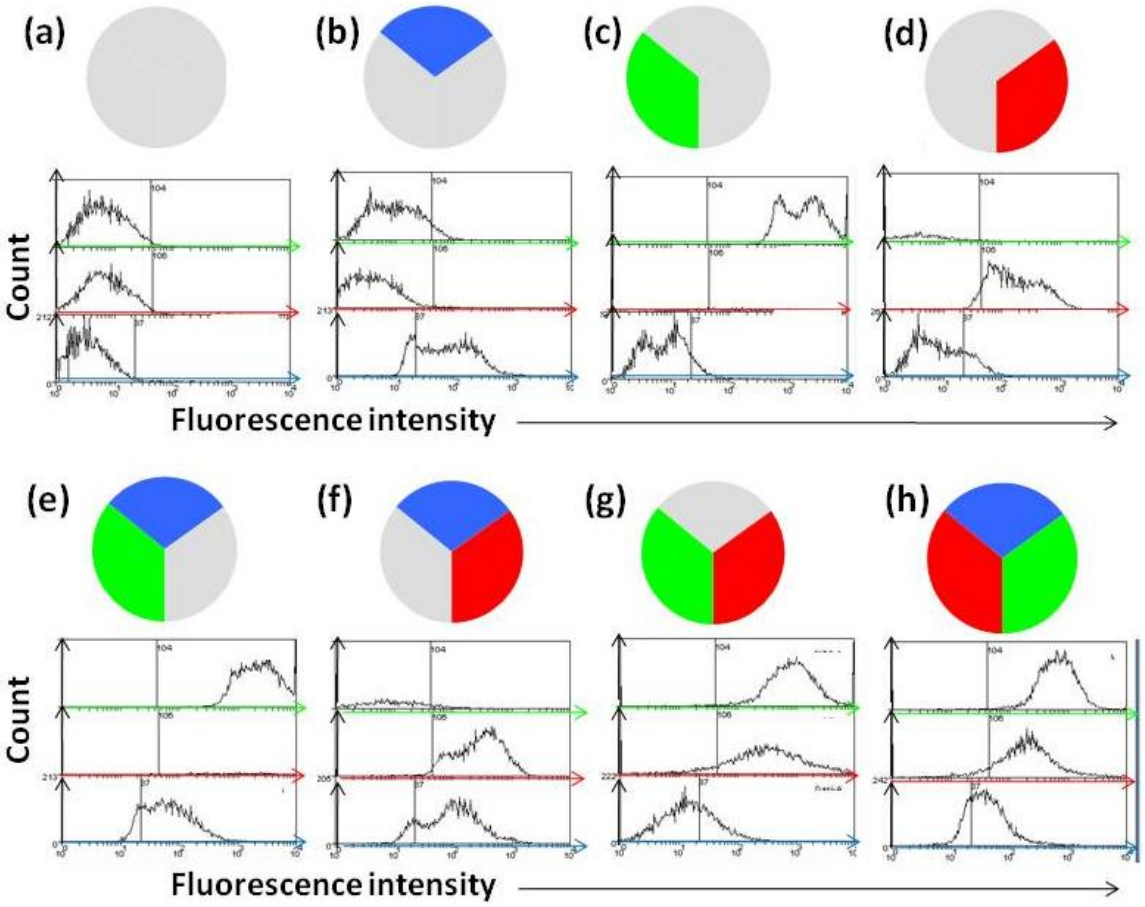


**Figure 3.9** Flow cytometry analysis of tricompartmental particles. Each plot comprises of an overlay of three individual histograms, with a corresponding symbol on top indicating the nature of dye loading in particles. For each plot, the y-axis represents particle count, and the green, blue and red x-axes denote the magnitude of fluorescence intensity from PTDPV, ADS406PT and ADS306PT dyes respectively. Particles without any dye (a) were first employed as a reference to determine background fluorescence, indicated by a vertical line in each plot. Once these threshold fluorescence histograms were established, particles with one dye (b-d) and different permutations of two dyes (e-g) were analyzed. Particles loaded with one dye only exhibited a fluorescence intensity shift corresponding to the dye, and particles with two dyes showed significant intensity shifts corresponding to both dyes. Finally, tricompartmental particles containing three dyes (h) were analyzed and found to exhibit a shift in fluorescence intensity in all three channels.

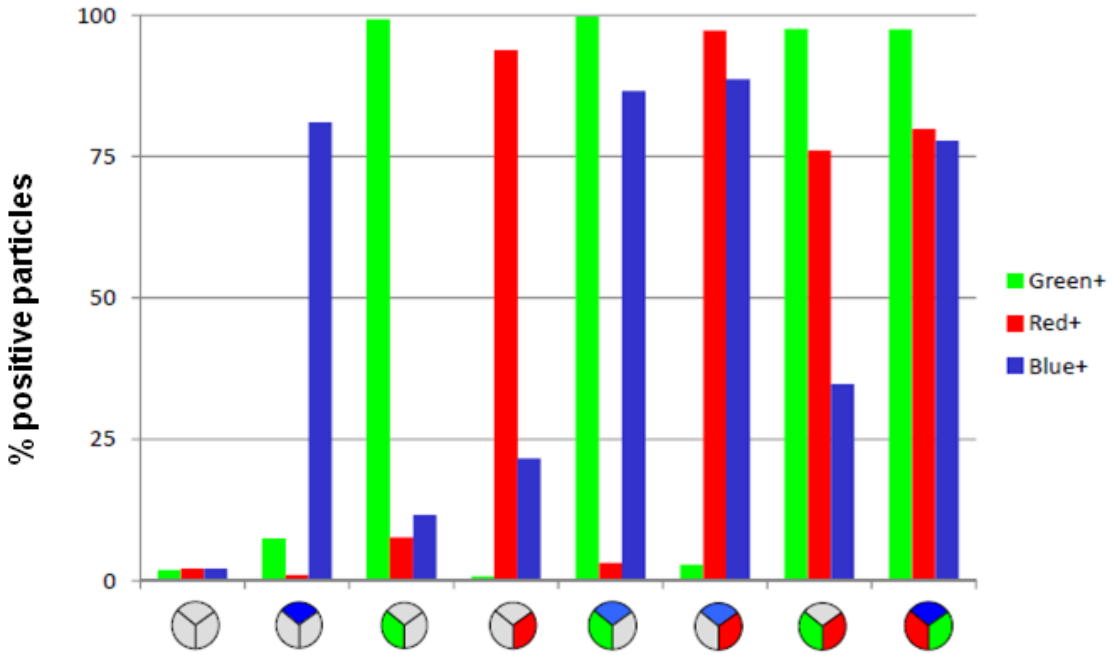


**Figure 3.10** Histograms depicting quantification of degree of blue (ADS406PT), green (PTDPV), and red (ADS306PT) fluorescence signals from tricompartmental particles with different permutations of dyes. The y-axis denotes the percentage number of particles, which showed positive fluorescence signal (greater than background fluorescence) for a given dye (indicated by blue, green and red bars) for a population of particles containing a given combination of dyes (indicated by a schematic on the x-axis). The sample size is 10,000 particles. Particles containing a single dye show an increase in fluorescence intensity for the corresponding dye. Similarly, particles containing two dyes show an enhancement of fluorescence signal corresponding to both dyes. Finally, tricompartmental particles containing all the three dyes exhibit an increase in fluorescence intensity in all the three channels.

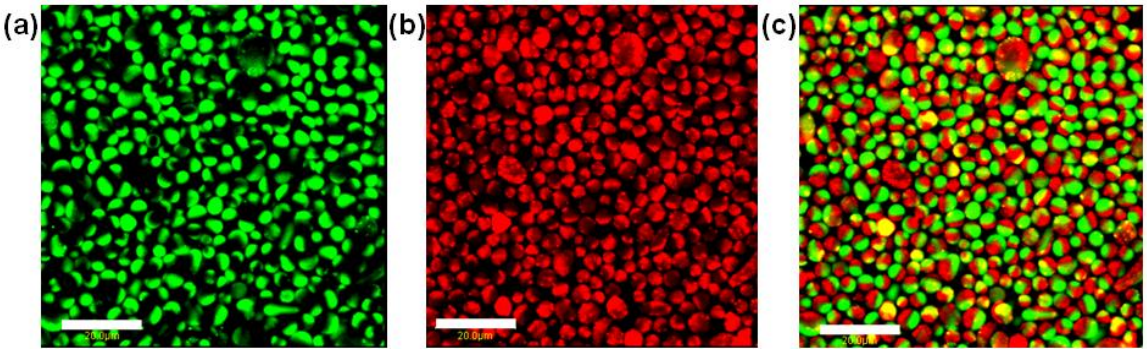


**Figure 3.11** (a-b) CLSM micrograph of bicompartmental microparticles after filtration. Green and red fluorescence depict PTDPV and ADS306PT respectively, followed by the overlay, (c). All scale bars represent 20 µm.

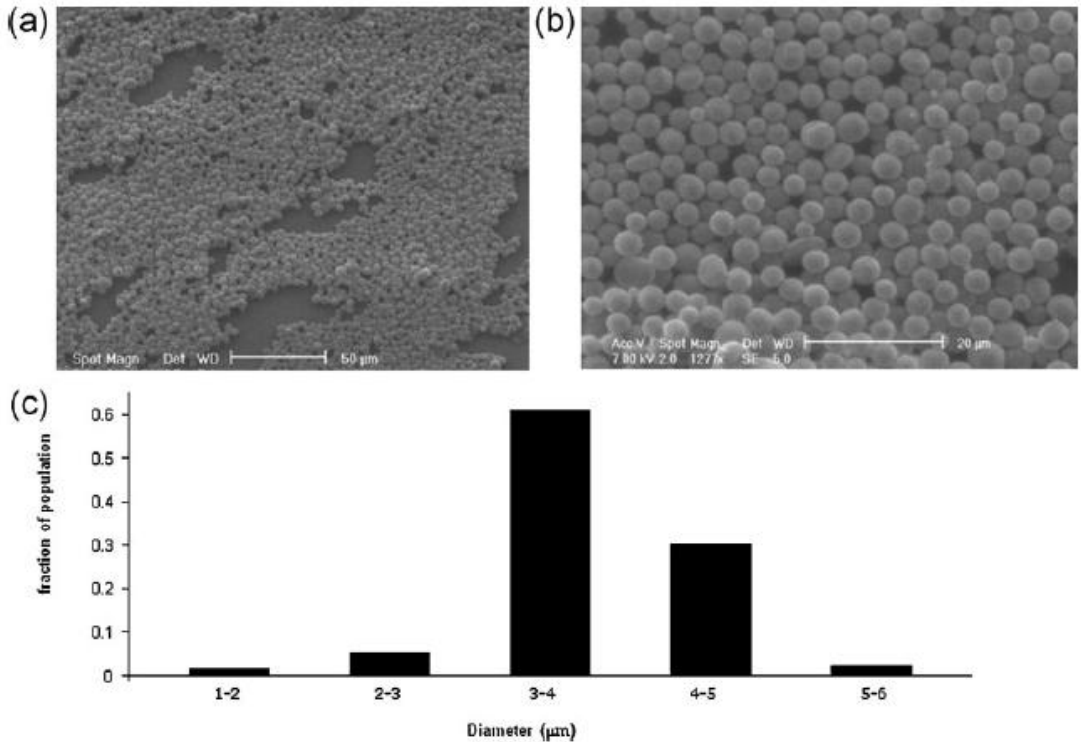


**Figure 3.12** (a) and (b): low and high magnification SEM images of bicompartmental PLGA particles post filtration. A flow rate of 0.17 ml/h and a voltage of 6.1 kV was employed in the co-jetting of a 4.5:100 w/w solution of PLGA 85:15 in 97:3 v/v Chloroform: DMF. The donut like flat shapes obtained during co-jetting were eliminated via filtration to yield optimized particles, with 84% of the total population in the size range of 3-5 μm, as shown in the size distribution in (c) obtained from representative SEM images.

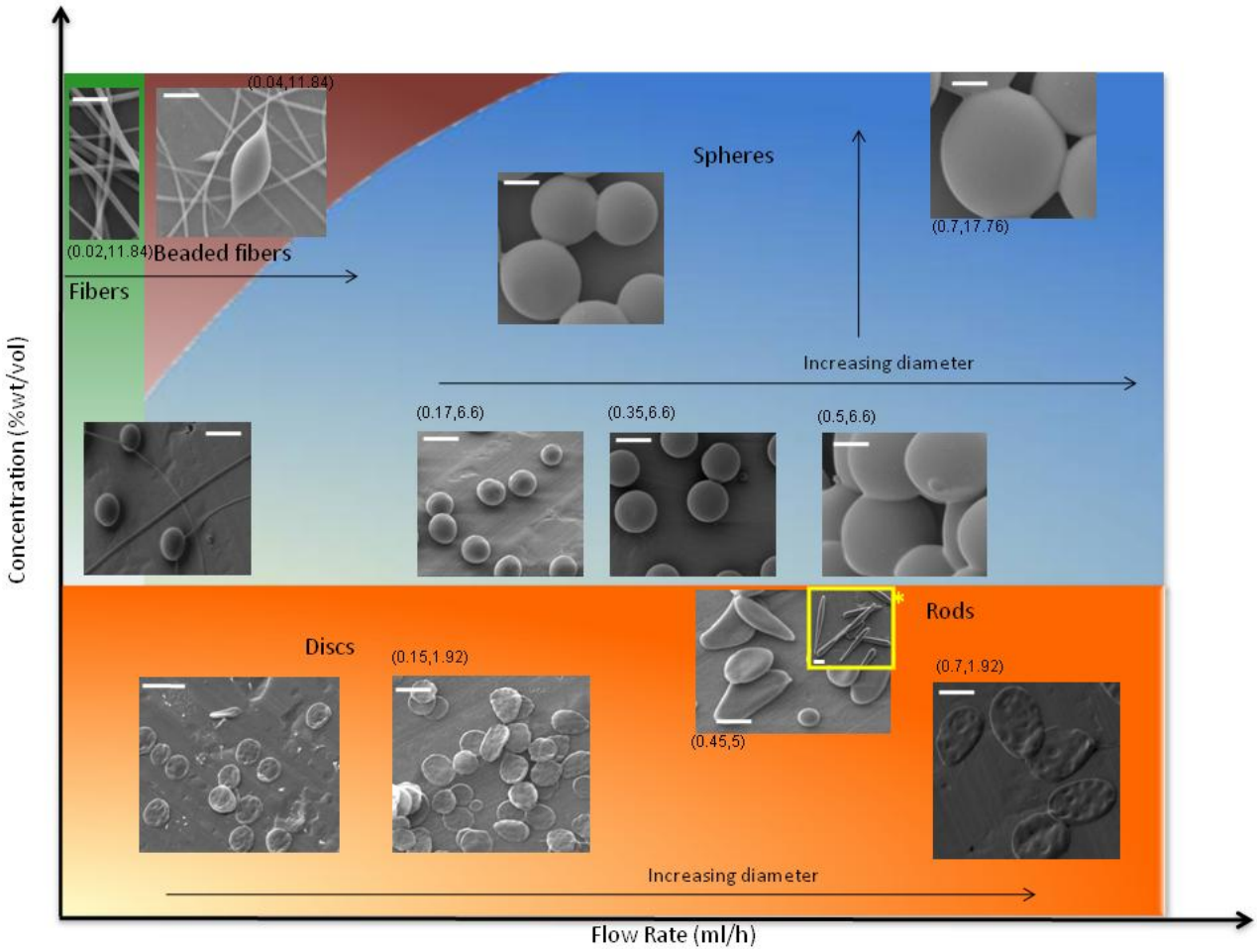


**Figure 3.13** Schematic depiction of effect of concentration and flow rate on size and shape of bicompartmental microparticles. At lower concentrations, bicompartmental discs are observed as a result of anisotropic solvent evaporation arising out of high surface/volume ratios afforded by small droplet sizes, which leads to the formation of a shell at the outer periphery, which collapses due to low overall polymer concentrations. This is observed even at higher flow rates, where particle shape is retained, but the diameter of the discs increases due to larger droplet sizes, as shown by the orange gradient. As the concentration is increased, the shape is somewhat affected due to availability of the polymer at the droplet core, which decreases the 'flatness' of the discs. Rods, indicated by an asterisk, are observed at a critical concentration (3.5:100) and flow rate (0.45 ml/h), but only upon the addition of triethylamine (3.5 vol% of solvent). As concentration is increased, spheres are observed due to increased structural stability imparted by increased solution viscosities. Increasing the polymer concentration or flow rate leads to increased sphere diameters till certain flow rates, depicted by the blue gradient. Fibers are observed at higher concentrations, but at low flow rates. At higher concentrations and higher flow rates, a greater amount charge is induced on the droplet, and a transition from fibers (green gradient), to beaded fibers (purple gradient), and then to particles is thus observed. All scale bars represent 5μm.

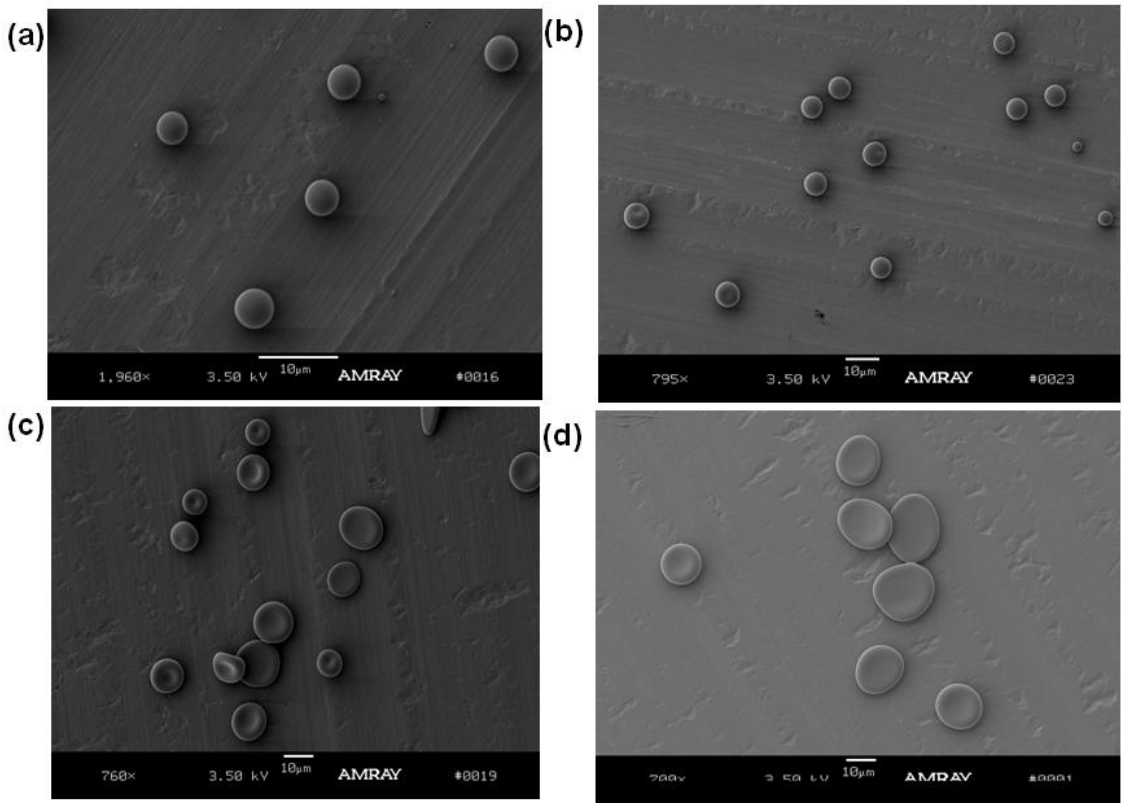


**Figure 3.14** Fabrication of templates for synthetic RBCs. All particles were synthesized from a 4.5:100 w/w solution of PLGA in 97:3 chloroform: DMF by volume using a single capillary needle. (a), (b), (c), and (d) represent flow rates of 0.4, 1.0. 1.4 and 2.0 ml/h respectively. Upon increasing the flow rate, particles not only increase in diameter, but also exhibit a shape transition from (a) completely spherical to (b) slightly collapsed, to (c) RBC like particles, and then to (d) flatter discs. This could potentially arise from the increase in the size of the droplet due to increase in flow rate, which increases the concentration gradient of the polymer during solvent evaporation, resulting in particle collapse and disc formation.

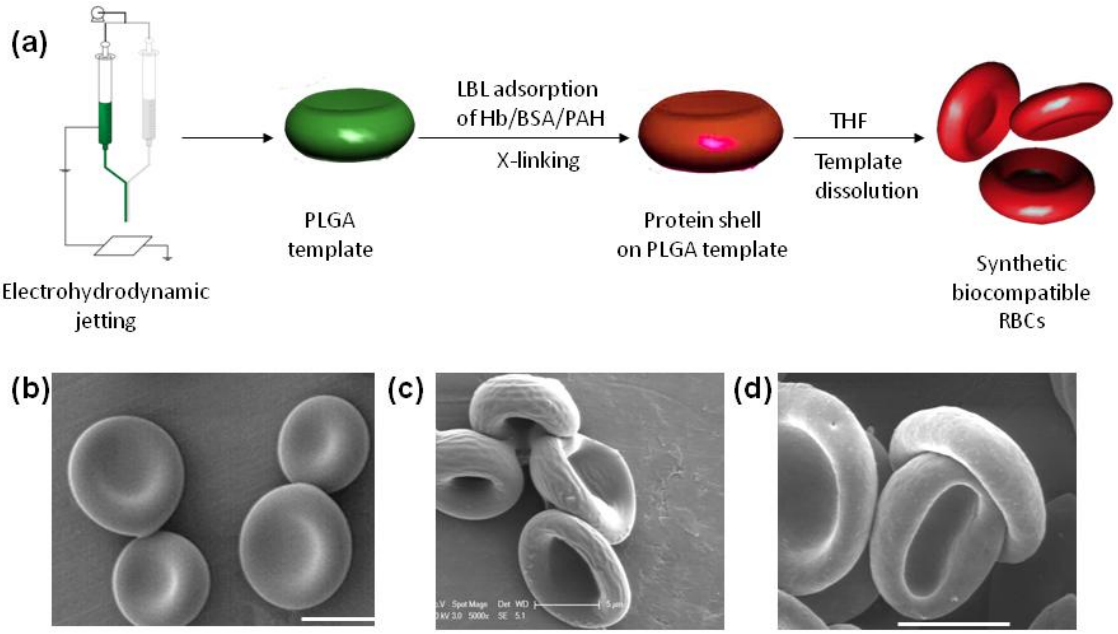


**Figure 3.15** (a): Scheme showing synthesis technique of RBC-mimicking particles. PLGA RBC-shaped templates were synthesized directly via electrohydrodynamic co-jetting or by incubating spheres synthesized from electrohydrodynamic jetting in 2-propanol. LBL coating on template, protein cross-linking, and dissolution of template core yielded biocompatible sRBCs (b) SEM images of PLGA templates. (c) Biocompatible sRBCs prepared from PLGA template particles by LbL deposition of PAH/BSA and subsequent dissolution of the polymer core. (d) Cross-linked mouse RBCs. sRBCs demonstrate striking resemblance to the natural counterparts. All scale bars denote 5µm.

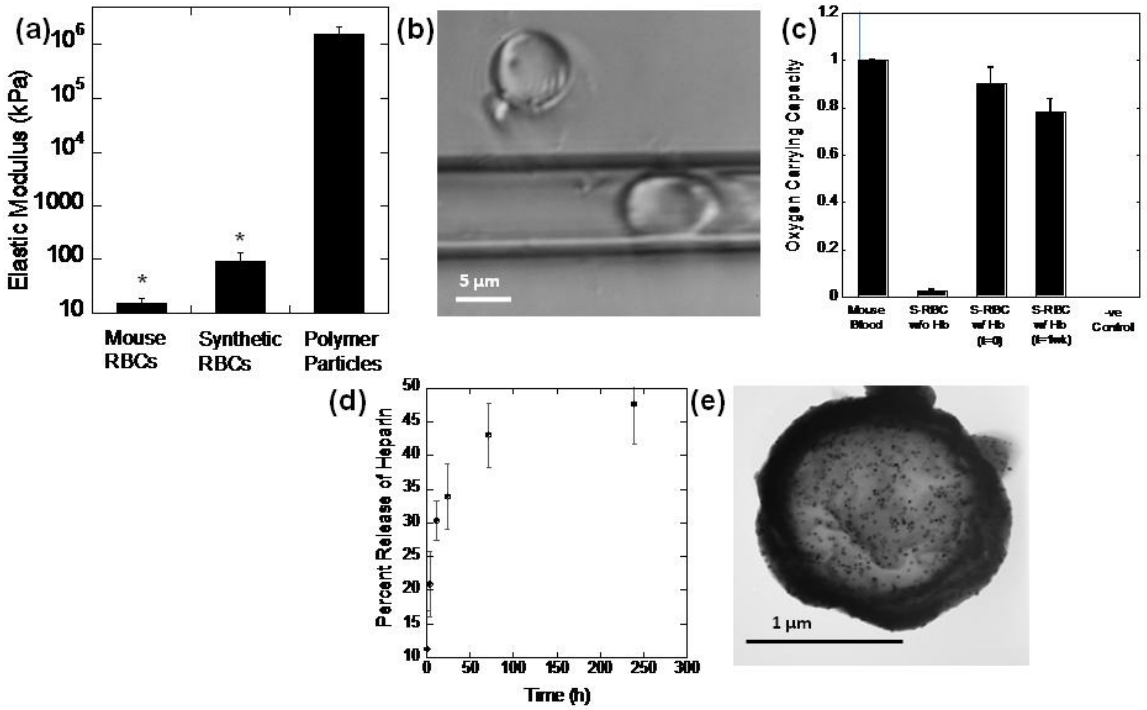


**Figure 3.16** Properties and biomedical applications of sRBCs. (a) Comparison of elastic modulus (measured via AFM) of sRBCs with mouse RBCs and PLGA particles (*, $P$ <0.001, $n$ = 5). (*b*) sRBCs (7±2 µm) flowing through glass capillary (5 µm inner diameter). The image also shows a particle outside the capillary (scale bar, 5 µm) (*c*) Oxygen carrying capacity of sRBCs demonstrated based on the chemiluminescence reaction of luminol. Cross-linking and exposure to the organic solvent reduces the oxygen carrying capacity, but coating the sRBCs with uncross-linked Hb increased the oxygen-binding capacity to levels comparable to mouse blood (S-RBC, $t$ =0). Ninety percent of oxygen carrying capacity was retained after 1 week (sRBC, $t$ =1 wk). BSA-coated particles were included as negative control (*, $P$ <0.01, $n$ =3). (*d*) Controlled release of radio labeled heparin from sRBCs over a period of 10 days ($n$ = 5). (e) TEM micrograph showing encapsulation of 30 nm iron oxide nanoparticles in RBC-shaped PLGA templates (scale bar 1µm).

**Table 3.1.** Electrohydrodynamic processing and solution parameters yielding particles of different shapes

| | Concentration [a] | Flow Rate (ml/h) | Triethylamine (%) [b] |
|---|---|---|---|
| Discs | 1.3 | 0.15 | - |
| Rods | 3.4 | 0.4 | - |
| Spheres | 4.3 | 0.17 | 3.6 |

[a] concentration in g per 100 g of solvent [b] concentration in vol% of solvent

## 3.7 References


[1] S. Mitragotri, J. Lahann, *Nat. Mater.* **2009**, *8*, 15.
[2] J. A. Champion, Y. K. Katare, S. Mitragotri, *Proc. Natl. Acad. Sci. USA* **2007**, *104*, 1901.
[3] J. P. Rolland, B. W. Maynor, L. E. Euliss, A. E. Exner, G. M. Denison, J. M. DeSimone, *J. Am. Chem. Soc.* **2005**, *127*, 10096.
[4] D. Dendukuri, D. C. Pregibon, J. Collins, T. A. Hatton, P. S. Doyle, *Nat. Mater.* **2006**, *5*, 365.
[5] K. P. Lok, C. K. Ober, *Can. J. Chem.* **1985**, *63*, 209.
[6] S. Xu, Z. Nie, M. Seo, P. Lewis, E. Kumacheva, H. A. Stone, P. Garstecki, D. B. Weibel, I. Gitlin, G. M. Whitesides, *Angew. Chem. Int. Ed.* **2005** *44*, 724
[7] K. H. Roh, D. C. Martin, J. Lahann, *Nat. Mater.* **2005**, *4*, 759.
[8] S. C. Glotzer, M. J. Solomon, *Nat. Mater.* **2007**, *6*, 557.
[9] K. H. Roh, D. C. Martin, J. Lahann, *J. Am. Chem. Soc.* **2006**, *128*, 6796.
[10] K. H. Roh, M. Yoshida, J. Lahann, *Langmuir* **2007**, *23*, 5683.
[11] M. Yoshida, K. H. Roh, J. Lahann, *Biomaterials* **2007**, *28*, 2446.
[12] S. Bhaskar, J. Hitt, S. L. Chang, J. Lahann, *Angew. Chem. Int. Ed.* **2009**, *48*, 4589.
[13] S. Bhaskar, K. H. Roh, X. Jiang, G. L. Baker, J. Lahann, *Macromol. Rapid Commun.* **2008**, *29*, 1655.
[14] C. Berkland, D. W. Pack, K. Kim, *Biomaterials* **2004**, *25*, 5649.
[15] J. Xie, L. K. Lim, Y. Phua, J. Hua, C. H. Wang, *J. Colloid Interface Sci.* **2006**, *302*, 103.
[16] J. Yao, L. K. Lim, J. Xie, J. Huab, C. H. Wang, *J. Aerosol Sci.* **2008**, *39*, 987.
[17] J. Liu, S. Kumar, *Polymer* **2005**, *46*, 3211.
[18] Y. Hong, Y. Lib, Y. Yin, D. Lia, G. Zou, *J. Aerosol Sci.* **2008**, *39*, 525.
[19] M. D. Abramoff, P. J. Magelhaes, S. J. Ram, *Biophot. Int.* **2004**, *11*, 36.
[20] S. Koombhongse, W. Liu, D. H. Reneker, *J. Polym. Sc. Part B: Polym. Phys.* **2001**, *39*, 2598.
[21] R. P. A. Hartman, D. J. Brunner, D. M. A. Camelot, J. C. M. Marijnissen, B. Scarlett, *J. Aerosol Sci.* **2000**, *31*, 65.
[22] D. S. Kohane, *Biotechnol. Bioeng.* **2007**, *96*, 203.
[23] S. R. Little, D. M. Lynn, Q. Ge, D. G. Anderson, S. V. Puram, J. Chen, H. N. Eisen, R. Langer, *Proc. Natl. Acad. Sci. U S A* **2004**, *101*, 9534.
[24] S. Jhunjhunwala, G. Raimondi, A. W. Thomson, S. R. Little, *J. Cont. Rel.* **2009**, *133*, 191.
[25] R. P. A. Hartman, D. J. Brunner, D. M. A. Camelot, J. C. M. Marijnissen, B. Scarlett, *J. Aerosol Sci.* **2000**, *31*, 65.
[26] M. Diez-Silva, M. Dao, J. Han, C. T. Lim, S. Suresh, *MRS Bull.* **2010**, *35*, 382.
[27] N. Doshi, A. Zahr, S. Bhaskar, J. Lahann, S. Mitragotri, *Proc. Natl. Acad. Sci. U S A* **2009**, *106*, 21495.
[28] Y. Fung, "*Biomechanics: Mechanical Properties of Living Tissues*", Springer, New York, 1993.
[29] A. Gutowska, Y. Bae, J. Feijen, S. J. Kim, *J. Cont. Rel.* **1992**, *22*, 95.

[30] D. Pouliquen, J. Le Jeune, R. Perdrisot, E. A., P. Jallet, *Magn Reson. Imaging* **1991**, *9*, 275.
[31] T. Neuberger, B. Schopf, H. Hofmann, M. Hofmann, B. von Rechenberg, *J Magn Magn Mater* **2005**, *293*, 483.
[32] P. A. Oldenborg, A. Zheleznyak, Y. F. Fang, C. F. Lagenaur, H. D. Gresham, F. P. Lindberg, *Science* **2000**, *288*, 2051.

# CHAPTER 4

# MULTICOMPARTMENTAL MICROFIBER SCAFFOLDS

This chapter has been adapted from the following published articles (with minor modifications):

1. Bhaskar, S., Lahann, J., 'Microstructured materials based on multicompartmental fibers', J. Am. Chem. Soc. **2009**, 131, 19, 6550-6551

2. Mandal, S., Bhaskar, S., Lahann, J., 'Micropatterned scaffolds for spatially controlled cell adhesion', Macromolecular Rapid Communications **2009**, 30, 19, 1638-1644

## 4.1 Introduction

The nano- and microstructure of the cellular microenvironment is a decisive factor related to key biological phenomena, such as cell morphology, adhesion, motility, or apoptosis. [1], [2], [3] This relationship has been best established for two-dimensional substrates, where a prosperity of surface structures has been realized using a wide range of different micro- and nanopatterning methods. [4, 5] Although studies based on two-dimensional

substrates provided a valuable, first insight into some of the governing parameters of cell/substrate interactions, they are doomed to fail as viable designs for cell culture scaffolds, because they do not account for cells' need for a three-dimensional microenvironment.[6]Towards this end, electrospinning of natural and synthetic functional polymers has been extensively used to produce micro- and nanofibers, which can provide a three-dimensional support structure[7-17] where the local geometry might be as important as the materials the fibers are made of. [18] Though the mechanical properties of these scaffold materials can be controlled, providing biological signals for guidance of cell growth that will determine the arrangement of cells and the ultimate shape is still a challenge. Versatile micropatterning methods, which can provide exceptional controlled spatial alignment and periodicity, are still exclusive features of flat substrates. In spite of undisputable success with fiber-based scaffolds,[19] sophisticated methods for micropatterning of three dimensional fiber scaffolds are essentially nonexistent. [20-22]

In this chapter, we demonstrate the microstructuring of scaffold materials by creating aligned multicompartmental microfibers via electrohydrodynamic co-spinning of two or more PLGA solutions, which yields well-defined microfibers with multiple, chemically distinct compartments. To demonstrate the versatility of this approach, multicompartmental microfibers with between two and seven individual compartments are shown, where individual compartments have distinct chemical compositions or are selectively surface-modified. Moreover, orientation, size, and arrangement of

the fiber compartments have been controlled in a highly predictable fashion. When multicompartmental fiber scaffolds are modified via spatially controlled peptide immobilization, a unique type of scaffold is obtained, which exhibits highly selective cell guidance at spatial resolutions that so far have been exclusively reserved for flat substrates.

## 4.2 Methods

### 4.2.1 Materials

PLGA 85:15 ($M_w$ 50-75,000 g/mol), poly[(m-phenylenevinylene)-alt-(2,5-dibutoxy-p-phenylenevinylene)] (MEHPPV), PTDPV, FITC, chloroform, DMF, copper sulfate pentahydrate ($CuSO_4.5H_2O$), sodium ascorbate, PBS and Tween-20 were purchased from Sigma-Aldrich, USA. Polythiophene dyes, ADS 406PT and ADS 306PT were purchased from American Dye Source, Canada. $N_3$-$CH_2$CONH-CSRARKQAASIKVAVSADR, $M_w$ = 2117 g/mol (peptide-azide) was purchased from TianMa pharmaceuticals, China.

### 4.2.2 Electrohydrodynamic co-spinning of PLGA microfibers

The basic experimental setup and jetting solution details for fabrication of fibers is described in chapter 2[23]. Fibers were deposited onto a grounded, aluminum foil covered spinning wheel (Synthecon, Inc., USA, modified to experimental requirements) rotating at 20 rpm, placed at a distance of ~5 cm from the capillary tip. The experiments were carried out at room temperature inside a fume hood with an average face velocity of 0.1 m/s. Three, four and

seven compartmental fibers were prepared by employing a corresponding number of capillaries in the desired spatial configuration.

### 4.2.2 Fiber characterization

For SEM, the microfiber scaffolds were spun on top of the aluminium substrate, sputter-coated with gold and their surface morphology was examined by a Scanning Electron Microscope (Philips XL30 ESEM, high vacuum mode). CLSM micrographs were obtained with a FluoView 500 confocal laser scanning microscope (Olympus, Japan). MEHPPV (and ADS406PT), PTDPV, and ADS306PT were excited by 405 nm UV, 488 nm Argon, and 533 nm Helium-Neon green lasers respectively. Optical filters of emission wavelength 430-460 nm, 505-525 nm, and 560-600 nm were used to visualize the fluorescence of MEHPPV, PTDPV, and ADS306PT respectively. For cross-sectional analysis, microfiber scaffolds were sectioned perpendicular to fiber length using a cryostat microtome (HM550 OMC, Microme, USA) maintained at -18$^{o}$C. The sections were collected on a charged glass slide (Fisher Scientific, USA) and imaged via CLSM. For Z-stack analysis, a section depth of 1 µm was assigned.

### 4.2.3 Selective surface modification using copper-catalyzed Huisgen heterocycloaddition reaction

A set of 5-6 single fibers (length ~ 2 cm) fibers were fixed on the aluminum substrate using tape, and incubated with 150 µL of a 0.47 mM peptide-azide solution in DI water, 50 µL of 0.01 M aqueous $CuSO_4.5H_2O$ solution, followed by 50 µL of 1M aqueous sodium ascorbate solution. The reaction was carried

out in 2 ml of DI water containing 0.01% v/v Tween-20 (Sigma, USA) for 10 h. The unreacted peptide was removed by washing with a 1% v/v Tween-20 in PBS. The fibers were resuspended in DI water and incubated with 10 µL of 0.01M FITC (dissolved in DMF) for 5 h. The unreacted FITC was removed by repeated washing with 1% v/v Tween-20 in PBS.

### 4.2.4 Cell incubation assay

NIH 3T3 fibroblasts (ATCC, USA) were cultured in T75 culture flasks in DMEM with 10% FCS at 37°C/ 5% $CO_2$. The cells were passaged at recommended confluence and cells from passages 5-9 were used for all experiments. Glass coverslips (Fisher Scientific) were PEGylated according to previously reported protocols[24]. Coverslips with surface modified microfibers were placed in six- well plates and a cell suspension in media without serum was added to the samples at a concentration of $1x10^5$ cells/$cm^2$ and incubated for 6 hours under culture conditions. At the end of 4 hours the samples were imaged using Phase Contrast Microscopy. For CLSM, a live-cell actin stain BODIPY-TMR-Cytochalasin D (Invitrogen) was added to the media and the samples were imaged under live-cell imaging conditions.

## 4.3 Results and Discussion

In principle, electrohydrodynamic co-jetting involves laminar flow of two (or more) different polymeric solutions through a set of capillaries, which are

arranged in a side-by-side configuration.[25] Under these conditions, a well-defined interface forms within the pendant droplet. Upon application of a certain threshold voltage, accumulation of surface charges results in the formation of a Taylor cone, yielding a polymer jet that retains the multiphasic geometry of the initial droplet through jet elongation, solvent evaporation, and polymer solidification. Multicompartmental fibers are deposited onto a counter-electrode, where individual compartments contain a palette of additives, such as dyes, biomolecules or functional polymers, depending on the composition selected for the initial jetting solutions. For potential use as scaffold materials, biodegradable PLGA polymers were selected as base materials of the fibers. PLGA was the dissolved in a mixture of chloroform and DMF, and formulated according to the specifications of a given experiment. Furthermore, a macromolecular dye with specific spectral emission signature was added to each jetting solution for cross sectional imaging via CLSM. A schematic for the experimental set-up used for the fabrication of bicompartmental microfibers is shown in Figure 4.1a. Here, one solution was loaded with polythiophene dye ADS 306PT (red fluorescence) and the other with ADS406PT (blue fluorescence). Figures 4.1b and 4.1c show the outcome of a typical electrohydrodynamic co-jetting experiment, which consists of a scaffold of individual microfibers comprising of distinct red and blue compartments and exhibiting narrow size distributions.

Spatial and temporal perturbations occurring during electrospinning; otherwise known as bending and kink instabilities, have been well

documented and analyzed. [26, 27] These arise principally from repulsive forces existing between highly charged polymer jets. A stable, continuous fiber can be fabricated via a lower charge to volume ratio in the stretching jet, which, at a given viscosity reduces whipping motion and kink instabilities. This is achievable by employing organic solutions of lower conductivities. [28]The commencement of entanglements in the polymer solution that stabilize the jet and inhibit breakup can be facilitated by increasing the polymer viscosity, which in turn is accomplished by increasing the solution concentration.[29] Furthermore, high volatility of chloroform results in a dynamic increase in viscosity during the spinning process, which further enhances jet stability. This effect is amplified by employing extremely low stream flow rates, of the order of 0.02-0.03 ml/h. Together, reduction in surface charge accumulation, coupled with inertial effects exerted by high apparent viscosities during spinning result in relatively low draw ratios, which in turn reduce the terminal ejection velocity at the leading edge of the jet. Consequently, the migration path of the jet is more “linear” and ordered, compared to the rapid whipping motion that is characteristic of extremely high draw ratios.[26] The relatively lower ejection velocity also provides a platform for the establishment of well aligned scaffolds. Taken together, all these factors result in an extremely stable, continuous electrohydrodynamic jetting process which can be sustained upto several hours, yielding multicompartmental fibers with fine interfaces, and well-controlled, narrowly distributed diameters.

When the electrohydrodynamic co-jetting is extended for several hours, denser fiber scaffolds can be prepared, which show remarkable orientation of the fibers (Figure 4.1b, c). These extended scaffolds with precisely aligned fibers can be prepared in a variety of sizes ranging from tens of square micrometers to several square centimeters (Figure 4.2). Interestingly, the herein described procedure for creating aligned fibers not only provides control over the actual fiber alignment, but can also yield scaffolds where the fiber compartments show an extraordinary parallelism (Figure 4.2). The ability to control the relative alignment of fiber compartment is an important feature, especially when designing scaffold materials that exhibit controlled cell guidance.

With the ability to create highly aligned scaffolds of two polymer solutions demonstrated, we turned our interest to the question, whether or not electrohydrodynamic co-spinning lends itself to fabrication of higher-order fiber scaffolds consisting of more than two independent compartments in each fiber. For this purpose, the initial binary setup was replaced by a three-nozzle configuration. Figure 4.3 shows CLSM images of a scaffold of fibers, which are comprised of three individual compartments. For simplicity, each inlet stream was comprised of the same base polymer, PLGA 8515, dissolved in 95:5 chloroform:DMF by volume, and was simply blended with appropriate polymer additives as needed for subsequent imaging steps. Figures 4.3a-c and Figures 4.4 a-d show longitudinal and cross sectional CLSM micrographs of individual fiber compartments respectively. These data reveal that dyes

initially loaded in the different jetting solutions are isolated to the corresponding compartments only. In addition, extremely sharp boundaries are observed at the interfaces between individual compartments. In spite of the added complexity that is associated with the transition from two to three outlet streams, the new fibers show the same, high-precision alignment of fibers as well as well oriented individual compartments, previously observed for bicompartmental fibers.

Once microstructured fibers with more than two compartments are fabricated, the arrangement of the individual compartments becomes another design parameter. Encouraged by the stable jet and well defined interface observed during bicompartmental co-spinning, we hypothesized that changing the macroscopic coordinates of the three- needle assembly would lead to different internal fiber architectures, which is critical for providing a vast design platform for 3D cell culture. For a fiber with three equally sized compartments (signified by red, green, and blue dyes, respectively) in a three dimensional space, there are in theory 4 optically distinguishable permutations of the internal fiber architecture, *i.e.,* three parallel stripes of red, blue, green [sRBG], blue, red, green [sBRG], and blue, green, red [sBGR] compartments, as well as one trigonal arrangement [pRGB] which we will refer to as “pie-shaped” fibers. To demonstrate the versatility of the electrohydrodynamic co-spinning approach, we set forth a series of experiments to realize all theoretically possible arrangements. Recognizing that the relative design of the outlet streams into the jetting droplet will play a

critical role in the architecture of the resulting fiber, we created a set of nozzles for electrohydrodynamic co-spinning, where the sequence of the incoming jetting solutions as well as their relative arrangement was controlled. Great care was taken that the electrohydrodynamic co-jetting conditions were otherwise unaltered. Figures 4.4a-c show cross sectional images of tricompartmental PLGA fibers, where the outlet streams of the spinneret were placed in a sequence. The inserts of these figures indicate the arrangement of the outlet streams. If the jetting solution containing the green dye was placed in the center, a microfiber scaffold with a [sBGR]-arrangement was prepared (Figures 4.3a, 4.4a). Placing the red or blue jetting solutions into the center space resulted in [sBRG]- or [sRBG]-microfiber scaffolds (Figures 4.3b-c and 4.4b-c). In contrast, a triangular arrangement of the outlet flows resulted in very distinctive [pRGB]-type fiber architecture (Figure 4.4d). Longitudinal Z stack analysis of this fiber further confirmed the presence of a pie shaped internal microstructure (Figure 4.5). We conclude based on these experiments that our electrohydrodynamic co-jetting technology is well-suited to not only control the exact topology of the deposited fiber scaffolds, but also to direct fiber spacing and compartment architecture and presentation with pristine precision.

Next, we elucidated the feasibility of using the electrohydrodynamic co-spinning process to create scaffolds with a higher number of compartments, where 4 or 7 outlet streams were used simultaneously. When these were arranged in a sequence of alternating jetting solutions, scaffolds were

prepared, which consisted of striped microfibers with 4 distinguishable compartments (Figure 4.6a). The precision of the compartments and their excellent alignment was comparable to the outcomes previously discussed for bi- and tricompartmental fibers. If, however, a square arrangement of outlet flows was used, the different compartments were found to arrange as alternating compartments (Figure 4.6b-c). Similarly, more complicated fibers consisting of seven compartments were prepared (Figure 4.7a), which possessed a striking resemblance to a flower. An exciting variation of this novel co-jetting technology is that the relative size of compartments can also be controlled with exceptional precision. Figures 4.6d and 4.7b show fiber meshes consisting of two different compartments, where one compartment was respectively three- or six-folds larger than the other compartment.

To be able to selectively address the surface of one compartment, we added PLPG [30] to one of the jetting solutions while forming a bicompartmental fiber. To verify the spatial confinement of the PLPG to one single compartment, fibers were reacted with a laminin-derived peptide that included a functional sequence of IKVAV, using copper-catalyzed Huisgen heterocycloaddition.[31] Under these conditions, triazole bonds were formed between the acetylene groups present in one of the compartments and an azide-modified variant of the peptide, as outlined in the reaction schemes in Figure 4.8a. Next, immobilized peptides were labeled by reaction of FITC with primary amino groups of the peptide and analyzed by CLSM. Fluorescence arising from conjugation of FITC was limited to the red compartment as

shown in Figure 4.8a. However, when a microfiber scaffold was prepared, where PLPG was added to both compartments, the peptide reacted everywhere as evidenced by the uniform distribution of the fluorescence arising from FITC conjugation (Figure 4.8b). Figure 4.8c shows fibers with no PLPG added to the jetting solutions, but was subjected to the copper catalyzed Huisgen heterocycloaddition in presence of the peptide. The negligible fluorescence signal indicates minimal non-specific adsorption of the peptide, thereby confirming that the fluorescence observed in Figures 4.8a and b was a result of covalent peptide immobilization onto the microfibers. This approach established the chemical distinction of the individual compartments of the microfibers and the ability to immobilize peptides with controlled spatial resolution on these microfibers.

With selectively modified microfibers at hand, the biological function of microstructured fiber scaffolds could now be elucidated in cell culture experiments (Figure 4.9). For this purpose, low-density microfiber scaffolds were deposited onto glass slides and selectively modified with the laminin peptide. [32] Bicompartmental microfiber scaffolds were modified by immobilizing the laminin peptide in one or two compartments (Figure 4.9a). In addition, bicompartmental microfibers without PLPG in either one of the compartments, but treated with the laminin peptide under copper-catalyzed Huisgen heterocycloaddition chemistry conditions and bicompartmental microfibers containing PLPG in both compartments, but without peptide modification were used as negative controls. The four sets of samples were incubated with NIH

3T3 fibroblasts in serum-free media for 6 hours followed by live-cell staining for actin. The microfibers were imaged using phase contrast microscopy and CLSM to observe relevant cell functions, such as cell spreading and cell orientation relative to the microfibers. In Figure 4.9, the CLSM images are shown along with insets representing the corresponding phase contrast images. Taken together, the images show cell adhesion only on microfibers that are modified with laminin peptide (Figures 4.9b and c). In the sample group, where only the red compartments have been modified with the peptide, cells adhere selectively to the red compartment only (Figure 4.9b). This is unambiguously confirmed by the phase contrast images. Not surprisingly, bicompartmental microfibers, where both compartments have been surface-modified with the laminin peptide, show rather uniform cell adhesion throughout the fiber scaffold (Figure 4.9c). Moreover, the CLSM images reveal that extensive cell spreading occurs only on fiber compartments that have been modified with the cell adhesion peptide, i.e., the red compartments for selectively modified microfibers (Figure 4.9b) and the red and blue compartments for uniformly modified fibers (Figure 4.9c). The cell adhesion and spreading on the microfibers in suggested that the fiber surface exhibited surface peptide ligands at a concentration sufficiently high to be recognized by the fibroblasts. In contrast, negligible cell adhesion is observed on surfaces that are void of the laminin peptide (Figures 4.9d and e).

Cell adhesion was quantified for the four groups corresponding to Figures 4.9b to 4.9e by counting the number of cells per length of fiber on the

basis of phase contrast images. Data were plotted as an average of 5 experiments (Figure 4.9f). The quantitative analysis indicates that the number of attached cells unambiguously depends on the peptide-modified surface area of the microfiber scaffolds. The average number of cells that attach to a bicompartmental microfiber with selective surface modification was 64% compared to a bicompartmental microfiber where both compartments were modified with the laminin peptide. Microfibers that were placed in close proximity of modified compartments of other fibers showed a higher number of non-specifically attached cells than individual fibers placed in isolation, possibly due to multiple interactions between the cells. Fibers without PLPG in either compartment, but subjected to copper-catalyzed Huisgen heterocycloaddition chemistry with the peptide, show negligible cell adhesion on the fiber surface (Figure 4.9f). Similarly, microfibers with PLPG in both compartments, but without peptide modification, do not support cell adhesion. These control data confirm that cell adhesion was indeed caused by specific interactions between the cell receptors and the laminin peptide.

## 4.4 Conclusions

The work demonstrated in this chapter points towards a new pathway of overcoming key challenges in the field of tissue engineering, namely the spatial control over cell adhesive properties of three-dimensional scaffolds. In terms of scaffold design, a series of new design parameters are introduced that have the potential to play a vital role in the development of the next generation of 3D

scaffolds, namely (i) internal fiber architecture, (ii) spatial configuration of the individual fiber compartments, (iii) long-range alignment of individual compartments within a scaffold and (iv) the precise control of the relative size of individual compartments. The ability to precisely control the internal architecture of multicompartmental fiber scaffolds gives rise to a number of secondary control parameters, such as controlled chemical composition, optical anisotropy, or spatially controlled surface modification. Here, we successfully employed the latter aspect of multicompartmental microfiber scaffolds for guided cell adhesion on bicompartmental microfibers. An interesting future application of this directional control over cell adhesion would be to create a designer scaffold with self-assembling cellular microenvironments. This scaffold could in turn be used for study of cell-signalling via co-culture as well as targeted drug delivery through polymer degradation. The major challenge here would be the parallel application of various orthogonal chemistries for ligand immobilization and minimizing cross-talk. Since the dependence of cell adhesion on fiber diameter is well-established the next challenge would involve combining the control over internal architecture with size. This would lead to an increase in design space resulting in tailor-made scaffolds. However, this would also entail a better understanding of the exact physical phenomena underlying fiber formation in the flow regimes employed herein. In conclusion, the ability to simultaneously control functionality within each microfiber makes this technology and constructs made out of these microfibers, a valuable addition to regenerative medicine.

## 4.5 Figures and tables

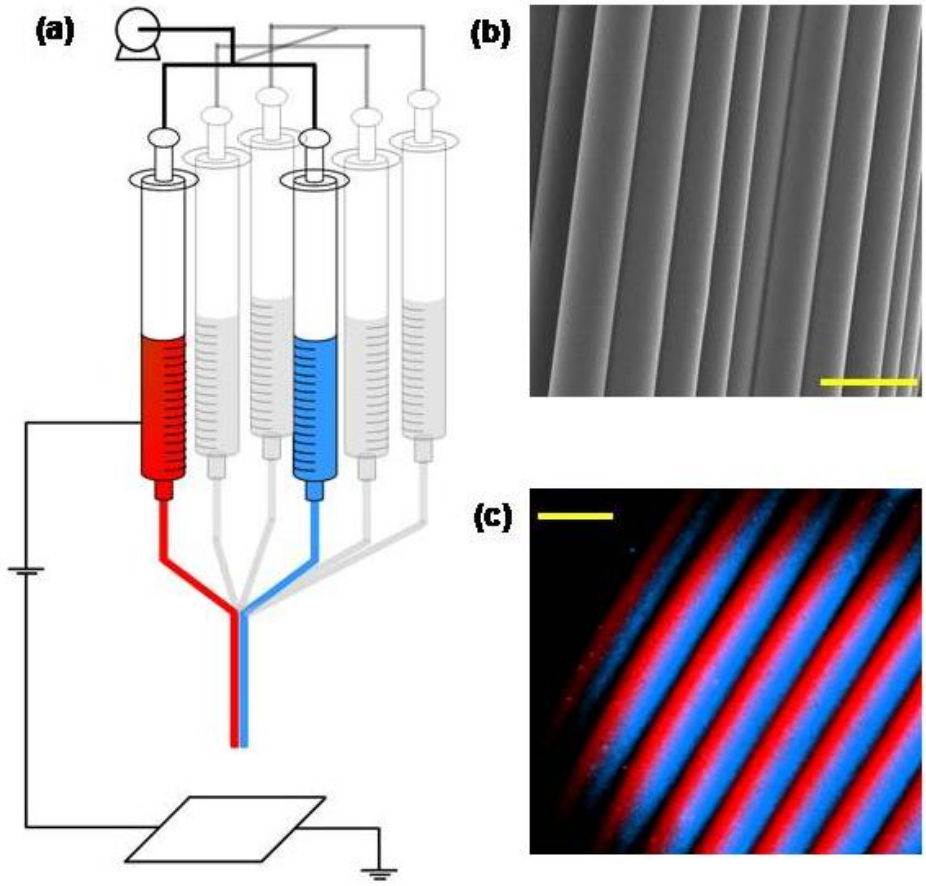


**Figure 4.1** (a) Schematic representation of the process for preparation of bicompartmental PLGA microfibers using a dual capillary assembly (red and blue). This approach can be extended to fabrication of multicompartmental microfibers by incorporating additional outlet streams (gray). (b) SEM image of aligned bicompartmental microfiber scaffold. (c) CLSM image of bicompartmental microfiber scaffold indicating a distinct bicompartmental geometry and excellent alignment of fiber compartments. Scale bars represent 20 µm.

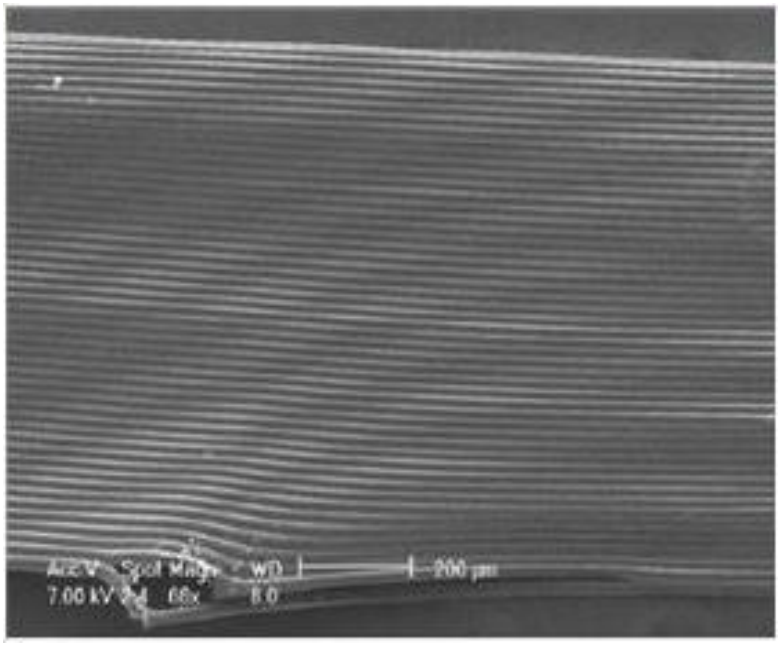


**Figure 4.2** SEM image of a highly aligned fiber sheet, resulting from spinning onto a wheel assembly rotated at 16-18 rpm. The length of the sheet spans 3 cm, which equals the circumference of the wheel. The scale bar represents 0.2 mm.

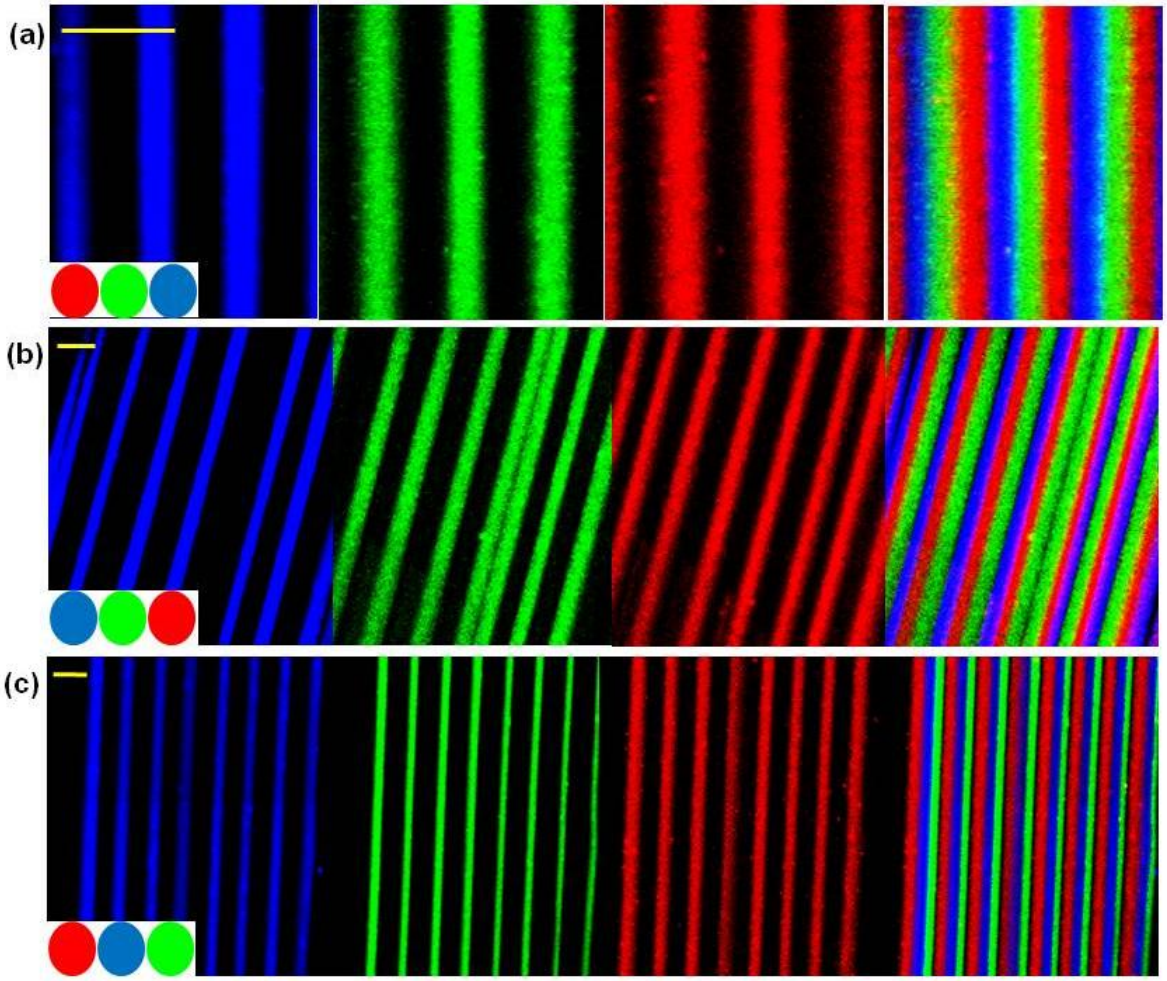


**Figure 4.3** Longitudinal CLSM micrographs of tricompartmental microfiber scaffolds prepared by side-by-side co-jetting of three PLGA solutions. Inset indicates number, spatial configuration, and fluorescence labeling of streams used during electrohydrodynamic co-jetting. Individual blue (B), green (G), and red (R) micrographs representing fluorescence from MEHPPV, PTDPV and ADS306PT dyes are shown independently followed by their overlay. Different sequences of outlet streams used during electrohydrodynamic co-jetting give rise to a corresponding change in the relative orientation of compartments in the fibers. (a) [sRGB] (b) [sBRG], and (c) [sRBG], where “s” stands for “sequential” and the letters denote the fluorescent labeling of solutions in the order in which they were positioned during co-spinning. All scale bars are 20 µm.

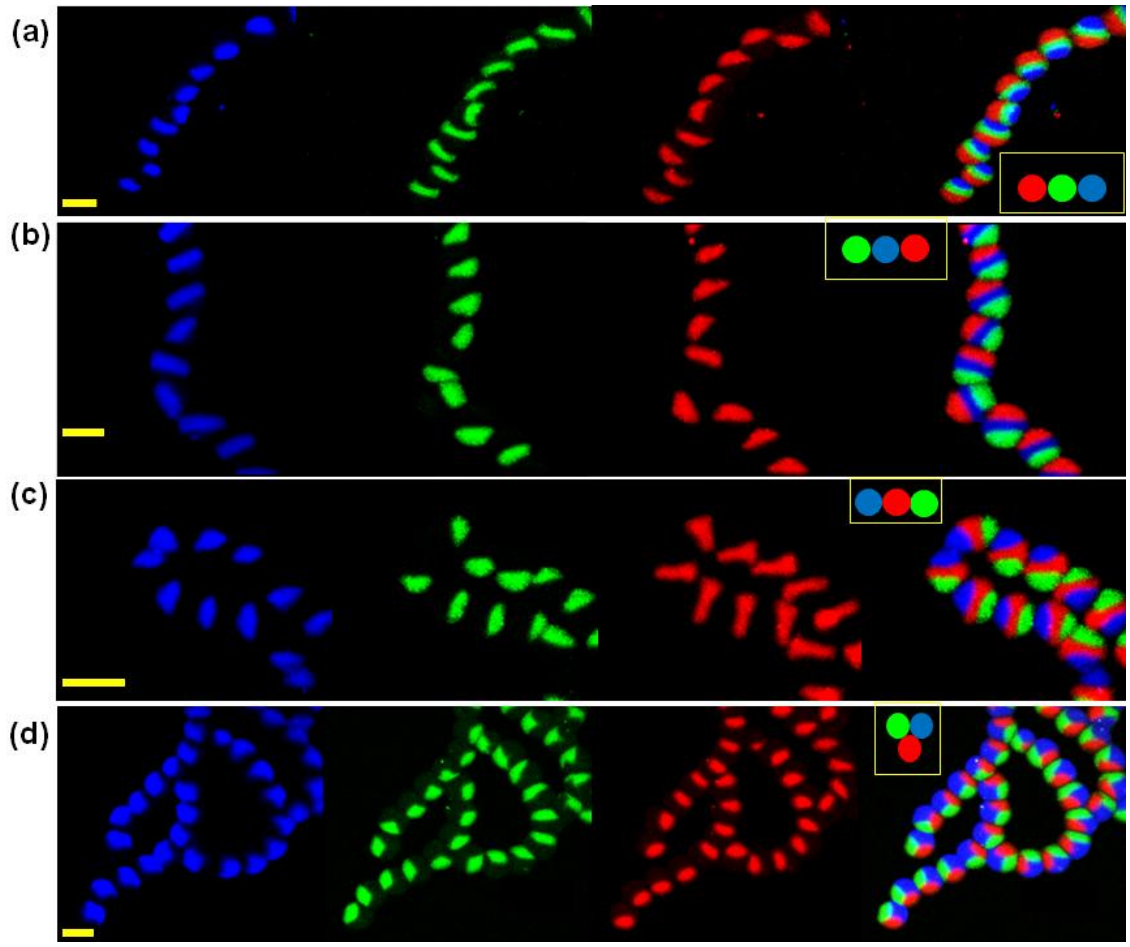


**Figure 4.4** Cross sectional CLSM images of tricompartmental fibers. Individual blue (B), green (G) and red (R) fluorescence images representing MEHPPV, PTDPV and ADS306PT dyes respectively are shown followed by the overlay. Inset indicates number, spatial configuration, and nature of fluorescence labeling (B, G, or R) of the PLGA solutions that were co-electrospun. (a-c) represent tricompartmental fibers obtained via a side-by-side needle configuration. (a) [sRGB] (b) [sBRG] and (c) [sRBG]. (d) Tricompartmental fibers resulting from a triangular positioning of needles, p[RGB]. 's' denotes 'side-by side', and 'p' denotes 'pie'. All scale bars represent 20 μm.

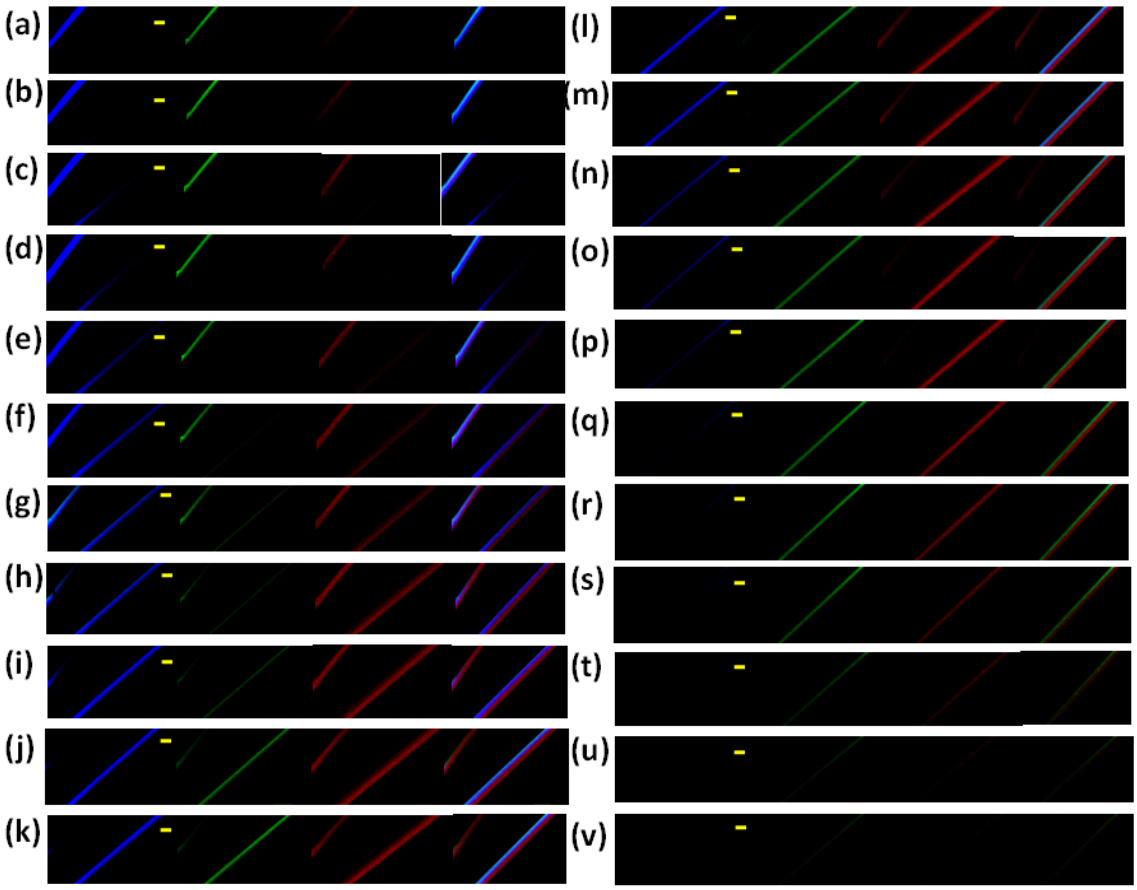


**Figure 4.5** Three-dimensional analysis of a tricompartmental microfiber. The panel of CLSM images showing longitudinal Z sections of a [pRGB] microfiber recorded at 1 μm increments ranging from the top (a) to the bottom (v) of the fiber. Individual blue (B), green (G) and red (R) fluorescence images representing MEHPPV, PTDPV and ADS306PT dyes respectively are shown, followed by the overlay. The initial sections (a-i) are dominated by blue and red fluorescence from the upper portion of the "pie" which consists of only two compartments, blue and red, as seen in the overlay. The green fluorescence is visible faintly, starting at g and appears at peak intensity in k and l which, located at 11μm and 12μm depths respectively, form areas of sharpest focus. At depths of 11 and 12 μm, the overlay appears cyan due to the overlap of the blue compartment and the green compartment which is situated directly below it. Thereafter, blue fluorescence progressively diminishes in intensity and is completely absent after p, because the sections comprise of only two compartments, red and green. Towards the later portion of the z-stack (m-v), fluorescence from red and green compartments alone is visible. All scale bars represent 15 μm.

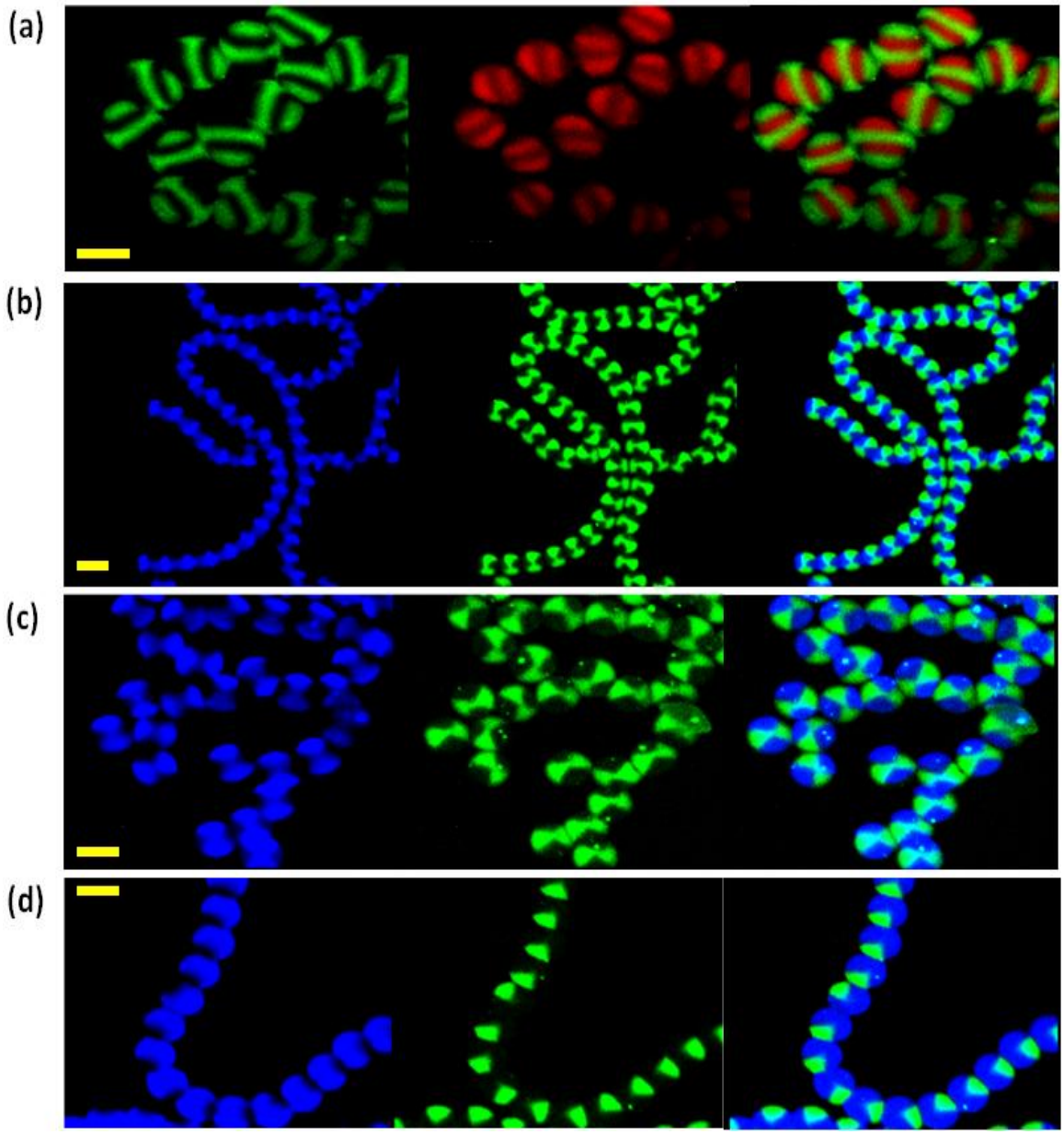


**Figure 4.6** CLSM images of tetracompartmental micro fiber cross sections**.** Blue (B), green (G) and red (R) fluorescence images representing MEHPPV, PTDPV and ADS306PT dyes respectively, are followed by the overlay. (a) Tetracompartmental microfibers showing alternating red and green compartments, via side-by side positioning of needles. (b) Tetracompartmental fibers resulting from a square shaped spatial arrangement of needles with oppositely spaced solutions labeled with the same dye (B and G), (c) Magnified image of b showing the compartments in greater detail. (d) Fibers with one out of four solutions labeled with PTDPV to give a smaller "quarter" compartment (green), and a blue compartment that is three folds larger. All scale bars represent 20 μm.

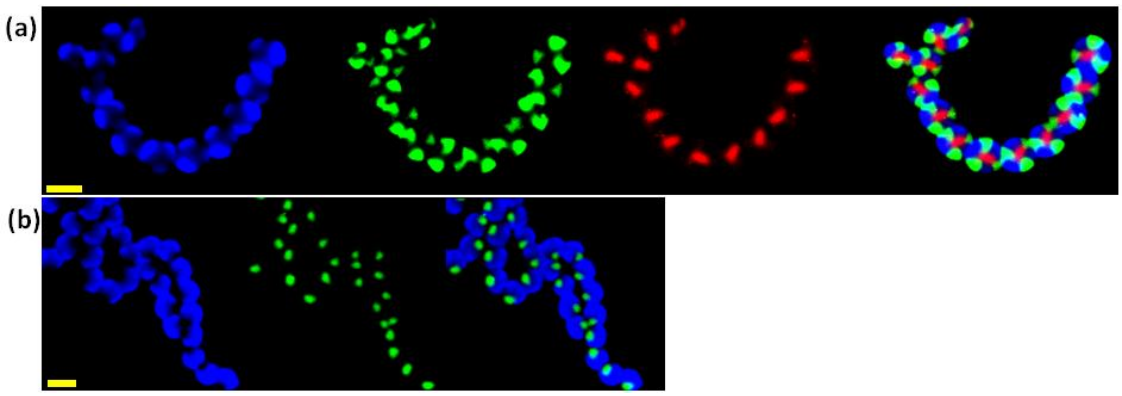


**Figure 4.7** CLSM images of heptacompartmental microfibers. Individual blue (B), green (G) and red (R) fluorescence images represent MEHPPV, PTDPV and ADS306PT dyes respectively are shown, followed by the overlay. (a) Heptacompartmental microfibers resembling a flower.(b) Fiber with one out of seven compartments labeled with PTDPV, and others with MEHPPV, resulting in one (green) compartment six fold smaller than the other blue compartment. All scale bars represent 20 μm.

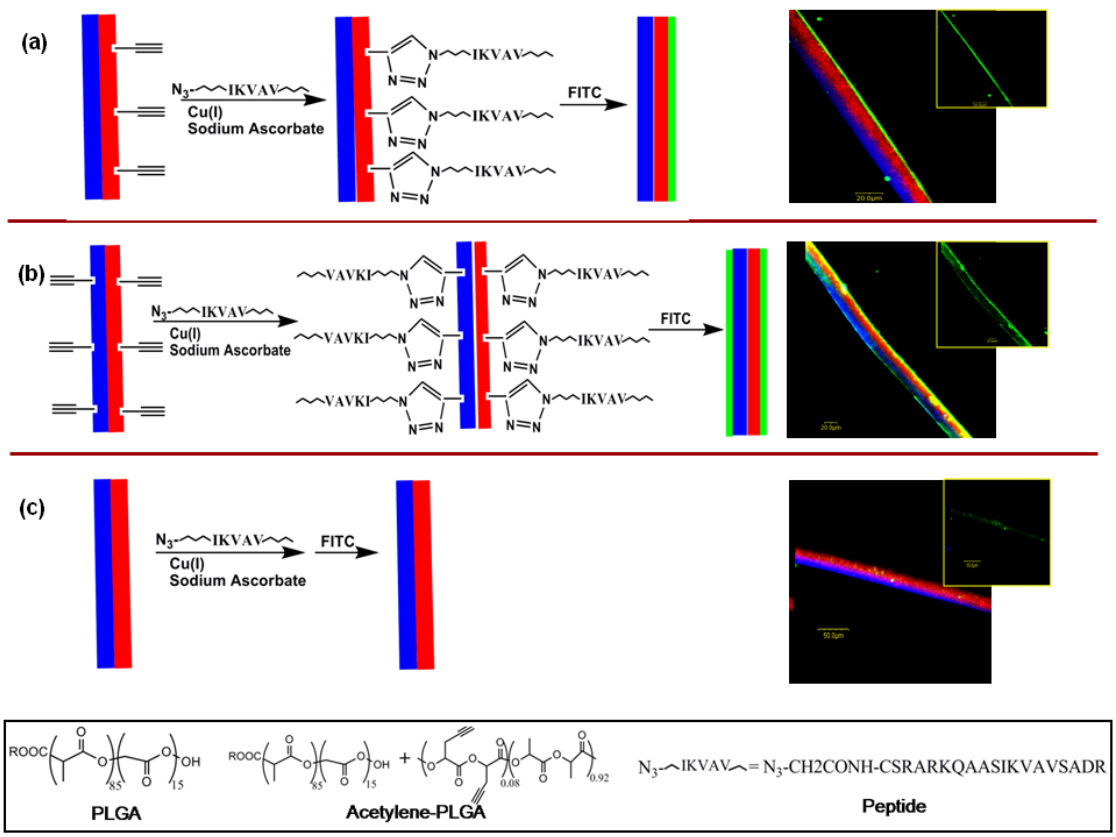


**Figure 4.8** Scheme and corresponding CLSM micrographs of bicompartmental microfiber confirming selective surface modification of with an azide-functionalized cell-binding peptide. Individual CLSM micrographs show blue, green and red fluorescence overlays with inlays representing green fluorescence only. (a) Bicompartmental fiber containing free acetylene groups in one compartment only, which was prepared by blending the PLGA with PLPG (~30 wt% of polymer). The acetylene-containing phase was labeled with ADS306PT (red fluorescence). The fibers were subsequently reacted with a azide- peptide via copper-catalyzed Huisgen 1,3-dipolar cycloaddition. The free amine groups of lysines in the peptide were then reacted with FITC, giving rise to green fluorescence in areas where the reaction occurred. Uniform peripheral green fluorescence due to FITC was seen alongside the red compartment only, indicating selective surface modification. (b) Control fiber containing acetylene groups in both compartments, when subjected to identical conditions resulted in green fluorescence alongside both compartments. (c) Fiber without acetylene groups did not exhibit significant green fluorescence indicating negligible non-specific binding of the peptide. Scale bars in a, b and c are 20 µm, 20µm and 50 µm, respectively.

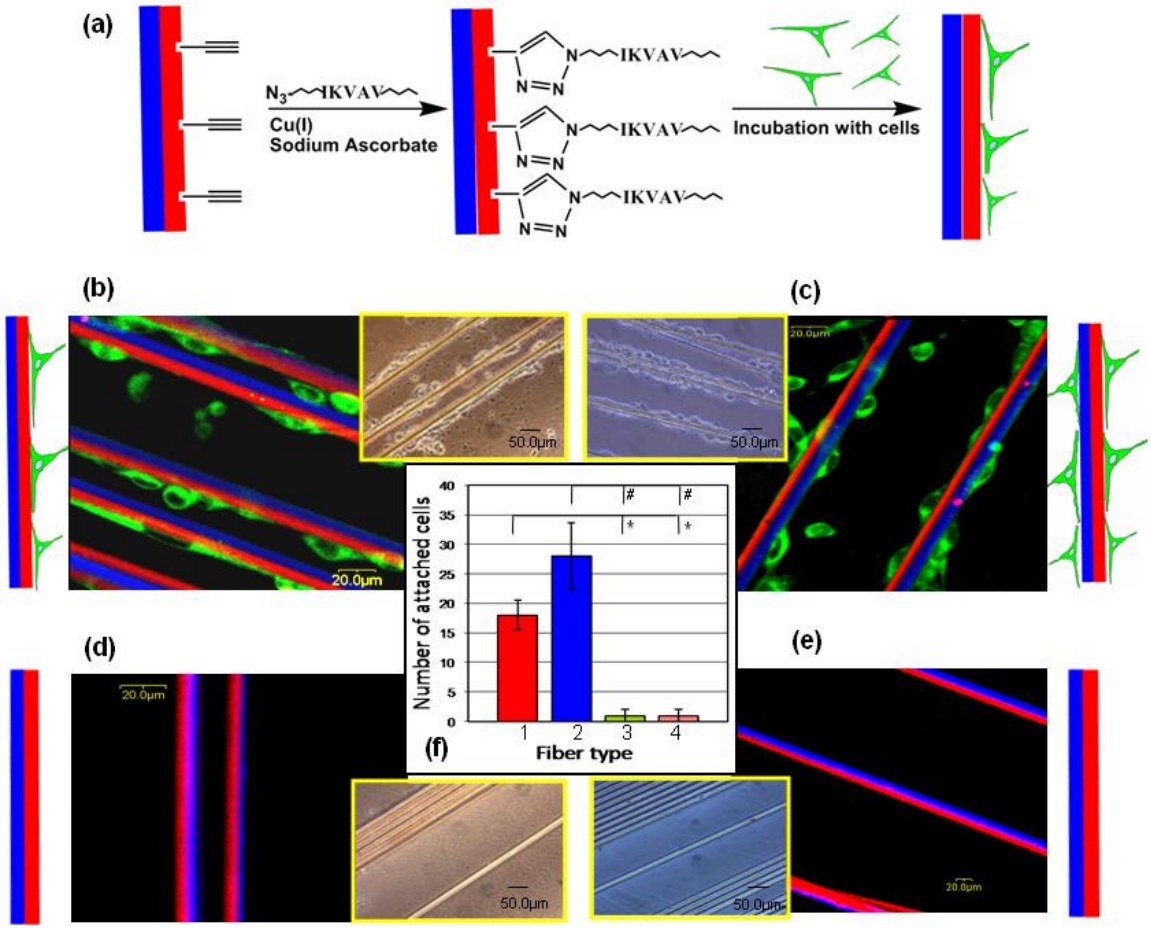


**Figure 4.9** Guided cell adhesion on bicompartmental microfiber scaffold selectively modified with IKVAV peptide. Bicompartmental microfiber scaffolds were modified selectively with a functional azide-peptide and incubated with fibroblasts. (a) Schematic showing selective surface conjugation of the azide-peptide onto red compartments only. The fiber mesh was then used as scaffold for fibroblast adhesion. (b-e) CLSM images as well as phase contrast micrographs (inserts) of bicompartmental microfibers. (b) PLPG was incorporated in the red compartment only followed by selective peptide conjugation resulting in cell adhesion alongside the red compartment. (c) PLPG introduced in red and blue compartments resulting in cell adhesion on both compartments (d) No PLPG introduced in either compartment, but subjected to click chemistry with peptide, resulting in negligible cell adhesion (e) PLPG in both compartments, but not conjugated with peptide resulting in negligible cell adhesion. (f) Plot quantifying cell adhesion for each fiber type with data plotted as an average from 5 experimental sets. Bars 1, 2, 3 and 4 in the plot represent average number of cells (± S.D.) attached to a standard length of fiber type described in b, c, d and e respectively. *$p \leq 0.05$ for data set 1 when compared to set 3 and 4, n=5. $^{\#}p \leq 0.05$ for data set 2 when compared to 3 and 4, n=5.

## 4.6 References


[1] D. M, M. O. Riehle, S. D. S, A. H, A. S. Curtis, *Eur J Cell Biol* **2004**, *83*, 159.
[2] C. S. Chen, M. Mrksich, S. Huang, G. M. Whitesides, D. E. Ingber, *Science* **1997**, *276*, 1425.
[3] D. Lehnert, B. Wehrle-Haller, C. David, U. Weiland, C. Ballestrem, B. A. Imhof, M. Bastmeyer, *J Cell Sci* **2004**, *117*, 41.
[4] W. F. Liu, C. S. Chen, *Adv Drug Deliv Rev* **2007**, *59*, 1319.
[5] L. Cao, D. Mooney, *Adv Drug Deliv Rev* **2007**, *59*, 1340.
[6] R. Murugan, S. Ramakrishna, *Tissue Engineering* **2007**, *13*, 1845.
[7] J. Venugopal, S. Low, A. T. Choon, S. Ramakrishna, *Journal of Biomedical Materials Research Part B-Applied Biomaterials* **2008**, *84B*, 34.
[8] I. K. Kwon, S. Kidoaki, T. Matsuda, *Biomaterials* **2005**, *26*, 3929.
[9] F. Yang, R. Murugan, S. Wang, S. Ramakrishna, *Biomaterials* **2005**, *26*, 2603.
[10] X. L. Jingwei Xie, Younan Xia*, *Macromolecular Rapid Communications* **2008**.
[11] M. Goldberg, R. Langer, X. Q. Jia, *Journal of Biomaterials Science-Polymer Edition* **2007**, *18*, 241.
[12] S. Liao, *Biomedical materials* **2006**, *1*, R45.
[13] C. P. Barnes, S. A. Sell, E. D. Boland, D. G. Simpson, G. L. Bowlin, *Adv. Drug Deliv. Rev.* **2007**, *59*, 1413.
[14] S. Y. Chew, Y. Wen, Y. Dzenis, K. W. Leong, *Current Pharmaceutical Design* **2006**, *12*, 4751.
[15] Q. P. Pham, U. Sharma, A. G. Mikos, *Tissue Engineering* **2006**, *12*, 1197.
[16] S. Liao, B. J. Li, Z. W. Ma, H. Wei, C. Chan, S. Ramakrishna, *Biomedical Materials* **2006**, *1*, R45.
[17] Z. W. Ma, M. Kotaki, R. Inai, S. Ramakrishna, *Tissue Engineering* **2005**, *11*, 101.
[18] J. E. Sanders, S. D. Bale, T. Neumann, *J Biomed Mater Res* **2002**, *62*, 222.
[19] D. W. Hutmacher, *J. Biomater. Sci. -Polym. Ed.* **2001**, *12*, 107.
[20] K. Park, Y. M. Ju, J. S. Son, K. D. Ahn, D. K. Han, *Journal of Biomaterials Science-Polymer Edition* **2007**, *18*, 369.
[21] Q. P. Pham, U. Sharma, A. G. Mikos, *Biomacromolecules* **2006**, *7*, 2796.
[22] F. Tian, H. Hosseinkhani, M. Hosseinkhani, A. Khademhosseini, Y. Yokoyama, G. G. Estrada, H. Kobayashi, *Journal of Biomedical Materials Research Part A* **2008**, *84A*, 291.
[23] K.-H. R. S. Bhaskar, X. Jiang, G. L. Baker J. Lahann, *Macromolecular Rapid Communications* **2008**.
[24] A. Papra, N. Gadegaard, N. B. Larsen, *Langmuir* **2001**, *17*, 1457.
[25] P. Gupta, G. L. Wilkes, *Polymer* **2003**, *44*, 6353.
[26] D. H. Reneker, A. L. Yarin, H. Fong, S. Koombhongse, *J. App. Phys.* **2000**, *87*, 4531.

[27] A. L. Yarin, S. Koombhongse, D. H. Reneker, *Journal of Applied Physics* **2001**, *89*, 3018.
[28] M. Cloupeau, B. Prunet-Foch, *J. Electrostat.* **1989**, *22*, 135.
[29] S. L. Shenoy, W. D. Bates, H. L. Frisch, G. E. Wnek, *Polymer* **2005**, *46*, 3372.
[30] S. Bhaskar, K. H. Roh, X. Jiang, G. L. Baker, J. Lahann, *Macromol. Rapid Commun.* **2008**, *29*, 1655.
[31] Z. P. Demko, K. B. Sharpless, *Angewandte Chemie-International Edition* **2002**, *41*, 2113.
[32] L. Kam, W. Shain, J. N. Turner, R. Bizios, *Biomaterials* **2002**, *23*, 511.

# CHAPTER 5

# MULTICOMPARTMENTAL MICROCYLINDERS

This chapter has been adapted from the following published article (with minor modifications):

Bhaskar, S., Hitt, J., Chang, S. L., Lahann, J., 'Multicompartmental microcylinders', Angew. Chem. Int. Ed. **2009**, 48, 25, 4589-4593.

## 5.1 Introduction

Motivated by their essential importance to major biomedical applications, such as drug delivery or medical imaging,[1] multifunctional colloids with controlled size,[2-6] shape, [6-10] and surface chemistry[10-13] have recently emerged. In some cases, such as phagocytosis of particles by macrophages, the shape of particles appears to be at least as important as its size [14-16]. In some instances, particles with cylindrical shapes appeared to be desirable. [14-16]. Beyond control of size and shape, future multifunctional colloids will require highly engineered internal particle architectures, as manifested by the

presence of multiple sub-structures and sub-compartments. In its simplest form, two compartments can be arranged concentrically in a particle resulting in core/shell architectures, where a shell compartment surrounds a center unit. A large number of multifunctional core shell particles have been synthesized.[17-21] Beyond core/shell particles,[21] a recently developed process based on electrohydrodynamic co-jetting can yield anisotropic bi- and tri-compartmental micro- and nanoparticles with spherical envelopes, where individual compartments are located next to each other.[22-25] While the number, size, and arrangement of individual particle compartments may be controlled in a highly predictable manner, their shape has been limited to spheres only. In this chapter, a simple, reliable, and scalable process, named microshredding that allows fabrication of multicompartmental colloids with defined cylindrical shapes is reported. The process involves the fabrication of multicompartmental microfiber bundles using electrohydrodynamic co-spinning followed by a microsectioning step to convert the microfiber bundles into multifunctional microcylinders with well-defined internal architectures. Microshredding establishes a versatile, low-cost, and potentially high throughput method for fabrication of rod-shaped colloids with controlled sizes, aspect ratios, shapes, and surface chemistries.

## 5.2 Methods

### 5.2.1 Materials, Electrohydrodynamic co-spinning and characterization

The materials (PLGA, fluorophores and solvents), protocol for fabrication of multicompartmental fibers, SEM and CLSM characterization are described in chapter 4. For selective phase modification experiments, a 30:70 w/w mixture of PLPG: PLGA 8515 was used to prepare the jetting solution. For size distribution studies, image analysis on SEM images was performed using “Image J” software.[26] . For z-stack analysis via CLSM, the slice thickness was 1.5 μm.

### 5.2.2 Cryosectioning and ultrasonication

Microfiber bundles (~3 cm in length) were harvested from the collecting substrate and vacuum-dried for 10 h. The bundles were cut into pieces of ~1 cm in length. These were placed parallel to each other in a rectangular polyethylene cryomold (Sakura Finetec, USA). Optimal Cutting Temperature (OCT) gel (Sakura Finetec, USA) was added and the mold was frozen at -70$^{o}$C for 5 min. This resulted in a rectangular block of solidified gel with fiber bundles embedded therein. The block was then detached from the mold and sectioned at a rate of about 70 sections/min using a cryostat microtome (HM550 OMC, Microme, USA) maintained at -20 °C. The sections were harvested in 50 ml centrifuge tubes and brought to room temperature. The OCT was dissolved by washing repeatedly with 2 vol. % Tween-20 in DI water. The sections were resuspended in PBS, containing 2% v/v Tween-20. The fiber bundles were then separated into individual microcylinders through an ultrasonic processor (Cole Palmer, USA) delivering 225 W at 20 kHz frequency. Sonication was pulsed, with an interval of 1.5 min between successive pulses (duration of each pulse was 24 s). The time

for complete dispersion varied between 15-25 min of sonication; mainly depending on number of fibers in the bundles.

### 5.2.3 Selective surface modification

Microcylinders were suspended in PBS containing 0.01% v/v Tween-20 to a final concentration of 65000 cylinders/ml. To this, 600 μL of 1mg/ml aqueous solution of Tetrafluorophenylazide-$(PEO)_3$-biotin (Pierce Pharmaceuticals, USA) was added, followed by 20 μL of 0.1 M (aq) $CuSO_4.5H_2O$ and 1.8 ml of 0.1 M sodium ascorbate (Sigma Aldrich, USA). The reaction mixture was vigorously agitated via magnetic stirring in dark for 9 h at room temperature. The microcylinders were washed repeatedly with PBS containing 2 % v/v Tween-20 through vortexing, centrifugation and resuspension. The cylinders were then suspended in 2 ml of PBS containing 0.1 % v/v Tween-20 and 1 % w/v Serum Bovine Albumin (Sigma Aldrich) and incubated with 4 μL of 1 μg/μl solution of Alexa Fluor-633 conjugated Streptavidin (Invitrogen, USA) for 2.5 h. The microcylinders were washed repeatedly with 2% Tween-20 in PBS and imaged by CLSM.

## 5.3 Results and discussion

Building on recent work that used co-jetting of two or more aqueous polymer solutions to create multicompartmental spheres with diameters in the range of hundreds of nanometers to several microns, we turned our attention to electrohydrodynamic co-jetting of PLGA from organic solvents.[27, 28] In a typical electrohydrodynamic co-jetting experiment, two identical solutions of PLGA were

pumped through a side-by-side capillary outlet system. Upon applying a potential difference between the needles and the collector (8.5-9.5 kV), the droplet was distorted into a liquid cone, while maintaining the interface between the two flowing solutions. In principle, both multicompartmental particles and fibers can be synthesized in this way and the experimental details that lead to fibers versus particles are described in chapters 1, 2 and 3.[28] For electrohydrodynamic co-spinning, the jet that ensued from the tip of the cone resulted in the formation of a single fiber, which deposited on the collecting substrate without break-up. Higher PLGA concentrations (18:100 w/w polymer: solvent) and low flow rates (between 0.02-0.04 ml/h) generally favor the formation of fibers. Incorporation of additional outlet streams enables fabrication of fibers with three or even four compartments,[29] while still maintaining the integrity and stability of the jet. This is important, because subsequent processing into microcylinders becomes only feasible, if multicompartmental fibers can be deposited as extended bundles of well-aligned microfibers. For this reason, a grounded spinning wheel positioned directly below the needles was used as collecting substrate. This is schematically depicted in Figure 5.1a. By rotation of the wheel assembly (16rpm), the fiber can be directed to deposit as an ordered bundle for long periods of time (up to 5h). Since this bundle results from continuous deposition of a single fiber, SEM micrographs of the bundles revealed near-perfect monodispersity with respect to cylinder diameter within a given bundle (Figure 5.1b). The simultaneous use of more than two jetting solutions was found to be a probate mean of extending the process to fabrication of large bundles of tri- and tetraphasic microcylinders.

Similarly, the co-spinning process with three or four outlet streams was extremely stable, could be sustained for several hours and resulted in tri- and tetracompartmental fiber bundles.

Once a reliable process for fabrication of extended bundles of multicompartmental microfibers was established, we elucidated conditions for converting the microfiber bundles into cylindrical colloids. A major focus was placed on creating monodisperse microcylinders with definable aspect ratios in an automated or semi-automated process. After evaluating a range of different methods, we ultimately turned to sectioning as the method of choice for preparing multicompartmental microcylinders, because it has been shown to be a straightforward, cost effective strategy for fabricating a variety of well defined nanostructures of different shapes and sizes.[30] In brief, fiber bundles with an approximate length of 3 cm were harvested, embedded in a mold using optimal cutting temperature gel and cryosectioned. The cylinder lengths can be conveniently controlled by adjusting the slice thickness and speed of the cryotome to create cylindrical particles with well-controlled aspect ratios. After dissolution of the embedment gel in water, the particles were suspended in PBS and subjected to pulsed ultrasonication in order to obtain well-dispersed cylinder populations.

Figure 5.1c shows bicompartmental cylinders made by microshredding. The average diameter of these cylinders is 14 μm and the average length is 5μm resulting in an aspect ratio of 0.36. While SEM images of cylindrical particles generally reveal smooth cylinder surfaces, the edges of cylinders occasionally

exhibited some degree of surface roughness along their longitudinal axis, which arose from disruption of cohesive forces forming the bundle or due to extensive sonication. Nevertheless, subsequent cross-sectional analysis confirmed the circular character of the multicompartmental microcylinders (Figures 5.1c and 5.4b). The quality of cylinders was found to depend on extent of dryness of the fiber during electrospinning, which in turn was found to vary with the different electrospinning process parameters. In addition, embedding the fiber bundles in the gel-matrix was crucial for the alignment of bundles relative to direction of microshredding. An exact positioning of the bundle normal to the shredding direction is essential for obtaining cylinders with perpendicular vertical and horizontal axes.

The overall aspect ratio of the cylinders could be controlled in two ways (1) tuning the electrospinning process parameters, namely flow rate and electric field strength controlled the diameter, and (2) a desired length could be assigned to the microfibers during cryosectioning. Figure 5.2 shows CLSM micrographs of bicompartmental microcylinders of different aspect ratios. The average aspect ratios are 1.3 (Figure 5.2a), 2.6 (Figure 5.2b) and 4.6 (Figure 5.2c), respectively, corresponding to cylinders with average lengths of 20, 39 and 80μm. The different cylinders were obtained by employing different sectioning intervals during cryosectioning. To visualize individual compartments, the microcylinders were characterized via CLSM. Small amounts (<0.1% by wt. of polymer in solution) of conjugated polymers with different spectral emission characteristics were incorporated into each compartment during co-spinning. In Figure 5.2,

corresponding compartments are equally sized and show a well-defined interface, as indicated by thin line of yellow color between the red and green compartments. Among the cylinders prepared and analyzed in this study, 100% of all cylinders were multicompartmental. The microcylinders are quite monodisperse with respect to diameter, the average distribution of the cylinder diameters being within 3 μm, as determined by SEM micrographs (Figure 5.3).

An interesting aspect of microcylinders with more than three compartments is, that the relative orientation of the compartments emerges as a new design feature, i.e., more than one permutation of microcylinders exists as to how three or more equally sized compartments can be arranged. Figures 5.4c-f show two types of tricompartmental microcylinders. Depending on the initial architecture of the microfibers, particles can be created, where the blue center compartment is sandwiched between two outside compartments indicated by red and green color (Figures 3c-d). In contrast, a “pie”-shaped particle architecture may also be obtained. For ‘pi -shaped’ microcylinders, a cylinder imaged with circular cross section oriented parallel to the microscopic lens is shown for clear visualization of distinct compartments (Figures 5.4e). The spatial compartmental orientation is clearly visible in these images. Additionally, tetracompartmental colloids were produced by loading opposing nozzles in a square configuration with the same fluorophores (blue and green). This is manifested in the “bow-tie” shapes observed in both blue and green fluorescence images, which, upon superimposition of confocal images obtained for different wavelengths, result in four perfectly shaped “quarter” compartments with a more pronounced interface

(cyan) towards the center (which is the area pulled by the electric field) (Figures 5.4g-h). Again, the phase distribution was identical for all cylinders of a given population suggesting a 100% yield. It is important to recognize that the distinctive internal architecture of each type of fiber that was produced via co-spinning was well preserved after embedding, sectioning and sonication into cylinders. Thus, the integration of these two processes may represent a robust platform for future scale-up.

We then proceeded to demonstrate spatio-selective surface modification of multicompartmental microcylinders by employing Huisgen 1, 3 - dipolar cycloaddition. [31-33] Towards this end, microcylinders with “big” and “small” compartments, i.e., tetracompartmental microcylinders with green dye in one phase and blue dye in the other three phases, were prepared. A small amount of PLPG was blended into the jetting solution of the smaller compartment, which resulted in the introduction of free acetylene groups in the bulk of the smaller compartment alone, while the cone stability was unaltered during co-spinning. We chose a tetracompartmental cylinder configuration because three fourths of the entire area, which would not be modified, can serve as an internal control. The microcylinders formed from these fibers were reacted with biotin-$(PEO)_3$-azide in presence of copper sulfate pentahydrate and sodium ascorbate. This resulted in covalent surface immobilization of biotin on one fourth of the cylinder surface. The cylinders were then incubated with Alexa Fluor 633 conjugated streptavidin, which binds to biotin with high selectivity. Red peripheral fluorescence due to streptavidin was seen only in one fourth of the lateral surface

of the cylinder (Figure 5.5), indicating successful selective modification. To further substantiate the spatioselectivity, three dimensional z-stack analysis was performed on a representative cylinder. A series of confocal images was recorded in 1.5 μm increments from top to bottom. These twenty individual slices clearly indicated the presence of green dye adjacent to the red fluorescence from streptavidin throughput the depth of the fiber. Next, a digitized perspective view was reconstructed from these slices, which allowed detailed examination in x, y and z directions and from different angles. These snapshots were sequenced to form a movie.[34] In the 3D CLSM micrograph, the green dye, present in one fourth of the surface is rendered almost invisible due to red fluorescence from streptavidin, as is seen from the front and side view. At higher magnifications, a yellow color is seen due to overlay of red and green. These results further consolidate the specificity of surface modification.

## 5.4 Conclusions

In conclusion, we have developed a novel process for fabrication of multifunctional, cylindrical colloids, named microshredding. Moreover, we have demonstrated fabrication of multicompartmental, nearly monodisperse, and biodegradable microcylinders with controllable number, size, and orientation of compartments. In addition, control over aspect ratio is achievable with this technique. Multicompartmental microcylinders with controlled surface patterns

may play an important role in the development of next generation biomaterials with precisely designable physical and chemical properties.[35]

## 5.5 Figures and tables

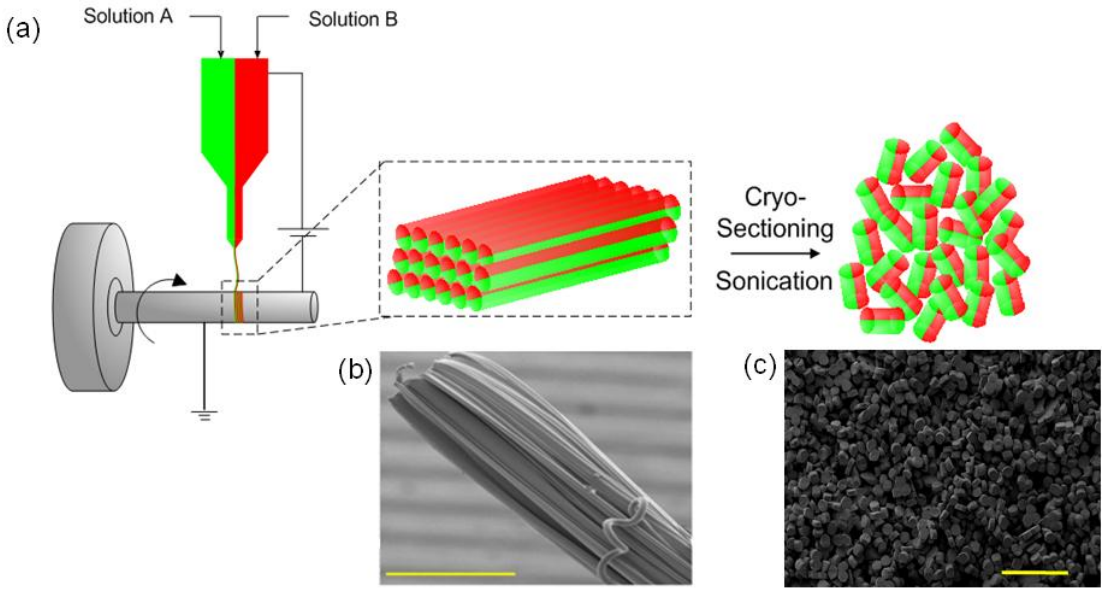


**Figure 5.1** (a) Schematic depicting the microcutting process, comprising of electrohydrodynamic co-spinning followed by cryosectioning. Two (or more) PLGA solutions, each labeled with a specific fluorophore, are pumped through a side-by-side capillary system under controlled laminar flow. Application of a potential difference to the droplet results in liquid cone formation, droplet stretching and ejection of a fiber, which are deposited onto a spinning wheel assembly that acts as a counter-electrode. The resulting fiber bundles are then subjected to cryosectioning, followed by sonication to yield uniform microcylinders. (b) SEM micrograph of bicompartmental fiber bundles obtained via electrohydrodynamic co-spinning (scale bar: 200 μm). (c) SEM micrograph of microcylinders prepared by microcutting (scale bar 100 μm).

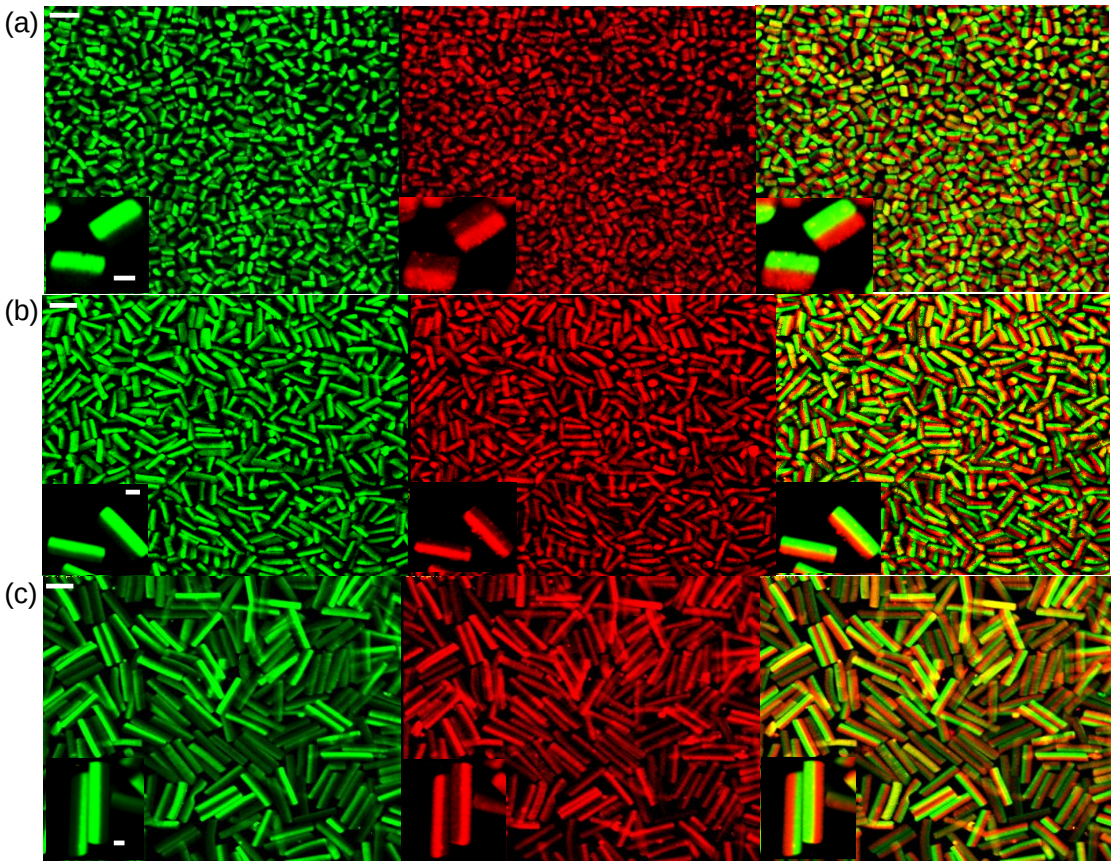


**Figure 5.2** (a)-(c). CLSMs of bicompartmental particles made of PLGA. Green and red fluorescence images (representing PTDPV and ADS306PT) depicting individual compartments are shown, followed by their overlay which shows the entire microcylinder. By varying the sectioning length, cylinders with different lengths and aspect ratios (a.r.) were prepared: (a) length 20 μm, a.r. = 1.3; (b) length 39 μm, a.r. = 2.6; and (c) length 80 μm, a.r. = 4.6. Inlays show high magnification images. Scale bars represent 50 μm for low-magnification images and 10 μm for inlays.

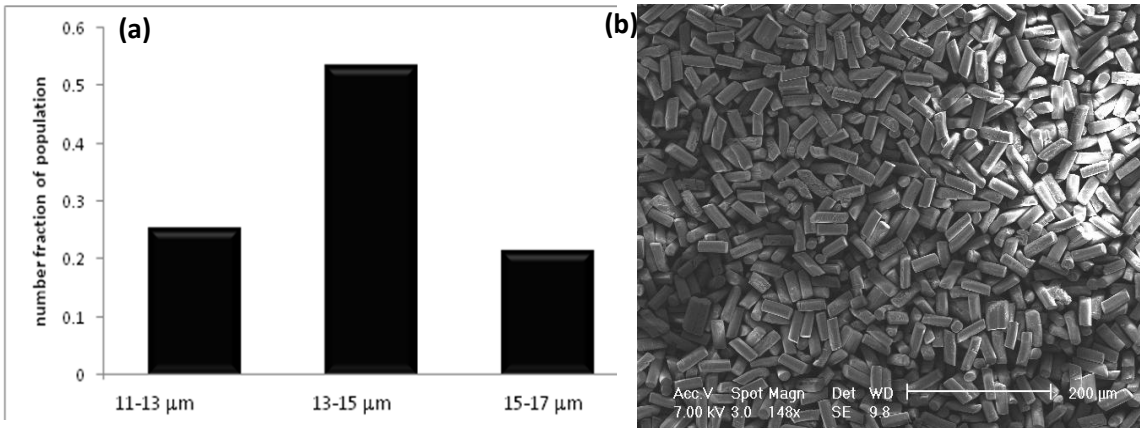


**Figure 5.3** (a) Size distribution analysis for cylinder diameter. Diameters were determined from Figure 1b using 'Image J' software

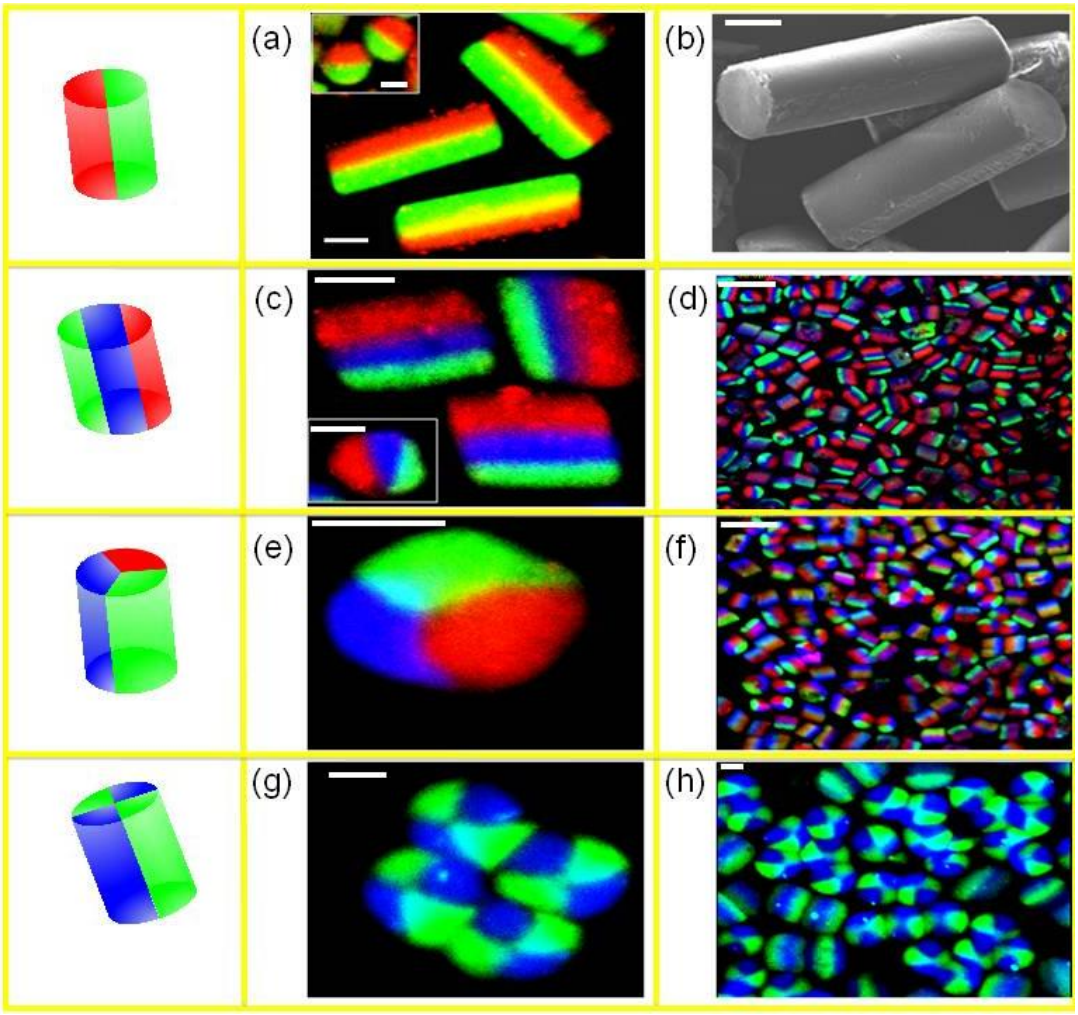


**Figure 5.4** Multicompartmental microcylinders prepared by microcutting. Cartoons indicate the number, nature of fluorescence labeling, and spatial presentation of the individual compartments. (a) CLSM image of bicompartmental microcylinders. Inlay shows cross-sectional view. (b) Corresponding high magnification SEM image. (c), (d) High- and low-magnification CLSM micrographs of tricompartmental microcylinders. Inlay of (c) depicts cross-sectional view. (e), (f) Cross-sectional view and corresponding low magnification micrograph of 'pie'-shaped microcylinders. (g), (h) High- and low-magnification CLSM images of microcylinders obtained via a square shaped capillary configuration where opposite quadrants are loaded with the same dye. Cross-sectional view is shown for better visualization of the individual compartments. Scale bars denote 50 μm for (d) and (f), and 10 μm for (a) - (c), (e), (g) and (h).

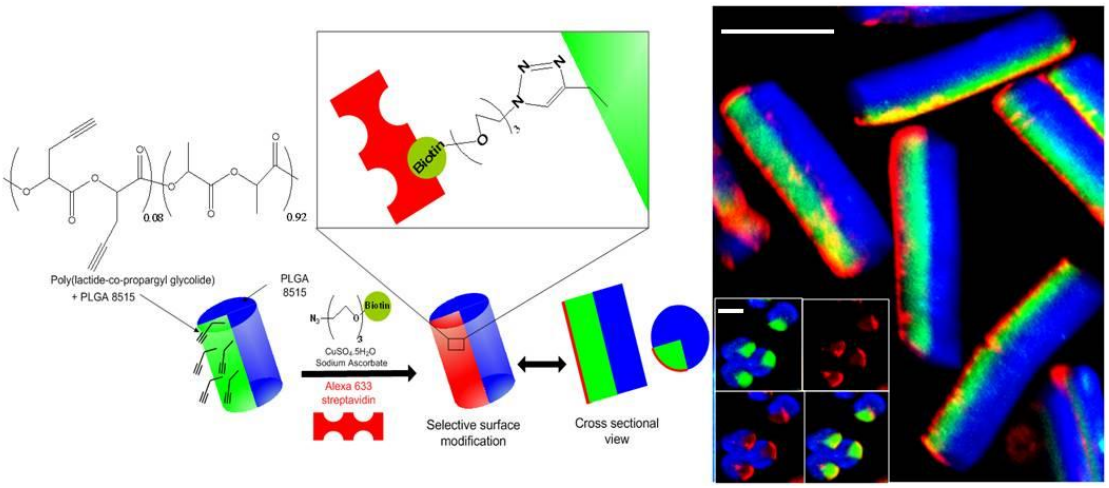


**Figure 5.5** Selective surface modification of multicompartmental microcylinders with streptavidin using 'click' chemistry. The bicompartmental microcylinders were comprised of a blue compartment, which was three-folds larger than the green compartment. The green compartment contained PLPG. After sectioning, the microcylinders were reacted with azide-biotin via copper catalyzed Huisgen heterocycloaddition; followed by incubation with Alexa Fluor-633 labeled streptavidin. The red peripheral fluorescence due to Alexa Fluor-633 was observed only on one fourth of the cylinder surface, both in axial and cross sectional CLSM micrographs (inset), confirming spatioselective surface modification. Scale bar represents 50 μm for the outer image and 20 μm for the inset.

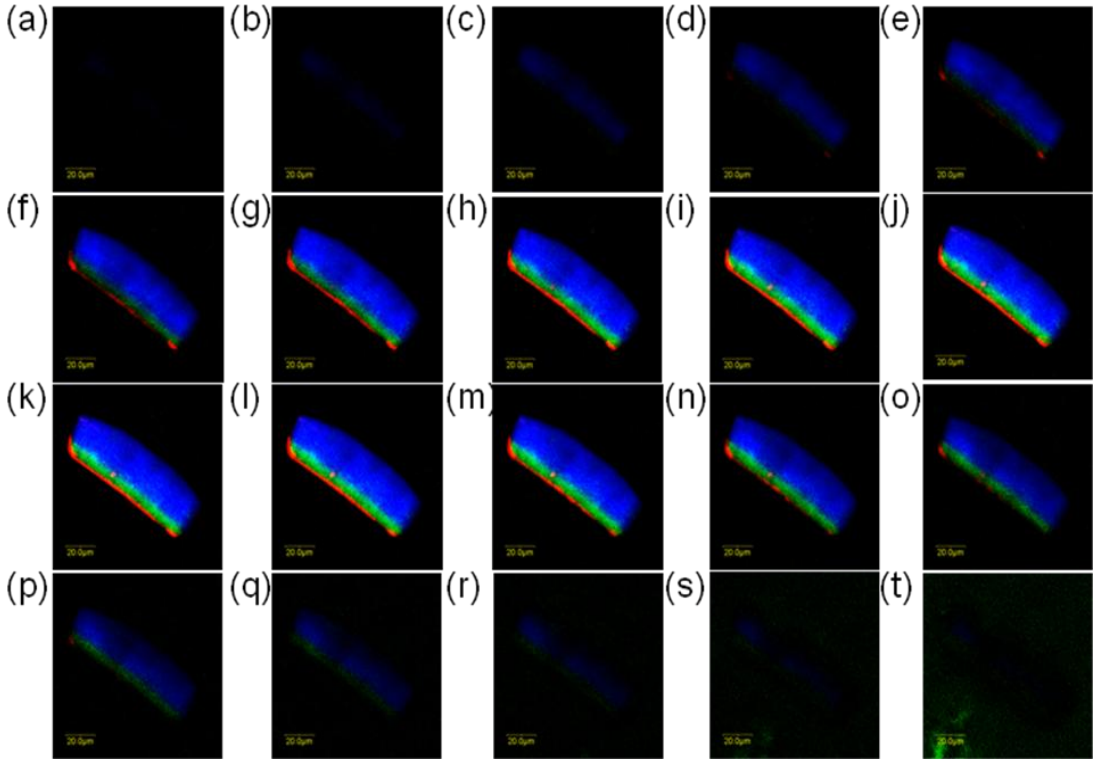


**Figure 5.6** Z stack-CLSM micrographs of a representative tetracompartmental microcylinder, modified with Alexa-633 labeled streptavidin over one compartment, i.e. one-fourth surface only. These images were utilized for a three dimensional reconstruction of the cylinder to visualize the localization of streptavidin in a perspective view, included as a movie. Blue, green and red fluorescence represent MEHPPV, PTDPV and Alexa-Fluor 633 respectively. The depth between successive images is 1.5 μm. As seen from individual sections, red fluorescence from Alexa-Fluor 633 is confined to the smaller green compartment only, at all depths.

## 5.6 References


[1] A. Walther, A. H. E. Muller, *Soft Matter* **2008**, *4*, 663.
[2] K. E. Sung, S. A. Vanapalli, D. Mukhija, H. A. McKay, J. M. Millunchick, M. A. Burns, M. J. Solomon, *J. Am. Chem. Soc.* **2008**, *130*, 1335.
[3] A. S. Utada, E. Lorenceau, D. R. Link, P. D. Kaplan, H. A. Stone, D. A. Weitz, *Science* **2005**, *308*, 537.
[4] S. Q. Xu, Z. H. Nie, M. Seo, P. Lewis, E. Kumacheva, H. A. Stone, P. Garstecki, D. B. Weibel, I. Gitlin, G. M. Whitesides, *Angew Chem Int Ed* **2005**, *44*, 724.
[5] C. Berkland, K. Kim, D. W. Pack, *J. Cont. Rel.* **2001** *73*, 59.
[6] D. Dendukuri, D. C. Pregibon, J. Collins, T. A. Hatton, P. S. Doyle, *Nat. Mater.* **2006**, *5*, 365.
[7] J. W. Kim, R. J. Larsen, D. A. Weitz, *Adv. Mater.* **2007**, *19*, 2005.
[8] J. P. Rolland, B. W. Maynor, L. E. Euliss, A. E. Exner, G. M. Denison, J. M. DeSimone, *J. Am. Chem. Soc.* **2005**, *127*, 10096.
[9] J. A. Champion, Y. K. Katare, S. Mitragotri, *Proc. Natl. Acad. Sci. USA* **2007**, *104*, 1901.
[10] S. L. Tao, K. Popat, T. A. Desai, *Nat. Protoc.* **2006**, *1*, 3153.
[11] H. Y. Chen, J. M. Rouillard, E. Gulari, J. Lahann, *Proc. Natl. Acad. Sci. USA* **2007**, *104*, 11173.
[12] J. C. Love, B. D. Gates, D. B. Wolfe, K. E. Paul, G. M. Whitesides, *Nano Lett.* **2002**, *2*, 891.
[13] O. Cayre, V. N. Paunov, O. D. Velev, *J. Mater. Chem.* **2003**, *13*, 2445.
[14] J. A. Champion, S. Mitragotri, *Proc. Natl. Acad. Sci. USA* **2006**, *103*, 4930.
[15] S. E. A. Gratton, P. A. Ropp, P. D. Pohlhaus, J. C. Luft, V. J. Madden, M. E. Napier, J. M. DeSimone, *Proc. Natl. Acad. Sci. USA* **2008**, *105*, 11613.
[16] Y. Geng, P. Dalhaimer, S. S. Cai, R. Tsai, M. Tewari, T. Minko, D. E. Discher, *Nat. Nanotechnol.* **2007**, *2*, 249.
[17] C. Berkland, E. Pollauf, N. Varde, D. W. Pack, K. Kim, *Pharm. Res.* **2007**, *25*, 1007.
[18] F. Caruso, R. A. Caruso, H. Mohwald, *Science* **1998**, *282*, 1111.
[19] D. G. Shchukin, G. B. Sukhorukov, H. Mohwald, *Angew. Chem. Int. Ed.* **2003**, *42*, 4472.
[20] S. Sengupta, D. Eavarone, I. Capila, G. Zhao, N. Watson, T. Kiziltepe, R. Sasisekharan, *Nature* **2005**, *436*, 568.
[21] A. Kazemi, J. Lahann, *Small* **2008**, *4*, 1756.
[22] K. H. Roh, D. C. Martin, J. Lahann, *Nat. Mater.* **2005**, *4*, 759.
[23] K. H. Roh, D. C. Martin, J. Lahann, *J. Am. Chem. Soc.* **2006**, *128*, 6796.
[24] K. H. Roh, M. Yoshida, J. Lahann, *Langmuir* **2007**, *23*, 5683.
[25] M. Yoshida, K. H. Roh, J. Lahann, *Biomaterials* **2007**, *28*, 2446.
[26] M. D. Abramoff, P. J. Magelhaes, S. J. Ram, *Biophot. Int.* **2004**, *11*, 36.
[27] C. Berkland, D. W. Pack, K. Kim, *Biomaterials* **2004**, *25*, 5649.
[28] S. Bhaskar, K. H. Roh, X. Jiang, G. L. Baker, J. Lahann, *Macromol. Rapid Commun.* **2008**, *29*, 1655.
[29] S. Mandal, S. Bhaskar, J. Lahann, *In preparation*.

[30] Q. Xu, R. M. Rioux, G. M. Whitesides, *ACS Nano* **2007**, *1*, 215.
[31] R. Huisgen, "*1,3-Dipolar Cycloaddition Chemistry"*, Wiley, New York, 1984, p. 1.
[32] H. C. Kolb, M. G. Finn, K. B. Sharpless, *Angew. Chem. Int. Ed.* **2001**, *40*, 2004.
[33] V. V. Rostovtsev, L. G. Green, V. V. Fokin, K. B. Sharpless, *Angew. Chem. Int. Ed.* **2002**, *41*, 2596.
[34] S. Bhaskar, J. Hitt, S. L. Chang, J. Lahann, *Angew. Chem. Int. Ed.* **2009**, *48*, 4589.
[35] S. Mitragotri, J. Lahann, *Nat. Mater.* **2009**, *8*, 15.

# CHAPTER 6

# COMPOSITIONALLY ANISOTROPIC ENCAPSULATION OF MAGNETITE NANOPARTICLES AND PIGMENTS IN MULTICOMPARTMENTAL MICROSTRUCTURES

## 6.1 Introduction

Recently, there has been substantial attention devoted towards fabrication of 'smart' or stimuli responsive materials for applications in displays, sensors, actuators and tunable viscosity fluids.[1] 'Smartness' not only involves precise control over structure and properties of materials to elicit a specific response to a stimulus, but also creation of unique directional interactions between micro/nanostructures to engineer assemblies that can be organized and 'disorganized' on cue.[2] The ability to induce a 'dual' stability relies on robust synthetic techniques to engineer anisotropy and directionality in micro/nanostructures.[3] Examples of assemblies via anisotropic interactions include nanoparticle superstructures from light-induced dipole-switching,[4] colloidal assemblies under AC electric fields,[5, 6] and assembly of nanoparticle amphiphiles.[7] Assemblies induced via magnetic fields are attractive for displays as magnetic field strength can be varied very easily to control the translation and

rotation of particles.[3, 8] Examples of anisotropic magnetic particle assemblies include linear,[9] staggered [3] and zig-zag chains,[10] 2D arrays,[10, 11] pyramids,[12] rings[13] and other complex shapes.[14] To date, several approaches for the preparation of Janus particles using microcontact printing,[15, 16] partial masking,[17-19] microfluidic co-flow,[20-22] and selective deposition[23-25] , and emulsification[8] have been reported. While most studies have focused on preparation of spherical Janus particles, more complex particles with precisely tunable internal architectures maybe desirable for generation of novel display devices. Furthermore, in most of the above processes incorporation of optical pigments is a challenge. These obstacles can be overcome via electrohydrodynamic co-jetting, where materials can incorporated into the bulk of the particle simply by blending them into the jetting solution. Till now, this process was limited to polymers.[26, 27] In this chapter, we demonstrate electrohydrodynamic co-jetting with colloidal suspensions, resulting in multicompartmental particles containing anisotropic distributions of magnetite nanoparticles (MNPs) as well as optical pigments, namely titanium dioxide ($TiO_2$) and carbon black (CB) for potential applications in displays.

## 6.2 Methods

### 6.2.1 Materials

PLGA 8515 (Mw 40,000–75,000 g / mol), PTDPV, MEHPPV, chloroform, DMF, and Tween -20 were purchased from Sigma-Aldrich, Inc. USA. All reagents were

used without further purification. Polythiophene polymer, sold under commercial name ADS 306PT (Mw 20,000–70,000 g/ mol) was purchased from American Dye Source, Canada. $TiO_2$, CB, and MNPs (30nm diameter and suspended in chloroform) were purchased from Tronox, Inc, USA, General Carbon Company, USA and Ocean Nanotech, USA respectively. A magnet (4" x 1" x 1" thick, NdFeB, and 4871 Gauss surface field) was a product of K&J Magnetics Inc, USA.

### 6.2.2 Electrohydrodynamic co-jetting

The following method was used to prepare jetting solutions: $TiO_2$ and carbon black (CB) were independently suspended in chloroform via sonication (concentration ranging from 0.025-0.03 g/ml). The polymer was weighed out into 3 ml glass vials Fisher #NC9708180). This was followed by addition of desired amount of magnetite suspension, followed by addition of the $TiO_2$ or CB suspensions. Finally, dyes were added in trace amounts, followed by bath sonication for 30 min. The protocol for electrohydrodynamic co-jetting to fabricate multicompartmental particles, aligned fibers and cylinders is outlined in chapters 3, 4, and 5 respectively. For fibers with larger (~200 µm) diameters, 18 gauge needles (Nordson EFD Inc, USA) were used during electrohydrodynamic co-jetting. 26 gauge needles were employed in all other cases.

### 6.2.3 Characterization

#### 6.2.3.1 Optical Microscopy

A Nikon optical microscope was used to examine the microstructures prepared by electrohydrodynamic co-jetting under white light in reflection imaging mode. CLSM images were obtained with a FluoView 500 confocal laser scanning microscope (Olympus, Japan). MEHPPV (and ADS406PT), PTDPV, and ADS306PT were excited by 405 nm UV, 488 nm Argon, and 533 nm Helium-Neon green lasers respectively. Optical filters of emission wavelength 430-460 nm, 505-525 nm, and 560-600 nm were used to visualize the fluorescence of MEHPPV, PTDPV, and ADS306PT respectively. Particles were also characterized for visible color effects using a Sigma SLR digital camera.

#### 6.2.3.2 SEM

Particles jetted on to the substrate were sputtered with gold and observed under an Amray FEG SEM.

#### 6.2.3.3 TEM

Particles were harvested from substrate, suspended in DI-$H_2O$ and sonicated for 10 s. Approximately 20 µL of 5 mg/ml particle suspension was cast onto a polyethylene mold (Ted Pella, USA), and water allowed to evaporate. Then a 100:43 w/w mixture of epoxy resin: initiator (Ted Pella #813-502 and #813-505) was mixed separately, degassed for 1 min. and poured onto the mold. The resin was allowed to cure overnight, and the blocks were sectioned by ultramicrotoming (Reichert Ultracut-E) to a thickness of 200 nm using a diamond knife (Diatome, USA). The sections were taken directly on plasma treated TEM-grids which were examined at 100kV (Philips CM-100) without any additional carbon coating.

## 6.3 Results and Discussion

The ultimate goal of anisotropic magnetic particles is to form the framework of display devices which would require particles of diameter ranges resolvable by the unaided human eye (~ 100 µm). In order to demonstrate the feasibility of anisotropic MNP encapsulation, electrohydrodynamic co-jetting was performed using jetting solution and process conditions that have been known to previously yield particles with a well defined anisotropy in the size ranges of 5-8 µm. The jetting solutions consisted of a 5:100 w/w soln. of PLGA 85:15 in 97: 3 chloroform: DMF (v/v), with a 5:100 wt. ratio of MNPs: PLGA in one compartment. A flow rate of 0.25 ml/h was employed. Figure 6.1a shows a digital photograph of a representative Taylor cone during this experiment, which shows a clear distinction between solutions. SEM images (Figure 6.1b) indicate spherical particle morphology. The TEM images (Figures 6.1c and d) reveal that MNPs are indeed encapsulated in one half of the particles.

With the ability to synthesize bicompartmental particles with anisotropic MNP distribution demonstrated, we sought to maximize their performance. Towards this end, we conducted a series of experiments with different MNP loadings. The jetting solutions consisted of a 6: 100 w/w soln. of PLGA 85:15 in 97:3 chloroform: DMF (v/v), with the desired loading of MNPs in one compartment and the flow rate was maintained at 0.34 ml/h. These loadings were defined as weight ratios between MNPs and PLGA. In addition to MNP: PLGA mass ratio of 5:100, two higher loadings, 8:100 and 11:100 were

investigated. The solutions were also loaded with MEHPPV and PTDPV dyes for CLSM imaging. No MNP aggregation was observed in the solution except in the case of 11:100, wherein aggregates were observed, which seemed to disperse after the solution was vortexed briefly. Great care was taken to ensure that jetting conditions were unaltered for all the solutions. At all loadings, the interface between the two jetting solutions could be maintained throughout the duration of the jet. Figures 6.2a, b and c show TEM images of particles loaded with increasing amounts of MNPs. The TEM images reveal that MNPs are indeed encapsulated in one half of the particles. However, increasing the MNP loading progressively increased aggregation of MNPs inside the PLGA particles, with the number and size of aggregates increasing with higher MNP loadings. The aggregation at higher loadings could be initiated from solvent evaporation in the Taylor cone, and get pronounced at higher loadings during particle formation by solvent evaporation in the droplet(s). Corresponding SEM images are shown in Figures 6.2d, e and f, which clearly show spherical particle shape. CLSM imaging revealed well defined anisotropy, as seen in individual blue and green fluorescence channels in Figures 6.3a, b and c. Furthermore, compartmentalization of MNPs was clearly visible through DIC microscopy at higher loadings (Figure 6.3c), which, when overlaid with corresponding CLSM images, unambiguously established bicompartmental character. A 5:100 wt ratio of MNP:PLGA was defined as optimal, judging from the uniform distribution of MNPs in the bulk of the particles and the response of particles[28] to external magnetic fields.

In order to amplify optical effects visible to the naked eye upon changes in the orientation of bicompartmental microparticles in response to an external magnetic field, we wished to incorporate $TiO_2$ and CB in bicompartmental PLGA microparticles, with CB and MNPs being present in the same compartment. A particle diameter range of 25-30 μm range was targeted. TEM images of CB and $TiO_2$ are shown in Figure 6.4 (a) and (b) respectively. Both pigments exist as polydisperse nanoparticles in the 50-150 nm range. These pigments were individually suspended in chloroform before being incorporated into the jetting solution. As an initial proof of concept, bicompartmental particles containing $TiO_2$ in one compartment only were prepared (Figure 6.5a-b). Towards this end, we employed a jetting solution of 9:100 w/w PLGA with the solvent being 1:1 chloroform: methylene chloride by volume, which yielded mostly spherical particles at flow rates of 3 ml/h. The use of high polymer concentrations, along with a highly volatile solvent mixture, results in a larger jet diameter, which, coupled with quicker solvent evaporation, yields particles with an average diameter of ~ 30 μm. The PLGA: $TiO_2$ ratio was 1:1, and the cone jet mode could be maintained in a stable manner, which is manifested in the well defined compartments of $TiO_2$ in the optical micrographs (Figures 6.5 a and b). Next, bicompartmental particles containing carbon black in one compartment only were fabricated, using jetting solution and process conditions exactly similar to those employed for $TiO_2$, except that the mass ratio of CB:PLGA in one solution was maintained at 14:100 (higher loadings resulted in aggregates of CB within particles) Again, optical micrographs (Figures 6.5 c-d) were indicative of

excellent distinction between individual compartments, with the half containing CB appearing distinctively darker than the other. It is noteworthy that the nanoparticle dispersions were not stabilized in any way and hence jetting times had to be carefully monitored in order to avoid precipitation of the pigments.

Encouraged by these observations, we then synthesized bicompartmental particles containing $TiO_2$ in one compartment and MNPs and CB in the other compartment. The average particle diameter is ~ 30 μm, as indicated in the SEM images (Figure 6.6 a). The mass ratios of $TiO_2$: PLGA and CB: MNP: PLGA are 5:100 and 14:5:100 respectively. The optical micrographs reveal sharp color contrasts between the $TiO_2$ and CB halves (Figure 6.6b). We then visualized the optical appearance of these particles via a digital camera. As shown in Figure 6.6c, black and white halves can be clearly resolved in all particles. TEM micrographs (Figures 6.7 a-c) further demonstrate the compartmentalization of the pigments and magnetite, with the magnetite nanoparticles appearing along with the carbon black in one compartment only (Figures 6.7 d-e).

While particle formation via electrohydrodynamic co-jetting is an attractive way to achieve anisotropic encapsulation of MNPs as well as pigments, distribution of compartments may not be perfectly half-half (which is observed to an extent in the optical micrographs in Figure 6.6b). This could be attributed to rapid jet formation and breakup during swirls in the Taylor cone,[26, 27] resulting in 'sandwich' type anisotropy which could affect the performance of display devices. In order to ensure an extremely well defined internal architecture, we turned towards bicompartmental fibers (explained in chapter 4). DIC and corresponding

CLSM micrographs of fibers loaded with 5:100 MNPs: PLGA by mass are shown in Figure 6.8. Not only was the jet stable and sustainable for long periods of time (~4h), near-perfect compartmentalization of MNPs in exactly half of the volume of the fiber was observed. This was confirmed in the TEM images (Figure 6.9a) which revealed a sharp demarcation between compartments (Figure 6.9b). The MNPs were well distributed within the bulk of the fibers (Figure 6.9c) at this loading. An MNP loading optimization study revealed magnetite aggregation similar to what was observed in spherical particles, however, in this case, the aggregates were large enough to be resolved via CLSM and DIC, as shown in Figures 6.10 b and c ( which show MNP:PLGA mass ratios of 7.5:100 and 9:100 respectively). Aggregation was amplified in case of fibers possibly due to impedance to Brownian motion of MNPs owing to high viscosities of the jetting solution. . The theoretical limit of the size of such an aggregate would be equal to the diameter of the jet stream, which was also observed (Figure 6.10 c).

Another advantage of fabricating anisotropic fibers is their ability to lend themselves to cylinder formation via microsectioning, as outlined in chapter 5, which are significantly more monodisperse than particles (directly after jetting and without filtration). Encouraged by the ability to form fibers with compartmentalized MNPs, we proceeded to section bundles of bicompartmental fibers and sonicate them to form bicompartmental microcylinders containing magnetite in one compartment only. These are shown in Figure 6.11a. These cylinders have lengths of 5 μm. At the magnetite loading employed (3:100), MNPs were not dislodged from the fibers during sonication. Since particle

orientation in response to an external magnetic field is dependent on the longest dimension of the responsive compartment,[3] investigation of anisotropies other than 'half-half' may be of interest. Towards this end, we fabricated heptacompartmental cylinders containing MNPs in the central and one peripheral compartment (Figure 6.11b). To the best of our knowledge, such complex anisotropies with respect to MNP distribution in the bulk have not yet been achieved.

In order to increase the optical visibility even further, we sought to fabricate particles with ~ 200 µm diameters. The electrohydrodynamic co-spinning process could be conveniently extended to yield fibers in this range simply by increasing solution viscosity (which was done by increasing the solution concentration to 23:100 w/w PLGA: solvent compared to 18:100 used hitherto, with the solvent being 95:5 chloroform: DMF by volume), employing larger diameter needles and using flow rates of 0.02 ml/h. Upon microsectioning, uniform, bichromal cylinders as shown in the digital photograph in Figure 6.12 were obtained, wherein the black and white compartments were discernible to the naked eye. The diameter and aspect ratio of these cylinders was 250 µm and 1 respectively. Figure 6.13 shows preliminary data demonstrating orientation of cylinders upon application of an external magnetic field.[28] When bichromal cylinders (aspect ratio: 2) containing MNPs in the black compartment are subjected to an external gradient magnetic field (Figure 6.13a), the MNP containing (black) side of the particles is oriented towards the magnet and hence, particles undergo an upward translational motion (Figure 6.13c). Field reversal

(magnet applied at the bottom of the cuvette) reverses particle orientation, and the white half is visible to the naked eye (Figure6.13b).[28]

## 6.4 Conclusions

In this chapter, the fabrication of particles with anisotropic encapsulation of MNPs and optical pigments, $TiO_2$ and CB, was demonstrated. SEM, TEM and CLSM analysis of particles revealed well defined compartments. Further control over internal architecture was achieved by fabricating fibers with MNPs in one compartment and then by converting fibers into monodisperse cylinders with controllable aspect ratios via microsectioning. Bi- and heptacompartmental microcylinders with anisotropic magnetite distribution were obtained in this manner. In addition, bichromal fibers with diameters of 250 μm were also fabricated electrohydrodynamic co-spinning, wherein the compartments were clearly discernible to the unaided eye. Finally, preliminary data showing orientation of cylinders in response to an external magnetic field were obtained. Future work would involve a detailed analysis of the response of these particles to magnetic fields, and of the assemblies thus generated.

## 6.5 Figures and tables

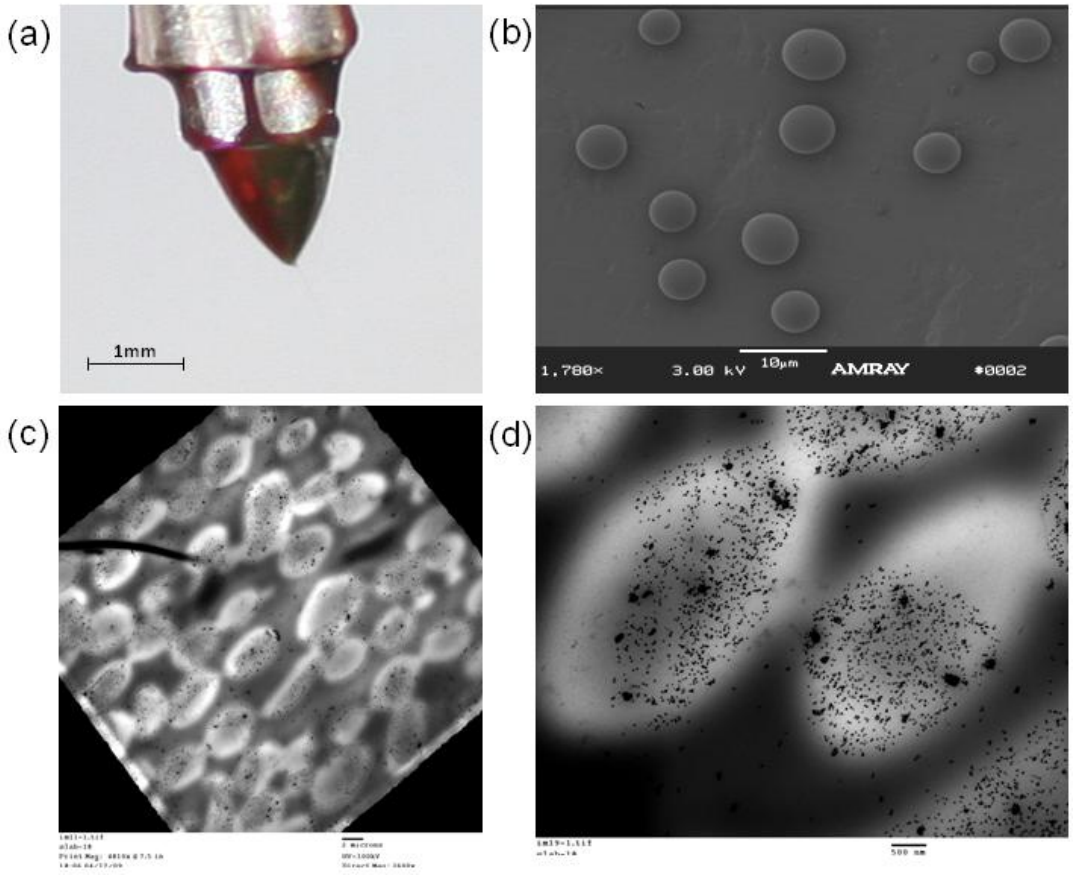


**Figure 6.1** Bicompartmental particles containing magnetite in one compartment only. (a) Digital photograph of Taylor cone showing a clear interface between the red and black solutions. The red solution contains 5:100 w/w PLGA 8515 in 97:3 v/v $CHCl_3$: DMF along with trace amounts of ADS306PT, the dark solution contains the same concentration of PLGA along with 5:100 w/w MNP: PLGA and trace amounts of PTDPV. A flow rate of 0.25 ml/h was employed. (b) SEM images of bicompartmental particles indicating spherical morphology (c)-(d) low and high magnification TEM images of particles showing compartmentalization of MNPs. Scalebars denote 2µm in (c) and 500 nm in (d).

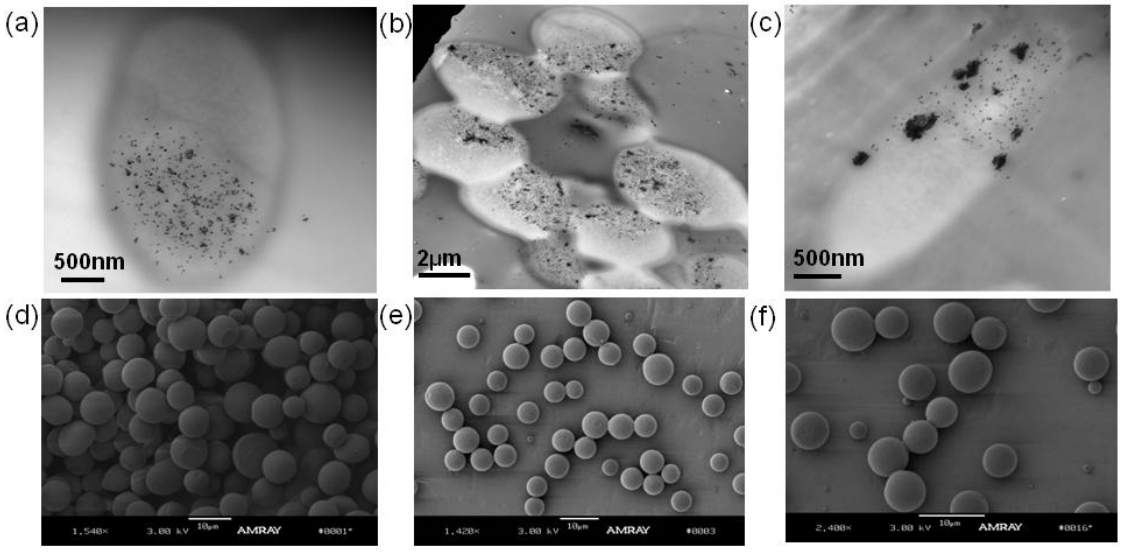


**Figure 6.2** Effect of MNP loading on compartmentalization of magnetite. All particles were made from a 6:100 w/w PLGA 85:15 in 97:3 CHCl3: DMF in both compartments at 0.34 ml/h and voltage varying from 6-6.3 kV. TEM and corresponding SEM images of particles with MNP: PLGA wt. ratio of (a), (d) 5:100, (b), (e) 8:100 and (c), (f) 11:100 are shown. SEM shows spherical particle morphology, however, at higher loadings, the MNPs were seen as aggregates in particles. Scalebars represent 10 µm for (d), (e) and (f).

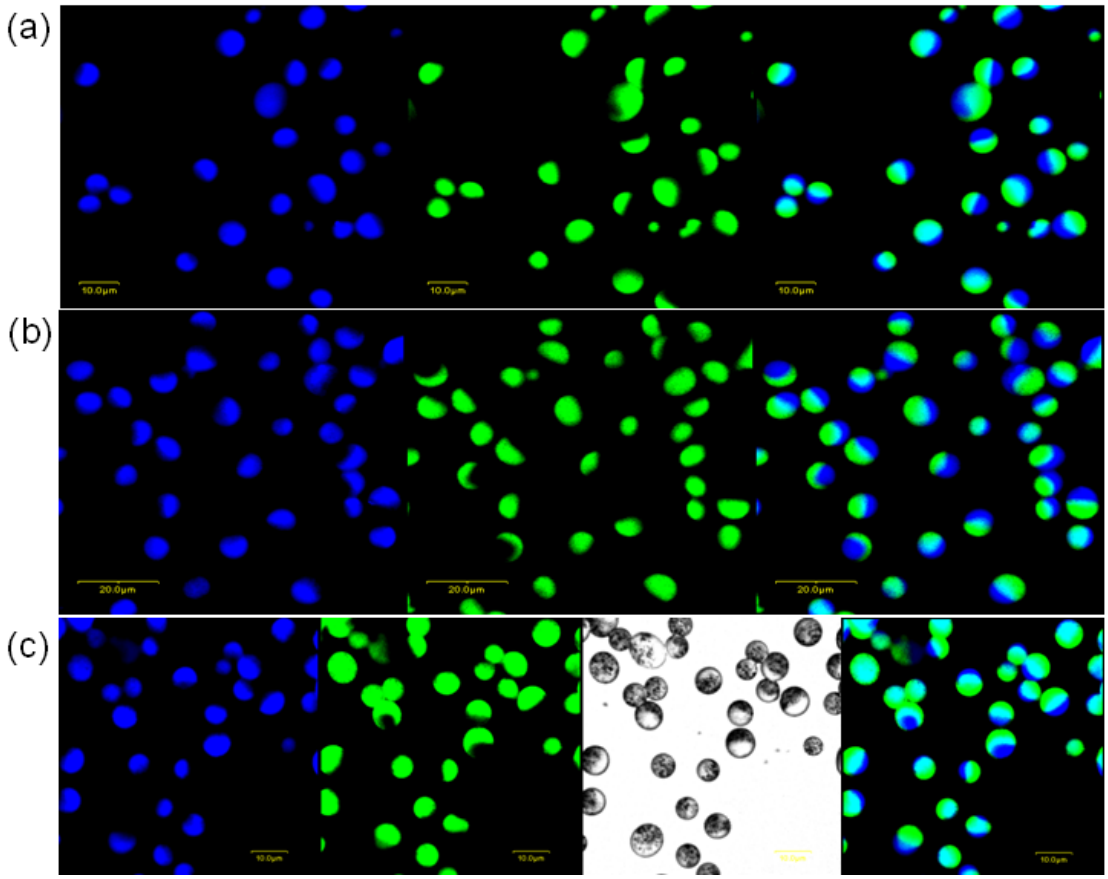


**Figure 6.3** CLSM images of particles with MNP: PLGA ratios of (a) 5:100 (b) 8:100 and (c) 11:100, (corresponding to the SEM images in Figure 6.2). Blue (from MEHPPV) and green (from PTDPV) fluorescence channels are shown, followed by the overlay. The green compartment contains magnetite, which could be observed via DIC at higher loadings as shown in (c). Scale bars represent 10 µm for (a) and (c), and 20 µm for (b).

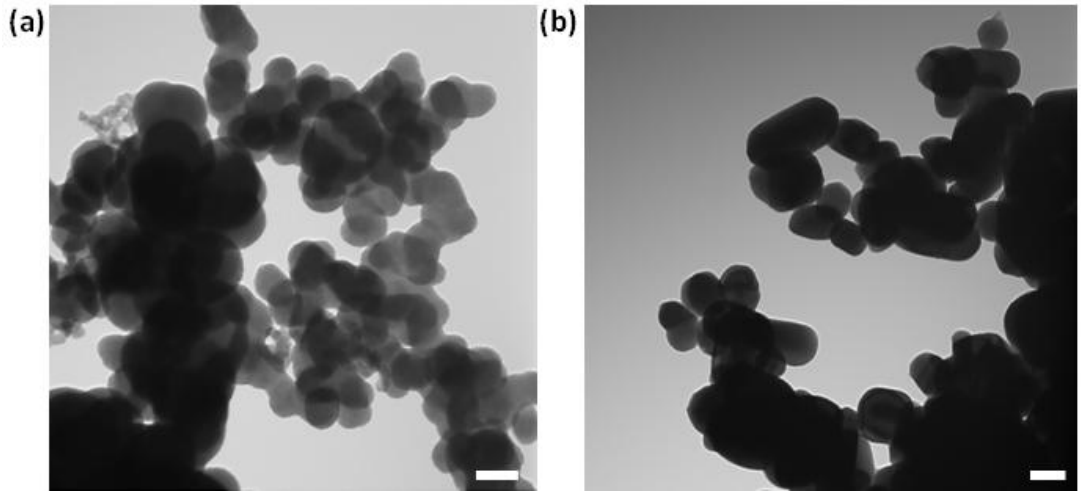


**Figure 6.4** TEM images of (a) Carbon black and (b) $TiO_2$ nanoparticles. All scale bars represent 100 nm.

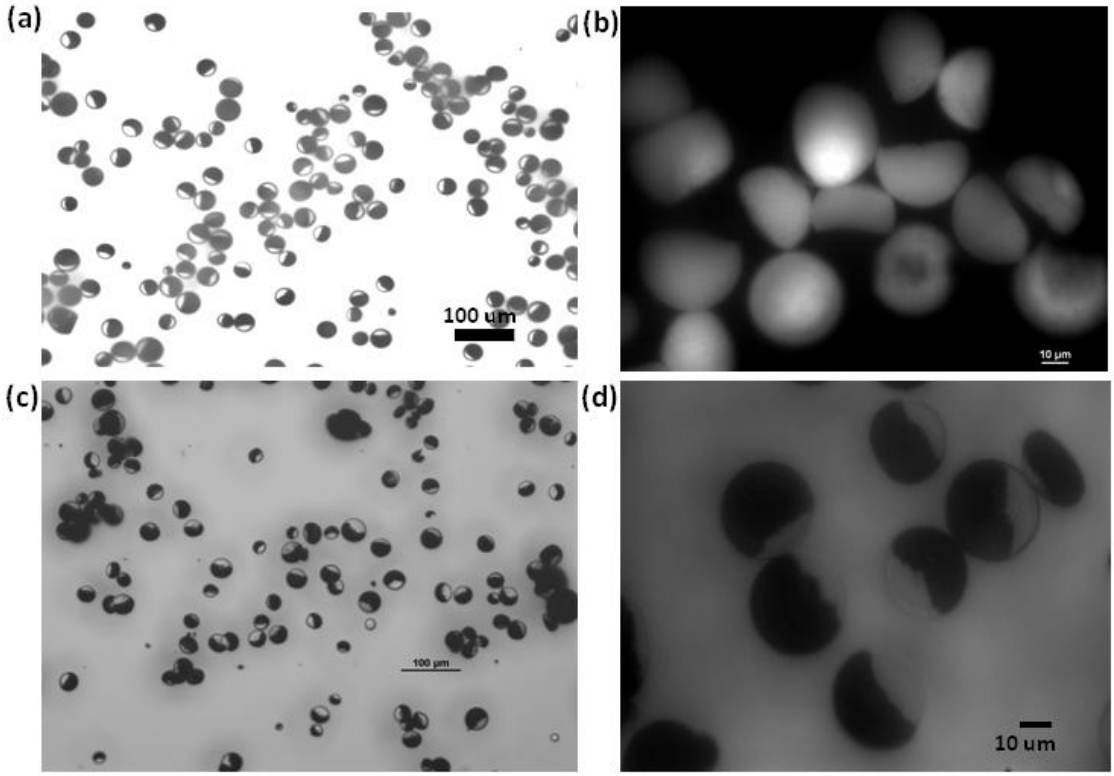


**Figure 6.5** Anisotropic encapsulation of optical pigments in bicompartmental PLGA particles. Low and high magnification optical micrographs of particles with (a)-(b): 1:1 w/w ratio of PLGA:$TiO_2$ in one compartment and PLGA only in the other compartment, and (c), (d) MNPs, CB and PLGA in a 5:14:100 ratio by wt. in one compartment and PLGA only in the other. All particles were synthesized using jetting solutions of 9:100 w/w PLGA 85:15 in 1:1 methylene chloride: chloroform at 3 ml/h.

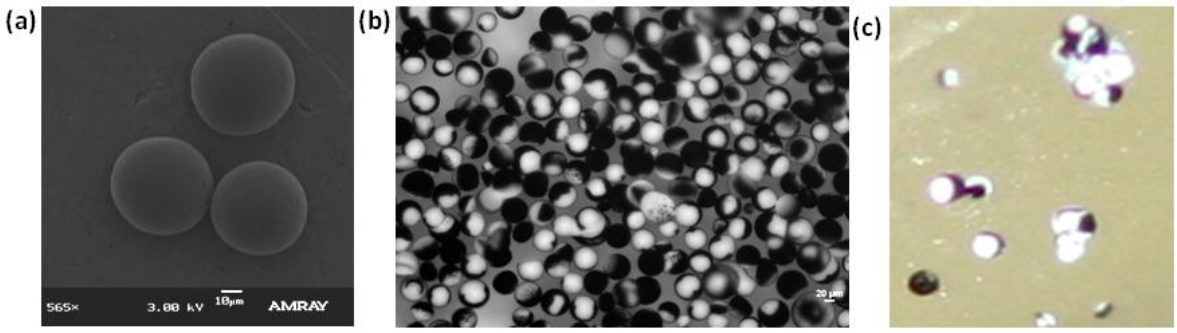


**Figure 6.6** Magnetically responsive bichromal microparticles (a) SEM image, (b) optical micrograph and (c) corresponding digital image of bicompartmental particles containing magnetite nanoparticles and carbon black pigment in one compartment and titanium dioxide in the other compartment.

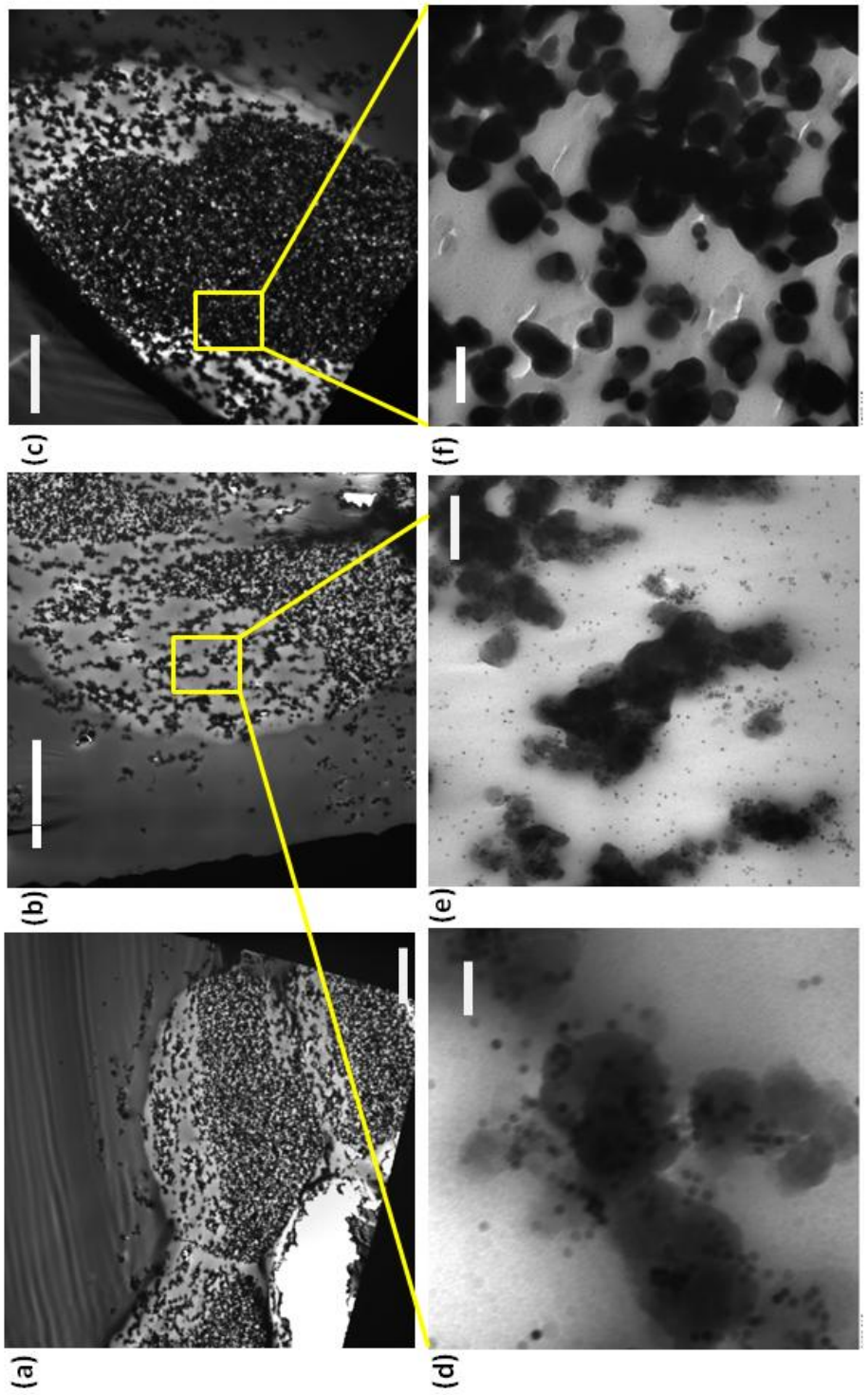


**Figure 6.7** TEM images of bichromal particles shown in Figure 6.6. (a)-(c) are low magnification images, (d)-(e) and (f) are zoomed in images of areas in opposite halves of particles, which exhibit magnetite nanoparticles interspersed with carbon black in one half (d-e) and $TiO_2$ only in the other (f). Scale bars represent 10 μm for (a)-(c), 100 nm for (d), 500 nm for (e) and 300 nm for (f).

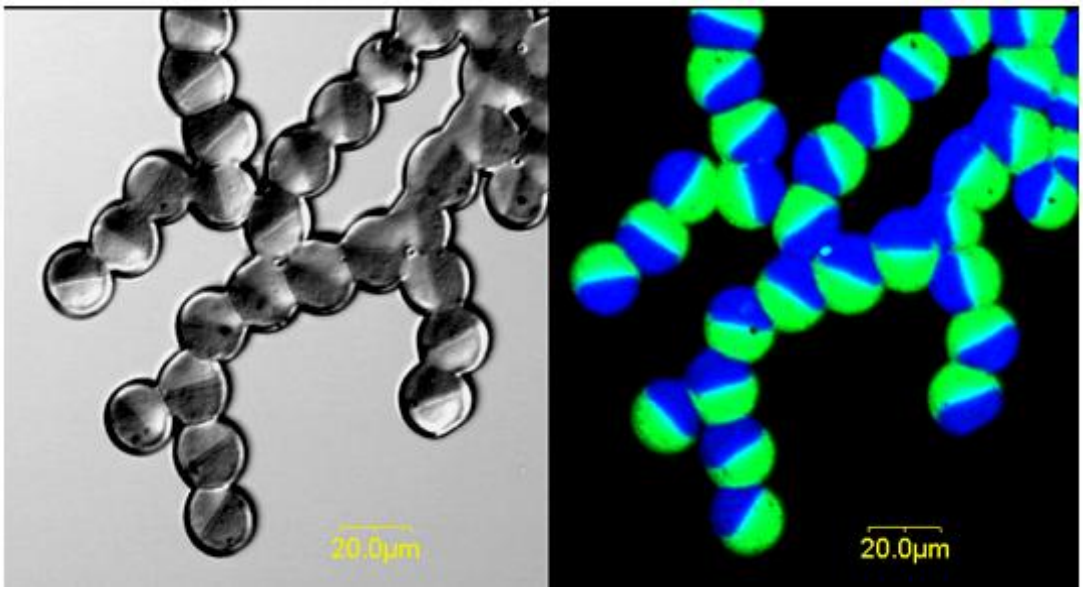


**Figure 6.8** DIC and corresponding CLSM image of bicompartmental fibers containing 30 nm diameter MNP's in one compartment only. MNP: PLGA wt. ratio in the green compartment is 5:100.

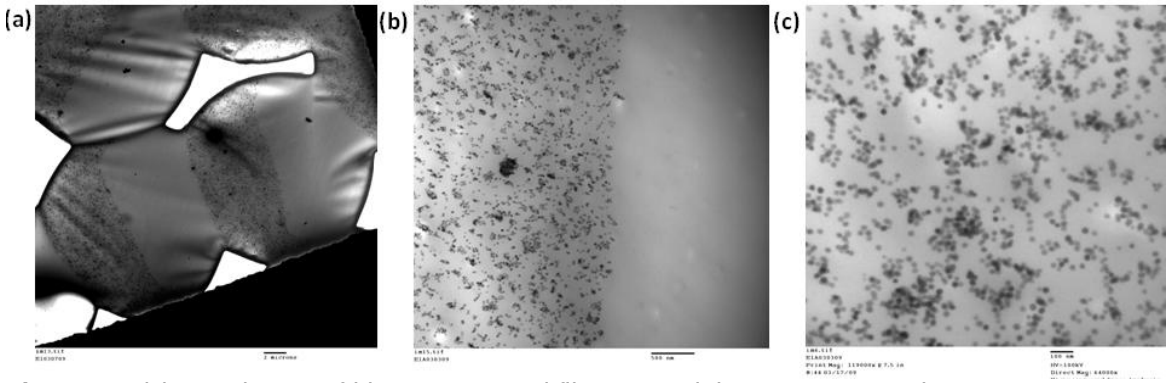


**Figure 6.9** (a) TEM image of bicompartmental fibers containing 30 nm MNPs in one compartment (b) high magnification image showing the interface (c) high magnification image showing distribution of MNPs in the bulk of the fiber. The scale bars are 2 µm for (a), 500 nm for (b) and 100 nm for (c).

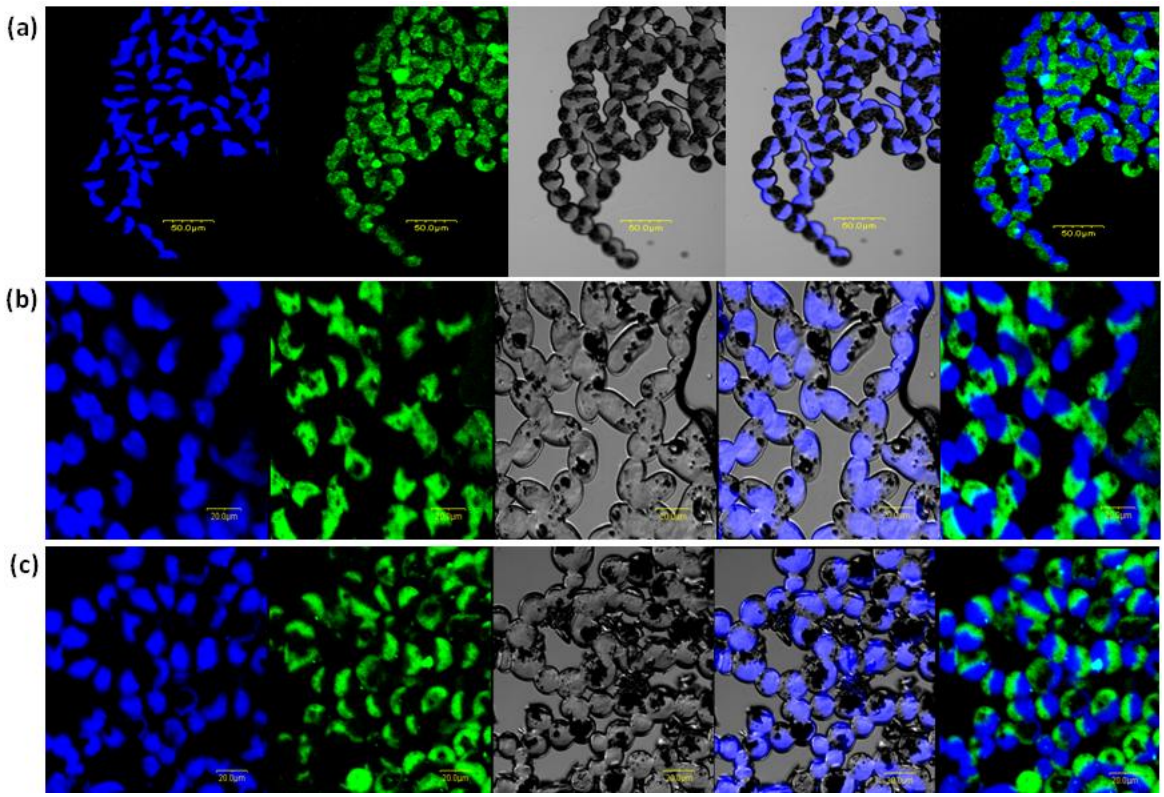


**Figure 6.10** Effect of increasing MNP loading in bicompartmental fibers. All CLSM images depict cross sections of bicompartmental PLGA fibers loaded with 5 nm diameter MNPs in one compartment only. Each image consists of a sequence 5 images : 1.blue fluorescence from MEHPPV, 2.green fluorescence from PTDPV, 3. DIC image, 4. an overlay of 1 and 3, and 5. an overlay of 1 and 2. (a), (b) and (c) represent MNP: PLGA wt. ratios of 4:100, 7.5:100 and 9:100 respectively. Scale bars represent 50µm for (a) and 20 µm for (b) and (c).

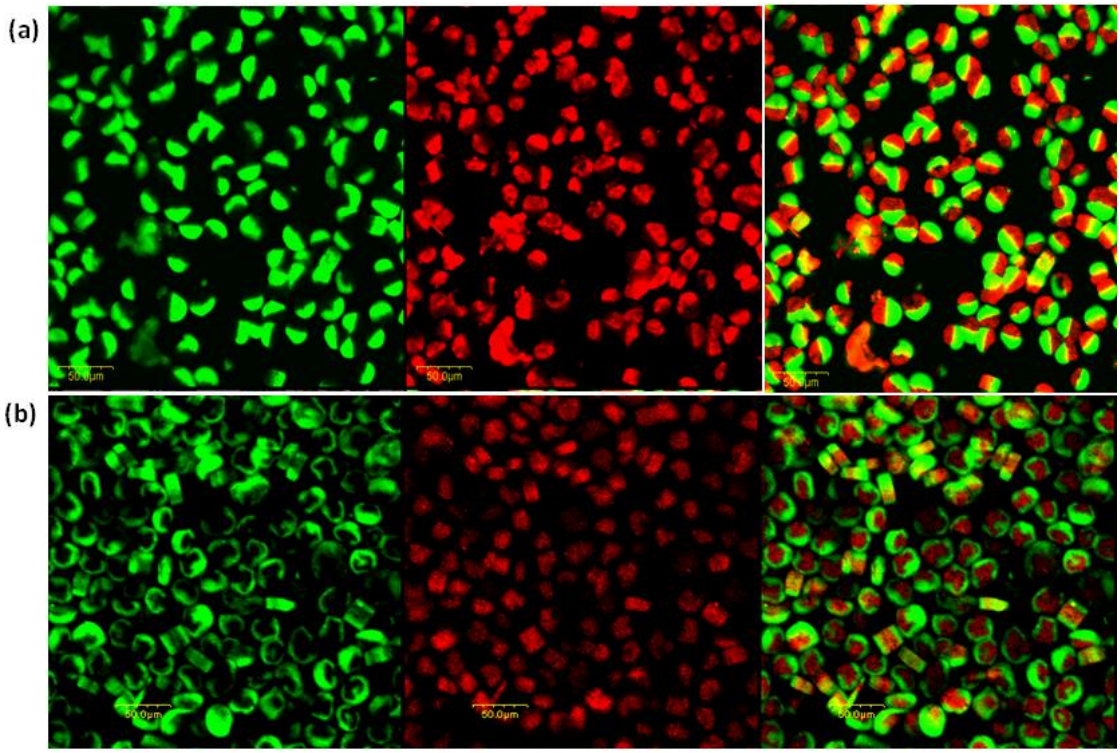


**Figure 6.11** CLSM images of (a) bicompartmental cylinders with MNPs in the red compartment, and (b) heptacompartmental microcylinders with magnetite in the central and one peripheral compartment. The length of both cylinders is 5 μm. All scale bars represent 50μm.

**Figure 6.12** Digital photograph of optically visible microcylinders containing 5:100 wt. ratio of $TiO_2$: PLGA in one compartment and 3:2:100 by wt. MNP:CB:PLGA in the black compartment. These cylinders were produced from fibers which were spun from solutions with greater viscosities (23:100 w/w PLGA in 95:5 Chloroform: DMF, 0.02 ml/h) using capillaries with larger diameters. Microcylinders have diameters of 250 μm and an aspect ratio of 1.

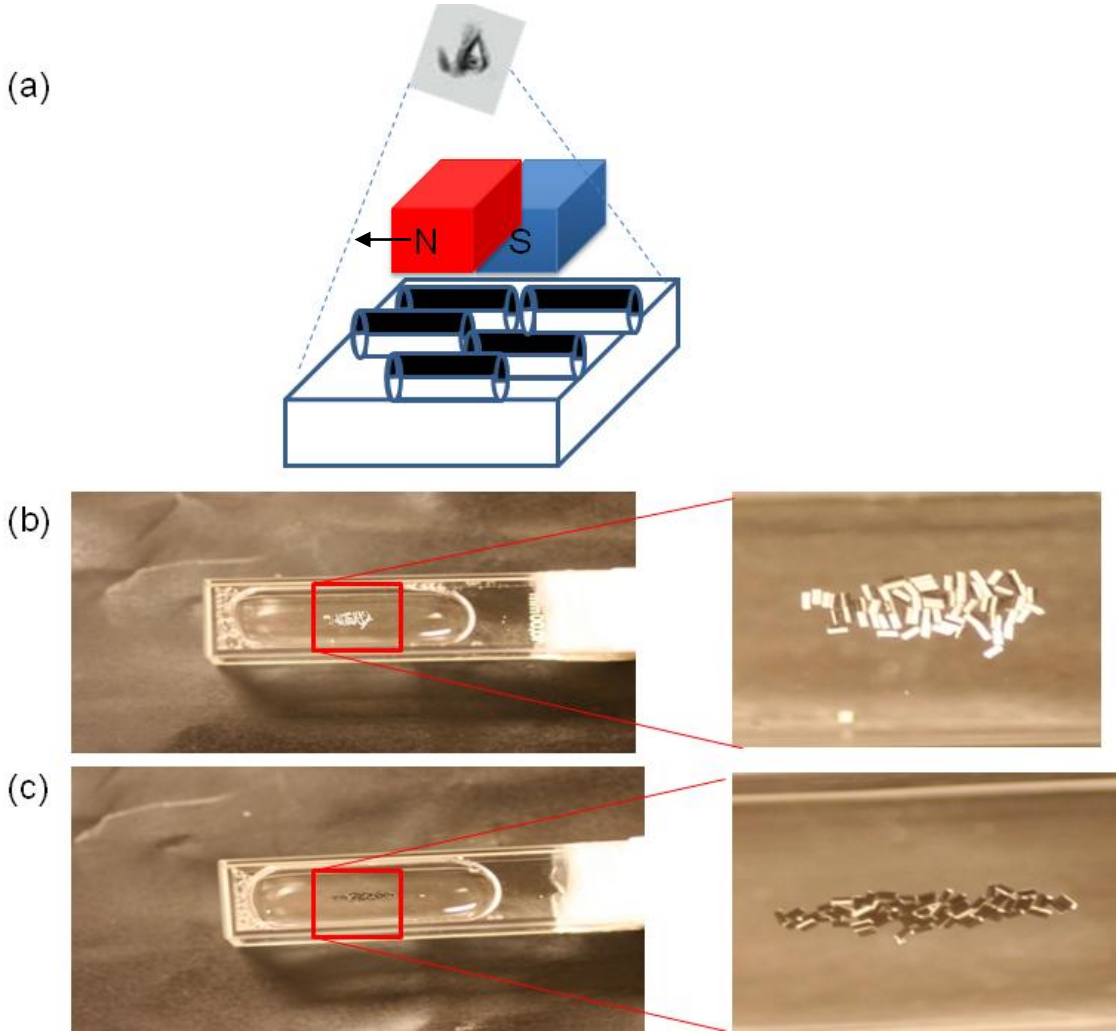


**Figure 6.13** Proof of concept of anisotropic particle switching in response to magnetic field (a) schematic depicting direction of magnetic field, direction of orientation of particles and the view to the observer. When a gradient magnetic field is applied as shown in (a), the cylinders orient the magnetite containing side towards the field and translate towards it. In doing so the longitudinal axes of the cylinders are aligned with the direction of the magnetic field. Depending on whether the field is applied at the bottom or top of the cuvette (width 1cm), (a) white or (b) black colored compartments are visible to the eye.

## 6.6 References


[1] F. Xia, L. Jiang, *Adv Mater* **2008**, *20*, 2842.
[2] M. Yoshida, J. Lahann, *ACS Nano* **2008**, *2*, 1101.
[3] S. K. Smoukov, S. Gangwal, M. Marquez, O. D. Velev, *Soft Matter* **2009**, *5*, 1285.
[4] R. Klajn, K. J. M. Bishop, B. A. Grzybowski, *Proc. Natl. Acad. Sci. USA* **2007**, *104*, 10305.
[5] K. P. Herlihy, J. Nunes, J. M. DeSimone, *Langmuir* **2008**, *24*, 8421.
[6] S. Gangwal, O. J. Cayre, M. Z. Bazant, O. D. Velev, *Physical Review Letters* **2008**, *100*.
[7] P. Akcora, H. Liu, S. K. Kumar, J. Moll, Y. Li, B. C. Benicewicz, L. S. Schadler, D. Acehan, A. Z. Panagiotopoulos, V. Pryamitsyn, V. Ganesan, J. Ilavsky, P. Thiyagarajan, R. H. Colby, J. F. Douglas, *Nat Mater* **2009**, *8*, 354.
[8] S. H. Kim, J. Y. Sim, J. M. Lim, S. M. Yang, *Angewandte Chemie-International Edition* **2010**, *49*, 3786.
[9] F. M. Pedrero, M. T. Miranda, A. Schmitt, J. C. Fernandez, *J. Chem. Phys.* **2006**, *125*, 084706.
[10] S. Gangwal, A. Pawar, I. Kretzschmar, O. D. Velev, *Soft Matter* **2010**, *6*, 1413.
[11] J. Rybczynski, U. Ebels, M. Giersig, *Colloid Surf. A-Physicochem. Eng. Asp.* **2003**, *219*, 1.
[12] L. E. Helseth, *Langmuir* **2005**, *21*, 7276.
[13] L. E. Helseth, R. M. Muruganathan, Y. Zhang, T. M. Fischer, *Langmuir* **2005**, *21*, 7271.
[14] R. M. Erb, H. S. Son, B. Samanta, V. M. Rotello, B. B. Yellen, *Nature* **2009**, *457*, 999.
[15] O. Cayre, V. N. Paunov, O. D. Velev, *Chem Commun* **2003**, *18*, 2296.
[16] H. Y. Koo, D. K. Yi, S. J. Yoo, D.-Y. Kim, *Adv Mater* **2004**, *16*, 274.
[17] Z. Bao, L. Chen, M. Weldon, C. E, O. Cherniavskaya, Y. Dai, J. B. H. Tok, *Chem Mater* **2002**, *14*, 24.
[18] V. N. Paunov, O. J. Cayre, *Advanced Materials* **2004**, *16*, 788.
[19] C. Casagrande, P. Fabre, E. Raphael, M. Veyssie, *Europhysics Letters* **1989**, *9*, 251.
[20] T. Nisisako, T. Torii, T. Higuchi, *Chem Eng J* **2004**, *101*, 23.
[21] T. Nisisako, T. Torii, T. Takahashi, Y. Takizawa, *Adv Mater* **2006**, *18*, 1152.
[22] Z. Nie, W. Li, M. Seo, S. Xu, E. Kumacheva, *J Am Chem Soc* **2006**, *128*, 9408.
[23] E. Hugonnot, A. Carles, M. H. Delville, P. Panizza, J. P. Delville, *Langmuir* **2003**, *19*, 226.
[24] H. Takei, N. Shimizu, *Langmuir* **1997**, *13*, 1865.
[25] A. B. Pawar, I. Kretzschmar, *Langmuir* **2007**, *24*, 355.
[26] K. H. Roh, D. C. Martin, J. Lahann, *Nat. Mater.* **2005**, *4*, 759.
[27] S. Bhaskar, K. H. Roh, X. Jiang, G. L. Baker, J. Lahann, *Macromol. Rapid Commun.* **2008**, *29*, 1655.
[28] S. Hwang, S. Bhaskar, J. Yoon, J. Lahann, *in preparation*.

# CHAPTER 7

# COMPOSITIONAL ANISOTROPY IN PLGA/PEI PARTICLES

## 7.1 Introduction

'Smart' materials, which can dramatically alter their physico-chemical makeup in response to an external signal, abound in nature. Examples include, but are not limited to self cleaning lotus leaves,[1] geckos that attach to a variety of surfaces,[2] anti-reflective coatings in the corneas of moths and butterflies,[3, 4] and ion channels in cells[5] that open and close in response to concentration gradients in their surrounding media.[6] Taking a cue from nature, several stimuli-responsive smart materials have been synthesized towards improved devices for controlled drug release,[7, 8] self healing coatings,[9] actuators,[10] and several other micro/nano structures that change in their environment in a controlled manner.[11] These materials include polymeric core –shell hybrid particles,[12] layer-by layer films,[13] block copolymers,[14] emulsions, micelles[14] and self assembled monolayers[15] that respond to a variety of stimuli such as temperature,[16] light,[17] and electric fields.[15] Most of these structures exploit the change in properties of the constituting polymer. For applications in tunable catalysis, sensors, and materials with reconfigurable designs,[11] particles that respond to multiple stimuli to produce changes in size, shape, and orientation can be envisioned. An important requirement for this would be the controlled

spatial distribution of materials, which differ drastically from one another into a single, cohesive unit to enable response to different stimuli in a sequential manner. In this chapter, this compositional anisotropy is achieved via incorporation of different materials into individual halves of bicompartmental particles. Specifically, we created particles with PLGA 8515, a hydrophobic polymer in one compartment, and poly(ethyleneimine) (or PEI), a pH responsive polycationic hydrogel in the other compartment via electrohydrodynamic co-jetting. The pH responsivity of PEI, the biodegradability of PLGA, and the ability to tailor their spatial distribution through co-jetting opens doors for several exciting applications in therapeutics and diagnostics.

## 7.2 Methods

### 7.2.1 Materials

PLGA 85:15 ($M_w$ 50-75,000 g/mol), MEHPPV, branched poly(ethyleneimine )($M_w$ = 750,000 g/mol, $M_n$ = 60,000 g/mol and $M_w$ 25000 g/mol), chloroform, DMF, PBS, sodium acetate, sodium carbonate, sodium bicarbonate and Tween-20 were purchased from Sigma-Aldrich, USA. ADS 306PT, a polythiophene macromolecular dye was purchased from American Dye Source, Canada. Dithiobis (succinimidyl propionate) (DSP) was purchased from Pierce pharmaceuticals, USA. Titanium dioxide ($TiO_2$) was purchased from Tronox, USA and carbon black pigment was purchased from General Carbon Company, USA.

### 7.2.2 Electrohydrodynamic co-jetting and particle characterization

The protocol followed for electrohydrodynamic co-jetting to produce bicompartmental particles as well as SEM and CLSM is described in chapters 2 and 3. In case of uncrosslinked particles, CLSM was performed by mounting glass coverslips coated with particles in microscope immersion oil.

### 7.2.3 Particle swelling studies

Swelling studies were carried out by suspending particles harvested from the aluminum foil after jetting in the appropriate buffer system via ultrasonication for 5 s, followed by incubation for the required amount of time under gentle agitation in a rotating microtube mixer (Labquake, USA). The buffers employed were 0.1M PBS (pH 7), 0.1M sodium acetate/acetic acid (pH 4.02), and 0.1M sodium bicarbonate/sodium carbonate (pH 10), each containing 2 vol. % Tween-20.

### 7.2.4 Zeta potential measurements

Zeta potential measurements on particles were performed using a Malvern Zetasizer Nano-ZS (Malvern Instruments, UK). Values reported are a mean of five measurements. Particle concentration used for measurements was 0.1 mg/ml in HPLC grade water, pH = 6.98 containing 2% tween-20.

### 7.2.5 FTIR spectroscopy

0.1 mg/ml solutions of different combinations of polymers with or without crosslinking were spin-coated on silica substrates coated with gold. FTIR spectroscopy was performed on a Nicolet 6700 spectrometer utilizing the grazing

angle accessory (Smart SAGA) at a grazing angle of 85$^{o}$. Data acquisition and analysis were performed using OMNIC software.

### 7.3 Results and discussion

In electrohydrodynamic co-jetting, an electrical potential is applied to two (or more) solutions that are pumped through a dual-capillary needle system under a laminar flow regime. In response to the electric field, the compound droplet that is generated at the tip of the capillary needle assembly distorts into a Taylor cone. An electrified jet containing millions of secondary droplets ensues from the tip of this Taylor cone, and the consequent increase in surface: volume ratio of the secondary droplets over several orders of magnitude results in rapid solvent evaporation and particle formation. This phenomenon, that can result in particles or fibers[18] is quite well documented for aqueous[19, 20] as well as organic solutions,[21, 22] as described in chapters 2, 3 and 4.

In order to fabricate anisotropic particles with tunable compartment sizes, it is crucial to incorporate polymers with different swelling characteristics in each of the jetting solutions. The experimental design for formulation of PEI/PLGA particles is shown in Figure 7.1. Here, one on the jetting solutions (shown in red) is comprised of PLGA only, whereas the other (shown in blue) consists of a mixture of PLGA and branched PEI. In addition, red and blue fluorophores, ADS306 and MEHPPV are added in trace amounts to the PLGA and PLGA/PEI solutions respectively to facilitate distinction between compartments via CLSM.

As an initial feasibility study, we conducted co-jetting experiments wherein a 7:100 w/w ratio of PLGA in 97:3 Chloroform: DMF (by vol.) constituted one of the jetting solutions, and the other jetting solutions contained a 7:100 w/w solution of a 50:100 w/w mixture of PLGA and PEI (Mw = 25,000 g/mol), also in 97:3 Chloroform: DMF by vol. A flow rate of 0.37 ml/h was employed. Application of electrical potential (5.7 kV) resulted in Taylor cone formation, ejection of an electrified jet containing secondary droplets, and particle formation via solvent evaporation. The Taylor cone as well as the jet were quite stable and could be sustained for several hours (~5h). The particles obtained are shown in Figure 7.2 a-c. CLSM micrographs (Figure 7.2a) show excellent compartmentalization of MEHPPV and ADS306PT fluorophores, indicative of a well-defined anisotropy in the bulk of all particles. In addition, SEM images are reflective of spherical particle morphology, and a broad particle size distribution ranging from 2 to 7 µm.

Once the ability to selectively incorporate PEI in one compartment was established, we focused our attention towards particle stabilization. In all previous electrohydrodynamic co-jetting experiments involving hydrogels, the particles formed are thermally crosslinked after the co-jetting process,[23-25] which constitutes an extra step towards particle synthesis. *In situ* incorporation of crosslinking agents in the jetting solutions constitutes an attractive strategy for almost instantaneous particle fabrication without introducing any changes in the experimental setup[26, 27] or post synthesis modifications.[28, 29] While *in situ* crosslinking during electrospinning has been employed previously for fabrication of polyvinyl alcohol nanofibers,[30] we report, for the first time, reactive

electrohydrodynamic co-jetting and anisotropic crosslinking from organic polymer solutions. We employed DSP, a homobifunctional molecule that reacts with the amine groups of the PEI to form amide bonds. DSP was added in a 0.1:1 mass ratio w.r.t PEI (Mw = 750,000 g/mol). Addition of DSP to the jetting solution produced an immediate turbidity in the jetting solution, presumably due to the beginning of crosslinking process. This did not, however, affect the stability of the jet for the duration of the experiment (~ 2h). Longer experiment times resulted in droplets of higher viscosities owing to crosslinking of the jetting solution in the syringe, resulting in flat, donut shaped particles, and even beaded fibers and fibers[21]. The longest time for which jetting could be sustained is a function of flow rate, polymer concentration, and amounts of PEI and DSP in the jetting solution. Since the amount of PEI in one half is essential for selective swelling, we systematically investigated particles from solutions with increasing amounts of PEI to determine an optimal loading. Figure 7.3 shows SEM images of particles formed from solutions containing increasing loadings of PEI in one compartment for a fixed amount of DSP (0.1:1 w/w DSP:PEI). All other jetting solution and process and solution parameters were kept constant. The amount of irregular particles showed an upward trend after when the PEI: PLGA ratio was increased beyond 1.5:1. When one compartment comprised of PEI only, beaded fibers and fibers were observed (Figure 7.3e). Apart from higher viscosities resulting from addition of higher amounts of PEI, increasing conductivity of the PEI solution could potentially be another deterrent to a stable jet. This is supported by the fact that particles in Figure 7.3e are smaller in diameter.[31]

Thus, a 1:1 PEI: PLGA ratio was determined to be optimal from the point of view of achieving a stable jet.

Once the ideal PEI loading was determined, we proceeded to analyze particle swelling. PEI contains primary amine groups that are protonated in acidic conditions. Hence, the density of similarly charged groups within the network strongly increases inducing a phase transition due to electrostatic repulsion. In an alkaline environment the gel deprotonates, resulting in a decrease of osmotic swelling pressure within the hydrogel, leading to shrinking.[32, 33] This is schematically depicted in Figure 7.4a. Particles at a neutral pH of 6.80 are shown in Figure 7.4c. Upon incubating the particles for 1.25h in pH 4.0 buffer, there is a clear increase in the size of the PEI compartment (Figure 7.4a), whereas on increasing the pH to 10.0, PEI shrinking is clearly discernible (Figure 7.4d), especially from the DIC micrographs. The hydrogel phase transition is visible despite the presence of the relatively hydrophobic PLGA comprising half of the compartment mass. Taken together, these results indicate relatively uniform crosslinking during the electrohydrodynamic co-jetting process. The extent of swelling was found to increase with time, as shown in Figure 7.5. Compared to 1.25h (Figure 7.5a), the size of the PEI compartment showed a marked increase at 48h (Figure 7.5b), at pH 4.02. The crosslinking of PEI was also analyzed via FTIR (Figure 7.6). Four polymer films were analyzed (i) PLGA only, (ii) PEI only, (iii) 1:1 PLGA:PEI w/w, and finally (iv) 0.1:1:1 DSP:PLGA:PEI w/w. The DSP containing solution showed a distinct amide (I) stretch at 1669.57 $cm^{-1}$, indicative of a monosubstituted amide. This band was not observed in any of the control

samples, conclusively proving the crosslinking reaction. Being a polycation, PEI also influences the zeta potential of the particles. Electrophoretic mobility measurements (Figure 7.7) revealed that the zeta potential of bicompartmental particles containing PEI in one compartment increases to 11.8mV from -19.1mV for monocompartmental PLGA particles at pH 6.80. While the (unswollen) particle diameter of the PEI/PLGA particles ranges from 2-7µm, smaller diameter particles (diameter range 3-5 µm) were employed for zeta potential measurements.

Several factors influence the swelling of PEI: molecular weight of the PEI, PEI loading, degree of crosslinking, particle crosslinking time, pH and swelling time. These parameters can be tuned independently or in a combined manner to produce particles with precisely defined swelling ratios, swelling times and internal architectures. We compared the effect of degree of crosslinking of PEI for a given molecular weight of PEI (750 kD), pH (7.0) and PEI loading (1:1 PEI: PLGA by wt. in one compartment). The degree of crosslinking can be controlled by varying the amount of DSP added to the jetting solution. Two particle populations were prepared: one with 0.1:1 DSP: PEI mass ratio (Figure 7.8 a-f), and one without DSP (Figure 7.8 g-l), and incubated in pH 7 buffer for different times. Particles containing DSP started to swell after 8h, and at 48h, exhibited a clear increase in the size of the PEI compartment relative to the PLGA compartment. On the other hand, particles without DSP started to swell at 0h and reached peak swelling at 8h. It is noteworthy that while swelling in crosslinked particles is due to penetration of water into the crosslinked hydrogel matrix,

swelling in uncrosslinked particles is indicative of the start of polymer dissolution. This is clearly seen at 8h, after which the PEI compartment starts to decrease in size (Figure 7.8i). After 48h, crescent shaped particles were observed (Figure 7.8l). Thus, control of crosslinking density can serve as a method to control the relative volume of compartments over time. Similar effects can also be observed by controlling the molecular weight of the PEI, as shown in Figure 7.9.

Another factor that influences particle swelling is the crosslinking time. While particle crosslinking begins in situ during electrohydrodynamic co-jetting, the time of the jetting process itself is relatively short (~2h), and it is highly likely that crosslinking would continue even after solvent evaporation in solid state,[34] albeit at a reduced rate. This is shown in Figure 7.10. Particles containing 0.075:1 wt ratio of DSP: PEI and 1:1 wt. ratio of PEI:PLGA were first synthesized. We defined 'T' as crosslinking time, i.e. the time elapsed between the start of jetting and beginning of swelling studies, and 't' as swelling time, i.e. time of incubation in the buffer. Particles with T=2h and t=6h, and T=15h and t=12h are shown in Figures 7.10a and b respectively. Particles with a shorter T exhibit a relatively higher degree of swelling of PEI due to a lower degree of completion of crosslinking. Thus, in order to precisely control the swelling rate for potential release of therapeutic payloads, it is important to investigate the time of completion of the reaction. Towards this end, we performed FTIR spectroscopy on drop cast polymer films with the same DSP:PEI:PLGA ratio as in particles, at regular time intervals. As shown in Figure 7.11, the intensity of the carbonyl stretch from DSP at 1755 $cm^{-1}$ decreases and the amide (I) stretch at 1651$cm^{-1}$

increases with increasing time, indicating the progress of the crosslinking reaction. The intensity of the peaks seems to plateau at ~72h, implying complete consumption of all the carbonyl groups in DSP. These times are obtained from flat films of polymer blends, however, in case of particles, the rate of crosslinking maybe faster owing to higher surface areas.

A distinctive advantage of selective swelling is the ability to achieve optical color changes. If an optical pigment is incorporated in the PEI compartment, the color effects of the pigment can be amplified by swelling of PEI. Combined with a different color in the other compartment, the suspension can be made to switch between colors by change of pH. This can be considered analogous to the appearance of a fish melanophore that appears dark when melanosomes are spread throughout the cell, and light when they are concentrated at the center.[35, 36] Towards this end, we incorporated white and black optical pigments, $TiO_2$ and carbon black respectively into PEI and PLGA compartments. All other jetting solution and process parameters were kept the same. When pH of the suspension was reduced to 4, the suspension appeared a lighter shade of grey due to the amplification of intensity of $TiO_2$ (Figure 7.12). On the other hand, due to shrinking of the hydrogel, the color of the suspension was a darker shade of grey. However, $TiO_2$, being superhydrophilic was found to constantly release from the particles. Surface modification of $TiO_2$ to reduce superhydrophilicity, or covalent coupling of a visible dye to the PEI backbone could be pursued in the future in order to observe greater color differences.

## 7.4 Conclusions

While previous chapters explored control over particle size, particle shape, number of compartments and selective surface modification, in this chapter, control over a new parameter; particle size between compartments was demonstrated via unique particles synthesized via electrohydrodynamic co-jetting of a pH responsive hydrogel (PEI) and a hydrophobic biodegradable polymer, PLGA8515. Crosslinking of PEI was performed in situ during co-jetting via addition of DSP, and the different variables affecting swelling, such as time, degree of crosslinking, pH and molecular weight of PEI were investigated systematically. Depending on the degree of crosslinking of the PEI compartment, it could be swollen or dissolved, both instances giving rise to unique particle geometries. PEI was shown to act as a synthetic melanocyte substitute through its ability to transport $TiO_2$ via swelling, changing the color of a suspension in the process. These particles have applications in siRNA delivery, biomimetic materials, diagnostic assays and as amphiphilic materials for self assembly.

.

## 7.5 Figures and tables

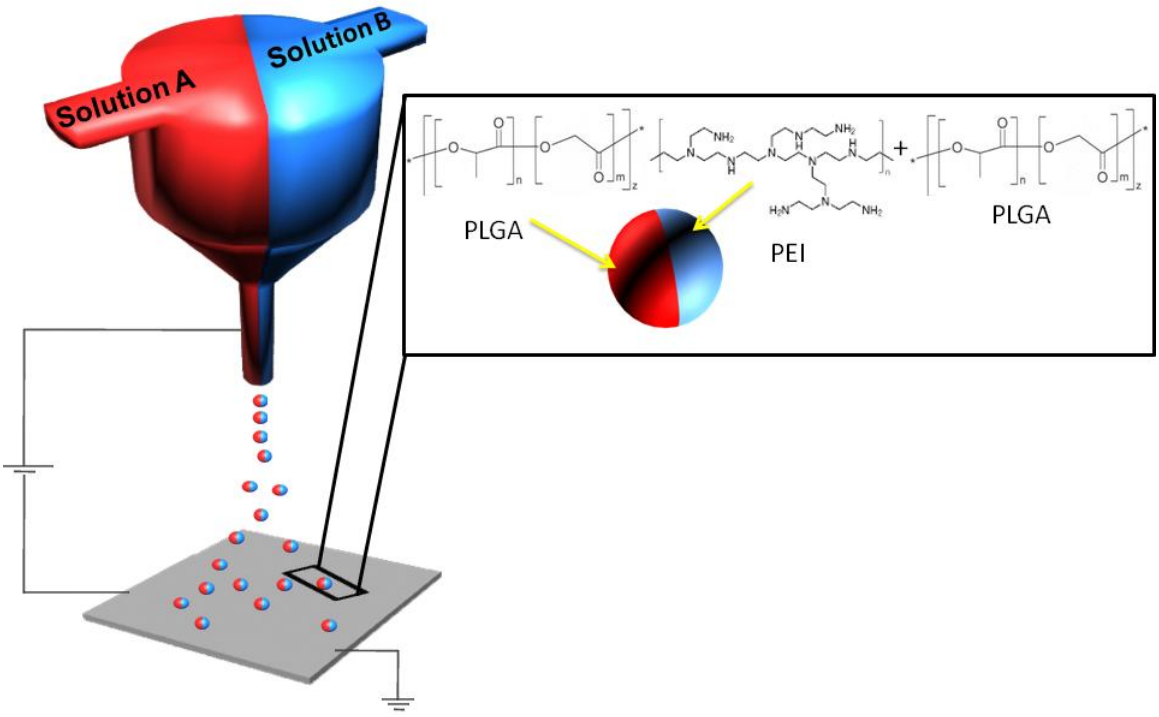


**Figure 7.1** Schematic showing the design of selectively swellable bicompartmental particles containing PEI and PLGA in one compartment and PLGA only in the other compartment.

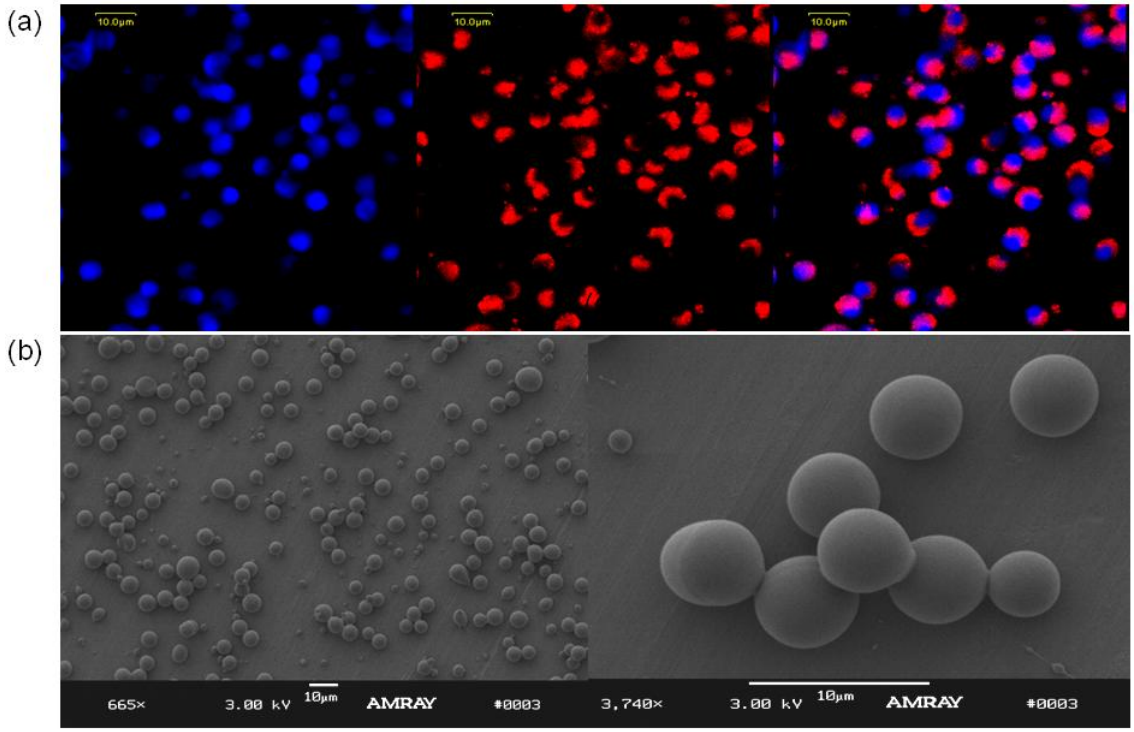


**Figure 7.2** Bicompartmental particles containing PLGA in one compartment and PEI/PLGA in the other compartment. (a) CLSM images of particles. Blue and red fluorescence images from MEHPPV and ADS306PT are shown, followed by the overlay. The blue compartment carries PEI (Mw 25kD). (b), (c) Low and high resolution SEM images of corresponding particles. All scale bars represent 10 µm.

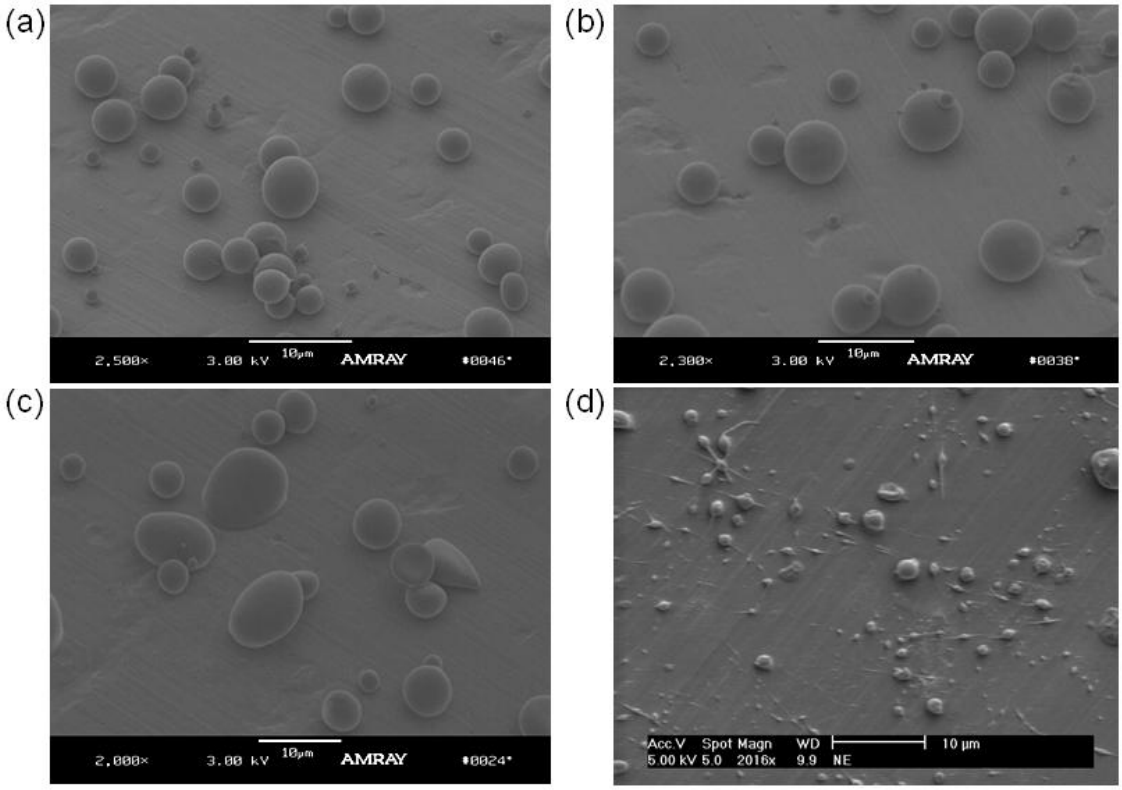


**Figure 7.3** SEM images of bicompartmental particles with PLGA in one compartment and increasing PEI: PLGA mass ratio in the other compartment. (a) 0.75:1 (b) 1:1 (c) 1.5:1 (d)1:0.

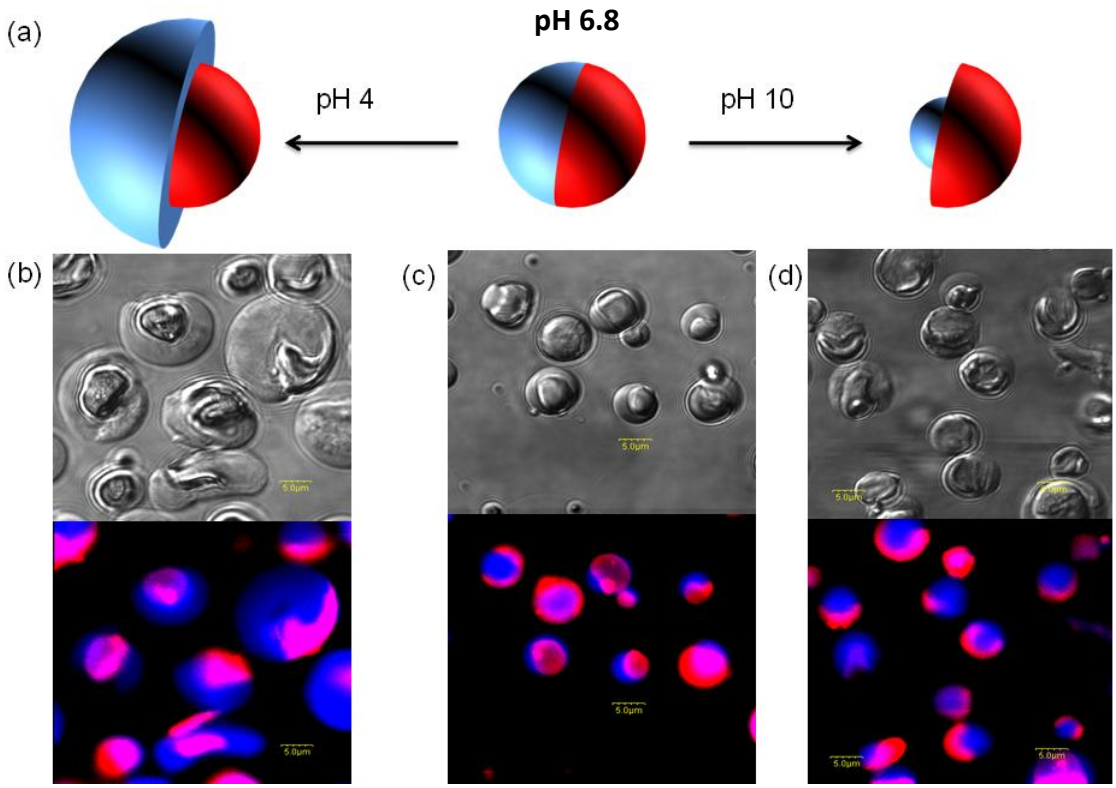


**Figure 7.4** pH sensitive anisotropic swelling of bicompartmental PEI/PLGA particles. (a) Scheme depicting pH dependent size change of the PEI compartment. PEI swells under an acidic pH due to the electrostatic repulsion generated by protonation of primary amine groups. At higher pH values, the net ion concentration difference is reduced, leading to deswelling of the hydrogel. (b), (c), (d) DIC and corresponding CLSM images particles at pH 4, 6.80 and 10.0 respectively, showing swelling and shrinking of the PEI (blue) compartment. All scale bars represent 5 µm.

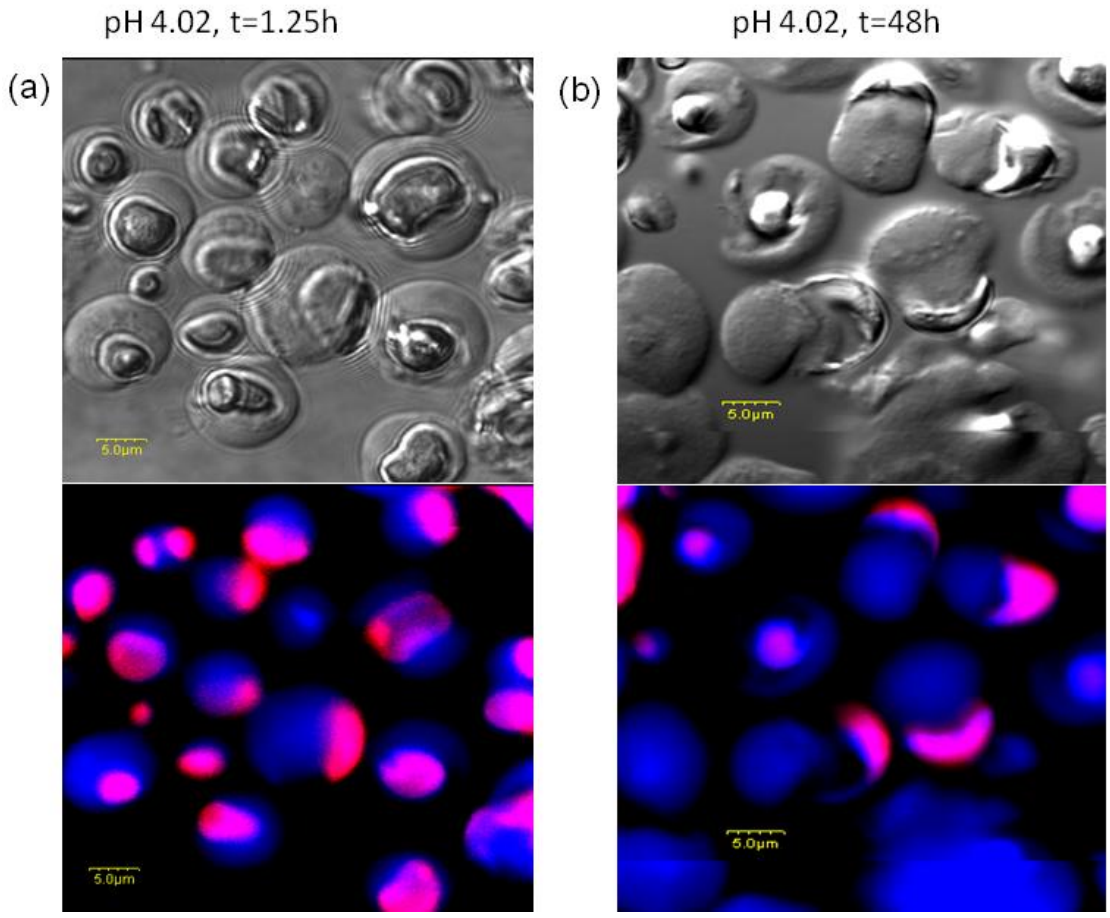


**Figure 7.5** Dependence of time on particle swelling.DIC and corresponding CLSM images of bicompartmental PEI/PLGA particles incubated in acetic acid/sodium acetate buffer are shown for (a) 1.25h and (b) 48h. There is a marked increase in the size of the PEI compartment between these two times.

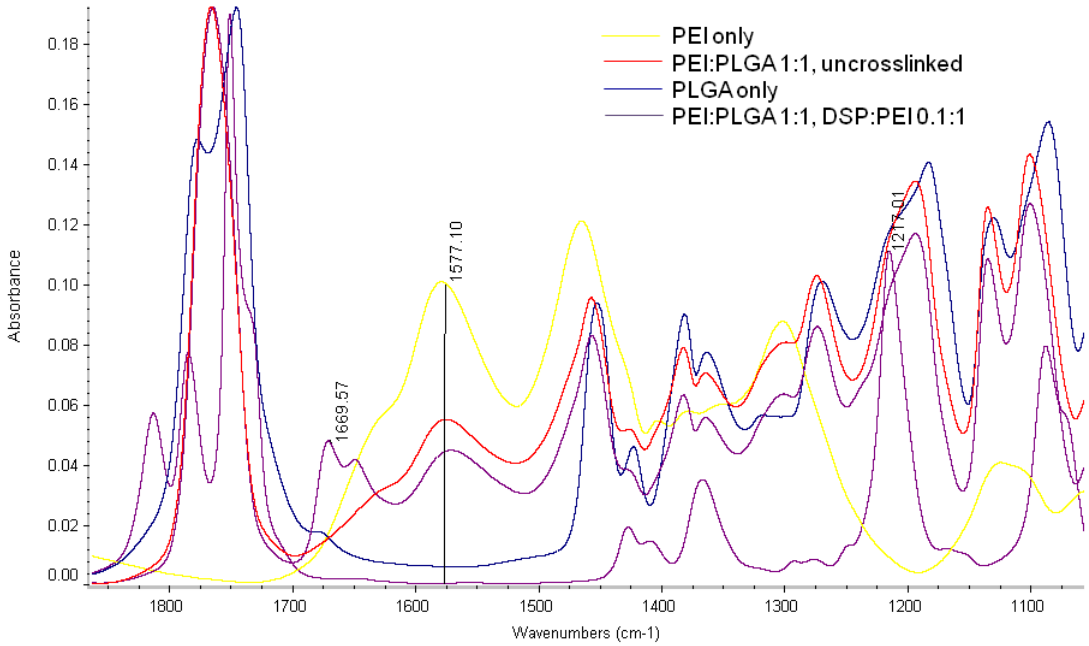


**Figure 7.6** FTIR analysis of crosslinking of PEI using DSP.

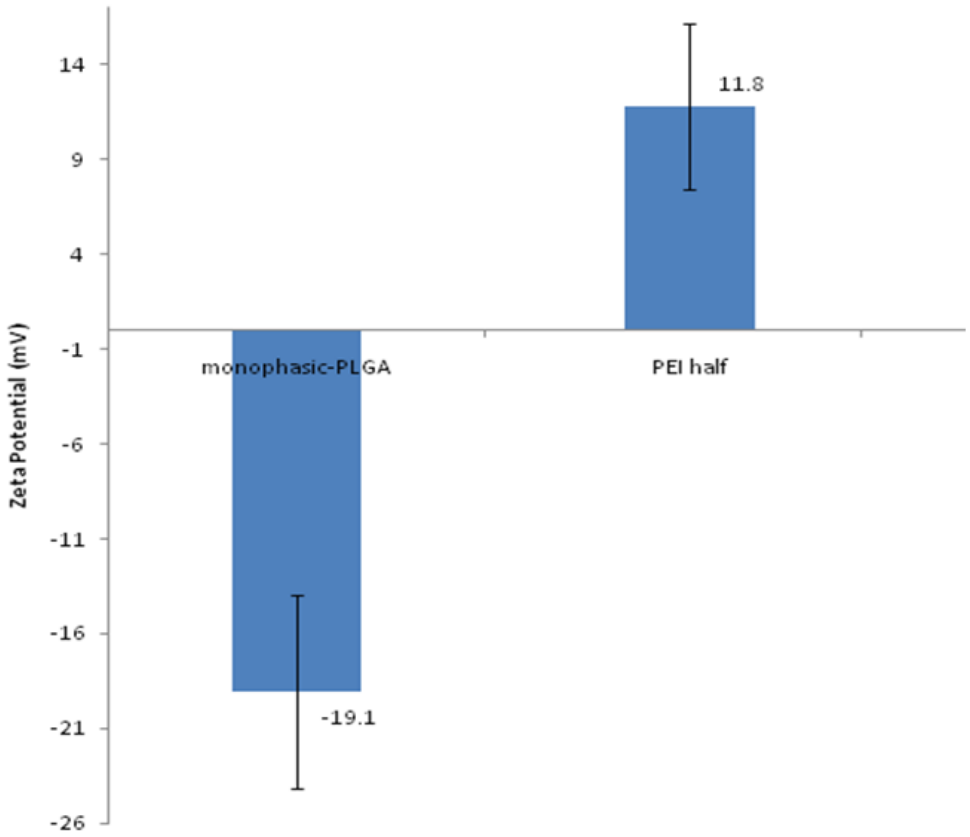


**Figure 7.7** Zeta potential measurements of monophasic PLGA particles and PEI/PLGA particles. Particles with diameters in the range of 2-5 µm were fabricated to facilitate electrophoretic mobility measurements. Particles containing PEI in one compartment show a significant increase in Zeta potential compared to the control.

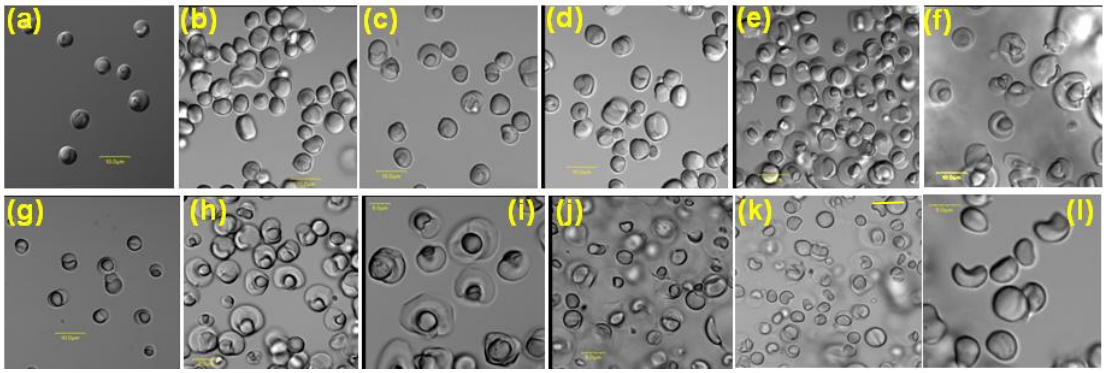


**Figure 7.8** Effect of degree of crosslinking of PEI on particle swelling over time at a given molecular weight of PEI and pH. (a)-(f) represent DIC images of bicompartmental particles comprising of 100:100 PLGA:PEI (Mw 750kD) in one compartment with a corresponding DSP:PEI mass ratio of 0.1:1, suspended in PBS, pH 7 at 0h, 5h, 8h, 15h, 25h, and 48 h respectively. On the other hand, (g)-(l) represent particles with exactly same composition but devoid of the crosslinker. Crosslinked particles retain their architecture even at 48h, at which point uncrosslinked particles lose their structural integrity owing of the dissolution of PEI into the aqueous buffer. Scale bars for (a)-(g) and (k) are 10 µm, rest 5 µm.

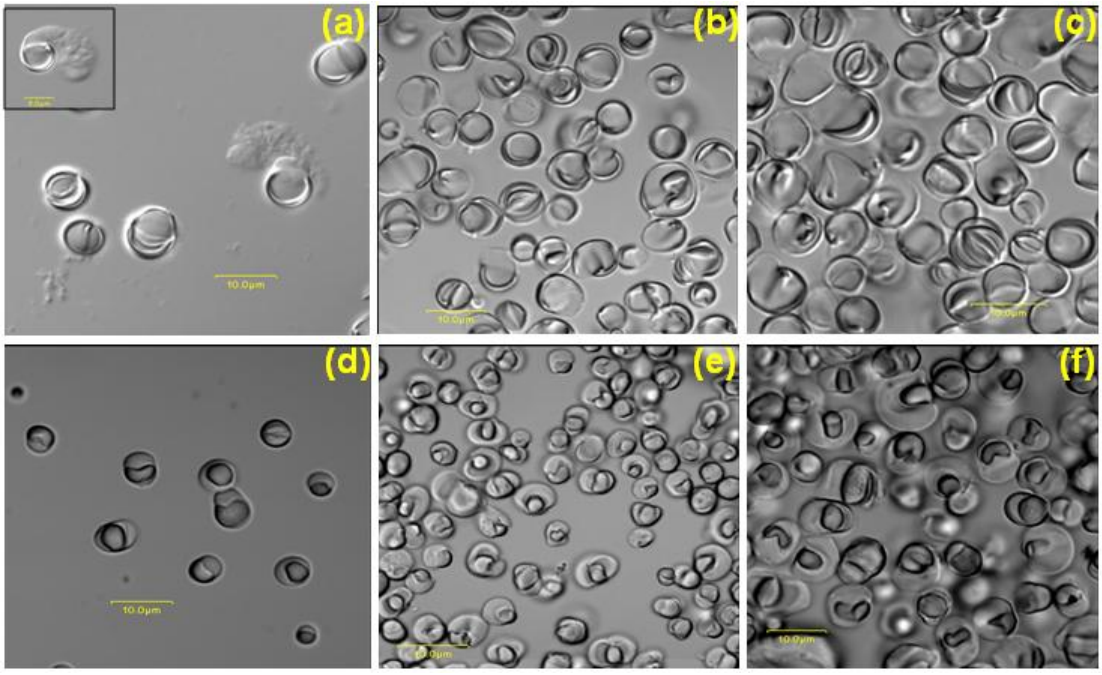


**Figure 7.9** Effect of molecular weight of PEI on particle swelling at a given degree of crosslinking and pH. (a)-(c) represent DIC images of bicompartmental particles comprising of 100:100 PLGA:PEI (Mw 25kD) in one compartment with a corresponding DSP:PEI ratio of 0:1 (no crosslinking), suspended in phosphate buffer of pH 7 at 0h, 4h, and 8h respectively and, (d)-(f) represent particles with exactly same composition but comprising of PEI of Mw 750 kD. In particles containing PEI of a lower molecular weight, the PEI does not swell but starts to dissolve out instantaneously, as seen in (a) and also the inset. On the other hand, particles containing higher molecular weight PEI start to swell, and retain their shape (with increased volume of the PEI compartment) at 8h, before finally dissolving at ~15h (as seen previously in Figure 5). Thus, control over molecular weight and the degree of crosslinking can be used to vary swelling rate, and correspondingly the release rate of an encapsulated payload. All scale bars denote 10 µm (scale bar for inset for (a) is 5 µm).

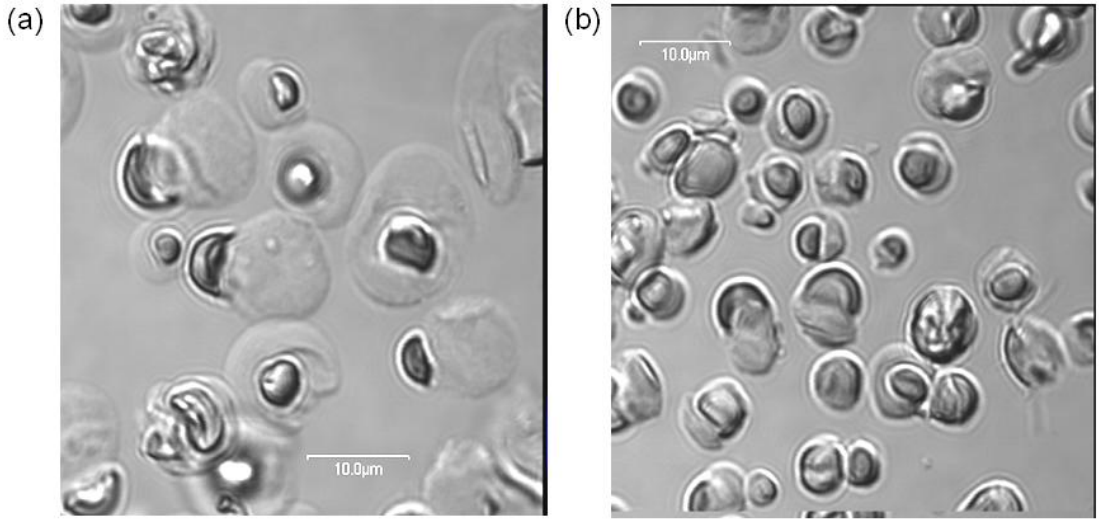


**Figure 7.10** Effect of crosslinking time on swelling of PLGA/PEI particles. Both particles contain 1:1 w/w PEI: PLGA in one compartment, with a DSP: PEI wt. ratio of 0.075:1 and incubated in a pH 4 buffer (a) DIC image of particles with T= 2h and t=6h (b) T= 15h and t=12h, where T = crosslinking time and t = swelling time.

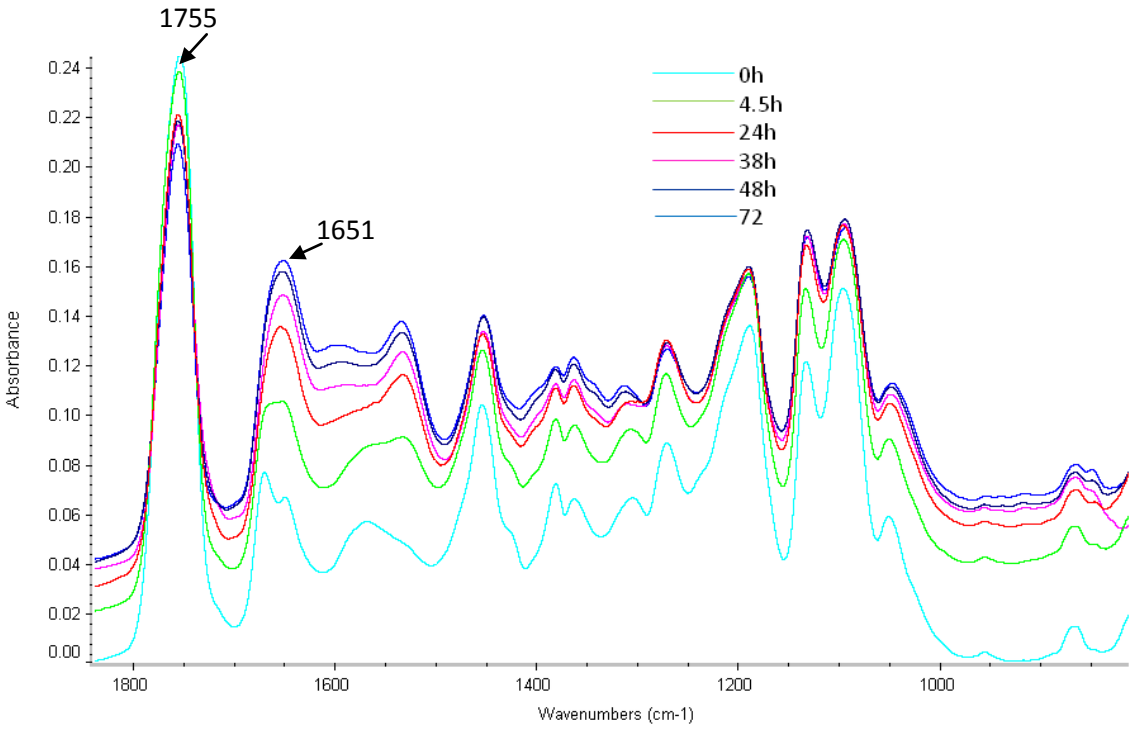


**Figure 7.11** FTIR analysis of kinetics of crosslinking of PEI via DSP. Drop cast films with 0.075:1:1 wt. ratio of DSP: PEI: PLGA were analyzed at regular intervals. With increasing time, the intensity of the carbonyl stretch at 1755 $cm^{-1}$ decreases and that of the amide stretch at 1651 $cm^{-1}$ increases. Both peaks appear to plateau at 72h, signaling complete consumption of carbonyl groups of DSP.

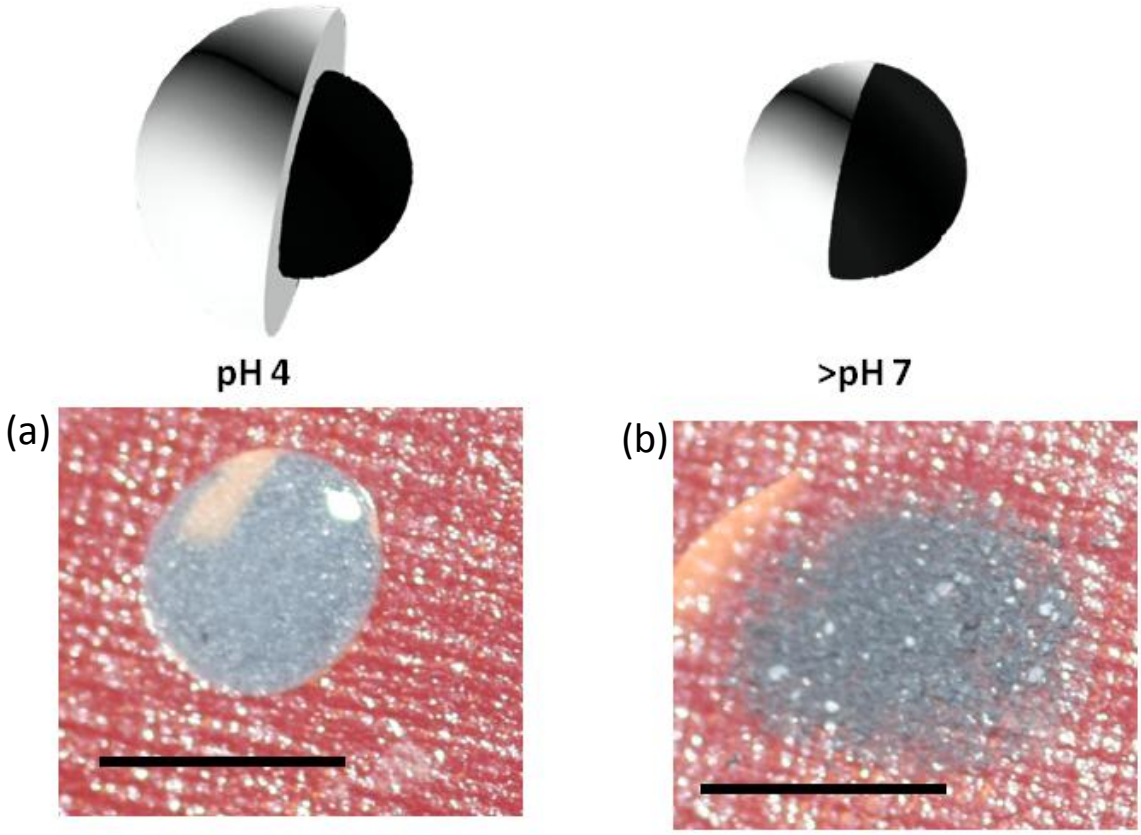


**Figure 7.12** Digital photographs of particle suspensions showing pH responsive color effects in anisotropic PEI/PLGA particles. Bicompartmental particles were fabricated by incorporating PEI, PLGA, DSP and $TiO_2$ in one compartment, and PLGA and CB in the other compartment. Upon changing the pH to 4, the swelling of PEI causes the particle suspension to appear significantly lighter (a) than at neutral pH (b). A schematic of the expected particle architecture is indicated above each photograph, and the scale bar for both images is 0.5 cm.

## 7.6 References


[1] Y. Liu, J. Tang, R. Wang, H. Lu, L. Li, Y. Kong, K. Qi, J. H. Xin., *J. Mater. Chem.* **2007**, *17*, 1071.
[2] H. Lee, B. P. Lee, P. B. Messersmith, *Nature* **2007**, *448*, 338.
[3] W. H. Miller, A. R. Moller, C. G. Bernhard, "*The Functional Organisation of the Compound Eye"*, Pergamon Press, Oxford, 1966.
[4] A. R. Parker, H. E. Townley, *Nat Nanotech* **2007**, *2*, 347.
[5] H. Bayley, P. S. Cremer, *Nature* **2001**, *413*, 226.
[6] F. Xia, L. Jiang, *Adv Mater* **2008**, *20*, 2842.
[7] S. J. Jhaveri, *et al Biomacromolecules* **2009**, *10*, 174.
[8] A. S. Hoffman, *J. Cont. Rel.* **2008**, *132*, 153.
[9] A. Misra, W. L. Jarrett, M. W. Urban, *Macromolecules* **2007**, *40*, 6190.
[10] Z. S. Liu, P. Calvert, *Adv. Mater.* **2000**, *12*, 288.
[11] M. A. C. Stuart, W. T. S. Huck, J. Genzer, M. Müller, C. Ober, M. Stamm, G. B. Sukhorukov, I. Szleifer, V. V. Tsukruk, M. Urban, F. Winnik, S. Zauscher, I. Luzinov, S. Minko, *Nat Mater* **2010**, *9*, 101.
[12] Y. Lu, Y. Mei, M. Drechsler, M. Ballauff, *Angew Chem Int Ed* **2006**, *45*, 813.
[13] V. Kozlovskaya, *et al Chem. Mater* **2008**, *20*, 7474.
[14] D. E. Discher, *et al Prog. Polym. Sci.* **2007**, *32*, 838.
[15] J. Lahann, S. Mitragotri, T.-N. Tran, H. Kaido, J. Sundaram, I. S. Choi, S. Hoffer, G. A. Somorjai, R. Langer, *Science (Washington, DC, United States)* **2003**, *299*, 371.
[16] C. A. Kavanagh, Y. A. Rochev, W. M. Gallagher, K. A. Dawson, A. K. Keenan, *Section Title: Pharmaceuticals* **2004**, *102*, 1.
[17] J. Y. Shin, N. L. Abbott, *Langmuir* **1999**, *15*, 4404.
[18] S. Bhaskar, J. Lahann, *J. Am. Chem. Soc.* **2009**, *131*, 6650.
[19] K. H. Roh, D. C. Martin, J. Lahann, *Nat. Mater.* **2005**, *4*, 759.
[20] K. H. Roh, D. C. Martin, J. Lahann, *J. Am. Chem. Soc.* **2006**, *128*, 6796.
[21] S. Bhaskar, K. M. Pollock, M. Yoshida, J. Lahann, *Small* **2010**, *6*, 404.
[22] S. Bhaskar, K. H. Roh, X. Jiang, G. L. Baker, J. Lahann, *Macromol. Rapid Commun.* **2008**, *29*, 1655.
[23] K. H. Roh, M. Yoshida, J. Lahann, *Langmuir* **2007**, *23*, 5683.
[24] M. Yoshida, K. H. Roh, J. Lahann, *Biomaterials* **2007**, *28*, 2446.
[25] M. Yoshida, K.-H. Roh, S. Mandal, S. Bhaskar, D. Lim, H. Nandivada, X. Deng, J. Lahann, *Adv Mater* **2009**, *21*, 4920.
[26] P. Gupta, S. R. Trenor, T. E. Long, G. L. Wilkes, *Macromolecules* **2004**, *37*, 9211.
[27] S. Kim, S. H. Kim, S. Nair, E. Moore, *Macromolecules* **2005**, *38*.
[28] Y. Ji, K. Ghosh, B. Li, J. C. Sokolov, R. A. F. Clark, M. H. Rafailovich, *Macromol. Biosci.* **2006**, *6*, 811.
[29] H. Liu, M. Zhen, R. Wu, *Macromol. Chem. Phys.* **2007**, *208*, 874.
[30] C. Tang, C. D. Saquing, J. R. Harding, S. A. Khan, *Macromolecules* **2010**, *43*, 630.
[31] C. Berkland, D. W. Pack, K. Kim, *Biomaterials* **2004**, *25*, 5649.

[32] A. Richter, G. Paschew, S. Klatt, J. Lienig, K. F. Arndt, H. J. P. Adler, *Sensors* **2008**, *8*, 561.
[33] S. V. Vinogradov, T. K. Bronich, A. V. Kabanov, *Adv. Drug. Del. Rev.* **2002**, *54*, 135.
[34] L. Yang, C. F. C. Fitie, K. O. van der Werf, M. L. Bennink, P. J. Dijkstra, J. Feijen, *Biomaterials* **2008**, *29*, 955.
[35] M. Wallin, *Biosci. Explained* **2002**, *1*, 1.
[36] M. Yoshida, J. Lahann, *ACS Nano* **2008**, *2*, 1101.

# CHAPTER 8

# TOWARDS ANISOTROPIC PARTICLE ASSEMBLIES

This chapter has been adapted from the following published article (with additional modifications):

1. Bhaskar, S., Gibson, C. T., Yoshida, M., Nandivada, H., Deng, X., Voelcker, N. H, Lahann, J., 'Engineering, characterization and directional self-assembly of anisotropically modified nanocolloids', Small **2011**, in press.

## 8.1 Introduction

Nano- and microparticles are the fundamental design elements in a variety of research areas, such as diagnostics, therapeutics or photonic crystals. Recent progress in particle engineering has continuously increased versatility and tunability in these applications.[1, 2] While a variety of techniques have been developed to precisely engineer nano- and microparticles with respect to shape, size, surface chemistry and mechanical properties,[3] control over anisotropic bulk and surface architectures are emerging as additional design parameters.[3, 4] Anisotropic particles may enable complex hierarchical assemblies needed for a

diverse array of applications such as photonic band gap materials,[5, 6] multiplexed bioassays,[7] vehicles for multiple therapeutic modalities,[8] biological sensors, biohybrid materials[9, 10] and miniaturized energy storage and conversion devices.[11] Synthetic processes[4, 6, 12-15] for anisotropic particles include lithographic techniques,[16] seeded polymerization[17] and self-assembly.[18] We have previously used electrohydrodynamic co-jetting for the fabrication of anisotropic particles.[19] In its simplest form, this process involves co-processing of two polymer solutions through a side-by-side dual capillary needle system under a laminar flow regime. Application of an electric field to the compound droplet generated at the tip of the capillary needles results in the distortion of the droplet into a Taylor cone and formation of an electrified jet, from which bicompartmental particles are generated. This process was first demonstrated from aqueous solutions of poly(acrylic acid-*co*-acrylamide) polymers.[19-21] In chapter 2, we extended this process to include particles and fibers comprised of apolar and biodegradable polymers, namely PLGA polymers, where, organic solvents are used during electrohydrodynamic co-jetting.[22-24] In chapter 3, systematic variation of jetting solution and process parameters allowed for control over shape and size.[25] In this chapter, we report on the selective surface modification of novel bi-, tri- and tetracompartmental particles for directed self-assembly in suspension as well on patterned substrates.

## 8.2 Methods

### 8.2.1 Confocal Raman Spectromicroscopy (CRS)

Electrohydrodynamic co-jetting of bi- and tetracompartmental particles, and their characterization via SEM and CLSM was carried out according to procedures described in chapters 2 and 3. Raman spectra and images were collected with a WiTEC alpha300R microscope in confocal imaging Raman mode using 40x (Numerical Aperture 0.6) objective with a 532 nm Nd-YAG green laser (2.33 eV) operating at constant power for each experiment up to a possible maximum of approximately 60 mW. The sample surface was held perpendicular to the excitation source. Spectral images were acquired using an integration time of 0.5 seconds per pixel with each image composed of 100 x 100 pixels. Each pixel corresponds to a separate Raman spectrum allowing thousands of spectra to be acquired during an image scan. Raman data was collected by the WiTEC Control software and analyzed in the WiTEC Project software.

### 8.2.2 Selective Surface Functionalization of Particles

Bicompartmental particles containing acetylene groups in one compartment only were harvested from the aluminum substrate and suspended in DI water containing 0.01vol. % Tween-20. To 20 ml of a 0.5 mg/ml suspension, 1.4 ml of 1 mg/ml solution of azide-PEO-biotin was added, followed by aqueous CuSO4*5H2O solution (0.2ml, 0.1M). Finally, sodium ascorbate (0.2 ml, 1M) solution was added, and the reaction was allowed to occur under magnetic stirring for 15 h at room temperature. In case of tetracompartmental particles, the amounts of all reagents were scaled by a factor of half. Particles were then

washed by addition of 20 ml DI water (containing 2 vol % Tween-20), vortexing, centrifugation and aspiration of the supernatant. This process was repeated 10-12 times. Particles were then resuspended in PBS buffer (pH 7.4) consisting of 0.1% (w/v) BSA and 0.02% (v/v) Tween-20.

### 8.2.3 Assembly of Particles on CVD Substrates

A conformal coating of poly(4-heptadecafluorononanoyl-p-xylylene-co-p-xylylene) was deposited on a ~3cm x 3cm silica substrates via CVD polymerization of 4-heptadecafluorononanoyl[2, 2]-paracyclophane.[26] This was followed by immobilization of biotin hydrazide via microcontact printing wherein poly(dimethylsiloxane) (PDMS) stamp consisting of square-shaped indentations (400 µm on a side) with 50 µm gaps between the square edges.[27] The patterned substrate was incubated for 2 h with streptavidin or Alexa Fluor 633-labeled streptavidin in PBS buffer (pH 7.4) containing BSA (0.1% w/v) and Tween-20 (0.02 vol.%). The substrate was washed three times with the incubating buffer and rinsed with DI-water. These substrates were then incubated with ~100 µl of an 8 mg/ml suspension of selectively biotinylated bicompartmental particles in PBS (containing 2% FBS and 1% Tween-20) for two hours, followed by gentle rinsing with 2% tween-20 in DI water. For each experiment, control particles without any immobilized biotin were also incubated with streptavidin presenting substrates in parallel. The surfaces were then imaged via CLSM.

### 8.2.4 Assembly of bicompartmental particles in suspension

Assembly of bi- and tetracompartmental particles was carried out at a particle concentration 6.5 x $10^7$ /ml with appropriate amounts of streptavidin (unconjugated or conjugated with Alexa Fluor 633, Invitrogen) in PBS containing 1 wt% BSA and 0.1 vol % tween-20 in PBS for 2h. Suspensions were imaged via CLSM. Statistical analysis was performed on CLSM images using Image J software.[28]

## 8.3 Results and discussion

After the fabrication and characterization of multicompartmental PLGA particles, described in chapter 3, we sought to selectively introduce chemical functionality, which is an essential requirement for directed self-assembly. Towards this end, we employed an acetylene functionalized derivate of PLGA, PLPG.[22, 29] During electrohydrodynamic co-jetting, PLGA blended with 23 wt.% PLA-co-PPGL was used as one of the jetting solutions, while the other solution(s) were comprised of PLGA only. All other solution and process parameters were identical. In order to confirm selective compartmentalization of the acetylene-containing particles, we co-localized the polymer with a fluorescence dye and used CLSM to confirm the multicompartmental character of the particles. This is shown in Figure 8.1, where one compartment (loaded with MEHPPV, a blue fluorophore) contains PLGA only, and the other (loaded with PTDPV, a green fluorophore) contains PLGA and PLPG. While the images suggest compartmentalization, this imaging approach has two potential disadvantages:

(1) Because the fluorescence dye and PLPG are not covalently linked to the polymer, tracking the dyes is an indirect approach that assumes identical distribution of polymer and dye throughout the particle. (2) The addition of dyes increases the complexity of the process. Thus, direct visualization of the PLPG polymer without the use of dyes would be desirable. We therefore initiated a series of experiments to evaluate the use of CRS for direct characterization of PLPG distributions in bicompartmental particles. The CRS technique has rapidly evolved as a powerful tool to characterize a diverse array of materials including drug eluting coatings,[30] the photopolymerisation of diacetylene gels[31] or the morphology of transition metal nanoparticulates.[32] It provides spatially resolved physical and chemical information about materials directly in their native state without the need for external markers, such as fluorescent dyes or radioactive labels. CRS has the potential to be particularly well-suited for the analysis of multicompartmental particles, because the confocal scanning mode facilitates high-resolution imaging, a feature required for imaging of individual particles.[33] The acetylene group of PLPG is associated with a strong Raman band at 2120-2100 $cm^{-1}$.[34] This group was hence used as a Raman label for mapping the vibrational signature of the acetylene groups within different areas of an isolated particle. Particles containing free acetylene groups in one compartment, but no fluorescence dyes, were prepared and imaged by CRS. Figures 8.2a and 8.2b show CRS images of bicompartmental particles, where the PLPG was comprised in 50% and 25% of the particle, respectively. The red-colored maps correspond to the intensity of the band at 1767 cm-1, which can be attributed to the ester

groups of PLGA [31] and is present throughout the particles. The yellow-colored maps are generated by plotting the intensity of the signal at 2122 cm-1. As mentioned above, this signal represents the carbon-carbon triple bond stretch indicative of the acetylene groups. The focal plane for the Raman spectral maps was located approximately at the midpoint of each particle. Figure 8.2c shows representative Raman spectra from the particle shown in Figure 8.2a. The position of the red spectral trace is denoted by the + and the position of the yellow spectrum by the x. The acetylene band at 2122 cm-1 can be clearly observed in Raman spectra of the yellow region of the particle image. In contrast, this band is absent in spectra of the red region of the particle. This confirms that the remaining volume of the particle is void of acetylene groups.

After establishing the selective compartmentalization of acetylene groups in bicompartmental particles, we proceeded to demonstrate their surface activity by selectively introducing biotin groups on the surface of particles through the Huisgen 1, 3-dipolar cycloaddition reaction between azides and terminal alkynes, widely known as 'click' chemistry.[35-37] Owing to its stability, orthogonality, efficiency, and ability to proceed under physiological conditions, 'click' reactions are being extensively applied towards the design of functional nanomaterials and polymers for pharmaceutical and biomedical applications.[36, 38-40] Bicompartmental particles containing PLPG and PLGA compartments labeled with PTDPV and ADS306 dyes, were reacted with azide-PEO-biotin in presence of $Cu^{+}$ ions generated by the reduction of $CuSO_4*5H_2O$ via sodium ascorbate. This resulted in the immobilization of biotin-azide on the surface of one

compartment only. In order to confirm the selectivity of the click reaction, we subsequently incubated the biotinylated particles with Alexa Fluor 633-labeled streptavidin. This is schematically depicted in Figure 8.3a. The fluorescence from streptavidin (magenta color) is clearly confined to one compartment only, as shown in Figures 8.3b and 8.3c for bicompartmental particles with 50% and 25% acetylene coverage, respectively. The fluorescence on one compartment is visible in a majority of the population of particles, thereby confirming the homogenous distribution of acetylene functionality in the compartment containing PLA-*co*-PPGL uniformity, the selectivity of the click reaction (Figure 8.4) and the absence of non-specific adsorption of streptavidin.

Once the ability of bicompartmental particles to undergo spatioselective chemical modification was demonstrated, we investigated self-assembly onto patterned surfaces. Self-assembly in colloidal and interfacial systems revolves around surfactants, polymers, and nano- and microparticles. These assemblies are 'organized', because a specific arrangement of molecules exists at surfaces and in colloidal aggregates. This leads to diverse properties by designing the molecular arrangement, which involves a multitude of interactions. The interplay between the different kinds of forces can give rise to exciting biomimetic phenomena, since many important biological reactions and processes occur at interfaces that are provided by membranes and vesicles. Compared to surfactants and polymers, particulate systems fabricated from polymers are of greater interest since the collective properties of the assembled "superstructures" can be fine-tuned by surface chemistry, crystallinity and relative orientation of the

individual particles. Thus, such structures have applications in a multitude of fields such as optics, electronics and theranostics.[41] The presence of multiple compartments in a single particle is ideal for self assembly since ordered structures can be conveniently built by introducing chemical,[42] charge induced or magnetic field induced responses[43] in individual compartments.

The binding of biotin with streptavidin is accompanied by a very large decrease in free energy, and the dissociation constant for the biotin-streptavidin complex is of the order of $10^{-14}$. Streptavidin is a tetrameric protein and can bind up to four molecules of biotin, due to which self assembly is feasible. Numerous hydrogen-bonding and Van der Waals interactions are involved in the binding and the complex is extremely stable over a wide variety of pH ranges.[44] Several methods have been employed to generate patterns of isotropic nanoparticles on surfaces, such as dip pen lithography,[45] patterning oligonucleotides via electron beam writing,[46] Marangoni-flow induced patterning of colloids,[47] and capillary flow of particles on top of patterned substrates.[18] Patterning bicompartmental particles introduces an additional parameter: the selective addressability of the surface of one hemisphere. The other hemisphere would be left free to react in an independent manner, for example allowing orthogonal detection/recognition of analytes, which is not possible without spatial confinement of functional groups due to compartmentalization. In order to test our hypothesis, monocompartmental particles with biotin groups were first incubated with patterned streptavidin surfaces. CLSM imaging of surfaces showed that particles were present only in areas containing streptavidin (Figure 8.5c). Additionally, a

particle population that was not reacted with biotin was tested as the control group. These particles did not form patterns on the substrate (Figure 8.5d) indicating that particle self-assembly was due to specific biotin-streptavidin interactions, and non-specific adsorption was minimal. We then incubated the surfaces with bicompartmental particles containing green and red dyes, as depicted schematically in Figure 8.6a. These particles had biotin groups on the surface of the green compartment only. Patterns formed by these particles are shown in Figure 8.6b. Particle orientation is clearly observed in the high magnification images (Figure 8.6c), where the red hemisphere is more apparent on the surface in comparison with the green. Randomly oriented particles were also observed in certain areas (Figure 8.7a), where both red and green hemispheres could be visualized on the surface in the same focal plane. In these areas, non-specific adhesion between the particles and the substrate occurred, which may be attributed to steric crowding of particles.

Once the ability to assemble and therefore orient the particles on flat substrates was established, preliminary studies regarding the assembly of particles in suspension were then performed. This is schematically shown in Figure 8.8a In order to test the feasibility of self aggregation of particles, monocompartmental particles containing surface biotin groups were prepared. Upon the addition of 0.4 μg/ml of streptavidin, the particles spontaneously organized themselves into aggregates (Figure 8.8b). On the other hand, control particles that did not contain biotin but were incubated with the same amount of streptavidin, remained relatively well suspended (Figure 8.8c). While each of

these aggregates contained an average of at 8-10 particles, introduction of compartmentalization provides the advantage of controlled assembly, with the precisely defined internal architectures making it possible to control the size of these aggregates, as well as their relative orientation. Figure 8.8d shows a suspension of bicompartmental particles surface modified with biotin on one compartment only, incubated with 0.4 µg/ml of streptavidin. Compared to monocompartmental particles, the aggregates comprise of two, three or four particles only, with the particles in the control suspension (without biotin) being well suspended, again suggestive of minimal non specific binding (Figure 8.8e).

Once the proof of concept of assembly in suspension was established, we turned our attention to controlling shape of the aggregates via control over internal architecture of the particles. Towards this end, we synthesized tetracompartmental particles from a square shaped arrangement of four capillary needles with acetylene PLGA in the opposite quadrants. Low and high magnification CLSM images of tetracompartmental particles are shown in Figures 8.9 a and b respectively. Our hypothesis was that the opposite quadrants would induce the formation of longer, chain-like assemblies. Upon incubation with 0.4 µg/ml streptavidin, these particles also exhibited spontaneous aggregation. However, these aggregates were predominantly chain shaped (Figure 8.9d and e), with each chain containing 4-7 particles. Longer assemblies were not observed. The effect of compartmentalization on the nature of assemblies is analyzed in Figure 8.10, where a statistical comparison of aggregates formed via addition of a constant amount of streptavidin to mono-, bi-

and tetracompartmental particles containing biotin on the entire surface, one half or two opposing quadrants is shown. In general, the number of specific aggregates is greater in the case of biotinylated particles, and non specific Van der Waal's interactions are greater in control samples. In case of monocompartmental particles, larger aggregates containing 4-20 particles constitute a sizable population, with 28.7% being tetramers-heptamers, and 24.17% being aggregates containing 8-20 particles. Dimers constitute only 9.91% of the population. On the other hand, dimers comprise of 27.78% of the population in case of bicompartmental particles, and these do not exhibit a significant number of aggregates containing 4-7 particles (5.56%), and no aggregates with 8-20 particles, suggestive of controlled binding owing to compartmentalization. In case of tetracompartmental particles, tetramers-heptamers form the majority of the population (23.85%), followed by dimers (20.08%). A major advantage of the criss-cross configuration of tetracompartmental particles is that they favor linear aggregates. 95% were found to occur as linear chains. On the contrary, 90% of aggregates containing 5-7, and 100% of aggregates containing 8-20 particles were found to be clumped together randomly in case of monocompartmental particles, signifying the importance of particle internal architecture in shape of the aggregates. It is noteworthy that it is not possible to tell apart specific and nonspecific aggregates in monocompartmental particles, however all aggregates were regarded as 'specific' due to the large number of particles in them (4-20).

Several factors affect the self assembly process; such as the number of acetylene groups available on the surface, the efficiency of the Huisgen cycloaddition reaction, particle size and size distribution, particle stabilization in suspension which again depends on particle size and charge distribution, concentration of streptavidin, and the ability of surface biotin groups to bind to the streptavidin molecules in solution which in turn depends on the spacer arm of the biotin ligand. These variables may together account for the fact that only ~50% of the entire population in the suspension seemed to undergo self assembly. Furthermore, the distribution of compartments in all particles may not be identical due to quick evaporation from the swirling solutions in the cone, as reflected in the 'sandwich' type particles seen in chapter 2. This would affect assembly, and the effect would be much amplified as the internal architecture becomes more complex, such as tetracompartmental particles. Future work should be directed towards a better knowledge and optimization of all the above variables.

## 8.4 Conclusions

In summary, we have further introduced selective chemical functionality throughout the bulk of bi- and tetracompartmental particles by incorporating an acetylene-functionalized PLGA derivative during the electrohydrodynamic co-jetting process. The acetylene groups can be used for direct visualization by Raman microscopy. In addition, we have shown selective chemical activity by modifying half (or one fourth) of particle surface with biotin, and assembling them on streptavidin presenting substrates with a fair degree of spatial orientation.

Future work will be directed towards conducting orthogonal chemical reactions on particles, while being attached to a substrate. Self assembly was also carried out in suspension, with a reasonable measure of control over the nature of assembly by tuning the number of compartments, with tetracompartmental particles exhibiting chain shaped assemblies, whereas bicompartmental particles assembled mostly into dimers. Similar multicompartmental particles may find applications for analyte recognition in diagnostic tests, in energy storage devices, or as biohybrid materials.

## 8.5 Figures and tables

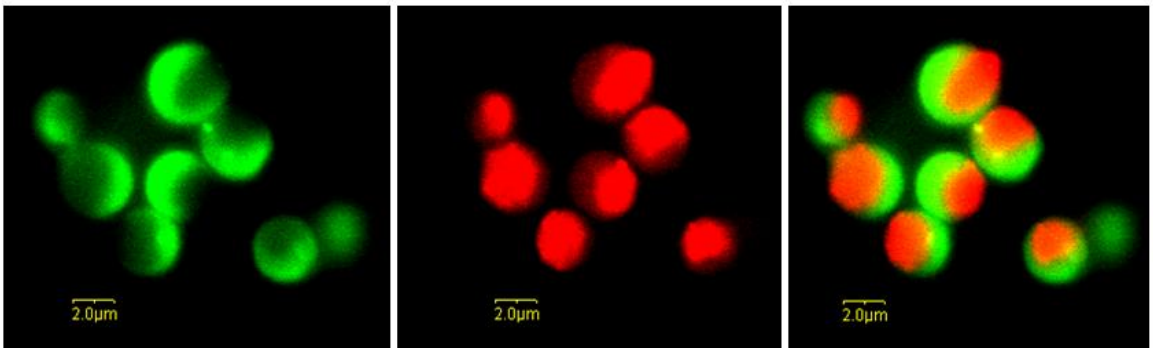


**Figure 8.1** CLSM images of bicompartmental particles. The blue compartment contains PLGA only, and the green compartment contains 23:77 w/w of PLPG: PLGA. Green and red fluorescence images, arising from PTDPV and ADS306PT are shown, followed by the overlay.

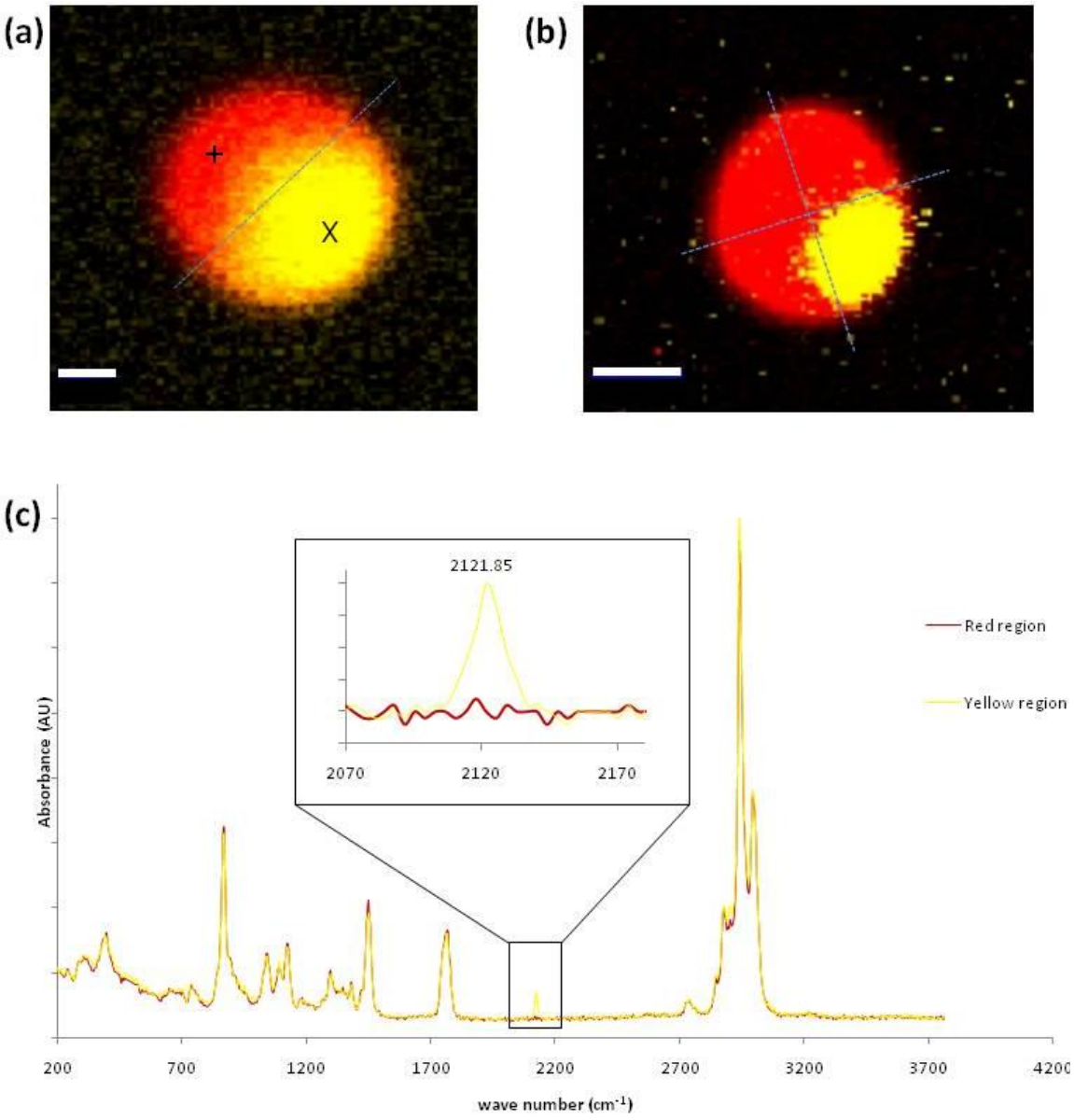


**Figure 8.2** (a) Raman image of a bicompartmental particle comprising of a 30:100 w/w ratio of PLGA: PLPG in one compartment only. (b) Raman-CLSM image of a tetracompartmental particle loaded with 23 wt. % PLPG in one out of four compartments. Dashed blue lines are drawn to guide the eye. (c) Raman spectra of biphasic particles. The red and yellow spectra correspond to the **+** and **X** positions in (a), respectively. The peak at 2121.85 $cm^{-1}$ corresponding to the acetylene functional group is absent in the red spectrum, but visible in the yellow spectrum, as also highlighted in the magnified spectrum shown in the inset. Scale bars denote 1 µm and 2 µm for (a) and (b), respectively.

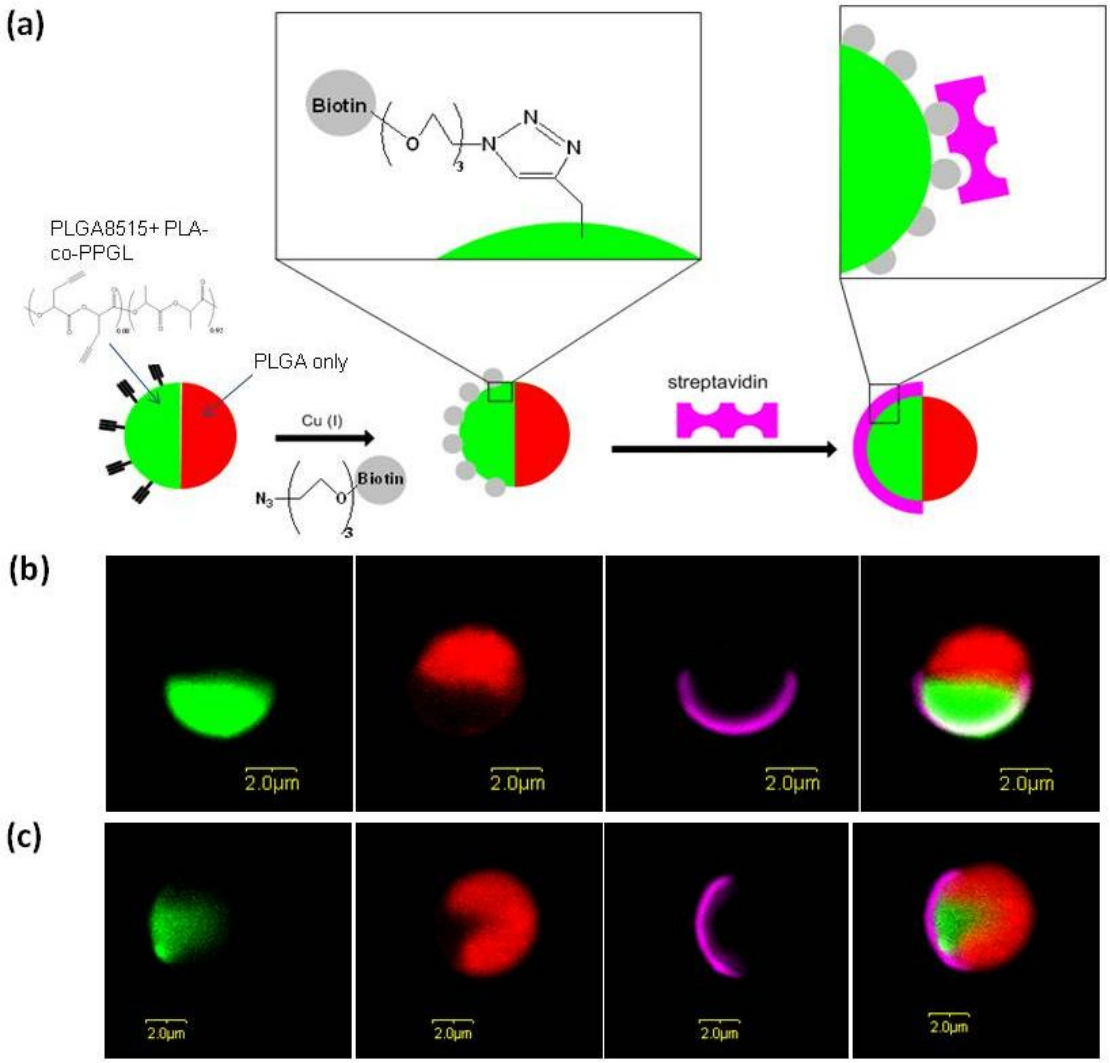


**Figure 8.3** (a) Schematic showing surface modification of bicompartmental particles containing acetylene groups in one compartment only (arising from PPGL incorporated into one of the two solutions during electrohydrodynamic co-jetting) with azide-PEO-biotin via copper catalyzed Huisgen 1,3-dipolar cycloaddition. The ability of the particles to selectively bind with biotin is then verified via incubation with Alexa Fluor 633-labeled streptavidin which results in spatioselective fluorescence. (b),(c) CLSM images of bi- and tetracompartmental particles surface modified with biotin on one compartment only. Green, red and magenta channels (indicating fluorescence from PTDPV, ADS306PT and Alexa Fluor 633-streptavidin) are shown, followed by the overlay, which confirms spatioselective presence of streptavidin, and hence biotin.

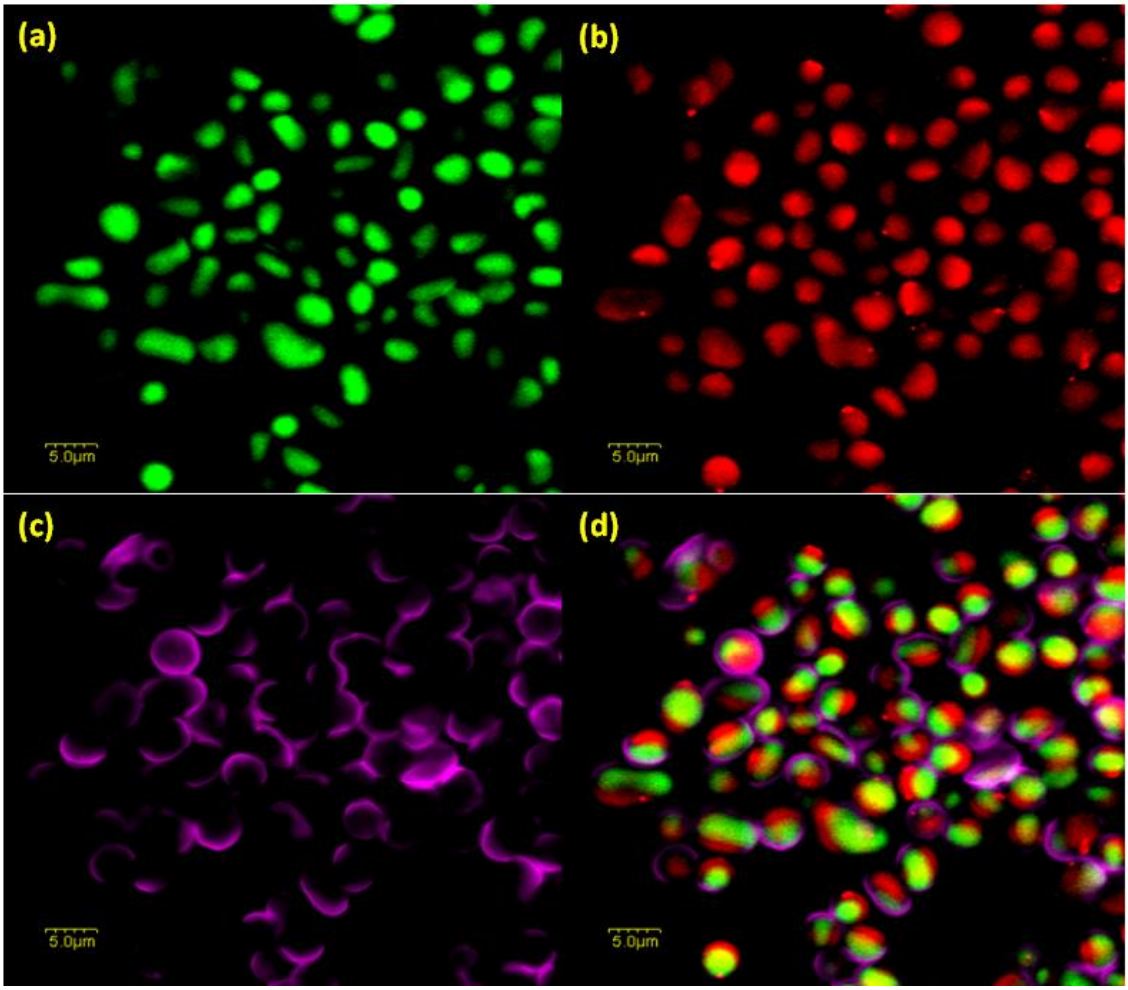


**Figure 8.4** CLSM image showing a large population of bicompartmental particles containing green (PTDPV) and red (ADS306PT) dyes, loaded with PLPG in the green compartment and selectively surface modified with biotin on this compartment only, as shown by the fluorescence of Alexa Fluor 633-labeled streptavidin (indicated in magenta).

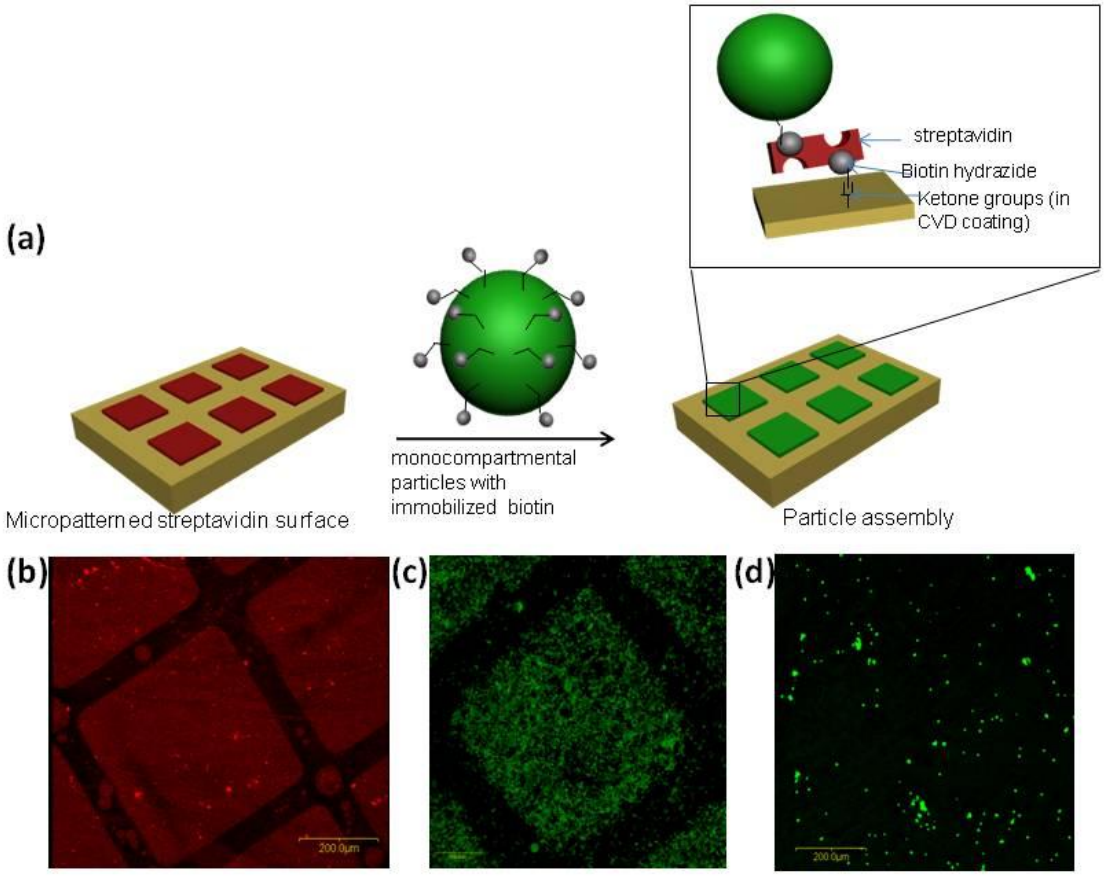


**Figure 8.5** (a) Schematic depicting proof of concept of self assembly of particles on CVD substrates. Monocompartmental particles containing acetylene groups were first surface modified with biotin via click chemistry. To prepare streptavidin presenting surfaces, poly [(4-formyl-p-xylylene)-co-(p-xylylene)] was first deposited on silica substrates via CVD polymerization of 4-formyl [2, 2]paracyclophane. The aldehyde groups in the CVD coating were microcontact printed with biotin hydrazide, followed by incubation of Alexa Fluor 633 streptavidin. The biotin-functionalized particles were then incubated with these surfaces. (b) CLSM image of CVD substrates immobilized with Alexa Fluor 633-labeled streptavidin. The selective red fluorescence indicates successful patterning of substrates with streptavidin. (c) CLSM image of biotinylated particles incubated with streptavidin presenting CVD substrates. (d) Control substrates incubated with particles without any surface biotin groups. These surfaces are mostly devoid of particles.

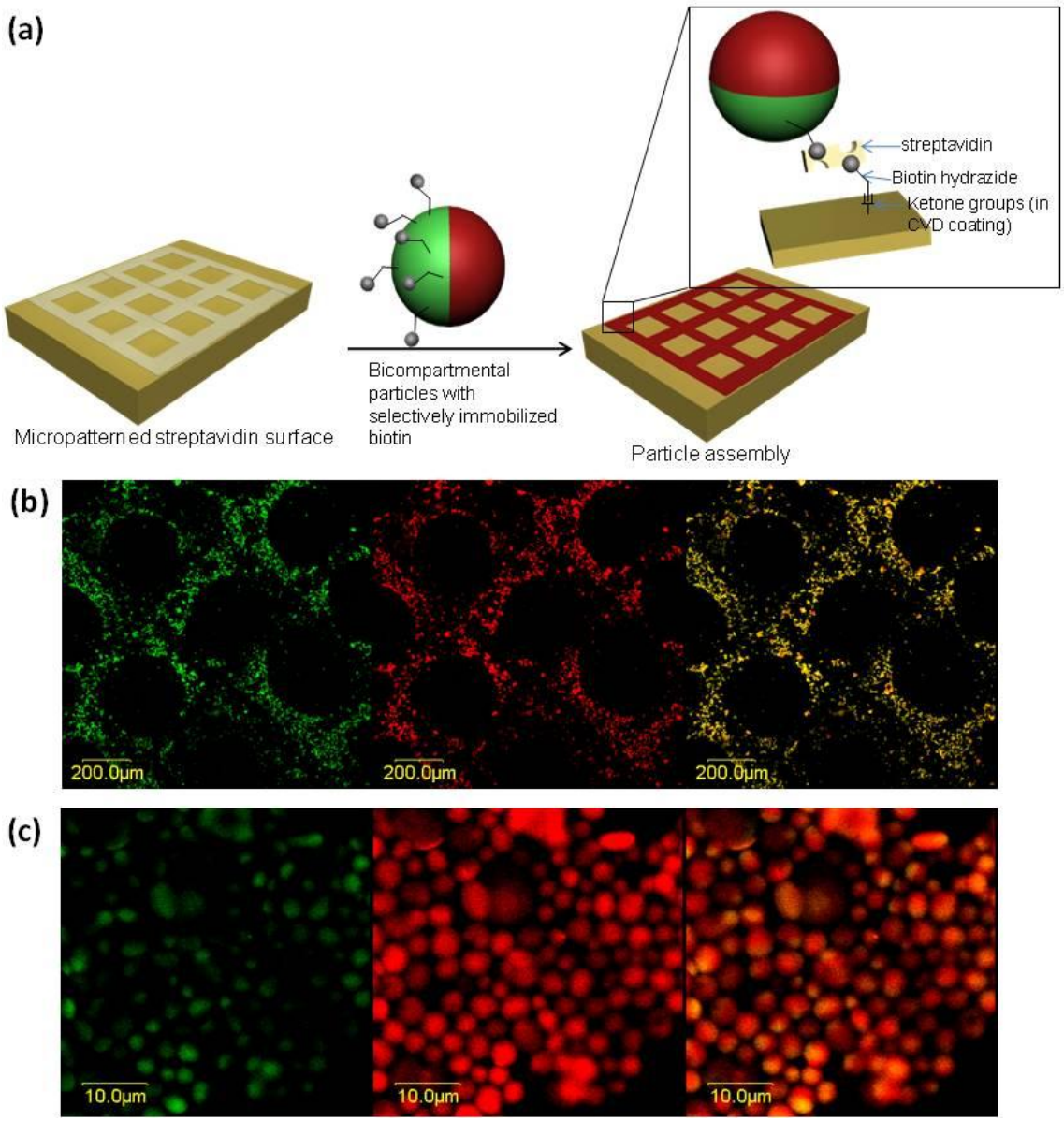


**Figure 8.6** (a) Scheme depicting the assembly of bicompartmental particles onto patterned streptavidin surfaces. A reactive CVD coating containing ketone functional groups is deposited on silica surfaces. This is followed by microcontact printing of biotin-hydrazide, followed by immobilization of streptavidin to yield patterned substrates. Bicompartmental particles (loaded with green and red dyes) containing surface biotin groups on the green compartment then spontaneously assemble on these substrates, and the selective binding of the green half leads to particle orientation. (b) CLSM image of particles as seen on the streptavidin substrates. (c) High magnification CLSM image showing particle orientation.

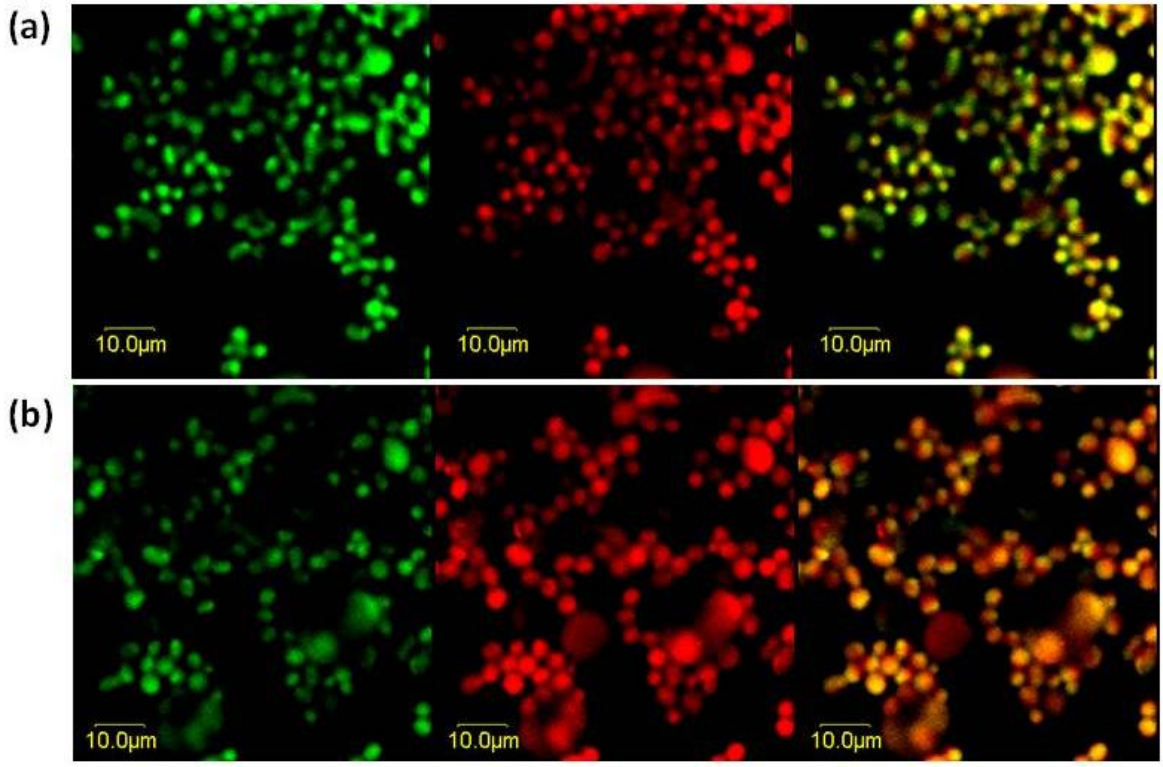


**Figure 8.7** (a) CLSM image showing a random orientation of bicompartmental particles containing biotin in one compartment only on streptavidin presenting CVD substrates. (b) Oriented particles, imaged at same fluorescent intensity levels at the same magnification, indicating that observation of orientation was not biased by changes in fluorescence intensity levels.

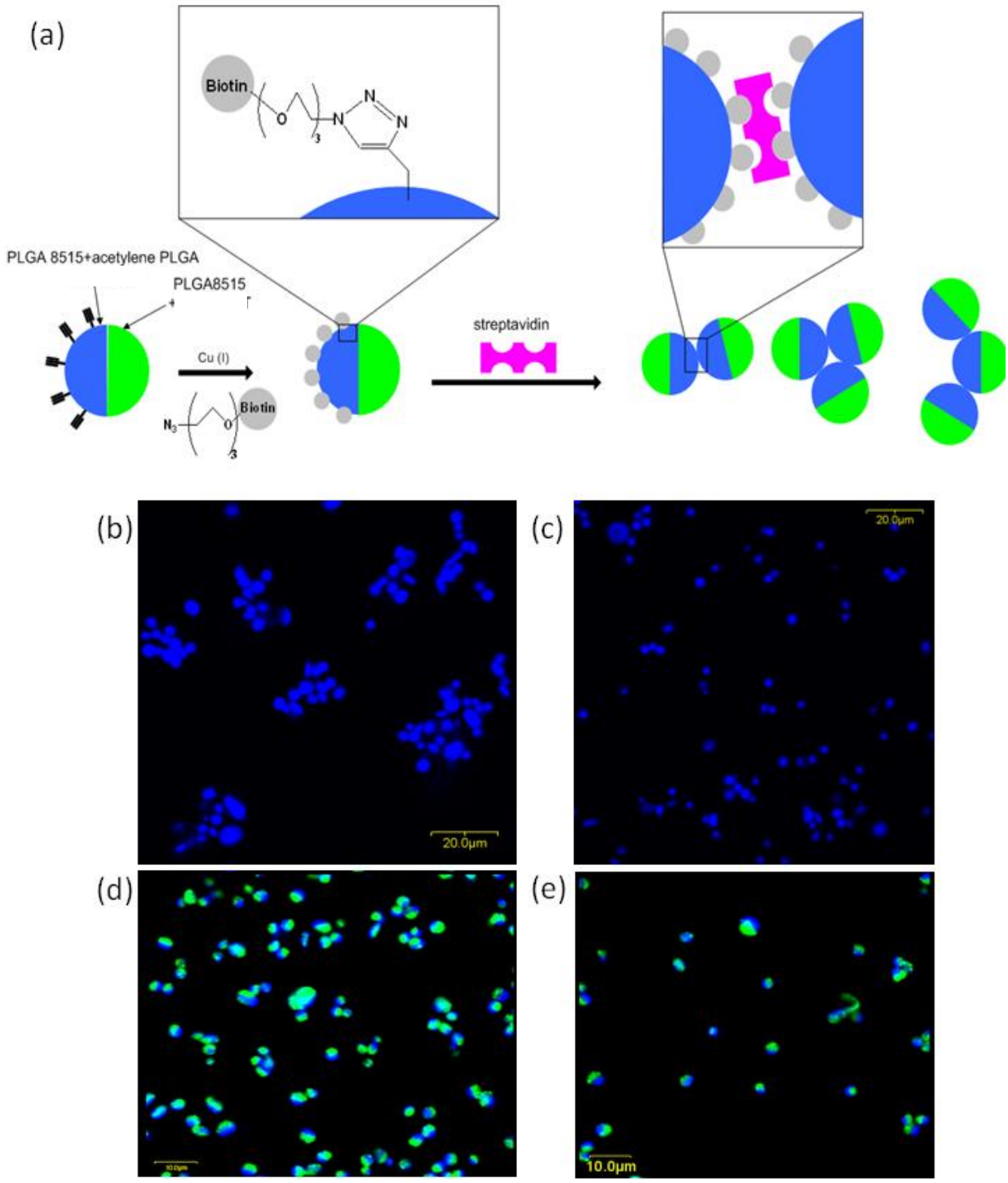


**Figure 8.8** (a) Schematic showing formation of controlled assemblies from anisotropic particles through biotin immobilized on particle surface through click chemistry, followed by addition of tetrameric streptavidin. (b) Proof of concept of self assembly illustrated on monophasic particles carrying surface biotin groups, in presence of 0.4 µg/ml streptavidin. The particles form aggregates seen in (b) which were not observed in the control population (c) which comprises of particles without immobilized biotin groups, to which streptavidin was added. When the same amount of streptavidin was added to bicompartmental particles containing surface biotin groups on one (blue) hemisphere only, smaller aggregates (dimers, trimers and tetramers) were seen (d), compared to the control, which seemed well dispersed.

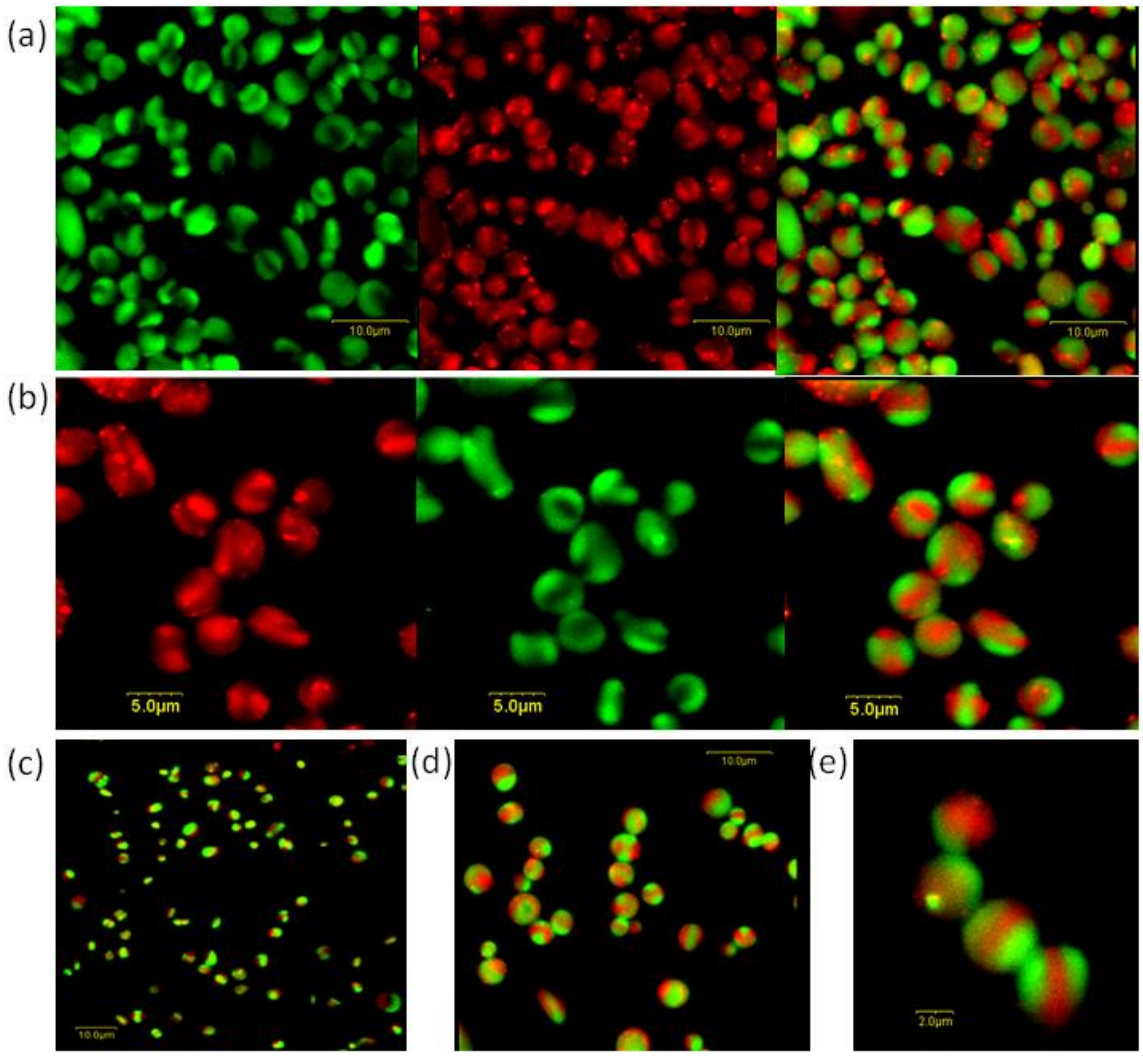


**Figure 8.9** Effect of particle architecture on assembly (a) and (b) represent low and high magnification images of tetracompartmental particles with PLPG in opposite quadrants (labeled green). After biotin immobilization, these particles formed chain shaped assemblies upon addition of streptavidin (0.4 µg/ml), compared to control particles (without biotin but with streptavidin present in the suspension), with the control particles shown in (c). (d) Assembled particles, (e) High magnification CLSM image in which the particle binding via the biotin containing (green) compartments is clearly visualized.

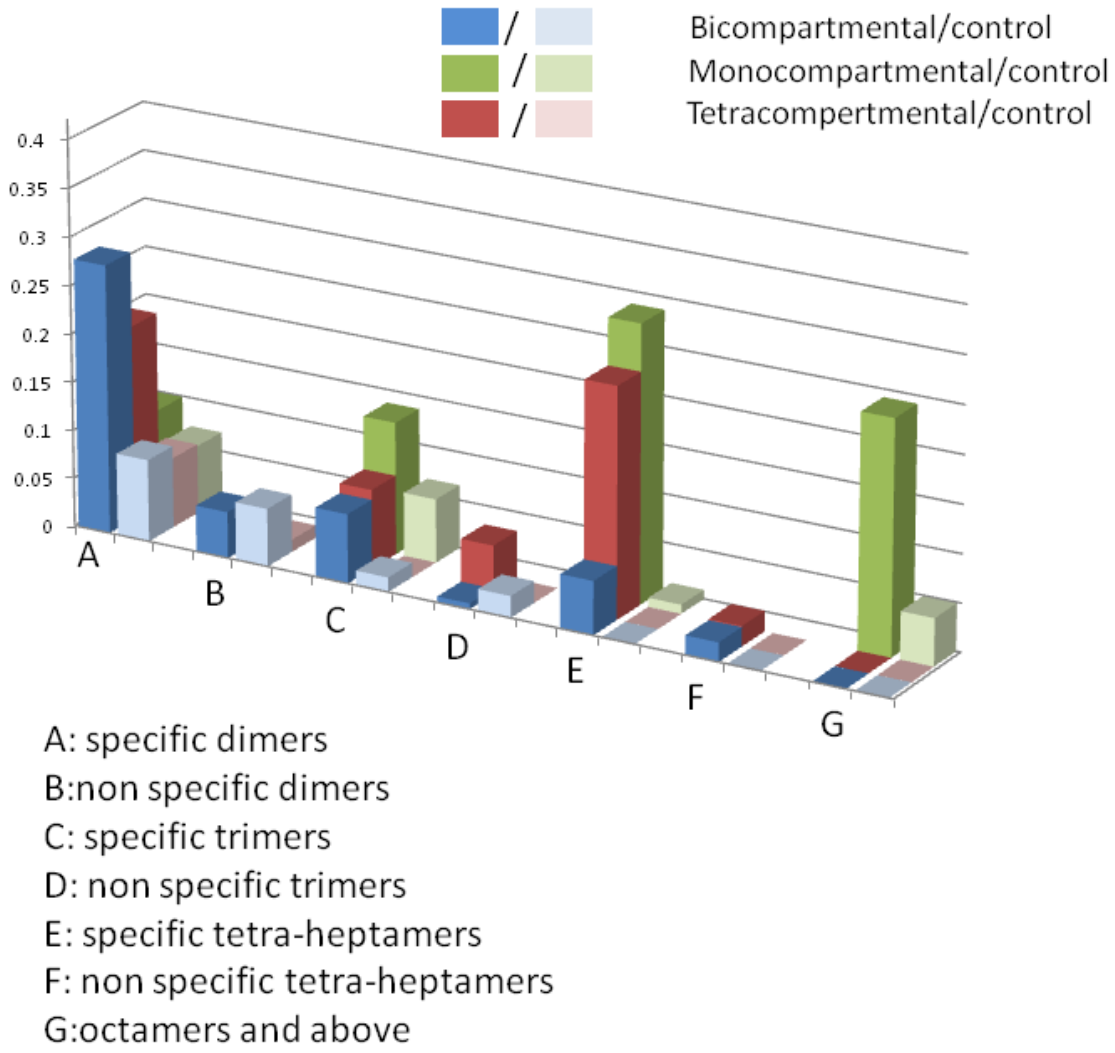


**Figure 8.10** Preliminary statistical analysis of self assembly depicting the effect of internal particle architecture on the nature of assembly. Three particle populations, monocompartmental (with PLPG and hence biotin uniformly distributed throughout particle surface), bicompartmental (with PLPG and hence biotin on one hemisphere) and tetracompartmental (with PLPG and hence biotin on opposite quadrants), were assembled by adding 0.4 µg/ml streptavidin to the suspension. These particles are indicated by green, blue and red colors respectively. For each type of particle, a control population with the same internal architecture, but without immobilized biotin was also assembled by addition of the same amount of streptavidin. The control mono-, bi- and tetracompartmental particles are indicated by light green, light blue and pink colors respectively. As shown in the bar graph, the population of assembled structures (the smallest being dimers) was greater in particles containing immobilized biotin compared to the corresponding control population. Bicompartmental particles favored more dimers, while 95% of tetracompartmental particles favored chain shaped assemblies with 4-7 particles per chain. Monocompartmental particles showed a greater population of assemblies with 4-7, however, 90% of these aggregates were clumped and not chain-like. Monocompartmental particles also favored assemblies between 8-20 particles, however all of them were found to occur as clumped aggregates.

## 8.6 References


[1] M. Grzelczak, J. Vermant, E. M. Furst, L. M. Liz-Marzan, *Acs Nano* **2010**, *4*, 3591.
[2] S. Srivastava, A. Santos, K. Critchley, K. S. Kim, P. Podsiadlo, K. Sun, J. Lee, C. L. Xu, G. D. Lilly, S. C. Glotzer, N. A. Kotov, *Science* **2010**, *327*, 1355.
[3] S. Mitragotri, J. Lahann, *Nat. Mater.* **2009**, *8*, 15.
[4] S. Jiang, Q. Chen, M. Tripathy, E. Luijten, K. S. Schweizer, S. Granick, *Advanced Materials* **2010**, *22*, 1060.
[5] A. M. Smith, S. Nie, *Acc. Chem. Res.* **2009**, *43*, 190.
[6] S. M. Yang, S. H. Kim, J. M. Lima, G. R. Yi, *J Mater Chem* **2008**, *18*, 2161.
[7] D. C. Pregibon, M. Toner, P. S. Doyle, *Science* **2007**, *315*, 1393.
[8] S. Sengupta, D. Eavarone, I. Capila, G. Zhao, N. Watson, T. Kiziltepe, R. Sasisekharan, *Nature* **2005**, *436*, 568.
[9] M. Yoshida, K.-H. Roh, S. Mandal, S. Bhaskar, D. Lim, H. Nandivada, X. Deng, J. Lahann, *Adv Mater* **2009**, *21*, 4920.
[10] A. J. Swiston, J. B. Gilbert, D. J. Irvine, R. E. Cohen, M. F. Rubner, *Biomacromolecules* **2010**, *11*, 1826.
[11] G. J. Snyder, E. S. Toberer, *Nat Mater* **2008**, *7*, 105.
[12] K. J. Lee, J. Yoon, J. Lahann, *Curr Opin Coll Int Sci* **2010**, *submitted*.
[13] A. Walther, A. H. E. Muller, *Soft Matter* **2008**, *4*, 663.
[14] M. Yoshida, J. Lahann, *ACS Nano* **2008**, *2*, 1101.
[15] F. Wurm, A. F. M. Kilbinger, *Angewandte Chemie-International Edition* **2009**, *48*, 8412.
[16] D. Dendukuri, D. C. Pregibon, J. Collins, T. A. Hatton, P. S. Doyle, *Nat. Mater.* **2006**, *5*, 365.
[17] J. W. Kim, R. J. Larsen, D. A. Weitz, *J Am Chem Soc* **2006**, *128*, 14374.
[18] Y. N. Xia, Y. D. Yin, Y. Lu, J. McLellan, *Advanced Functional Materials* **2003**, *13*, 907.
[19] K. H. Roh, D. C. Martin, J. Lahann, *Nat. Mater.* **2005**, *4*, 759.
[20] K. H. Roh, D. C. Martin, J. Lahann, *J. Am. Chem. Soc.* **2006**, *128*, 6796.
[21] K. H. Roh, M. Yoshida, J. Lahann, *Langmuir* **2007**, *23*, 5683.
[22] S. Bhaskar, K. H. Roh, X. Jiang, G. L. Baker, J. Lahann, *Macromol. Rapid Commun.* **2008**, *29*, 1655.
[23] S. Bhaskar, J. Hitt, S. L. Chang, J. Lahann, *Angew. Chem. Int. Ed.* **2009**, *48*, 4589.
[24] S. Bhaskar, J. Lahann, *J. Am. Chem. Soc.* **2009**, *131*, 6650.
[25] S. Bhaskar, K. M. Pollock, M. Yoshida, J. Lahann, *Small* **2010**, *6*, 404.
[26] Y. Elkasabi, H. Nandivada, H. Y. Chen, S. Bhaskar, J. D'Arcy, L. Bondarenko, J. Lahann, *Chem. Vap. Deposition* **2009**, *15*, 142.
[27] H. Nandivada, H. Y. Chen, J. Lahann, *Macromolecular Rapid Communications* **2005**, *26*, 1794.
[28] M. D. Abramoff, P. J. Magelhaes, S. J. Ram, *Biophot. Int.* **2004**, *11*, 36.
[29] X. Jiang, E. B. Vogel, M. R. Smith III, G. L. Baker, *Macromolecules* **2008**, *41*, 1937.

[30] A. Belu, C. Mahoney, K. Wormuth, *Journal of Controlled Release* **2008**, *126*, 111.
[31] V. Haridas, Y. K. Sharma, R. Creasey, S. Sahu, C. Gibson, N. H. Voelcker, *New J. Chem.* **2010**, *in press*.
[32] E. U. Donev, R. Lopez, L. C. Feldman, R. F. Haglund, *Nano Letters* **2009**, *9*, 702.
[33] A. A. v. Apeldoorn, H. J. v. Manen, J. M. Bezemer, J. D. d. Bruijn, C. A. v. Blitterswijk, C. Otto, *J. Am. Chem. Soc.* **2004**, *126*, 13226.
[34] D. Lin-Vien, N. B. Colthup, W. G. Fateley, J. G. Grasselli, "*The handbook of infrared and raman characteristic frequencies of organic molecules"*, Academic Press, San Diego, 1991.
[35] H. Nandivada, H. Y. Chen, L. Bondarenko, J. Lahann, *Angewandte Chemie-International Edition* **2006**, *45*, 3360.
[36] H. Nandivada, X. Jiang, J. Lahann, *Adv Mater* **2007**, *19*, 2197.
[37] Q. Wang, T. R. Chan, R. Hilgraf, V. V. Fokin, K. B. Sharpless, M. G. Finn, *Journal of the American Chemical Society* **2003**, *125*, 3192.
[38] J. E. Moses, A. D. Moorehouse, *Chemical Society Reviews* **2007**, *36*, 1249.
[39] A. H. El-Sagheer, T. Brown, *Chem. Soc. Rev.* **2010**, *39*, 1388
[40] C. E. Hoyle, C. N. Bowman, *Angew Chem Int Ed Engl.* **2010**, *49*, 1540.
[41] S. C. Glotzer, M. J. Solomon, *Nat. Mater.* **2007**, *6*, 557.
[42] D. Dendukuri, T. A. Hatton, P. S. Doyle, *Langmuir* **2007**, *23*, 4669.
[43] C. Mangeney, M. Fertani, S. Bousalem, M. Zhicai, S. Ammar, F. Herbst, P. Beaunier, A. Elaissari, M. M. Chehimi, *Langmuir* **2007**, *23*, 10940.
[44] S. Miyamoto, P. A. Kollman, *Proteins: Structure, Function and Genetics* **1993**, *16*, 226.
[45] W. K. Lee, Z. T. Dai, W. P. King, P. E. Sheehan, *Nano Letters* **2010**, *10*, 129.
[46] H. Y. Lin, L. C. Tsai, C. D. Chen, *Advanced Functional Materials* **2007**, *17*, 3182.
[47] Y. Cai, B. M. Z. Newby, *Journal of the American Chemical Society* **2008**, *130*, 6076.

# CHAPTER 9

# FUTURE DIRECTIONS

## 9.1 Environmental variables in electrohydrodynamic co-jetting

As outlined in chapter 1, jet-breakup and particle formation during electrohydrodynamic atomization are complex processes influenced by a variety of factors, two of which are solution and process variables. These two parameters were investigated extensively in this dissertation (Chapter 3). Beyond jet breakup, particle formation is driven by solvent evaporation, which in turn in governed by environmental factors, most importantly ambient air temperature and relative humidity.[1] Humidity has been previously found to induce pore formation during electrospinning; this has been attributed to phase separation of the polymer due to condensation of water on fiber surface during evaporation.[2, 3]. Such structures were also observed in this work, and are described in Figure 9.1. These particles were made via the exact same conditions described for bicompartmental spheres in Chapter 3, but during periods of different humidity (>40% as opposed to 35-40% for smooth spheres as seen previously), which resulted in particles with a porous surface microstructure. Porosity was observed homogenously throughout the particle surface (Figures 9.1 a-b) in some instances and anisotropically in others (Figure 9.1d-e), while compartmentalization was retained perfectly in both cases (Figures 9.1c and f).

The reason for anisotropic porosity is not clear, and it is possible that extremely small variations in solvent ratios in both solutions, coupled with humidity effects may be a reason. Also, it is noteworthy that a majority of shape and size variations in particles described in chapter 3 are applicable to a single polymer system: PLGA8515 at a constant temperature and relative humidity range (23-25 $^{o}$C, 35-40%). An understanding of effects of all solution, process and environmental parameters on a given polymer system is necessary to further tailor and control particle properties. Towards this end, it is desirable to build an electrohydrodynamic co-jetting instrument capable of controlling the environment precisely.[1, 2] In order to better observe evaporation of droplets (and the different phenomena that govern formation of discs, rods and spheres), it is also desirable to combine the electrohydrodynamic co-jetting setup with a high speed camera.[4, 5] Process optimization through fabrication of the above described next generation electrohydrodynamic co-jetting setup would be beneficial towards understanding mechanisms behind particle formation and create particles with a specific set of properties 'on-demand' in the future.

## 9.2 Future challenges

While the previous section outlined process challenges, some of the broader challenges associated with the practical applicability of anisotropic particles, particularly w.r.t targeted drug delivery and self assembly are outlined in this section.

The ultimate goal of biodegradable anisotropic particles is targeted cancer therapeutics, where different compartments are envisioned to carry out specific functions simultaneously yet independently (analogous to a biological cell). For instance, one could imagine a tricompartmental particle composed of three types of PLGA polymers with increasing degradation times (which can be achieved by altering the molecular weight or Lactide/Glycolide ratio), where the first, quick-degrading compartment would release an antiangiogenic drug (such as angiostatin),[6] the second compartment with an intermediate degradation time incorporate PEI, which upon endocytosis by the tumor cells would release siRNA by increasing its size at endosomal pH, while the third compartment, with the longest degradation time would contain MRI imaging agents to facilitate biomedical imaging. In order to achieve this goal, several challenges need to be overcome, which include but are not limited to reduction of particle size, obtaining a narrow particle size distribution and selective encapsulation of drugs in different compartments. Similarly, particle size reduction is also desirable for self assembly, as the attractive Van Der Waal's forces are a direct function of particle diameter.

In this dissertation, fibers with diameters in the range of 3-20 μm have been predominantly synthesized and discussed. For extravasation from blood, particle diameters of <100 nm are necessary.[7] In addition to lowering concentration and reducing flow rate (as described in chapter 3), particle size reduction can be achieved by using low molecular weight polymers which would reduce solution viscosity, increasing the amount of non-volatile/high boiling

solvent in the jetting solution which would facilitate greater thinning of the jet, and by varying the diameter of the capillaries used. The smallest particle diameters achieved using a combination of above parameters are in the range of 50-150 nm, and are shown in Figure 9.2a. These particles contain PLGA 7525 in one compartment and PLGA5050 (both possessing $M_w$ = 10 kD) in the other. Both jetting solutions consisted of 7:100 PLGA:solvent by wt., with the solvent being 78:22 Chloroform:DMF by vol. Also, the resolution limit imposed by diffraction needs to be overcome in order to distinguish between compartments, for which it may be desirable to employ techniques such as STED microscopy in case of fluorophores or transfer to microscopy techniques that do not require a fluorophore , such as CRS.

While the particles described in Figure 9.2a meet the criteria for extravasation, their size distribution is quite broad. In order to achieve narrow size distributions, lower flow rates, lower conductivities and lower applied electric fields are desirable.[8] However, in order to generate droplets of sub 100 nm sizes, the non volatile solvents used during co-jetting give rise to higher applied voltages, thereby promoting the transition from varicose breakup mode to the kink mode, which is accompanied by a increase in particle polydispersity. Additionally, almost all therapeutic drugs are low molecular weight compounds, hence compartmentalizing them is a challenge as they may diffuse across jetting solutions in the Taylor cone. Particles with compartmentalized drugs (as shown in Figure 9.2b) have been produced, however, it is possible that the diffusion was prevented by virtue of higher instantaneous viscosities achieved by using volatile

solutions of high molecular weight polymers. Diffusion maybe a concern while trying to fabricate smaller diameter particles from low molecular weight polymer solutions with low viscosities. Particle sieving or filtration is an option, as shown in chapter 3, however, challenges such as low yields and release/degradation of drugs during filtration are concomitant.

The microsectioning process described in chapter has been demonstrated to be a viable option for fabrication of cylindrical microstructures with vastly improved size distributions compared to particles obtained via electrohydrodynamic co-jetting. An alternative strategy to fabricate monodisperse particles would utilize these cylindrical particles. Heating these cylinders above their glass transition temperatures along with surface energy minimization in aqueous media result in change of shape from cylinders to spheres. This is illustrated Figure 9.3. These particles contain PLGA 8515 in one compartment and a mixture of PLGA and fluorinated polyhedral oligomeric silsesquioxane (F-POSS) in the other compartment. F-POSS is a low surface energy material and the differences in hydrophobicity between compartments can induce self assembly at air-water interfaces. CLSM images of particles formed via shape shifting (Figures 9.4 b and c) show that they retain the anisotropy of cylinders, indicative of the directionality of the shape shifting process.

The particles discussed in this dissertation are in the diameter range of ~20μm. Future work towards fabricating smaller diameter particles would involve reducing fiber diameter. This may be achieved by (i) employing a high rpm collection wheel that would cause fiber thinning during deposition and (ii)

obtaining smaller section thicknesses via ultramicrotoming. The shape shifting process offers several advantages. Since the cylinders are fabricated from fibers which in turn result from high viscosity jetting solutions, low molecular weight drugs may successfully be retained in individual compartments without diffusion. Fabrication of monodisperse particles with sub micron diameters with distinctly resolvable anisotropy in bulk and surface for *in vivo* and self assembly applications would form the starting point for future directions of this dissertation.

## 9.3 Figures and tables

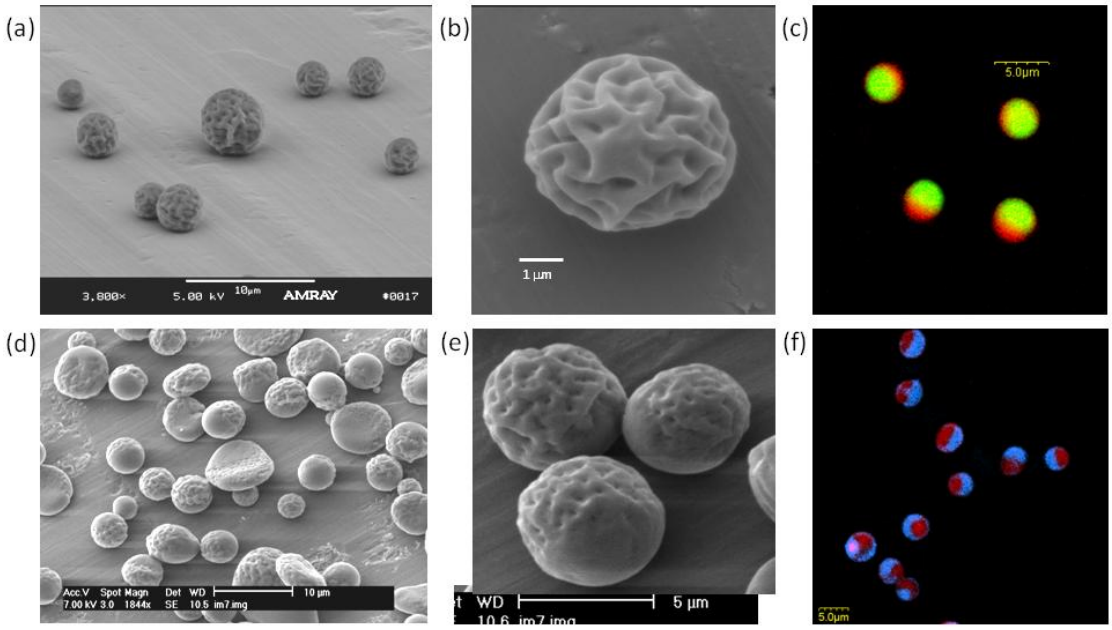


**Figure 9.1** Effect of environmental variables on electrohydrodynamic co-jetting (a)-(b) low and high resolution SEM images and (c) CLSM images of bicompartmental particles with porous surface microstructure. (d)-(e) low and high resolution SEM images and (f) CLSM images of bicompartmental particles with porosity on one half only. Both these particles were produced from a 4.5:100 w/w solution of PLGA 8515 in 97:3 Chloroform:DMF in each jetting solution. These particles were jetted at T=23-25 $^{o}$C and R. H >40%. Unfortunately, a clear record of humidity was not maintained and future studies with a temperature and humidity controlled jetting setup are needed to further investigate the cause of and differences in porosity. Smooth particles (described in chapter 2 and 3) were a result of R.H of 35-40%.

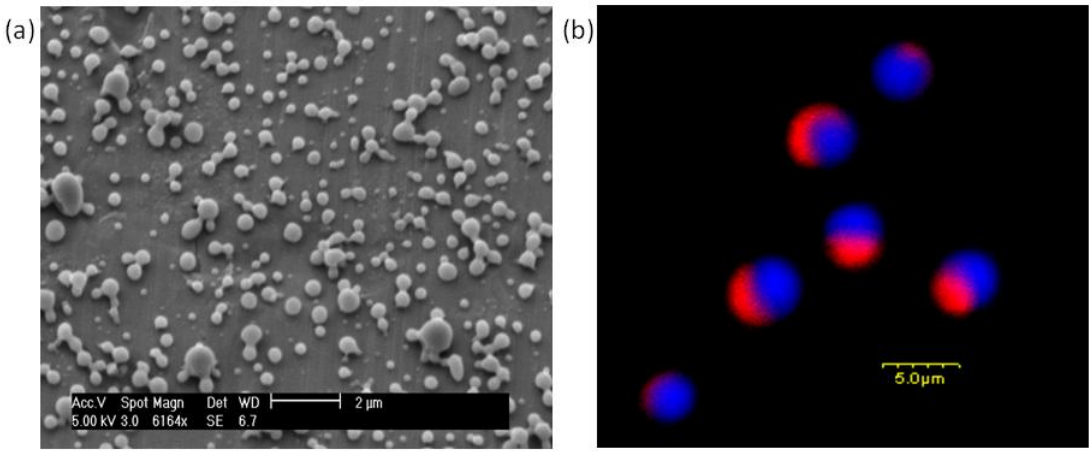


**Figure 9.2** (a) Bicompartmental particles with diameters in the range of 100 nm-1 µm. These were made from 7:100 w/w PLGA (10kD, Purac Biomaterials) in 78:22 Chloroform: DMF by vol., at flow rates of 0.2 ml/h. the compartments could not be resolved via CLSM, and other techniques such as STED microscopy need to be performed in the future in order to resolve compartments. (b) Bicompartmental particles containing chemotherapeutic drug doxorubicin in one compartment only, made from a 4.5:100 w/w solution of PLGA 8515 in 97:3 chloroform: DMF, red fluorescence represents doxorubicin and blue fluorescence represents ADS 406PT.

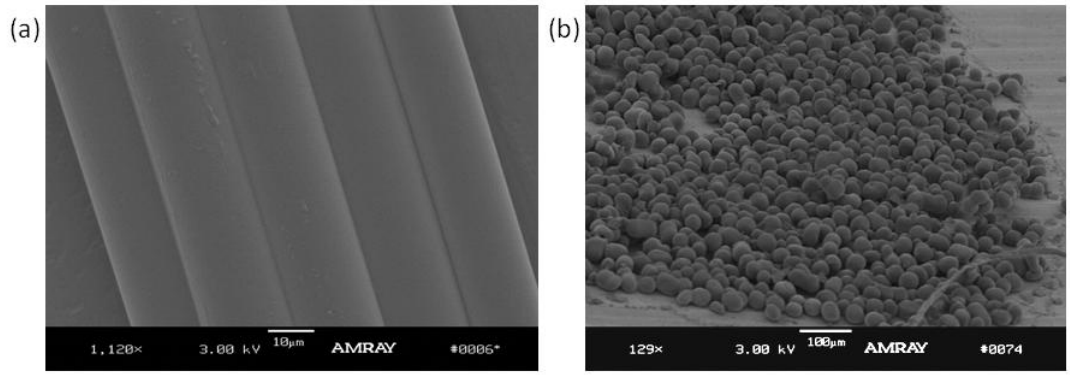


**Figure 9.3** (a) Bicompartmental fibers containing F-POSS in one compartment only. These were made from two jetting solutions, one containing 18:100 w/w PLGA in 95:5 CHCl3:DMF with trace amounts of PTDPV dye, and the other consisting of 18:100 w/w of PLGA + F-POSS , with POSS:PLGA being = 1:10 by wt. in 1:1 Hexafluorobenzene:chloroform along with trace amounts of blue MEHPPV dye. (b) SEM of images of spheres made via shape shifting.

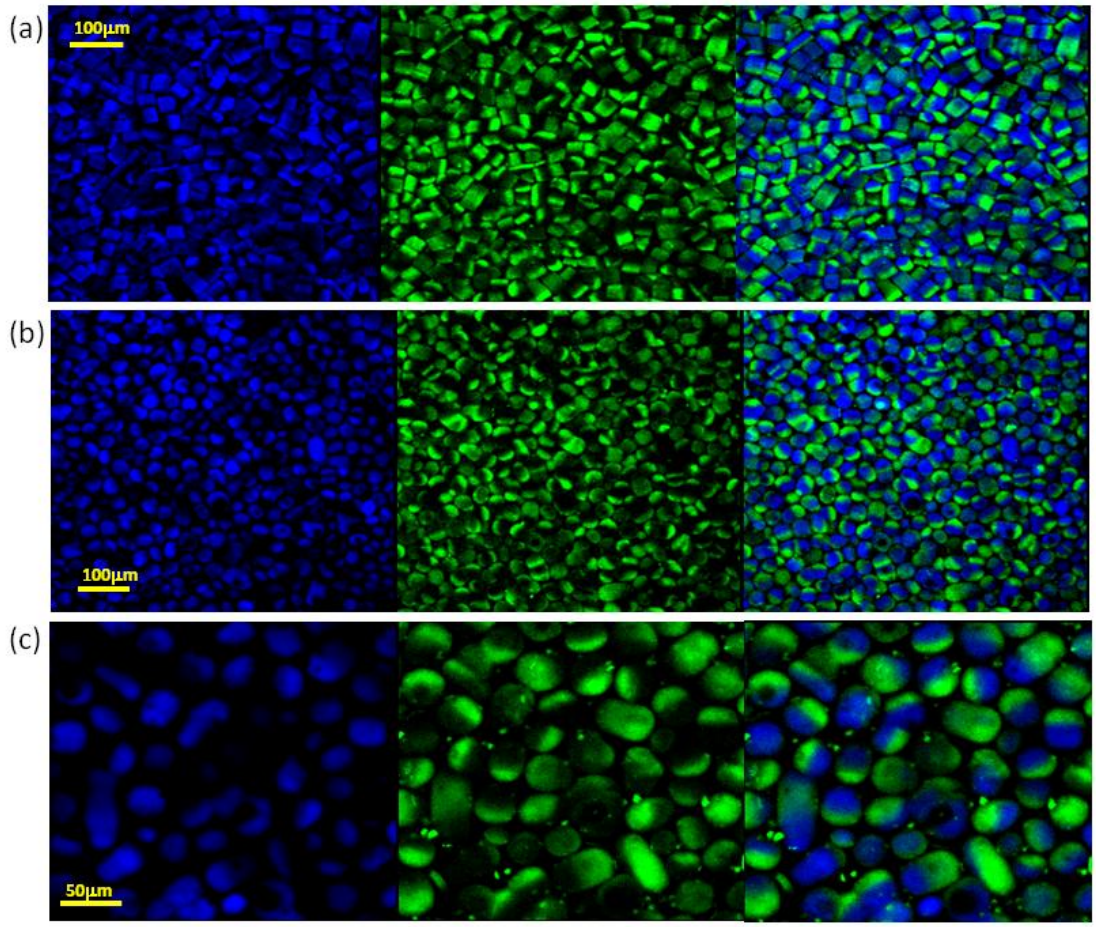


**Figure 9.4** (a) CLSM images of bicompartmental cylinders containing F-POSS in one compartment only. Blue and green fluorescence channels (representing fluorescence from MEHPPV and PTDPV) are shown, followed by their overlay. The green compartment consists of PLGA only, and blue compartment consists of in 95:5 CHCl3:DMF with trace amounts of PTDPV dye, the other compartment consists of F-POSS and PLGA, with POSS:PLGA = 1:10 by wt. in 1:1 hexafluorobenzene:chloroform along with trace amounts of blue MEHPPV dye. (b) , (c) low and high magnification CLSM images of spheres made via shape shifting.

## 9.4 References

[1] M. A. Costolo, J. D. Lennhoff, R. Pawle, E. A. Rietman, A. E. Stevens, *Nanotechnology* **2008**, *19*, 1.
[2] C. L. Casper, J. S. Stephens, N. G. Tassi, D. B. Chase, J. F. Rabolt, *Macromolecules* **2004**, *37*, 573.
[3] M. Bognitzki, W. Czado, T. Frese, A. Schaper, M. Hellwig, M. Steinhart, A. Greiner, J. H. Wendorff, *Advanced Materials* **2001**, *13*, 70.
[4] T. Han, D. H. Reneker, A. L. Yarin, *Polymer* **2007**, *48*, 6064.
[5] A. L. Yarin, S. Koombhongse, D. H. Reneker, *J. App. Phys.* **2001**, *89*, 3018.
[6] M. S. Oreilly, L. Holmgren, Y. Shing, C. Chen, R. A. Rosenthal, M. Moses, W. S. Lane, Y. H. Cao, E. H. Sage, J. Folkman, *Cell* **1994**, *79*, 315.
[7] S. Mitragotri, J. Lahann, *Nat. Mater.* **2009**, *8*, 15.
[8] R. P. A. Hartman, D. J. Brunner, D. M. A. Camelot, J. C. M. Marijnissen, B. Scarlett, *J. Aerosol Sci.* **2000**, *31*, 65.

# APPENDIX

## ISOPROPANOL INDUCED PARTICLE COLLAPSE

In chapter 3, electrohydrodynamic atomization was employed to create biodegradable red blood cell shaped templates which in turn were used to fabricate hydrogel particles mimicking the physico-chemical properties of RBCs. While such particles can be made directly during jetting, another process that resulted in similar particles is described in this section. When monocompartmental spherical particles made from PLGA 8515 (Figure A1 b, 4.5:100 w/w ratio of PLGA8515 in 97:3 Chloroform:DMF by vol.) via electrohydrodynamic atomization were harvested from the substrate and incubated in isopropanol for 12h, the particles collapsed into RBC like particles. The SEM images indicate uniformly collapsed particles (Figure A1 c). The CLSM and corresponding DIC images (Figure A1 d) show the migration of the dye into the periphery of the particles. The reason for this collapse is not clearly understood, considering that isopropanol was found to be a non solvent for PLGA 8515. The collapse was observed regardless of the number of compartments in the spherical particles; CLSM and DIC images of collapsed bi- and tri-compartmental particles are shown in Figures A2 a-d which exhibit a clear migration of the dyes to the periphery of the particles, remarkably, the anisotropic nature of the particles is retained after collapse. The reasons for this remain

unclear as well. Two reasons for particle collapsed may be suggested: (i) the particles underwent a loss of mass due to polymer fluidization via interaction between the polymer, isopropanol and residual solvents in the particle and/or (ii) The particles were hollow to begin with and collapsed due to osmotic pressure exerted by the external environment. To investigate mechanism (i), particles were synthesized from PLGA 8515 dissolved a range of solvents with different volatilities: acetonitrile (Figure A3a) and 1:1 THF: DMF by vol (figure A3b). We hypothesized that the particles containing a greater proportion of non volatile solvents would collapse more readily, however, the opposite was observed. Particles made from acetonitrile collapsed readily to the point of dissolution (Figure A3a), whereas those made from larger amounts of DMF (with similar diameters as those resulting from more volatile solvents) did not collapse at all (Figure A3b). This maybe due to higher polymer concentrations. Spherical particles synthesized from a low molecular weight PLGA (10kD) from 97:3 chloroform: DMF collapsed readily and even seemed to lose their structural integrity (Figure A3c). From this standpoint, the collapse of PLGA 8515 particles may represent a point between spheres and complete dissolution. Furthermore, when particles synthesized from 97:3 Chloroform DMF were dried in vacuum for 12h to remove residual solvent, they still collapsed (data not shown). However, SEM analysis of collapsed particles revealed some debris (Figure A5), which may support this mechanism. Mechanism (ii) seems unlikely considering that CLSM images of particles show dyes distributed uniformly in the bulk of particles. However, a detailed cross-sectional analysis of particles maybe required.

Particle aggregation induced by harvesting them from the collecting substrate seems to be an important factor that favors collapse, because when the collecting substrate (a piece of Al foil onto which particles deposit as a fine monolayer during the jetting process) containing particles was incubated directly in isopropanol, the collapse was not observed (Figure A4). Once collapsed, the entire mass of particles formed an aggregate which was difficult to disperse into individual particles even after ultra-sonication. To summarize, several other factors may play a role in inducing collapse: nature of solvent (polarity), polymer molecular weight, transport of the solvent and non-solvent in the polymer and arrangement of polymer chains in the spherical particles after electrohydrodynamic processing, and a more detailed study of these different variables is required before an exact mechanism can be proposed.

## Figures and tables

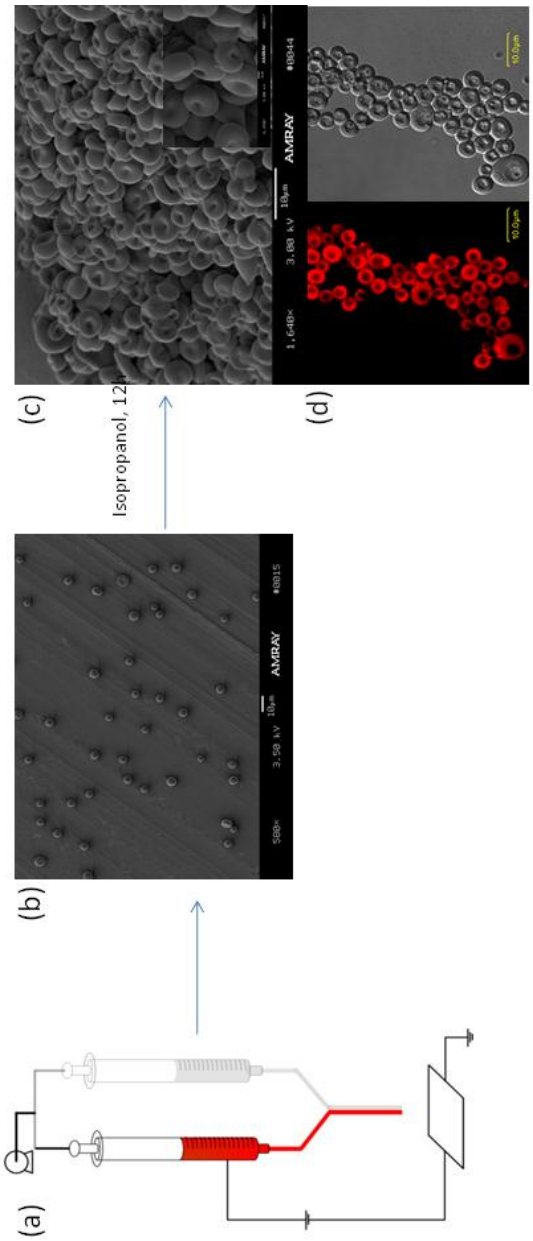


**Figure A1.** (a) Schematic depicting electrohydrodynamic co-jetting from single and dual capillaries. (b) Monophasic PLGA 8515 particles directly after jetting from a 4.5:100 w/w PLGA : solvent with the solvent being 97:3 Chloroform:DMF by vol., the flow rate was 0.4 ml/h and the voltage was 6kV. The solution was also labeled with ADS306PT, a red polythiophene fluorophore. (c) Collapsed particles after incubation of (b) in isopropanol for 12 h. Inset shows magnified image. (d) CLSM and corresponding DIC image of collapsed particles with fluorescence from the dye being visible only at the periphery of the particle. All scale bars depict 10 µm, and scale bar in the inset depicts 1 µm.

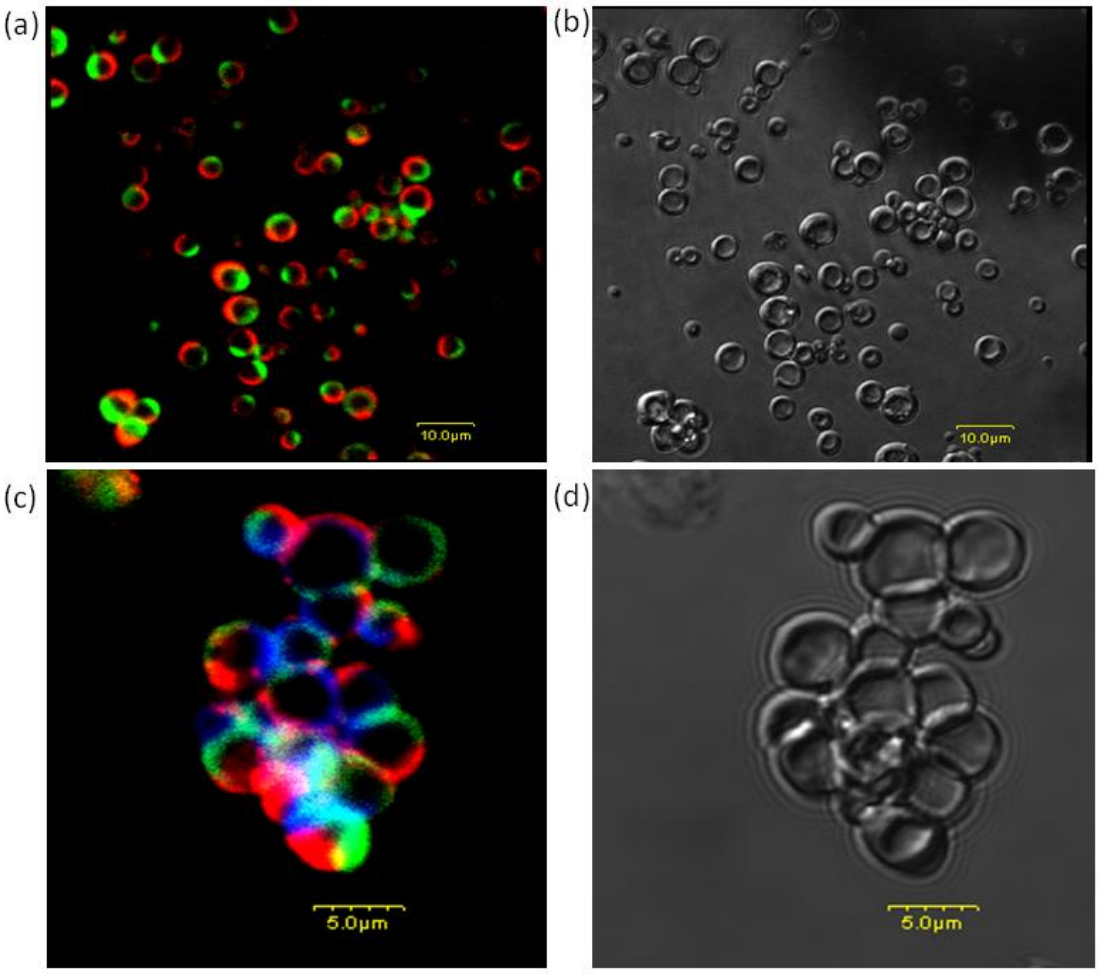


**Figure A2** CLSM and corresponding DIC images of (a)-(b) Bicompartmental particles and (c)-(d) Tricompartmental particles resulting from isopropanol induced particle collapse.

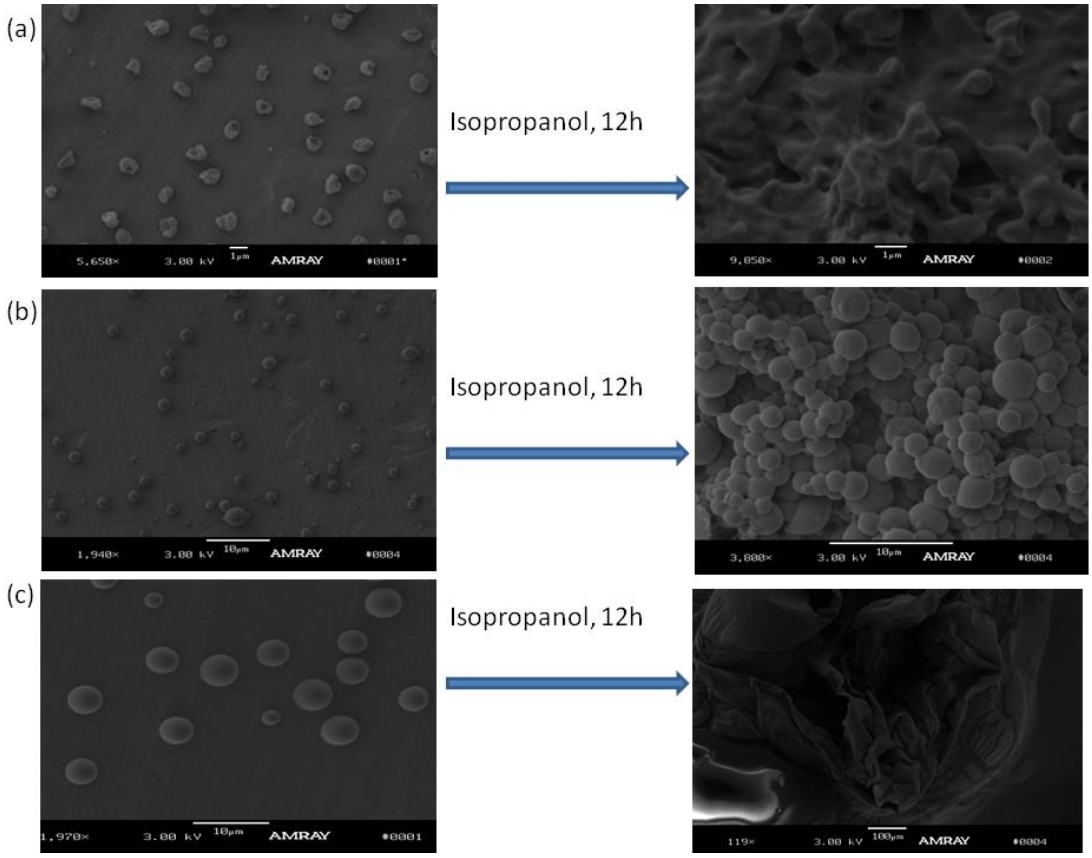


**Figure A3** (a) Particles synthesized from 7:100 w/w PLGA 8515 in acetonitrile at 0.2 ml/h. Particles seem to collapse to the point of dissolution/disintegration after incubation in isopropanol (b) Particles made from 11:100 w/w PLGA 8515 in 1:1 THF: DMF, which do not collapse after isopropanol incubation. (c) Particles synthesized from a low molecular weight (10kD, Purac biomaterials) PLGA dissolved in 97:3 Chloroform: DMF, before and after isopropanol incubation. Scale bars indicate 1µm for (a) and 10 µm for all others.

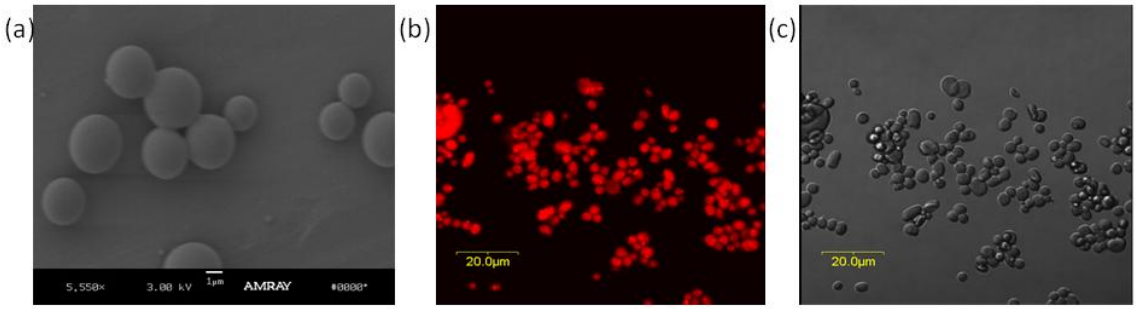


**Figure A4** Effect of particle aggregation on isopropanol induced collapse. The collecting substrate containing a monolayer of monophasic particles was incubated with isopropanol for 12h, which did not result in particle collapse, as shown in (a) SEM image of particles after isopropanol incubation (b)-(c) CLSM (and corresponding DIC) image showing distribution of dyes throughout the bulk of the particles.

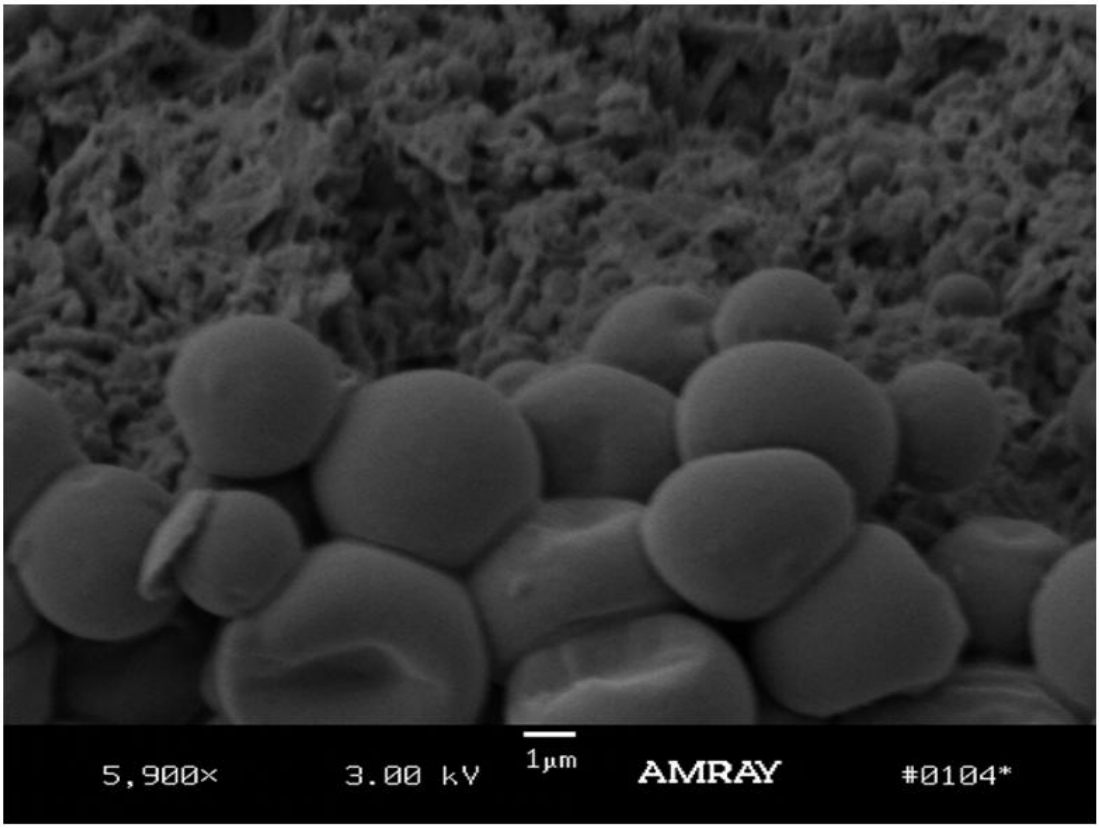


**Figure A5.** SEM images of monophasic collapsed PLGA particles showing debris in the background, indicative of collapse through mass loss from particles.